



NATIONAL AUTONOMOUS UNIVERSITY OF MEXICO
MASTER AND DOCTORAL PROGRAM IN ENGINEERING
INSTITUTE OF ENGINEERING
STRUCTURES

EXPERIMENTAL AND NUMERICAL STUDY OF CONCRETE COLUMNS LATTICED WITH A
STEEL JACKET

THESIS
MASTER IN STRUCTURAL ENGINEERING

MASTER THESIS BY:
JORFRAN ALCARAZ VÁZQUEZ

SUPERVISORS:
DR. SERGIO MANUEL ALCOCER MARTÍNEZ DE CASTRO
Institute of Engineering, UNAM

DR. AMADO GUSTAVO AYALA MILIÁN
Institute of Engineering, UNAM

CIUDAD UNIVERSITARIA, CD. MX.,

JANUARY 2025



UNIVERSIDAD NACIONAL AUTÓNOMA DE MÉXICO
PROGRAMA DE MAESTRÍA Y DOCTORADO EN INGENIERÍA
INSTITUTO DE INGENIERÍA
ESTRUCTURAS

ESTUDIO EXPERIMENTAL Y NUMÉRICO DE COLUMNAS DE CONCRETO ENCAMISADAS
CON ELEMENTOS METÁLICOS

TESIS
QUE PARA OPTAR POR EL GRADO DE:
MAESTRO EN INGENIERÍA

PRESENTA:
JORFRAN ALCARAZ VÁZQUEZ

TUTORES:
DR. SERGIO MANUEL ALCOCER MARTÍNEZ DE CASTRO
Instituto de Ingeniería, UNAM

DR. AMADO GUSTAVO AYALA MILIÁN
Instituto de Ingeniería, UNAM

CIUDAD UNIVERSITARIA, CD. MX.,

ENERO 2025

JURADO ASIGNADO:

Presidente: Dr. Oscar Alberto López Bátiz

Secretario: Dr. Amado Gustavo Ayala Milián

1^{er}. Vocal: Dr. Sergio Manuel Alcocer Martínez de Castro

2^{do}. Vocal: Dr. Juan José Pérez Gavilán Escalante

3^{er}. Vocal: Dr. Marcos Mauricio Chávez Cano

Lugar donde se realizó la tesis: Ciudad Universitaria, Instituto de Ingeniería, U.N.A.M., CD. MX., MÉXICO.

TUTORES DE TESIS:

DR. SERGIO M. ALCOCER MARTÍNEZ DE CASTRO

DR. AMADO GUSTAVO AYALA MILIÁN

FIRMA

FIRMA

Contents

ABSTRACT	VIII
ACKNOWLEDGEMENTS	IX
LIST OF FIGURES	X
LIST OF TABLES	XV
NOTATION	XVI
ABBREVIATIONS	XVII

1 INTRODUCTION

1.1 MOTIVATION OF THE STUDY	1
1.2 SCOPE	3
1.3 MAIN GOALS	3
1.4 SPECIFIC GOALS	4
1.5 BACKGROUND AND CONTEXT	4
1.5.1 OLD RC BUILDINGS	5
1.5.2 MEXICO IN CONTEXT	6

2 LITERATURE REVIEW

2.1 INTRODUCTION	8
2.2 EXPERIMENTAL PROGRAMS	9
2.3 ANALYTICAL MODELS	11
2.4 STEEL JACKET PARAMETERS	12
2.4.1 GROUT MATERIAL	13
2.4.2 STRIP CONFIGURATION	13
2.4.3 ANGLE SIZE	14
2.4.4 CONNECTION TO SPECIMEN HEAD	14
2.5 FINAL REMARKS	15

3 EXPERIMENTAL STUDY

3.1	OBJECTIVES AND SCOPE	16
3.2	EXPERIMENTAL PROGRAM	16
3.2.1	SPECIMEN DETAILS	17
3.2.2	DESIGN CRITERIA	18
3.2.3	CONSTRUCTION PROCESS	19
3.2.3.1	<i>Preliminary Works</i>	19
3.2.3.2	<i>Column and Foundation Steel Work</i>	19
3.2.3.3	<i>Concrete Placement</i>	20
3.2.3.4	<i>Steel Jacket</i>	21
3.2.4	TEST PREPARATIONS	22
3.2.5	MATERIALS	22
3.2.5.1	<i>Hydro-Stone</i>	22
3.2.5.2	<i>Concrete</i>	22
3.2.5.3	<i>Sika Grout</i>	23
3.2.5.4	<i>Reinforcing Steel Bars</i>	24
3.2.5.5	<i>Steel Angles and Battens</i>	24
3.2.5.6	<i>Anchors</i>	24
3.2.6	LOADING SYSTEM	24
3.2.7	LOADING PROTOCOL	25
3.2.7.1	<i>Load Control</i>	26
3.2.7.2	<i>Displacement Control</i>	26
3.2.8	MODEL SUPPORTS	26
3.2.9	INSTRUMENTATION	27
3.2.9.1	<i>External</i>	27
3.2.9.2	<i>Internal</i>	29
3.2.10	DATA ACQUISITION	29
3.3	DEFINITION OF STUDY PROTOTYPES	30
3.3.1	SPECIMEN CO	30
3.3.2	SPECIMEN CO*	30
3.3.3	SPECIMEN S8	31
3.3.4	SPECIMEN S9	31
3.4	PARAMETER DEFINITION	32
3.4.1	DRIFT RATIO AND HYSTERESIS CURVE	32
3.4.1.1	<i>Drift Components</i>	32

3.4.2	ROTATION	33
3.4.3	SHEAR DISTORTION	33
3.5	EXPERIMENTAL RESULTS	34
3.5.1	SPECIMEN CO	34
3.5.1.1	<i>Damage Evolution</i>	34
3.5.1.2	<i>Final Damage State</i>	36
3.5.1.3	<i>Hysteresis Behaviour</i>	36
3.5.1.4	<i>Column Rotation</i>	37
3.5.1.5	<i>Foundation Rotation and Sliding</i>	38
3.5.1.6	<i>Strain Gauges Readings</i>	39
3.5.2	SPECIMEN CO*	40
3.5.2.1	<i>Damage Evolution</i>	40
3.5.2.2	<i>Final Damage State</i>	43
3.5.2.3	<i>Hysteresis Behaviour</i>	44
3.5.2.4	<i>Column Rotation</i>	45
3.5.2.5	<i>Foundation Rotation and Sliding</i>	45
3.5.2.6	<i>Strain Gauges Readings</i>	46
3.5.3	SPECIMEN S8	47
3.5.3.1	<i>Damage Evolution</i>	47
3.5.3.2	<i>Final Damage State</i>	53
3.5.3.3	<i>Hysteresis Behaviour</i>	53
3.5.3.4	<i>Column Rotation</i>	54
3.5.3.5	<i>Foundation Rotation and Sliding</i>	55
3.5.3.6	<i>Crack Width History</i>	55
3.5.3.7	<i>Strain Gauges Readings</i>	56
3.5.4	SPECIMEN S9	59
3.5.4.1	<i>Damage Evolution</i>	59
3.5.4.2	<i>Final Damage State</i>	64
3.5.4.3	<i>Hysteresis Behaviour</i>	64
3.5.4.4	<i>Column Rotation</i>	65
3.5.4.5	<i>Foundation Rotation and Sliding</i>	66
3.5.4.6	<i>Crack Width History</i>	66
3.5.4.7	<i>Strain Gauges Readings</i>	67
3.5.5	COMPARISON	70
3.5.5.1	<i>Crack Pattern</i>	70
3.5.5.2	<i>Lateral Load Bearing Capacity</i>	72

3.5.5.3	<i>Response Envelopes</i>	73
3.5.5.4	<i>Stiffness</i>	75
3.5.5.5	<i>Ductility</i>	77
3.5.5.6	<i>Strain Gauges Comparison</i>	77
3.5.5.7	<i>Column Local Deformation</i>	78

4 FINITE ELEMENT ANALYSIS **81**

4.1	THEORETICAL BASIS	81
4.1.1	FINITE ELEMENT FORMULATION	82
4.1.1.1	<i>3D Solid Elements</i>	82
4.1.1.2	<i>Truss 3D Elements</i>	83
4.1.1.3	<i>External Cable</i>	83
4.1.1.4	<i>Interface Element</i>	84
4.1.1.5	<i>Global and Local Coordinate Systems for Element Load</i>	85
4.1.2	CONSTITUTIVE MODELS	86
4.1.2.1	<i>General Considerations</i>	86
4.1.2.2	<i>Concrete</i>	86
4.1.2.3	<i>Reinforcing Stress-Strain Laws</i>	97
4.1.2.4	<i>Interface Material Model</i>	98
4.1.3	FULL NEWTON-RAPHSON METHOD FOR THE NUMERICAL SOLUTION	99
4.2	MODELLING	99
4.2.1	MATERIAL PARAMETERS	100
4.2.1.1	<i>Concrete</i>	100
4.2.1.2	<i>Steel Plates</i>	101
4.2.1.3	<i>Reinforcing Steel</i>	101
4.2.1.4	<i>Post-tensioned Bars</i>	102
4.2.1.5	<i>Steel Angles and Battens</i>	102
4.2.1.6	<i>3D Slab-Foundation Interface</i>	102
4.2.1.7	<i>3D Steel-Concrete Interface for Steel Jacketing</i>	103
4.2.2	TOPOLOGY	103
4.2.3	MESHING	105
4.2.4	CONTACTS DEFINITION	106
4.2.5	BOUNDARY CONDITIONS AND SUPPORTS	108
4.2.6	LOAD STEPS	108

4.2.7	MONITORING POINTS	109
4.2.8	SOLUTION PARAMETERS	110
4.3	MODEL CALIBRATION	111
4.3.1	BOUNDARY CONDITIONS	111
4.3.2	MESH ANALYSIS	121
4.3.3	MATERIAL PARAMETER ANALYSIS	121
4.4	FINAL REMARKS	122
5 RECOMMENDATIONS		123
<hr/>		
5.1	EXPERIMENTAL	123
5.2	NUMERICAL	125
6 CONCLUSIONS		126
<hr/>		
6.1	EXPERIMENTAL TESTS	126
6.2	NUMERICAL ANALYSIS	127
6.3	FUTURE WORKS	128
7 APPENDIX		129
<hr/>		
7.1	MATERIALS STRESS VS STRAIN TEST CURVES	129
7.1.1	REINFORCING STEEL USED IN SPECIMENS CO, CO*, S1, S2 AND S3	129
7.1.2	CONCRETE CYLINDER TEST OF SPECIMEN CO	130
7.1.3	CONCRETE CYLINDER TEST OF SPECIMEN S8 AND S9	130
7.1.4	STEEL TEST CURVES OF ANGLES AND BATTENS	131
7.2	STRAIN GAUGES RECORD OF INTERNAL AND EXTERNAL INSTRUMENTATION	132
7.2.1	INTERNAL STRAIN GAUGE OF SPECIMEN CO	133
7.2.2	INTERNAL STRAIN GAUGE OF SPECIMEN CO*	135
7.2.3	STRAIN GAUGE OF SPECIMEN S8	137
7.2.3.1	<i>Internal Strain Gauges</i>	<i>137</i>
7.2.3.2	<i>External Strain Gauges</i>	<i>139</i>

7.2.4	STRAIN GAUGE OF SPECIMEN S9	141
7.2.4.1	<i>Internal Strain Gauges</i>	141
7.2.4.2	<i>External Strain Gauges</i>	143

8	REFERENCES	145
----------	-------------------	------------

DEDICATORY

And there you stand, making my life possible. Raise my hands up to heaven, but only you could know. My whole world stands in front of me, by the look in your eyes. My whole life stretches in front of me, reaching up like a flower, leading my life back to the soil... My love, my wife, my lifetime partner.

Alison A. García Rentería

To the woman who taught me the power of unconditional love, where mistakes are just stepping stones, and forgiveness is the cornerstone of our bond. Here's to the ever-enduring love of a mother.

Beatriz Vázquez Martínez

To the brother that have brought me joy and support till the very last.

Jyan Alcaraz Vázquez

To my close family

José Francisco Vázquez Martínez

Beatriz Martínez Delgado

José Francisco Vázquez Martínez Jr.

Rocco

For the love of life
There's a trade off
We could lose it all
But we'll go down fighting

— *David Alan Batt (DS)* —

ABSTRACT

An experimental (chapter 3) and numerical study (chapter 4) was performed with the aim of evaluating two proposals for steel jacketing (SJ) to strengthen reinforced concrete (RC) columns. The experimental study involved testing two RC columns, with rectangular sections measuring 45x90 cm, under lateral reverse cyclic loading. These tested columns were externally strengthened using a latticed SJ made up of steel angles and battens of grade A36 steel. The tested RC columns had typical deficiencies observed in concrete structures in Mexico City in the 1950s, such as insufficient and inadequate transverse reinforcing, stirrup hooks at 90 degrees, and low concrete strength. The two tested proposals of SJ had the following characteristics: the first consisted of rectangular angles with a flange width of 152.4 mm (6 inches), while the second consisted of rectangular angles with a flange width of 50.8 mm (2 inches). Both proposals maintained a constant width of 76.2 mm (3 inches) for the battens, a thickness of 6.35 mm (1/4 inch) for the angles and battens. Two previous experimental study specimens were used as benchmarks for comparing the lateral response of the tested RC columns strengthened with SJ. The benchmark specimens had the same dimensions, reinforcing detailing, and material properties as the specimens strengthened with SJ.

A finite element analysis (FEA) was performed using ATENA Software, in which three models were created: one SJ proposal and the two benchmark specimens (section 4.2). The aim of the FEA was to investigate the parameters involved in the overall lateral response for the SJ specimen. The approach in the finite element models (FEMs) of the three specimens involved the imposition of lateral monotonic displacement, to compare the numerical response with the backbone curves derived from the hysteresis curves of the experimental programme. The principal characteristics of the FEMs were the use of the symmetry plane as presented in the experiments (geometrically and for load application), the use of a multi-linear function for the constitutive model of the reinforcing steel, the implementation of a 3D interface between the RC foundation and the reaction slab, and between the SJ and the RC column, and the use of the Full Newton-Raphson Method for the solution.

The important findings from the results of the specimens tested with SJ in the experimental programme were the change of the brittle shear failure mode, observed in the benchmark specimens, to a more ductile flexural failure mode, generating a plastic hinge in the foundation-reaction slab joint. Additionally, the SJ significantly increased the strain capacity and ductility, and enhanced the lateral displacement capacity by up to 3.23 times for the S9 specimen. Furthermore, the SJ reduced the occurrence of cracks, controlled their width through passive confinement, and distributed the crack patterns within the column's core.

Regarding the results of the experimental programme and the numerical analysis, the numerical representation of the principal cracks recorded in the benchmark specimens, which exhibited brittle shear failure, was accurately depicted in the FEA. For the experimental backbone curves of the three specimens modelled, the FEM accurately represented the overall lateral behaviour, including the plastic strain in the SJ in the same zones as recorded in the experimental programme. Furthermore, the lateral monotonic displacement imposition approach used in the FEA proved to be sufficient to represent the overall behaviour of the specimens modelled. Finally, the most important material parameters that control the lateral behaviour in the FEA were the fracture energy, the tension stiffening, and the tensile strength of concrete.

Keywords: RC Column; Steel Jacketing; Strengthening Technique; Numerical Analysis; Finite Element Modelling; Shear Brittle Failure; Plastic Hinge; Hysteretic Response; Lateral Monotonic Displacement Imposition; Fracture Mechanics.

ACKNOWLEDGEMENTS

Dr. Amado Gustavo Ayala Milián¹

Dr. Sergio Manuel Alcocer Martínez de Castro¹

Dr. Guillermo Martín Roeder Carbo²

Dr. Óscar Alberto López Bátiz³

Dr. Marcos Mauricio Chávez Cano¹

M. I. José Juan Pérez Fabila¹

M. I. Rogelio Guevara Lima¹

Ing. Osvaldo Contreras Reyes³

M. I. Juan José Gómez García³

Dr. Carlos Emiliano González Calva¹

Dr. Héctor Rodrigo Amezcua Rivera¹

Dr. César Paniagua¹

Dr. Renato Berrón Ruíz⁴

Arturo Fuente Lara⁵

Ing. Vanessa Yadei González Ángel³

Ing. José E. Andrade Gamboa⁵

Ing. Sara Palma Martínez⁵

Ing. Carlos F. Vargas Altamirano⁵

A la Universidad Nacional Autónoma de México y al Instituto de Ingeniería

Al Consejo Nacional de Humanidades, Ciencias y Tecnologías, CONAHCyT

Al noble pueblo de México, cuya generosidad me ha proporcionado el apoyo económico para forjar mi camino académico, le debo una gratitud eterna. En mi alma llevaré, como un faro luminoso, el deber de servir a la sociedad.

¹ Instituto de Ingeniería, Universidad Nacional Autónoma de México

² Universidad de Colima

³ Centro Nacional de Prevención de Desastres

⁴ El Instituto para la Seguridad de las Construcciones en la Ciudad de México, Gobierno de la Ciudad de México

⁵ Universidad Nacional Autónoma de México

LIST OF FIGURES

Fig. 1.1—Example of potential local collapse due to a failure of a column	2
Fig. 1.2—Steel jacketing in a column using steel angles and battens (Stelios, 2023)	2
Fig. 1.3—Elevation view of a non-ductile RC frame. Taken from Aboutaha (1994).	6
Fig. 2.1—Confinement due to SJ: (a) effective confinement in elevation; (b) confinement pressure distribution at batten level; (c) effective confinement in plan. Taken from Nagaprasad (2009).	9
Fig. 2.2—Schematic diagrams of load on steel jacket. Taken from Badalamenti (2010).	9
Fig. 2.3—Confining pressure distribution at batten level. Taken from Sen & Begum (2017).	12
Fig. 2.4—Effect of grout materials on the ultimate load capacity. Taken from Sen & Begum (2017).	13
Fig. 2.5—Effect of strip configuration: (a) strip spacing; (b) strip thickness. Taken from Sen & Begum (2017).	14
Fig. 2.6—Effect of angle size on ultimate axial load capacity (Sen & Begum, 2017)	14
Fig. 2.7—Effect of steel angle connectivity to specimen head on ultimate axial load capacity (Sen & Begum, 2017)	15
Fig. 3.1—General dimensions of specimen	18
Fig. 3.2—Steel Jacketing	18
Fig. 3.3—Reinforcing steel bars detailing: (a) column; (b) foundation	18
Fig. 3.4—Internal instrumentation procedure: (a) surface preparation; (b) strain gauges placed; (c) protection cover (courtesy: S. M. Alcocer)	19
Fig. 3.5—Steel work: (a) foundation; (b) column; (c) final work	19
Fig. 3.6—Formwork procedure: (a) main materials; (b) pouring of release agent; (c) work finished (courtesy: S. M. Alcocer)	20
Fig. 3.7—Concrete pouring for the foundation: (a) first concrete layer; (b) vibration works; (c) surface finishes	20
Fig. 3.8—(a) Preparation of cylinders of the foundation and column concrete mix; (b) specimen final state (courtesy: S. M. Alcocer)	21
Fig. 3.9—Steel jacketing: (a) fillet weld detail for each specimen, frontal and lateral view; (b) plane view	21
Fig. 3.10—(a) lifting and placed of pre-armed steel jacket; (b) pouring of Sika grout	22
Fig. 3.11—View of the load system: (a, c) elevation view; (b, d) plan view	25
Fig. 3.12—Load control history	26
Fig. 3.13—Displacement control history	26
Fig. 3.14—Supports for reaction slab: (a) plane view; (b) elevation view	27
Fig. 3.15—Location of external instrumentation: (a) lateral transducer; (b) face transducers; (c) micrometres; (d) LED location	28
Fig. 3.16—External strain gauges in steel jacket	29
Fig. 3.17—Location of strain gauges, north face view	29
Fig. 3.18—Specimen CO at the beginning of the test: (a) north; (b) south; (c) east and (d) west face (courtesy: S. M. Alcocer)	30
Fig. 3.19—Specimen CO* at the beginning of the test: (a) north; (b) south; (c) east and (d) west face (courtesy: S. M. Alcocer)	30
Fig. 3.20—Detail of specimen S8	31

Fig. 3.21—Detail of specimen S9	31
Fig. 3.22—Drift main components: (a) total lateral deformation; (b) lateral flexural deformation; (c) lateral shear deformation. Adapted from Aguilar-Ramos (1997).	32
Fig. 3.23—Zones established for the calculation of rotations and curvatures	33
Fig. 3.24—First cracks: (a) front face; (b) first crack; (c) second crack	35
Fig. 3.25—First horizontal cracks at middle height: (a) load = +196.1 kN, east face; (b) load = -196.1 kN, west face	35
Fig. 3.26—Damage at drift +0.005 and -0.005 respectively: (a) load = -636.5 kN; (b) load = +649.7 kN (courtesy: S. M. Alcocer)	35
Fig. 3.27—Damage at drift ± 0.01 : (a) Drift +0.01; (b) south face; (c) west face; (d) damage at -0.01 (courtesy: S. M. Alcocer)	35
Fig. 3.28—Crack evolution: (a) drift +0.005; (b) drift +0.01; (c) drift +0.015; (d) drift +0.02; (e) final state (courtesy: S. M. Alcocer)	36
Fig. 3.29—Column O final state, end of test (courtesy: S. M. Alcocer)	36
Fig. 3.30—Hysteresis plot of specimen CO	37
Fig. 3.31—Rotation of zones in concrete column core using micrometres	37
Fig. 3.32—Rotation of zones in concrete column core using displacement transducer	38
Fig. 3.33—Foundation history of rotation (a) and sliding (b) of the specimen CO	38
Fig. 3.34—Internal strain gauges that recorded yielding: red (yield); green (elastic)	39
Fig. 3.35—Yielding recorded by strain gauges in specimen CO	40
Fig. 3.36—First horizontal cracks at load control protocol: (a) +196.13 kN; (b) second +196.13 kN; (c) -196.13 kN	41
Fig. 3.37—First inclined cracks at drifts: (a) +0.005; (b) -0.005; (c) second +0.005; (d) second -0.005	41
Fig. 3.38—Damage at drift of: (a) +0.01; (b) -0.01; (c) zero drift	41
Fig. 3.39—Damage at a drift of: (a) +0.015; (b) -0.015	42
Fig. 3.40—Damage at a second drift of: (a) +0.015; (b) -0.015	42
Fig. 3.41—Damage at a drift of +0.02	42
Fig. 3.42—Damage at a drift of -0.02	42
Fig. 3.43—Damage at a second drift of +0.02	43
Fig. 3.44—Damage at a second drift of -0.02	43
Fig. 3.45—Crack evolution of specimen CO* for positive drift peaks	43
Fig. 3.46—Final damage state	44
Fig. 3.47—Hysteresis plot of specimen CO*	44
Fig. 3.48—Rotation of zones in concrete column core using micrometres	45
Fig. 3.49—Rotation of zones in concrete column core displacement transducers	45
Fig. 3.50—Foundation history of rotation (a) and sliding (b) of the specimen CO*	46
Fig. 3.51—Internal strain gauges that recorded yielding: red (yield); green (elastic); yellow (damaged or not recorded)	46
Fig. 3.52—Yielding recorded by strain gauges in specimen CO*	47
Fig. 3.53—Specimen S8: (a) first horizontal crack LE in east face; (b) in west face LW; (c) north face	48
Fig. 3.54—First inclined crack: (a) north face; (b) south face; (c) second inclined crack	48

Fig. 3.55—(a) Transverse crack parallel to steel batten at a drift of +0.0005	49
Fig. 3.56—Damage at a drift of +0.01: (a) north face; (b) south face; (c) west face; (d) zero load	49
Fig. 3.57—Damage at a drift of +0.02: (a) north face; (b) east face; (c) south and west face	49
Fig. 3.58—Damage at a drift of +0.03: (a) north face; (b) damage in foundation-column joint; (c) south and west face	50
Fig. 3.59—Damage at a drift of +0.04: (a) north face; (b) white wash peeling on batten; (c) south and west face	50
Fig. 3.60—Damage in the steel jacket at a drift of +0.045	50
Fig. 3.61—Damage at a drift of +0.05: (a) north face; (b) concrete crack in foundation-column east face joint; (c) fell off the white wash of middle batten	51
Fig. 3.62—Damage state at a drift of +0.06: (a) north face; (b) bottom batten buckling; (c) south face	51
Fig. 3.63—Damage state at a drift of -0.06	51
Fig. 3.64—Damage state at a drift of +0.07	52
Fig. 3.65—Damage state at a drift of +0.08	52
Fig. 3.66—Damage evolution of the positive drift peaks	52
Fig. 3.67—Final damage state	53
Fig. 3.68—Fracture of longitudinal bars in specimen S8 in east and west face	53
Fig. 3.69—Hysteresis plot of specimen S8	54
Fig. 3.70—Rotation of zones in concrete column core using micrometres	54
Fig. 3.71—Rotation of zones in concrete column core using displacement transducer	55
Fig. 3.72—Foundation history of rotation (a) and sliding (b) of specimen S8	55
Fig. 3.73—Crack width history for labelled cracks for Specimen S8	56
Fig. 3.74—Internal strain gauges that recorded yielding: red (yield); green (elastic); yellow (damaged or not recorded)	56
Fig. 3.75—Yield recorded by strain gauges in specimen S8	57
Fig. 3.76—External strain gauges that recorded yielding: red (yield); yellow (elastic); purple (damaged or not recorded)	58
Fig. 3.77—Yield recorded by external strain gauges of specimen S8	59
Fig. 3.78—Specimen S9 at the beginning of the test	59
Fig. 3.79—First horizontal crack at load control of ± 196 kN	60
Fig. 3.80—First inclined cracks at drift of ± 0.0005	60
Fig. 3.81—Damage at drift of ± 0.01	61
Fig. 3.82—Damage state at drift of -0.015	61
Fig. 3.83—Damage state at drift of ± 0.02	61
Fig. 3.84—Damage at drift of ± 0.03	61
Fig. 3.85—First appearance spalling of white wash in middle steel batten at drift of +0.035	62
Fig. 3.86—Damage state at drift of ± 0.04	62
Fig. 3.87—Damage state at drift of ± 0.05	62
Fig. 3.88—Damage state at drift of ± 0.055 when occurred the fracture of a longitudinal bar related to east face	62
Fig. 3.89—Damage at drift of ± 0.06	63
Fig. 3.90—Damage state at: (a) drift ± 0.07 ; (b) drift +0.08	63
Fig. 3.91—Damage evolution of the negative drift peaks	63

Fig. 3.92—Final damage state of specimen S9	64
Fig. 3.93—Fracture of longitudinal bars in specimen S9 in west and east face	64
Fig. 3.94—Hysteresis plot of specimen S9	65
Fig. 3.95—Rotation of zones in concrete column core using micrometres	65
Fig. 3.96—Rotation of zones in concrete column core using displacement transducers	66
Fig. 3.97—Foundation history of rotation (a) and sliding (b) of specimen S9	66
Fig. 3.98—Crack width history for labelled cracks for Specimen S9	67
Fig. 3.99—Internal strain gauges that reached yielding: red (yield); green (elastic)	67
Fig. 3.100—Yielding recorded by strain gauges in specimen S9	68
Fig. 3.101—External strain gauges that recorded yielding: red (yield); yellow (elastic); purple (damaged or not recorded)	69
Fig. 3.102—Yielding recorded by external strain gauges of specimen S9	69
Fig. 3.103—Backbone curves of hysteresis curves	74
Fig. 3.104—Elastic stiffness comparison	75
Fig. 3.105—Stiffness degradation of studied specimens	76
Fig. 3.106—Lateral displacement related to the beginning of yield of the monitored reinforcing bars	78
Fig. 3.107—Lateral displacement related to the beginning of yield of the monitored steel jacket	78
Fig. 3.108—Diagonal displacement recorded by face transducers	79
Fig. 3.109—Horizontal displacement recorded by face transducers	80
Fig. 4.1—3D Solid Elements in ATENA (Červenka et al., 2013)	83
Fig. 4.2—Truss 3D element CCIsoTruss in ATENA (2013)	83
Fig. 4.3—ATENA CCEXternalCable element (adapted from ATENA)	84
Fig. 4.4—ATENA CCIsoGap interface element (Červenka et al., 2013)	85
Fig. 4.5—Local and global coordinate systems for truss and 3D surface load solid element	85
Fig. 4.6—Uniaxial stress-strain law for concrete. Adapted from ATENA (2013).	89
Fig. 4.7—Exponential crack opening law. Adapted from ATENA (2013).	90
Fig. 4.8—Compressive stress-strain diagram	91
Fig. 4.9—Softening-displacement law in compression	91
Fig. 4.10—Definition of localization bands. Adapted from ATENA (2013).	92
Fig. 4.11—Stages of crack opening. Adapted from ATENA (2013).	92
Fig. 4.12—Biaxial failure function for concrete. Adapted from ATENA (2013).	93
Fig. 4.13—Tension stiffening diagram (Taken from ATENA Theory)	94
Fig. 4.14—Rotated crack model. Stress and strain state. Adapted of ATENA (2013).	94
Fig. 4.15—Fixed crack model. Stress and strain state. Adapted of ATENA (2013).	95
Fig. 4.16—Tensile softening and characteristic	97
Fig. 4.17—The multi-linear stress-strain law for reinforcing	97
Fig. 4.18—Failure surface for interface elements. Taken from ATENA (2013).	98
Fig. 4.19—Stress-strain and biaxial failure law	102
Fig. 4.20—Symmetry plane used in the FE model	103

Fig. 4.21—General Macroelements for specimens	104
Fig. 4.22—Foundation-Column mesh compatibility	105
Fig. 4.23—Final mesh of specimens	106
Fig. 4.24—Contacts in the model	107
Fig. 4.25—Boundary conditions and supports of the model	108
Fig. 4.26—Loads due to constructive process: (a) supports; (b) ALP load; (c) USPL load; (d) LDI load	109
Fig. 4.27—General monitoring points	110
Fig. 4.28—Specimen CO FE results: comparison between fixed end response and 3D interface implementation	111
Fig. 4.29—Specimen CO FE response in step 500 with 3D Interface implemented	113
Fig. 4.30—Specimen CO* FE results	114
Fig. 4.31—Specimen CO* FE response in step 500 with 3D Interface implemented	115
Fig. 4.32—Specimen S9 FE results	116
Fig. 4.33—Strain comparison for FEM and experimental test	117
Fig. 4.34—Specimen S9 FE response in step 500 with 3D Interface implemented	118
Fig. 4.35—Representation of bucking of west face reinforcing steel bar on load step 500 for specimen S9	119
Fig. 4.36—Representation of fracture of west face reinforcing steel bar on load step 500 for specimen S9	119
Fig. 4.37—Reinforcing steel Von Misses Stress state sequence for specimen S9	120
Fig. 7.1—Stress vs strain curves of reinforcing steel, Var. $\varnothing = 9.525$ mm [3/8 in]	129
Fig. 7.2—Stress vs strain curves of reinforcing steel, Var. $\varnothing = 25.4$ mm [1 in]	129
Fig. 7.3—Stress vs strain curves for concrete column cylinder test of specimen CO	130
Fig. 7.4—Stress vs strain curves for concrete column cylinder test of specimen S8 and S9	130
Fig. 7.5—Stress vs strain curves for concrete foundation cylinder test of specimen S8 and S9	131
Fig. 7.6—Stress vs strain curves for steel of angles and battens of steel jacketing	131

LIST OF TABLES

Table 3.1—Main variables studied by S. M. Alcocer	17
Table 3.2—Concrete order specification	20
Table 3.3—Mechanical properties of concrete in study specimens	23
Table 3.4—Mechanical properties of reinforcing steel used in specimen CO, CO*, S1, S2 and S3	24
Table 3.5—Internal strain gauge yielding history of specimen CO	39
Table 3.6—Internal strain gauge yielding history of specimen CO*	46
Table 3.7—Internal strain gauge yielding history of specimen S8	57
Table 3.8—External strain gauge yielding history of specimen S8	58
Table 3.9—Internal strain gauge yielding history of specimen S9	68
Table 3.10—External strain gauge yielding history of specimen S9	69
Table 3.11—Crack pattern comparison of positive drifts up to +0.02	71
Table 3.12—Crack pattern of specimens S8 and S9 in higher drift peaks	72
Table 3.13—Ductility of each specimen	77
Table 4.1—Default formulas of material parameters	88
Table 4.2—Properties defined for concrete macroelements	100
Table 4.3—Definition points for the multilinear stress-strain law for reinforcing in the model	102
Table 4.4—Macroelements for the specimens	103
Table 4.5—Macroelements mesh information	105
Table 4.6—Model contact definition	107
Table 4.7—Load steps to run	109
Table 4.8—Tolerances and limits defined for the Newton-Raphson solution method	110
Table 7.1—Internal strain gauge nomenclature	132

NOTATION

A_g	Gross area of concrete section
A_v	Area of shear reinforcement within spacing s
b_w	Width of compression face of member
d	Distance from extreme compression fibre to centroid of longitudinal tension reinforcement
E_c	Modulus of elasticity of concrete
E_s	Modulus of elasticity of reinforcing steel bars
f'_c	Nominal or measured compressive strength of concrete
f'_{cE}	Expected compressive strength of concrete
f_f	Calculated flexural strength of the concrete
f_t	Calculated tensile strength of concrete
f_{sy}	Yield strength for reinforcing steel bars
f_{su}	Ultimate strength for reinforcing steel bars
f_{ytE}	Expected yield strength reinforcing steel bars
G_c	Modulus of rupture for concrete
h	Distance between the applied lateral load and the fixed end (RC column-foundation joint)
M_u	Maximum moment applied
N_u, P_{UG}	Axial load applied on the RC column
R	Drift ratio
R_F	Drift ratio component due to flexure deformation
s	Centre-to-centre spacing of items, such as longitudinal reinforcement, transverse reinforcement or battens in SJ
V_c	Nominal shear strength provided by concrete
V_R	Nominal shear strength of RC column
V_s	Nominal shear strength provided by shear reinforcement
V_u	Maximum shear applied
α_i	Horizontal distance between micrometres installed on the east and south faces of the column in the load step i
Δ_F	Lateral flexural deformation component of horizontal displacement
Δ_S	Lateral shear deformation component of horizontal displacement
Δ_T	Total horizontal displacement measured at the level of application of the lateral load of specimens
γ_S	Drift ratio component due to shear deformation
θ_F, θ_S	Angle formed due to Δ_F and Δ_S , respectively
θ_i	Rotation of the horizontal column section in the i zone
ℓ_{Ei}, ℓ_{Wi}	East and north lecture of the micrometre installed on the east and south faces of the column in the load step i
λ_s	Size effect factor (ACI, 2019) or reduction factor (CDMX, 2023a).

ABBREVIATIONS

CENAPRED	Centro Nacional de Prevención de Desastres (National Centre for Disaster Prevention)
DMM	Dynamic Measurement Machine
FEA	Finite Element Analysis
FE	Finite Element
FEM	Finite Element Methods
FRP	Fibre-Reinforced Polymer
LEG	Laboratorio de Estructuras Grandes (Large-Scale Structures Laboratory)
LVDT	Linear Variable Differential Transducer
PBEE	Performance-Based Earthquake Engineering
PPE	Personal Protective Equipment
SJ	Steel Jacket
TLF	Total Lagrangian Formulation
ULF	Updated Lagrangian Formulation

1 INTRODUCTION

Summary

Rehabilitation is considered one of the most important and widespread aspects of civil engineering. Rehabilitation involves a process used to restore and/or improve performance of deficient structure or structural component to a predetermined performance level. Two main categories are recognized in rehabilitation: repair and strengthening. This study will specifically focus on strengthening technique using steel jacketing, which is one of the most effective and commonly used techniques for strengthening reinforced concrete (RC) columns.

1.1 Motivation of the Study

It is widely recognized that structures sustain damage during seismic events. Only a limited number of structures equipped with seismic protection systems remain undamaged. When damage occurs, it becomes necessary to rehabilitate either the main structural system or specific structural elements. The concept of rehabilitation arises from the need to restore the occupancy of a structural element or enhance its structural properties. This requirement becomes apparent when the primary structure undergoes damage due to actions such as earthquakes, windstorms, snowstorms, or significant alterations in the building's intention of use such as: changing the occupancy type of the structure to one that is more demanding or unexpected in the original structural design. Columns are a vital structural element; for most of the construction nowadays, columns are the primary element to carry on vertical loads. The fundamental stability of the structure is intricately tied to the efficiency of the vertical load-carrying system. In essence, any failure occurring within a single column has the potential to propagate and inflict damage upon the neighbouring structural elements, as depicted in Fig. 1.1. This interdependence underscores the critical importance of ensuring the resilience and integrity of individual columns, as their performance directly impacts the overall stability and safety of the entire structure. Consequently, comprehensive measures and assessments are imperative to enhance not only the isolated columns but also the interconnected elements, mitigating the risk of widespread structural damage in the event of a failure. Observations indicate that in significant earthquakes, the collapse of RC buildings is commonly linked to the loss of the gravity-load carrying capacity in vertical members, particularly columns and the insufficient lateral load strength of the vertical support elements of the structure (Bazán & Meli, 2000; Khedmatgozar Dolati, 2023).

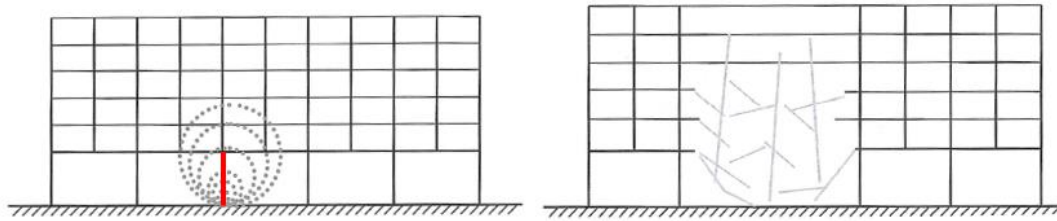


Fig. 1.1—Example of potential local collapse due to a failure of a column

The majority of existing buildings, even in highly developed countries, was constructed using older standards that had minimal or no seismic provisions. Consequently, these buildings generally have significantly lower strength to earthquake loads compared to modern standards. These buildings exhibit poor construction practices, lower-grade materials, inadequate use of stirrups, short lap splices, and insufficient detailing. They also lack of inadequate supervision and poor workmanship. Consequently, older RC buildings have very low and unreliable ductility, and RC columns as well. Additionally, the aging of the framing system, carbonation of concrete, and corrosion of reinforcing steel bars further reduce their ability to withstand earthquake loads. As a result, the lateral capacity of older RC columns is significantly lower (often less than 50%) compared to columns designed to modern standards (Stelios, 2023). The necessity of seismic assessment and strengthening of RC columns is evident to protect human lives, minimize economic losses and damages, and safeguard the infrastructure. In this aspect, one of the most used seismic upgrades and strengthen of RC columns are latticed steel jackets (see Fig. 1.2). The use of external reinforcement of steel plates, steel angles and battens to strengthen reinforced concrete members was one of the most popular methods and widely used in retrofit applications several decades ago (Stelios, 2023). However, due to the past seismic events, more specifically in Mexico (earthquake $M_w = 8.2$ and 7.1 , September 2017), the use of SJ as a rehabilitation has been used and increased popularity in the construction industry.

The primary purpose of using steel jackets is to enhance the axial and lateral capacity (shear) of reinforced concrete members. Steel jackets are affixed to the outside of the concrete member using epoxy adhesives, sometimes with additional fastening using bolts or dowels installed into holes drilled into the concrete surface with epoxy resins.



Fig. 1.2—Steel jacketing in a column using steel angles and battens (Stelios, 2023)

Retrofitting with steel jacket is considered to be a valid and reliable method to enhance the overall seismic performance of a structure (Salman & Al-Sherrawi, 2018). It can effectively be used to upgrade RC buildings for improved lateral strength, axial load carrying capacity, passive confinement, ductility, and shear strength. Compared to other methods, SJ have a lesser effect on the stiffness of the existing system, although this can vary depending on how the steel plates are connected to the concrete member and adjacent members. Additionally, the weight of steel plates is minimal relative to the overall weight of the existing building, resulting in a negligible increase in the structural mass of the system.

The design of the steel jacket as strengthening is relatively uncertain; the plate can be considered as typical external reinforcing steel bars, assuming there is sufficient bond between the plate and the concrete substrate. Typically, relying solely on epoxy adhesives is insufficient, and additional fastening through bolts should be implemented to prevent debonding. The analysis of the contribution provided by steel jackets in RC columns, aimed at enhancing their response to lateral loads, is of great interest to many professionals in the field of civil engineering. This is due to a lack of understanding of the detailed behaviour when employing this type of strengthening, as well as insufficient information regarding its behaviour in seismic situations. Additionally, there is no consensus on how to properly incorporate the steel jacketing into the analysis and modelling, and we lack regulations that provide clear guidelines on the approach to be followed in this regard.

This thesis is centred on investigating steel jacketing as a technique for repair and strengthening, with the aim of elucidating the behaviour and modelling of strategies used in professional practice. The objective is to improve comprehension of the factors influencing the design and modelling of reinforced concrete columns and metallic jacketing. The work was driven by the need to develop a comprehensive modelling frame to evaluate the main variables involved in the deep behaviour of RC columns latticed with steel jacketing.

1.2 Scope

In this thesis, the scope encompasses the investigation of the nonlinear behaviour of rectangular reinforced concrete columns latticed with a steel jacket. The study aims to analyse how these columns, with their specific structural enhancements, respond under lateral displacement demand, considering the complexities and nonlinearities that arise in such scenarios. By focusing on this particular aspect, the research seeks to provide a deeper understanding of the performance and potential advantages of using a steel jacket to improve the lateral strength of reinforced concrete columns. The research encompasses an experimental and numerical procedure, in which the hysteresis behaviour of real scale RC specimens reinforced with SJ are explored for the experimental tests, and the overall lateral behaviour using a monotonic lateral displacement imposition approach are used for the numerical analysis.

1.3 Main Goals

The development and calibration of a nonlinear numerical model of the tested specimens aims to simulate various configurations of steel jackets and to explore the main variables that influence the overall lateral behaviour of the latticed specimens. This involves creating a detailed and accurate computational representation of the specimens, incorporating the material properties, geometric characteristics, and boundary conditions observed in the physical tests. The calibrated numerical model will enable a comprehensive analysis of the contribution of the SJ to the lateral load-bearing capacity. This includes understanding the contributions of different variables, such as the width and placement of the steel jacket, the type of concrete used, and the loading conditions. The insights gained from this exploration will provide valuable guidelines for designing more resilient and efficient reinforced concrete columns with steel jackets in real-world applications.

1.4 Specific Goals

- Perform experimental tests of real size rehabilitated concrete columns rehabilitated with latticed steel jackets;
- Study the experimental behaviour of the steel jacket and its strength contribution to the lateral load-bearing capacity;
- Model the concrete column using finite element method;
- Model the steel jacketing and simulate the lateral behaviour the interaction with the concrete column;
- Calibrate the numerical models.

To achieve the aforementioned objectives, an examination of current literature was performed, alongside the implementation of a real size experimental test. Additionally, a numerical model was constructed to simulate and analyse in detail the behaviour observed in the experimental results.

Nonlinear continuum finite element analyses were performed using ATENA software (Červenka et al., 2002). This software is specifically equipped with distinctive features designed for concrete structures, including specialized bond models that account for the interface between concrete and steel bars.

Task undertaken in this study include:

- Test reinforced concrete columns and RC columns latticed with two arrangements of steel jacketing by means of lateral load up to failure to study the nonductile behaviour;
- Calibrate with continuum finite element models to experimental tests to capture the nonlinear behaviour of concrete columns up to lateral collapse;
- Test materials to determine the mechanical properties.

Outcomes of the work include:

- Findings of this study can be employed to modify modelling parameters and acceptance criteria for retrofit concrete columns that implements steel jacketing. Furthermore, the findings in this thesis can help to determine the key parameters of the concrete material that are being affected due to the implementation of the steel jacketing.

1.5 Background and Context

Today's society demands resilient structures, which requires design and construct structures that not only fulfil the basic needs of the social order but also remain functional even after catastrophic events like earthquakes. The safety of people involves ensuring that no part or the entirety of a building collapses, posing a threat to life. Additionally, the safety of the building's contents, appendages, and services means they can continue functioning as expected even after an earthquake. The safety of individuals in a building depends on the building's ability to withstand earthquake shaking and remain standing afterward (Murty et al., 2022).

A building not only need to have considerations of strength and serviceability, ductility is a significant factor that must be addressed in structural design. It is crucial to ensure that if a structure is subjected to extreme loading leading to failure, it will exhibit ductile behaviour. This means the structure should not fail abruptly and brittlely without warning, but rather should be capable of significant deformations near its maximum load-carrying capacity. The ability of a structure to undergo large deformations before failure provides clear warning signs and can prevent total collapse, potentially saving lives. Ductile

behaviour also enables the redistribution of bending moments in structural design, accommodating elastic bending patterns (Park & Paulay, 1933). In regions prone to seismic activity, like Mexico City, ductility becomes even more critical. Current seismic design codes typically require structures to withstand moderate earthquakes elastically. However, in the event of a severe earthquake, the structure must rely on its ductility to survive without collapsing. Designers must have special attention to details such as the amount of longitudinal reinforcing steel bars, proper anchorage of reinforcing, and other aspects to ensure ductile behaviour. These measures help avoid brittle failures, such as shear and bond failures.

The leading subject nowadays is the Performance-Based Earthquake Engineering (PBEE), which aims to design and built structures that meet the performance expectations of owners, stakeholders, and society. The focus to performance-based design is the capability to predict the performance of the structure under various levels of ground motion intensity. Traditionally, a building was deemed to have acceptable performance if it avoided collapse (Miranda, 2010). However, recent earthquake events have highlighted the importance of achieving a certain level of economic loss control, which is essential for both owners and society. Anyway, the duty now is not only design with better standards, quality controls and technological advances, but also to protect old buildings from collapse due to a ground motion. Advancement in society requires more than just sophisticated, efficient, and safe constructions; it is essential to protect vulnerable structures for the reason that they are the ones that lead to human losses during catastrophic events.

1.5.1 Old RC Buildings

The fundamental observation about older buildings is their difference from modern construction practices, lacking the stringent standards we adhere today in both design and construction. This is widely acknowledged and requires little elaboration, as it underscores the necessity for upgrading and strengthening older structures. However, the critical inquiry is not just about recognizing these differences, it is about understanding the specific nature of these differences, which is where the discussion becomes intriguing. Upon closer examination of older buildings over a significant period, one discovers that design and construction practices within a particular region and time share many commonalities. Factors such as material grades, member sizes (columns and beams), the presence of shear walls, foundation types and dimensions, and reinforcing details (including rebar and stirrup sizes, detailing, and steel grades) exhibit remarkable similarities across buildings within the same region constructed during the same era. These commonalities are typically associated with changes in structural codes mandated by governing authorities.

It is widely recognized that the majority of existing buildings were designed without provisions for seismic strength. However, even older building codes included provisions for minimum design requirements (Aboutaha et al., 1999), most notably the "minimum reinforcing ratio". In theory, assuming and implementing a minimum level of reinforcing, rather than conducting a detailed site survey, would be sufficient. Moreover, theoretically speaking, this approach would also err on the side of safety.

Most existing buildings and civil infrastructure suffer from seismic deficiencies. Therefore, when it comes time to consider extending their service life through structural and architectural upgrades, the need for seismic retrofitting to fulfil strength and serviceability becomes apparent. Besides, it is often decided to upgrade the earthquake strength of facilities that still meet their functional requirements and fulfil their purpose from an architect's point of view, but are clearly unsafe in the event of an earthquake (Alper & Fardis, 2014). Light confinement in columns was allowed in seismic regions in the United States and Mexico until the early 1970s, before seismic design provisions were introduced to address seismic vulnerabilities. Subsequent evidence after earthquakes indicates that shear failures in non-ductile columns often lead to axial collapse.

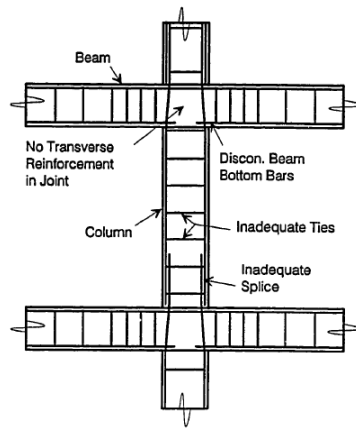


Fig. 1.3—Elevation view of a non-ductile RC frame. Taken from Aboutaha (1994).

Experimental studies have demonstrated that a column designed to resist gravity loads typically experiences axial failure when shear strength significantly degrades. Conversely, columns that undergo flexural yielding before shear failure exhibit greater deformation capacity compared to those that do not yield before shear degradation (Khedmatgozar Dolati, 2023).

There are several deficiencies in old RC columns that ground motions lead in evidence. One of the most common deficiencies is the absence of transverse reinforcing, this is the primary issue in most cases involving existing buildings and is often the main reason for requiring strengthening (Stelios, 2023). In new construction, building codes impose rigorous regulation on the layout of hoops, specifying minimum hoop diameter, maximum hoop spacing, and proper anchorage with a 135-degree bend inside the concrete core. With the implementation of capacity design principles introduced in the 1980s, it can now be ensured that a ductile failure mechanism in bending will occur before any catastrophic brittle failure in shear.

All the previously described issues with RC buildings and columns underscore the urgent necessity to upgrade these structures to comply with nowadays standards and regulations. Over time, changes in building codes and a deeper understanding of structural behaviour under various loads have revealed that many existing buildings may not meet the required safety and performance criteria. Addressing these deficiencies is not merely about compliance; it is about ensuring the safety and longevity of our built environment. Therefore, it is crucial to implement effective rehabilitation and retrofitting techniques. These techniques are designed to enhance the structural integrity and performance of RC buildings and columns. Rehabilitation involves repairing and restoring the structural elements to their original condition or better, while retrofitting focuses on upgrading the structural capacity to resist future loads, including those from seismic events, wind, and other environmental factors. Achieving satisfactory levels of ductility, strength, and resilience through these methods means that buildings will be better able to withstand and recover from extreme events.

1.5.2 Mexico in Context

The earthquakes of September 2017 in Mexico City emphasized the vulnerability of certain buildings and the need to implement strengthening strategies to reduce or control seismic risk. In addition to the damages and collapses in Mexico City, the earthquakes caused severe damage in the epicentral zones to structures with strict seismic design and in buildings with inappropriate designs and construction processes for a high-seismic zone. Overall, the earthquakes showed that a proper process of conceptualization, analysis, design, construction, supervision, operation, and maintenance of buildings and infrastructure leads to acceptable performance.

In Mexico City, the scenario is similar in the sense that the observed damages were mostly in self-built single-family homes. However, the damages were concentrated in structures located to the east and south of the city, known as the lake zone, which amplifies ground accelerations. In contrast to other states, Mexico City experienced a considerable number of collapses of apartment buildings with 3 to 9 levels. These collapses depended on a series of intrinsic factors and the combination of several of them, including the age of the buildings, mostly constructed before 1985, corner configuration of the buildings, use of column and flat slab structures, and the number of levels related to the dominant period of the structures between 0.5 and 1 second. Perhaps most notably, many of the buildings had weak/soft floors. Among the extrinsic factors that affected the performance of the collapsed structures is that most of them were located in the transition zone (zone between a soft and hard soil). This fact is related to two important aspects: the dominant period of the soil and the proximity to the hillside area. By reducing the thickness of the soft soil column beneath the structure, higher-frequency movements tend to be amplified, particularly within the period range of the damaged structures. Additionally, the fact that the structure was located near the edge of the former lake could have amplified ground movement induced by wave reflection on the hillside.

One of the most commonly observed damages in Mexico City following the earthquakes was the shear failure of concrete columns. This type of structural failure occurs when the columns, which are designed to support the vertical loads of a building, are subjected to lateral forces such as those generated by seismic activity. The intense shaking during an earthquake can cause the concrete and reinforcing steel bars within these columns to crack and fail, compromising the structural integrity of the entire building. This phenomenon was particularly prevalent in Mexico City due to the unique geotechnical conditions, including the soft, clay-rich soil that amplifies seismic waves, exacerbating the effects of the tremors on buildings (Alcocer et al., 2022). The widespread occurrence of shear failure in concrete columns highlighted the need for improved construction practices and the implementation of more stringent building codes to enhance earthquake resilience.

Based on the damages observed in RC structures during the structural assessments of various buildings, it became evident that restoration and strengthening were essential to ensure their safety and integrity. The structural evaluations revealed significant vulnerabilities that needed to be addressed to prevent future failures, particularly in earthquake-prone areas (Alcocer et al., 2022). One of the most widely implemented techniques, recommended by numerous structural engineering firms, was the use of steel jacketing with a lattice configuration. This method involves wrapping the existing concrete columns or beams with a steel jacket, which is designed in a lattice pattern to provide additional support and enhance the load-bearing capacity of the structure. The steel jacket helps to confine the concrete, reducing the risk of shear failure and improving the overall ductility and strength of the building. This technique not only addresses the immediate structural deficiencies but also enhances the building's resilience against future seismic events, making it a crucial component of the retrofitting process in earthquake-affected regions.

The challenge with this strengthening technique lies in the insufficient technical, theoretical, and experimental evidence regarding the detailed behaviour of steel jacketing when implemented in RC columns. Despite its widespread use and the promising results observed in practical applications, the lack of comprehensive studies and documented performance data has raised concerns about its reliability and effectiveness under various conditions. This gap in knowledge has emphasized the urgent need to establish standardized guidelines and regulations to ensure the consistent and safe application of steel jacketing for structural strengthening. Developing such a normative framework would involve rigorous research, extensive testing, and collaboration among industry experts, academic institutions, and regulatory bodies. The goal would be to thoroughly understand the interactions between steel jackets and RC columns, optimize design parameters, and define best practices for installation and maintenance. By addressing these issues, the proposed standards would provide engineers with the necessary tools and knowledge to confidently implement steel jacket, ultimately enhancing the safety and resilience of buildings reinforced using this technique.

2 LITERATURE REVIEW

Summary

This chapter briefly includes some of the main research that has been carried out worldwide, abroad on the technique of rehabilitation of concrete column using steel jacketing.

2.1 Introduction

Numerous studies worldwide have explored the use of steel jacketing as a retrofit and strengthening technique. Below, some of the most significant research focused on the implementation of steel jacketing in rectangular transverse section RC columns are detailed.

One of the most useful research papers is the work done by Sen and Begum (2017), in which they encompass the most notable research papers from the last 15 years. The study primarily focused on investigate existing experimental works and analytical models available in the literature. Subsequently, a comparative analysis was performed to identify the key parameters influencing the behaviour of RC columns strengthened with steel angles and strips. The majority of the research papers focused in the axial behaviour of the reinforced columns, which is not the aim of this actual research thesis, but the findings of those research papers help to understand the main variables that govern the behaviour of RC columns latticed with steel jackets.

One of the important findings of the research of Sen and Begun is the existence of a gap identified in the literature, that is the lack of sufficient studies on RC columns reinforced with steel angles and strips under combined bending and axial loads. Therefore, further research is necessary to understand their behaviour under these conditions fully. This additional research is essential to develop comprehensive guidelines for designing and assessing the adequacy of RC columns strengthened with steel angles and strips. One of the key aspects mentioned in the research work by Sen and Begum (2017) is the passive confinement provided by the SJ. This passive confinement works only when the dilatancy of the concrete column starts, this is, when the axial or lateral loads changes the transverse section of the RC column. Also, in this stage, cracks appear in the structural element. When the compressive stress in the strengthened concrete column approaches its uniaxial compressive strength, lateral strains increase significantly due to progressive crack. At this point, the steel strips engage to resist the tensile forces, thereby delaying failure (Nagaprasad et al., 2009). Typically, the confinement effect, measured as confining pressure, is greatest near the areas where the strips are applied, as shown in Fig. 2.1.

Badalamenti et al. (2010) and Nagaprasad et al. (2009) mentioned the combined effect of the confinement provided by SJ due to axial and bending deformation. The contribution of steel angles can be incorporated to predict the strength of jacketed columns by considering the composite action. In this approach, the angles are assumed to be subjected to both axial load and

bending moment (see Fig. 2.2). The axial load results from the column's shortening in directly loaded columns, or from friction at the strip levels in indirectly loaded columns. The bending moment is induced by the expansion of the concrete (Badalamenti et al., 2010).

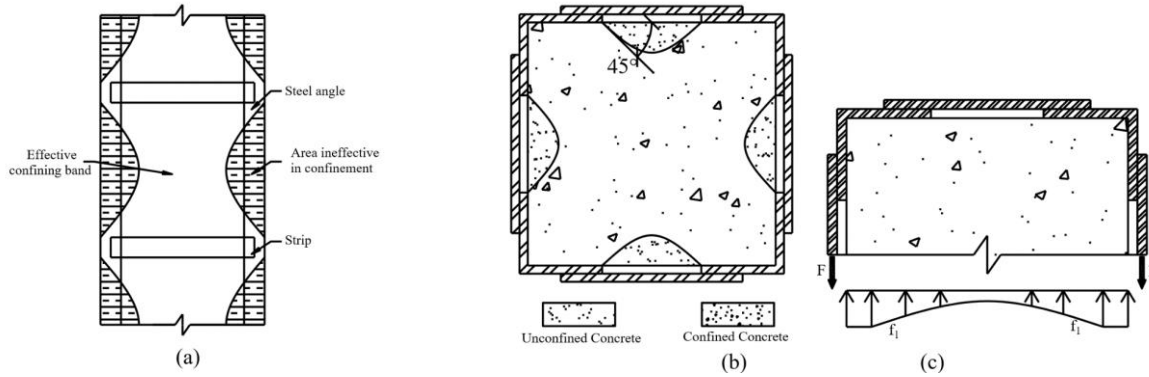


Fig. 2.1—Confinement due to SJ: (a) effective confinement in elevation; (b) confinement pressure distribution at batten level; (c) effective confinement in plan. Taken from Nagaprasad (2009).

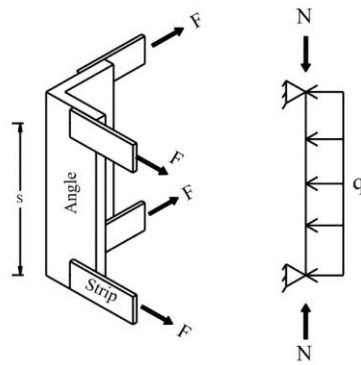


Fig. 2.2—Schematic diagrams of load on steel jacket. Taken from Badalamenti (2010).

In synthesis, incorporate the effect of confinement provided by the SJ for of RC columns is very important to develop a theoretical approach that aims to predict the nonlinear behaviour.

2.2 Experimental Programs

Some researchers performed experimental programs to investigate the impact of various key parameters and/or to develop analytical models for predicting load capacity of RC columns reinforced with SJ. The next section provides a brief review of some of the available studies on this strengthening process.

Tarabia and Albakry (2014) performed an experimental program with 10 samples to study the axial behaviour and effectiveness of RC columns strengthened with steel angles and battens. The study considered parameters such as the size of the steel angles, strip spacing, grout material between column sides and angles, and the connection between the steel angle and the specimen's head.

Several conclusions were drawn from the study:

- The increment of ultimate axial load capacity is a consequence of the strength capacity of the corner angles and the confinement provided by the strips (Sen & Begum, 2017);
- The ductility of the jacketed column increased by at least 50% in most cases, indicating the effectiveness of this strengthening procedure for seismically deficient columns;
- To be economical, using cement as a binder between the steel angle and the old column surface was recommended.

Abdel-Hay and Fawzy (2014) investigated the impact of partially strengthening defected RC columns using various methods. In their study, two samples were reinforced with steel angles and strips. The results indicated that increasing the height of the jacket (i.e., the length of the angle) significantly enhances both the ultimate load capacity and ductility of the columns (Sen & Begum, 2017). This can be an effect of the increase in the contact area of the strips and the subsequent increase in the confinement volume.

Khalifa and Al-Tersawy (2014) performed an experimental program with seven column samples to evaluate improvements in axial load capacity, stiffness, and ductility. They compared the performance of the steel angles and battens strengthening method with another steel caging jacketing method, which used four steel plates on the column faces. Their findings indicated that increases in load capacity and ductility primarily depend on the strip thickness, while stiffness depends on both strip thickness and spacing.

Elsamny et al. (2013) performed experiments on columns jacketed with steel angles and strips under eccentric vertical loading. The study focused on the parameters of eccentricity, angle area, and the number of strips. Results showed a decrease in the load-carrying capacity of the strengthened columns with increased eccentricity, ranging from 10-40% depending on the number of strips. This highlighted an important area for future research, as the number of strips was found to be ineffective, a result attributed to the large spacing of strips used in the study. Consequently, a recommendation for future studies was proposed regarding the maximum spacing of strips.

Campione (2013) primarily focused on developing an analytical model, but also carried out experimental work to validate the model and examine the impact of batten spacing under axial load. The study concluded that a directly loaded strengthened column behaves as a composite member, exhibiting both confinement effects and composite actions. The results indicated that the ductility of strengthened columns increases as the batten spacing decreases.

Giménez et al. (2009) performed tests on 14 strengthened columns using steel angles and strips. The study aimed to investigate several factors: the effect of the column's loading and unloading state during strengthening, the impact of using epoxy or cement mortar as a binder between the concrete and steel angle, and the effect of a capital on load transmission to the column. The results concluded that the composite behaviour of the steel angle and concrete at the column ends is not significant. Additionally, it was found that epoxy mortar has a negligible effect on load capacity, and that unloading the column before strengthening improves its capacity.

Delgado et al. (2005) experimentally studied RC columns retrofitted using various methods under cyclic loads. They found that RC columns jacketed with steel angles and strips exhibited slightly better performance compared to those jacketed with steel plates. This improvement is attributed to the use of angle profiles connected by strips at the corners, which delays the spalling of cover concrete, especially in critical zones.

Dolce et al. (2003) examined different local strengthening methods on 24 column specimens to investigate the impact of confinement on ductility and strength. They performed cyclic loading-unloading compression tests on strengthened and unstrengthened columns. The conclusive remarks highlight the ductile behaviour observed in the strengthened columns.

Previous studies have consistently highlighted the confinement effect provided by steel jacketing, as well as its beneficial impact on load capacity and ductility. However, the majority of the experimental tests are focused in the axial behaviour, something that draws a partial view of the behaviour of SJ in RC columns, exposing the necessity to make further investigation to have a deeper understanding also in the lateral behaviour of this strengthening technique.

2.3 Analytical Models

This section is not intended to be a compilation of formulas; instead, the analytical models are presented as conceptual frameworks. Various models have been proposed to predict the load capacity of steel angle and strip-strengthened RC columns, considering the composite action of the core concrete and the local buckling of the steel elements. All the analytical models discussed here focus on the axial behaviour of RC columns.

The proposed formula of Khalifa and Tersawy (2014) predict the axial load capacity of steel angle and strip strengthened RC columns, considering the composite action of core concrete and local buckling of steel elements. The model accounts for the confinement provided by the assembly of steel angles and strips. Concrete confinement is incorporated by the factor m_c . To account for the contribution of steel angles to the capacity, a continuously supported beam (at strips) with axial and bending loads is considered. These loads may cause buckling of the steel angle and/or axial deformation of the strips. A reduction factor, m_s , to the yield stress has been prescribed to account for this effect.

Tarabia and Albakry (2014) proposed a straightforward analytical model to assess the axial load-carrying capacity of strengthened RC columns. This model assumes rigid corner angles that do not buckle before yielding and have no flexural deformation. The confined concrete stress model by Badalamenti et al. (2010) has been adopted. The confinement pressure has been derived considering the deformation compatibility of the concrete column and steel cage, using a similar approach to Calderón et al. (2009). The contribution of steel angles to ultimate capacity has been calculated for direct and indirect loading of strengthened column considering the shortening of column and friction respectively.

Campione (2010) proposed a model for designing concrete columns strengthened with steel angles and battens, considering both direct and indirect axial loads on the angles. This model considers the contribution of confinement pressure and the load capacity of the steel angle under direct loading to determine the compressive strength. To determine the confining pressure, it assumes a sudden decrease in confinement pressure at the steel battens (see Fig. 2.3), while it remains nearly uniform along the length of the angle. Finally, a simplified method for measuring confinement pressure is prescribed, which is justified when the battens have lower stiffness than the corner steel angles.

The contribution of steel angles to the axial load capacity has been evaluated by considering the combined effects of axial and bending forces on the angles. The axial force results from the shortening of the column, while the bending force arises from the reduction in lateral expansion of the column due to confinement.

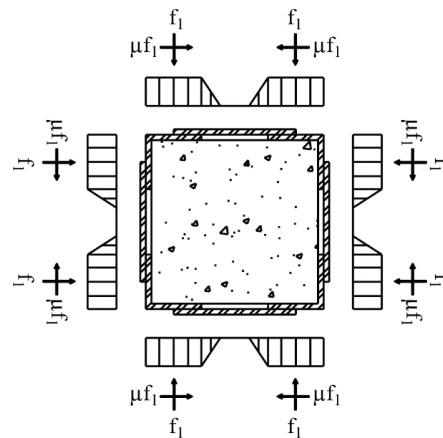


Fig. 2.3—Confining pressure distribution at batten level. Taken from Sen & Begum (2017).

In the previously mentioned analytical models, the goal is to predict axial capacity by incorporating variables that have proven important in experimental programs, such as the depth of steel angles and battens, thickness of the steel jacket, and spacing of battens. The next chapter covers some of these parameters as studied in various experimental programs (Sen & Begum, 2017).

2.4 Steel Jacket Parameters

Based on experimental work and analytical models, it is clear that multiple factors significantly influence the ultimate load capacity of steel angle and strip-jacketed reinforced concrete columns.

These factors include but are not limited to (Sen & Begum, 2017):

- **Grout Material:** The type and properties of the grout used to fill gaps and bond the steel elements to the concrete core affect the composite action and overall integrity of the column;
- **Strip Spacing:** The distance between strips affects the overall stability and load distribution within the column. Proper spacing ensures that the load is evenly distributed and prevents local failures;
- **Strip Thickness and Configuration:** The thickness and arrangement of the strips contribute to the strength and stiffness of the jacket. Thicker strips can handle more load, while the configuration can enhance the composite action between the steel and concrete;
- **Cross-Section of Steel Angles:** The dimensions and shape of the steel angles are crucial in providing additional support and enhancing the load-bearing capacity of the column. Larger cross-sections generally offer better performance under axial loads;
- **Connection of Steel Angles to the Specimen Head:** The method and quality of the connection between the steel angles and the specimen head play a vital role in ensuring that the angles effectively contribute to the column's strength. A secure connection minimizes the risk of detachment or slippage under load.

In summary, the combined effect of these factors determines the ultimate load capacity of steel angle and strip-jacketed RC columns. As previously mentioned, these parameters focus solely on axial behaviour, highlighting the need to also explore lateral behaviour.

2.4.1 Grout Material

Grout is used to fill the gap between the steel jacket and the concrete column, ensuring a total and continuous contact between both materials. D. Sen and M. Begum (2017) analysed the experimental data of Tarabia and Albakry (2014) found that the change in compressive behaviour using grout or epoxy is not enormous, as depicted in Fig. 2.4. So, the use of cement as grout material rather than epoxy has been recommended. Similar conclusion has been drawn by Giménez et al. (2009).

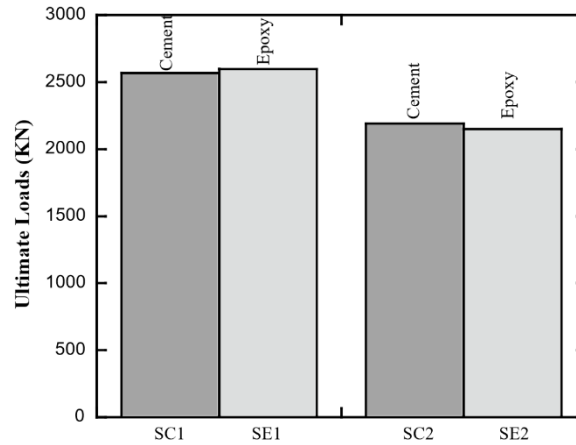


Fig. 2.4—Effect of grout materials on the ultimate load capacity. Taken from Sen & Begum (2017).

The results are important because it means that the material does not need to be specialized, only well-made and placed and have a good compression strength (between 20 to 25 MPa).

2.4.2 Strip Configuration

Strips are meant to achieve confinement and resist the buckling of steel angles. The configuration of the strips, including their spacing and thickness, is the single most important parameter affecting the failure location of strengthened RC columns (Sen & Begum, 2017). Strips are generally spaced equally along the length of the column. However, adding two smaller-section strips at the top and bottom significantly increases load capacity compared to equally distributed strips (Giménez et al., 2009).

Elsamny et al. (2013) also investigated the effect of strip distribution. They tested specimens with unequally distributed strips, where strips were closely spaced at the top and bottom but had only one strip in the middle. Failure occurred between the widely spaced strips. Strip thickness also impacts confinement and, consequently, load capacity. Fig. 2.5a and Fig. 2.5b illustrates the effects of strip spacing and thickness on ultimate capacity, respectively. Additionally, the ductility of strengthened RC columns increases as strip spacing decreases (Campione, 2013).

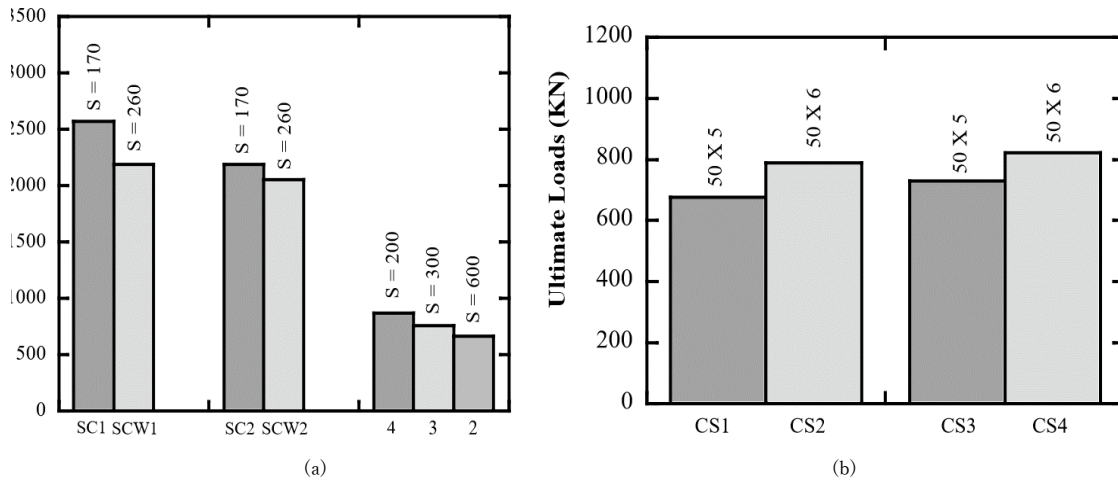


Fig. 2.5—Effect of strip configuration: (a) strip spacing; (b) strip thickness. Taken from Sen & Begum (2017).

2.4.3 Angle Size

Steel angles and strips are typically provided to achieve passive confining pressure. However, steel angles must also bear axial loads, which are transferred through frictional shear and column shortening. Fig. 2.6 shows the effect of changes in the cross-section of steel angles on load capacity, using the data of Khalifa & Al-Tersawy (2014) and Makki & Nimnim (2015). The cross-section size also influences the crushing and loss of cover at failure. Wider steel angles provide greater confinement, resulting in less crushing and cover loss, although the failure mode remains the same as with narrower angles (Elsamny et al., 2013).

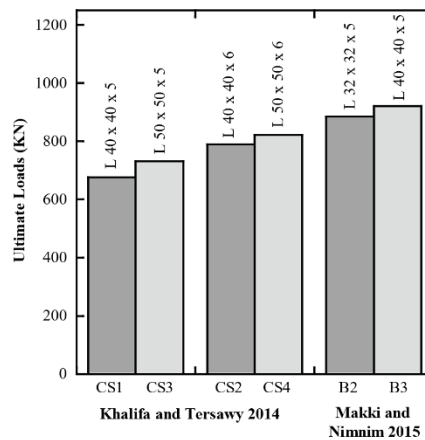


Fig. 2.6—Effect of angle size on ultimate axial load capacity (Sen & Begum, 2017)

2.4.4 Connection to Specimen Head

The connection of steel angles to the specimen head is crucial for accurately simulating real-world connectivity in reinforced concrete columns. There are two primary approaches to loading: direct and indirect.

- Direct Loading Approach: This method is suitable when it is feasible to connect the steel angles directly to the slab and beam. In this scenario, the steel angles are integrated into the load path, effectively sharing the axial loads with

the concrete core. This direct connection ensures that the angles reach their yield point before the overall failure of the column, thereby increasing the ultimate load capacity. Fig. 2.7 illustrates how the ultimate load capacity is enhanced with the direct loading approach;

- Indirect Loading Approach: This method is used when connecting the steel angles to the slab is not feasible. In this case, the load is applied indirectly, and the angles do not contribute as directly to the load-bearing process. While this method still provides additional confinement and strength, it is generally less effective than direct loading in terms of increasing the ultimate load capacity.

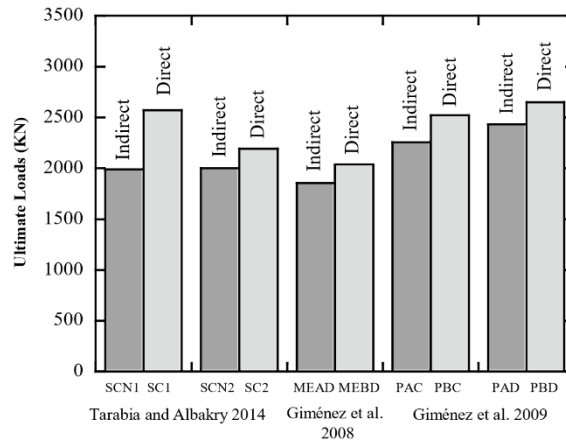


Fig. 2.7—Effect of steel angle connectivity to specimen head on ultimate axial load capacity (Sen & Begum, 2017)

2.5 Final Remarks

Column strengthening is a quick solution to address the deficiency in the axial and lateral load-carrying capacity of RC columns. Among various methods, strengthening with steel angles and strips is one of the easiest and most effective. Several analytical models have been established in many research works to predict the compressive capacity of RC square columns strengthened with steel angles and strips. However, there is a deficiency in the capacity prediction models for lateral-loaded strengthened RC columns. Additionally, studies on the formulation of interaction diagrams are insufficient, necessitating further mathematical models and/or experimental work to check the adequacy of strengthened RC columns. Comparative studies indicate that strip configuration, loading approach on the steel angle, and the length of the retrofitting zone are key parameters significantly influencing the capacity of RC columns strengthened with steel angles and strips (Sen & Begum, 2017). Again, there still lack of experimental, numerical and analytical work to also address the lateral behaviour for this strengthening technique.

3 EXPERIMENTAL STUDY

Summary

An experimental study was performed, aimed at evaluating two proposals for steel jacketing for rectangular-section RC columns. The study involved testing two reinforced concrete columns, with rectangular sections measuring 45x90 cm, under reverse cyclic loading. These columns were externally strengthened using angle and battens made of grade A36 steel. The tested RC columns exhibited typical deficiencies observed in concrete structures in Mexico City during the 1950s, such as: insufficient and inadequate transverse reinforcing, stirrup hooks at 90 degrees, low concrete strength, among others.

Two proposals for steel jacketing were tested: the first consisted of rectangular angles with a flange width of 152.4 mm (6 inches), while the second consisted of rectangular angles with a flange width of 50.8 mm (2 inches). Both proposals maintained constant the width of the battens 76.2 mm (3 inches), the thickness of angles and battens 6.35 mm (1/4 inch), and the spacing between battens. The tests were performed at the Large-Scale Structures Laboratory (LEG) of the National Centre for Disaster Prevention (CENAPRED). The experimental study is in charge and reported by Alcocer (2023), elaborated for the Institute for Construction Safety (ISC) from Mexico City.

3.1 Objectives and Scope

The main objectives are to determine the contribution to the lateral-bearing capacity of steel jacketing as strengthening for RC columns that need improve its behaviour, this studying two variants of the steel jacketing found in the daily practice of technique and strengthening in Mexico. The scope is the lateral behaviour of the concrete column with the steel jacket focused in the lateral strength and the drift, using the hysteresis and the backbone curves for analyses.

3.2 Experimental Program

The experimental programs, the design criteria, construction process, property of materials, loading protocol, instrumentation, data acquisition and the main experimental procedure are described. This program is based on the *Experimental Study of Concrete Columns Reinforced with Steel Elements* performed by the Institute of Engineering of the UNAM (Alcocer, 2023), study that was based in the Aboutaha (1994) research of RC columns controlled by shear that were rehabilitated using partial steel casing. Axial load is not considered in Alcocer tests, neither this research thesis, this to compare

results with Aboutaha and to isolate the shear behaviour of specimens¹. The main variables considered in the study of Aboutaha are mentioned in Table 3.1. In this thesis, the S8 and S9 specimens were tested and examined both experimentally and numerically, evaluating the impact of incorporating a small steel angle in one case (S8) and a larger steel angle in the other (S9). For further references, the specimens will be labelled by their ID in reference to the Table 3.1.

Table 3.1—Main variables studied by S. M. Alcocer

Specimen	ID	Steel angle width and batten thickness mm [in.]	Steel base plate	Batten width mm [in.]	Angle width mm [in.]	Batten spacing mm [h ^(a)]	Connection of steel jacket to concrete
Column O	CO	-	-	-	-	-	-
Column O*	CO*	-	-	-	-	-	-
S-2-1/4-h	S1	6.35 [1/4]	Yes	50.8 [2]	152.4 [6]	900 [h]	Grout
S-2-1/4-h/2	S2	6.35 [1/4]	Yes	50.8 [2]	152.4 [6]	450 [h/2]	Grout
S-2-1/4-h/4	S3	6.35 [1/4]	No	50.8 [2]	152.4 [6]	225 [h/4]	Grout
S-2-1/4-h/2-2	S4	6.35 [1/4]	No	50.8 [2]	50.8 [2]	450 [h/2]	Grout
S-2-1/4-h/2-4	S5	6.35 [1/4]	No	50.8 [2]	101.6 [4]	450 [h/2]	Grout
S-2-1/4-h/2-A-2-C-1	S6	6.35 [1/4]	No	50.8 [2]	50.8 [2]	450 [h/2]	Bolts ^(b)
S-2-1/4-h/2-A-2-C-2	S7	6.35 [1/4]	No	50.8 [2]	50.8 [2]	450 [h/2]	Bolts ^(b)
S-3-1/4-h/2-A-2	S8	6.35 [1/4]	No	76.2 [3]	50.8 [2]	450 [h/2]	Grout
S-3-1/4-h/2-A-6	S9	6.35 [1/4]	No	76.2 [3]	152.4 [6]	450 [h/2]	Grout

^(a) The h means the column height of the transverse section;

^(b) Bolts was used to connect steel angles and battens to concrete column.

3.2.1 Specimen Details

The general dimensions of the specimen are presented in Fig. 3.1. The specimen had a rectangular foundation with a 200x200 cm transverse area, with a 70 cm height. The column had a rectangular transverse section of 45 cm of base and 90 cm high, and 170 cm long.

¹ This represents a more stringent examination for columns with insufficient lap splicing, as the axial compressive load diminishes the tensile force transmitted through the splices.

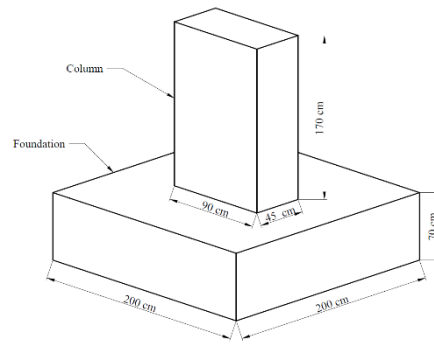


Fig. 3.1—General dimensions of specimen

The steel jacket was made by longitudinal steel angle sections installed in each corner of the RC column, and transverse steel battens welded onto the angle, with the spaces between the steel jacket and column filled with cement mortar (see Fig. 3.2).

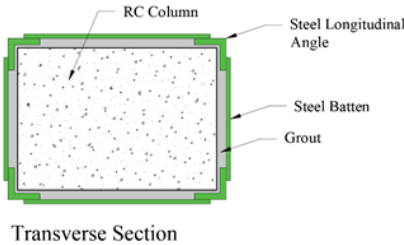


Fig. 3.2—Steel Jacketing

3.2.2 Design Criteria

The design criteria underwent evaluation based on the hydraulic jack's maximum capacity load. Calculations for reinforcing steel bars were performed in accordance with ACI 318 (2019) standards. The longitudinal steel of the columns was made up by 16 reinforcing bars of diameter 2.54 cm (8 in.), and stirrups of diameter 0.9525 cm (3 in.) spread 40 cm to a height of 120 cm of the column. In the next 50 cm, stirrups were placed at 10 cm, as shown in Fig. 3.3.

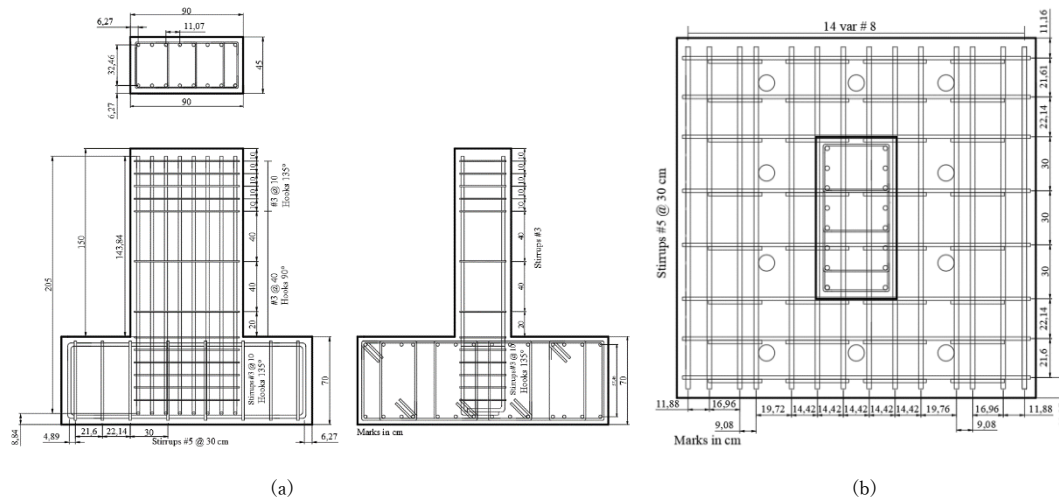


Fig. 3.3—Reinforcing steel bars detailing: (a) column; (b) foundation

3.2.3 Construction Process

According to the process observed in daily life constructions, the specimens were constructed under strict accordance with the structural design and detailing, with a tolerance of $\pm 3\%$ of error. The process was performed in the LEG of the CENAPRED by construction workers.

3.2.3.1 Preliminary Works

The chronology of the preliminary work was:

1. Foundation and column reinforcing steel bars were bent individually;
2. The locations where the strain gauges would be placed were established;
3. The surface of the reinforcing bars to be instrumented were smoothed using paper sand and cleaned using ethanol;
4. Strain gauges were placed in position using specific glue and protection cover to prevent damage caused by pouring the mixed concrete (see Fig. 3.4).

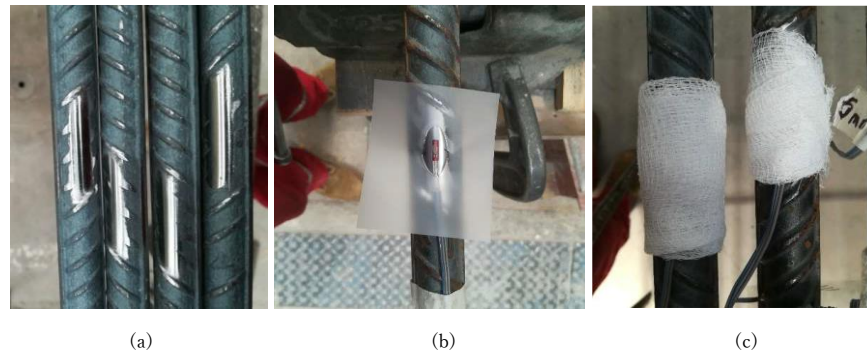


Fig. 3.4—Internal instrumentation procedure: (a) surface preparation; (b) strain gauges placed; (c) protection cover (courtesy: S. M. Alcocer)

3.2.3.2 Column and Foundation Steel Work

After the instrumentation of the reinforcing steel bars, the first steel work was for the foundation steel, construction was carried out by construction workers (see Fig. 3.5a). Next, the column steel was placed (see Fig. 3.5b).



Fig. 3.5—Steel work: (a) foundation; (b) column; (c) final work

Once that column and foundation steel were ready, the wood formwork were placed, according to the formwork calculus and design. Before the placement of the foundation and column reinforcing, a release agent was applied in the faces of the formwork (see Fig. 3.6b). Finally, the reinforcing steel bars were lifted and placed using a crane.

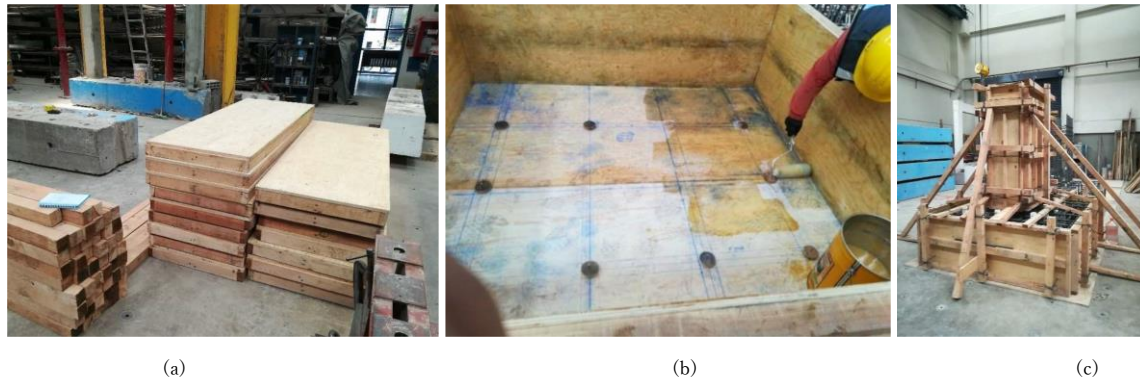


Fig. 3.6—Formwork procedure: (a) main materials; (b) pouring of release agent; (c) work finished (courtesy: S. M. Alcocer)

3.2.3.3 Concrete Placement

The concrete placement of the foundation and columns was done on different days. First, the concrete for the foundation was placed, and two days later the concrete for the columns. The decision of pouring concrete in two stages was to replicate the daily practice. In the Table 3.2 the specifications of the ready-mix concrete order are shown.

Table 3.2—Concrete order specification

Specimen part	f'_c MPa [kg/cm ²]	Concrete class	Aggregate max. size mm	Slump mm
Column (any)	19.61 [200]	Class 1 ^[1]	19.05	140
Foundation	34.32 [350]			

^[1] In accordance with (CDMX, 2023a)

The concrete of the foundation was poured in two phases, each layer was compacted, this to accomplish a good compaction of the two concrete layers. The concrete of the columns was placed in a similar way to that of the foundation. Slump tests were carried out, obtaining the specified value. The concrete placement of the columns was done in three layers. The compaction of the concrete was done using an electric vibrator (see Fig. 3.7b). During placement of the top layer, the vibrator was introduced no more than 5 cm into the immediate bottom layer.

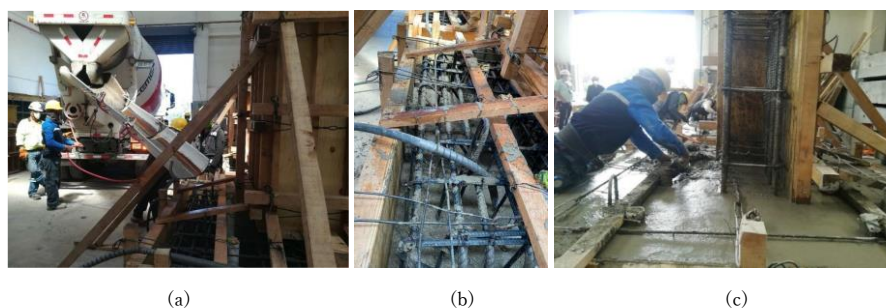


Fig. 3.7—Concrete pouring for the foundation: (a) first concrete layer; (b) vibration works; (c) surface finishes

To assess the compressive strength and elastic modulus of the concrete, six standard cylinders of 15 cm diameter and 30 cm height were selected for sampling. Each batch of concrete, with a total of 6 m³ per truck, generated three cylinders. The cylinders were constructed following the standard procedure, involving three layers compacted with 25 blows using a bar with a bullet tip (see Fig. 3.8a). The columns and cylinders were maintained in a moist environment to accomplish the concrete curing process. After seven days of casting, columns were extracted, and a thorough inspection of the internal instrumentation was performed. A multimeter was employed for this verification, with a reading of 120 Volts, indicating the functionality of the strain gauges. The final construction state of the columns is presented in Fig. 3.8b.



Fig. 3.8—(a) Preparation of cylinders of the foundation and column concrete mix; (b) specimen final state (courtesy: S. M. Alcocer)

3.2.3.4 Steel Jacket

The steel jacket was assembled in the LEG of CENAPRED, where steel angles and battens were cut to size, according to the specimen to be tested. The weld type used was fillet, work done by construction workers (see Fig. 3.9). Once the steel jacket was placed on the columns (Fig. 3.10a), *Sika grout* was placed (Fig. 3.10b) as a means of adhesion between the steel and the concrete to transmit the forces with no slip between materials.

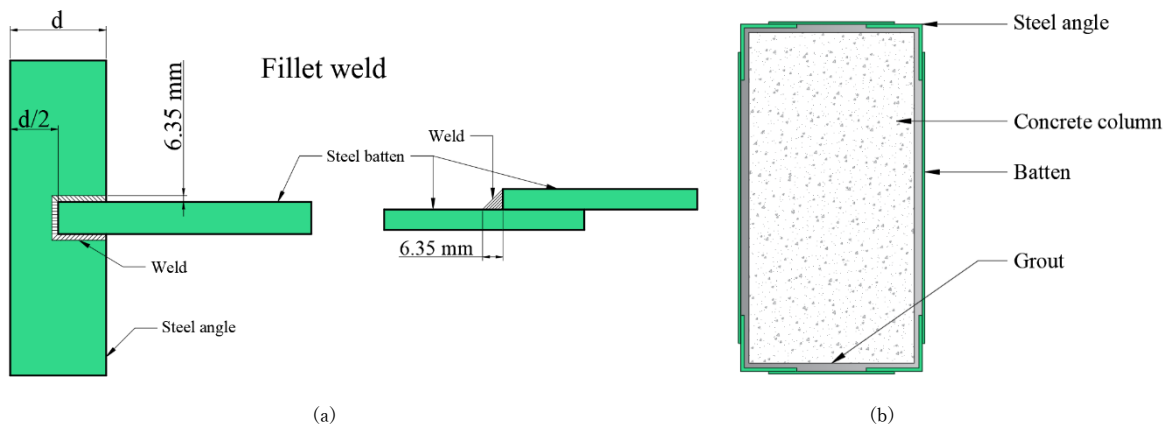


Fig. 3.9—Steel jacketing: (a) fillet weld detail for each specimen, frontal and lateral view; (b) plane view



Fig. 3.10—(a) lifting and placed of pre-armed steel jacket; (b) pouring of Sika grout

3.2.4 Test Preparations

To prepare for the test, the specimen was initially lifted using an overhead crane and positioned to its final state, with the north face of the column aligned accordingly. Before installing the column, a hydro-stone bed was applied in the contact area to ensure optimal contact between the foundation and the reaction slab. Once the specimen was correctly positioned, anchor bars were placed and post-tensioned as described in section 3.2.8. Additionally, the hydraulic jack system connected to the column was set up. This system involved steel plates connected to the column with a post-tensioned bar. Each bar was post-tensioned to apply a total force on the steel plate equal to 490.33 kN (50 t). To prevent any relative displacements between the concrete and hydraulic jack, a hydro-stone mix was poured between the steel plates and the column.

3.2.5 Materials

Below are the mechanical properties of the materials used in the experiments. This data was gathered from datasheets, theoretical approach and laboratory test results.

3.2.5.1 *Hydro-Stone*

Hydro-Stone Gypsum Cement is specifically designed for applications requiring exceptional strength and strength to water absorption. It is well-suited for use in both tooling & prototyping and art & statuary applications (USG, 2018). For the experimental study, Hydro-Stone was used to accomplish perfect contact between reaction slab and specimen foundations. Its final compressive strength is 68.9 MPa (700 kg/cm²).

3.2.5.2 *Concrete*

The mechanical properties of the concrete, which were defined by theoretical approach and laboratory test, are listed in the Table 3.3. The Poisson's ratio ν is estimated equal to 0.2, as recommended by CDMX (2023a).

Table 3.3—Mechanical properties of concrete in study specimens

Specimen part	f'_c ^[1]	f_t ^[2]	f_f ^[2]	E_c ^[1]	G_c ^[3]
	MPa [kg/cm ²]				
Column CO	24.06 [245.35]	1.86 [18.96]	2.16 [22.02]	20,153.1 [205,504.5]	8,379.1 [85,626.9]
Column CO*	22.11 [225.44]	1.79 [18.25]	2.06 [21]	17,775.3 [181,258]	7,406.4 [75,524.3]
Column S8-S9	23.75 [242.15]	1.85 [18.67]	2.14 [21.78]	13,662.8 [139,322.2]	5,692.8 [58,050.9]
Foundation CO	40.1 [409]	3.36 [34.26]	5.38 [54.86]	28,100 [286,540.3]	11,708.3 [119,391.8]
Foundation CO*	41.83 [426.51]	3.43 [34.98]	4.07 [41.5]	31,826 [324,535]	13,260.8 [135,222.5]
Foundation S8-S9	32.69 [333.33]	2.69 [27.38]	3.60 [36.51]	16,313.8 [166,354.5]	6,797.4 [69,314.4]

^[1] Taken as the average strength concrete cylinders (see section 7.1.2);

^[2] Calculated using Eq. 3.2 and Eq. 3.3 (CDMX, 2023a);

^[3] Calculated using Eq. 3.1 (Hassoun & Akthem, 2009).

$$G_c = \frac{E_c}{2(1 + \nu)} \quad \text{Eq. 3.1}$$

$$f_t = \begin{cases} 0.38\sqrt{f'_c} \rightarrow 20 \leq f'_c \leq 35 \text{ MPa} & (\text{Concrete Type 2}) \\ 0.47\sqrt{f'_c} \rightarrow 25 \leq f'_c < 40 \text{ MPa} & (\text{Concrete Type 1}) \end{cases} \quad \text{Eq. 3.2}$$

$$f_f = \begin{cases} 0.44\sqrt{f'_c} \rightarrow 20 \leq f'_c \leq 35 \text{ MPa} & (\text{Concrete Type 2}) \\ 0.63\sqrt{f'_c} \rightarrow 25 \leq f'_c < 40 \text{ MPa} & (\text{Concrete Type 1}) \end{cases} \quad \text{Eq. 3.3}$$

where f'_c is the maximum average compression stress of the concrete cylinders; f_t is the calculated tensile strength of the concrete; f_f is the calculated flexural strength of the concrete; E_c is the average elastic modulus of tested concrete cylinders; and G_c is the calculated shear modulus of the concrete.

3.2.5.3 Sika Grout

Sika Grout Constructor is a ready-to-use mortar for general construction processes. It exhibits fluid and semi-fluid consistency and is composed of cement, aggregates with controlled particles, appropriately dosed water-reducing and fluidizing additives to manage volume changes. The compressive strength one day after pouring is 26.97 MPa (275 kg/cm²), and its final compressive strength (after 28 days) is 45.11 MPa (460 kg/cm²) (Sika, 2022).

3.2.5.4 Reinforcing Steel Bars

The reinforcing steel were a hot rolled deformed reinforcing bars, Grade 42. The mechanical properties of the reinforcing steel used in the specimen CO, CO*, S1, S2 and S3 are listed in the Table 3.4. The stress vs strain curves of the steel tested are shown in section 7.1.1.

Table 3.4—Mechanical properties of reinforcing steel used in specimen CO, CO*, S1, S2 and S3

Bar diameter	f_{sy}	f_{su}	ϵ_{sy} ^[1]	ϵ_{sh} ^[2]	ϵ_{su}	E_s ^[3]
mm [in.]	MPa [kg/cm ²]	MPa [kg/cm ²]	mm/mm	mm/mm	mm/mm	MPa [kg/cm ²]
9.525 [3/8]	440 [4,486.75]	510 [5,200.5]	0.0023	0.0139	0.022	178,298.6 [1,818,139.7]
25.4 [1]	453 [4,619.3]	590 [6,016.3]	0.0023	0.0100	0.022	184,830.3 [1,884,744.5]

^[1] Strain recorded for the end of the proportionality stage of the stress-strain curve;

^[2] Average value of the end of the perfect plastic stage of the stress-strain curve;

^[3] Average value calculated according to measured values of the stress-strain curve.

3.2.5.5 Steel Angles and Battens

Steel used in angles and battens to make the steel jacket had f_{sy} of 320 MPa (3,263 kg/cm²) taken from material test, and E_s of 205,939 MPa (2,100,000 kg/cm²) taken from the literature.

3.2.5.6 Anchors

The steel of anchors used to fix the foundation to the reaction slab are high strength bars, Grade 105, with f_{sy} of 724 MPa (7,380 kg/cm²), the diameter of the bar is 3.18 cm (1 ¼ in.).

3.2.6 Loading System

The first load system consists in hydraulic jack (see Fig. 3.11a) with a capacity of 981 kN (100 t) for the first specimen (Specimen CO), controlled manually with an electric pump. The second load system (used for further specimens after specimen CO) consisted in two hydraulic jacks (see Fig. 3.11c) with a capacity of 981 kN (100 t) each, electronically controlled with an electric pump and a PC station. The hydraulic jacks were installed on the reaction wall using a plate with post-tensioned bars (see Fig. 3.11a, c). A 40 x 80 cm plate was also placed between the jack and the column to transmit the load. With this configuration a uniform distribution of the lateral load is accomplished. The main goal of load system is to accomplish the follow:

- Generate stresses equivalent to those of an earthquake on the columns, trying to apply the lateral load at the desired height;
- Do not restrict deformation to crack propagation;
- Have stiffness enough to load similar specimens, with higher lateral strength.

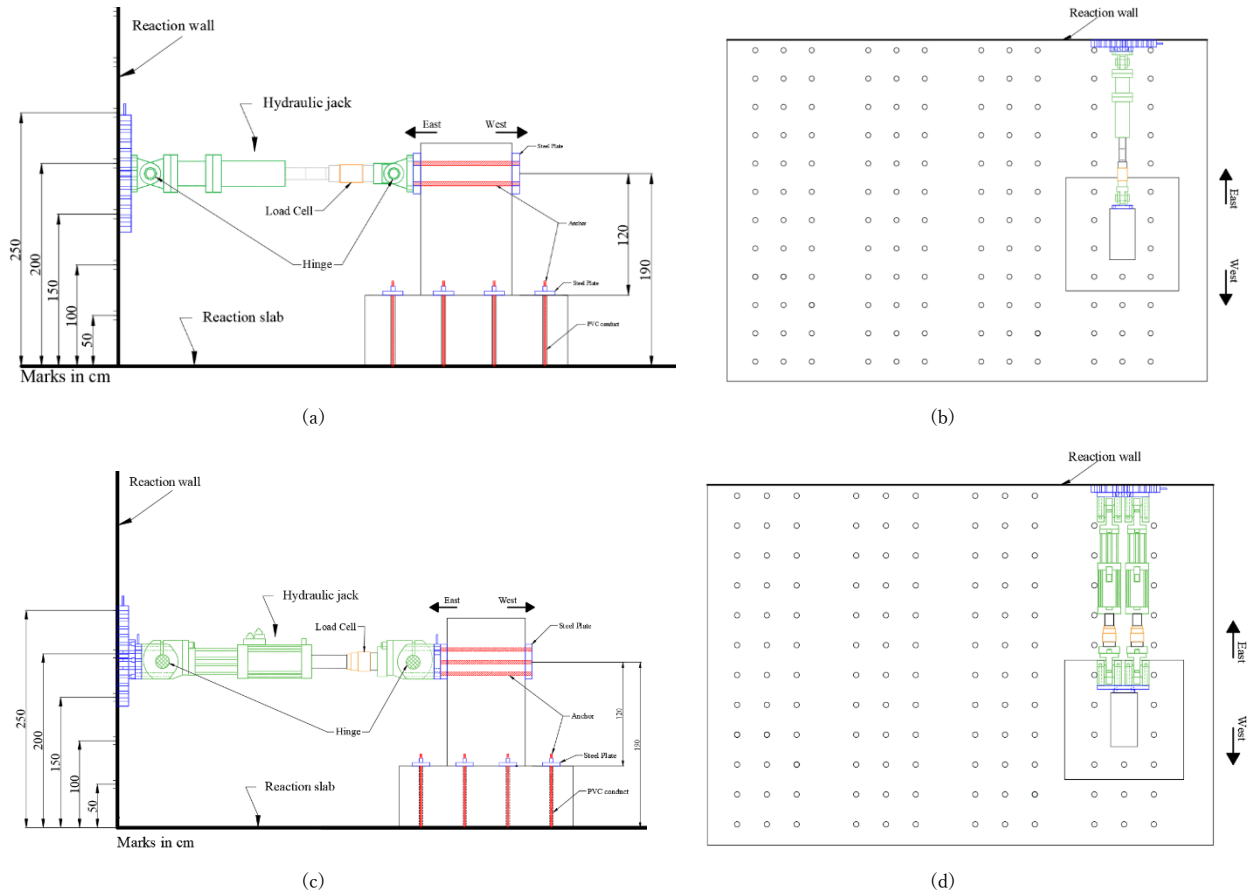


Fig. 3.11—View of the load system: (a, c) elevation view; (b, d) plan view

3.2.7 Loading Protocol

According to the ACI 374 technical committee, the load history can be applied by two methods: load control or displacement imposition control. In the load procedure, in first place load control was used, in second place displacement control. In order to compare the results of this study and the one mentioned before (Aboutaha, 1994), and using ACI 374.2R-13 recommendations, the models were tested to failure through a cyclic loading assessment, applying alternating cycles of lateral loading (ACI, 2013).

Load history can be seen in Fig. 3.12. The exit of the piston of the hydraulic jack push the model towards the west. When the piston was retracted, the model moves eastward. The cycles were considered positive when the horizontal jack pushes, that is, when west face of the column is subject to compression and the east face to tension. A positive semi cycle, which in this document will be designated as +X, is followed by another, of the opposite sign, both completed one load cycle. The reference to negative half cycles will be made with the notation -X.

3.2.7.1 Load Control

The loading control was performed first, applying a cycle of 49.1 kN (5 t) to verify that readings was in order. Then, two cycles of 98.1 kN (10 t) and subsequently two cycles of 196 kN (20 t).

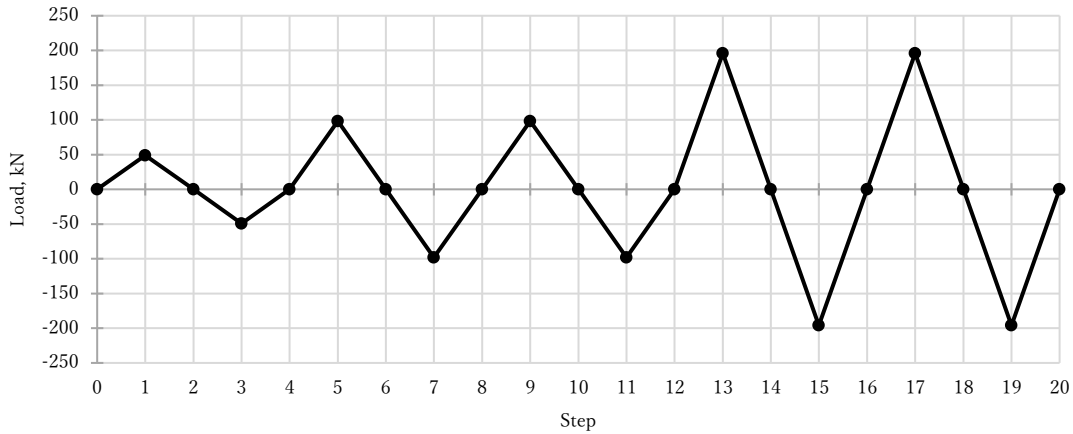


Fig. 3.12—Load control history

3.2.7.2 Displacement Control

The second part was controlled by displacement, contemplating two load cycles for each of the drift values starting with a drift of 0.5%, so the following cycles were carried out in increments of 0.5%. The end of displacement history is defined as the drift that causes a loss of lateral strength of 70%.

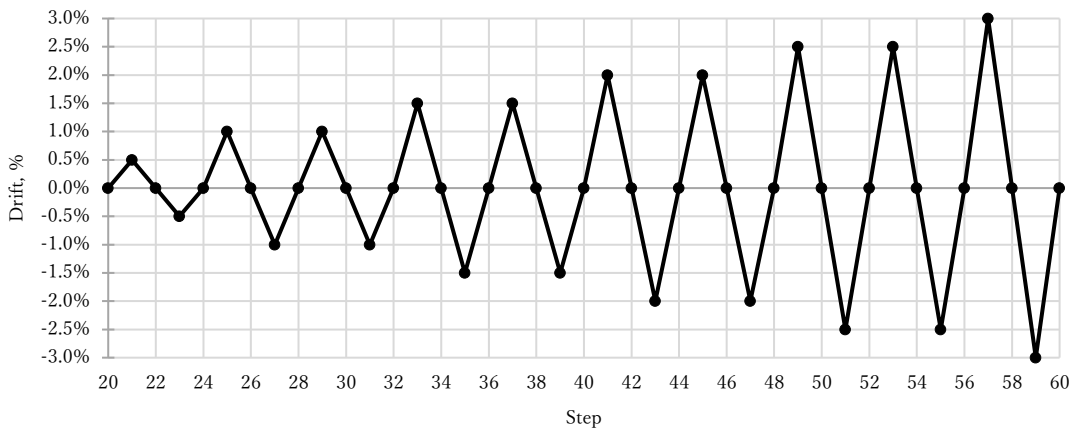


Fig. 3.13—Displacement control history

3.2.8 Model Supports

Each model was fixed in its foundation by applying post-tensioned using anchor bars which pass through the foundation by PVC conducts (see Fig. 3.14). Each bar was post-tensioned with a 245.3 kN (25 t) force, using a portable hydraulic jack. In order to ensure uniform contact between the load-bearing frame and the models, for each model, a 1 cm thick Hydro-Stone bed was placed between the foundation and the reaction slab. To assure the perfect connection between the hydraulic jack and the

concrete column, a system of plates connected to the column with post-tensioned bars was used, the post-tensioned force in each bar was such that the force in the steel plate to the column was 490 kN (50 t).

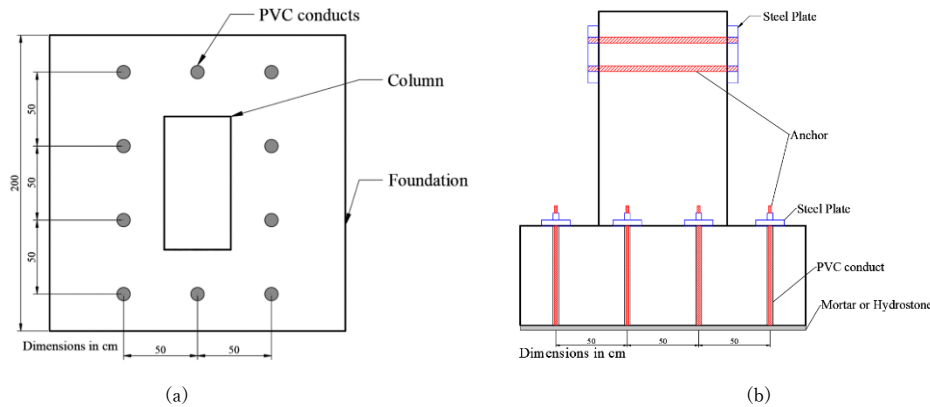


Fig. 3.14—Supports for reaction slab: (a) plane view; (b) elevation view

3.2.9 Instrumentation

The instrumentation was placed at points considered relevant in order to study the local and global behaviour of the structure. Four types of instruments were used: load cells, displacement transducers, dynamic measurement machine (DMM) and electrical strain gauges.

3.2.9.1 External

In order to measure the deformations of the element, two sides of the column were instrumented with displacement transducers of different measurement ranges. In addition to these, transducers were placed at three different heights with the objective of measuring the rotation and curvature of the column when it was subjected to horizontal loading. In total 25 transducers were placed (see Fig. 3.15a).

The list of instruments is as follows:

- 6 CDP 50 mm length for vertical instruments;
- CDP 25 mm length for horizontal and inclined instruments;
- CDP length 200 mm placed at the height of the load application;
- 1 SDP length 200 mm placed at the height of the load application;
- 1 SDP length 100 mm to measure the lateral displacement in middle span of column;
- 1 SDP length 100 mm to measure the lateral displacement in $\frac{1}{4}$ span of column;
- 1 SDP length 50 mm para to measure the lateral displacement of the foundation;
- 6 micrometres to measure rotation of the column;
- 2 micrometres to measure rotation in the foundation.

The DMM used was the Optotrak Certus HD which, through photogrammetry and high-speed triangulation techniques, provides space tracking of different targets marked with small LEDs. For this experiment, the LEDs were placed at the intersecting of the grid drawn on the north face of the specimen and in the centre of the two lower quadrants at each end; its arrangement is shown in Fig. 3.15d. The system was programmed to save 10 reading per second and in each reading the X, Y and Z coordinates of each LED were recorded separately. For the steel jacket, the external strain gauges are presented in Fig. 3.16 (the south and east faces were not instrumented).

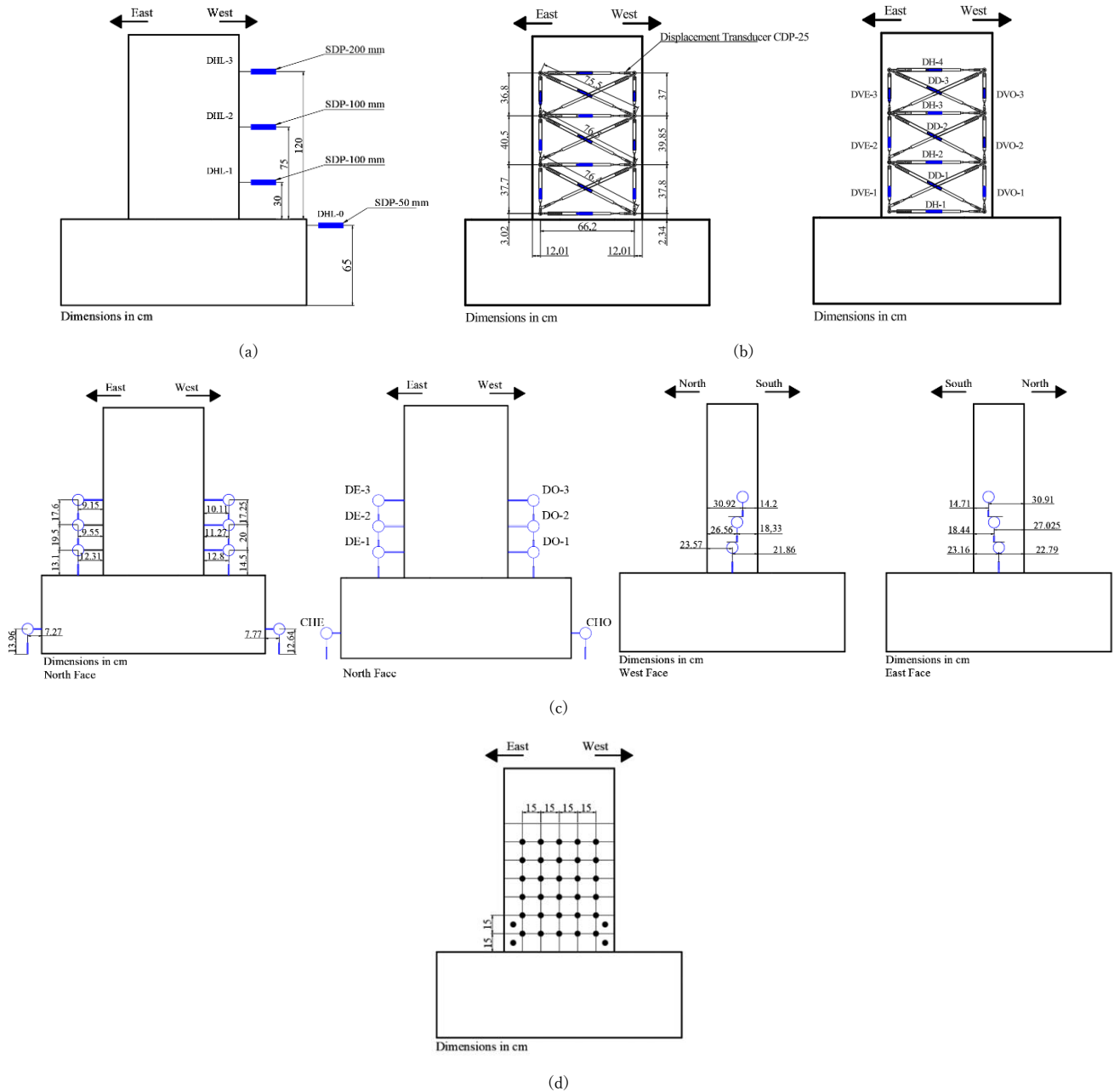


Fig. 3.15—Location of external instrumentation: (a) lateral transducer; (b) face transducers; (c) micrometres; (d) LED location

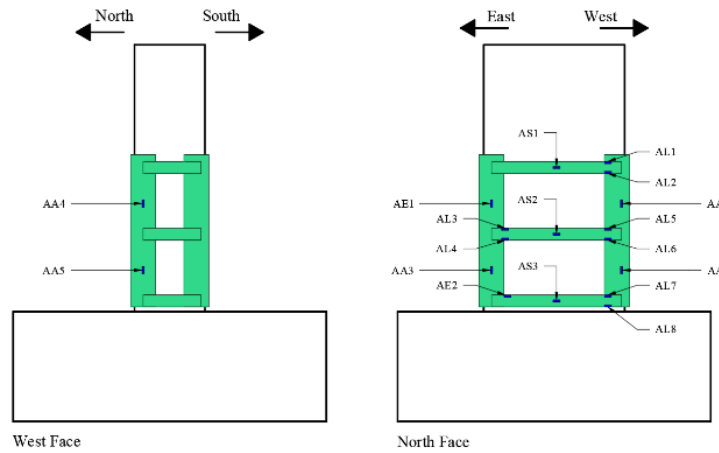


Fig. 3.16—External strain gauges in steel jacket

3.2.9.2 Internal

The internal instrumentation consists of placing strain gauges at different points to measure strains that occur in the reinforcing steel, both longitudinal and transverse. Fig. 3.17 shows the position of the strain gauges, Table 7.1 in section 7.2.1 deeply explains the nomenclature. For instance, L stands for longitudinal bar, T stands for transverse bar.

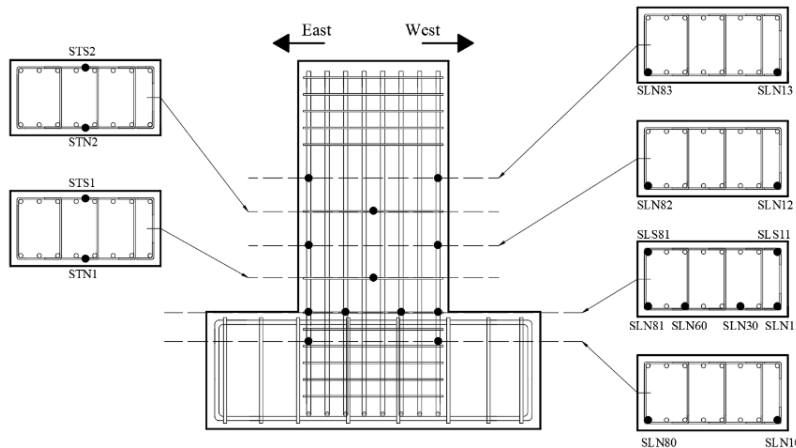


Fig. 3.17—Location of strain gauges, north face view

3.2.10 Data Acquisition

The data acquisition setup utilized a TDS recorder and a personal computer. The recorder received analogue signals from the measurement instrument channels, converting them into digital signals transmitted to the computer. A dedicated program on the computer both graphed and stored the data on a magnetic device in a format suitable for subsequent analysis. This equipment was accompanied by a program developed at CENAPRED, facilitating real-time monitoring of select channels. These monitored channels, acting as controls during testing, included the load applied to the hydraulic jack and the horizontal displacement of the column measured by the transducer DHL-3. Additionally, a real-time plot of the hysteresis curve served for observation and monitoring purposes. The recorded data played a crucial role in determining the timing of data collection during the trial. Overall, the described system allowed for comprehensive data capture, real-time monitoring, and subsequent analysis, showcasing a sophisticated approach to experimental instrumentation and control.

3.3 Definition of Study Prototypes

3.3.1 Specimen CO

The specimen CO (specimen O in Table 3.1) was the original column, meaning it was without steel jacket. The characteristics and distribution of the reinforcing steel are based on columns tested by Aboutaha (1994), which exhibit features from the 1960's, representing non-ductile columns. This specimen is used as benchmark to compare the behaviour of further specimens with steel jacketing. The test was controlled by load until reaching 196.1 kN (20 t), and subsequently, it was controlled by displacements. During the test, at the end of each peak, cracks were marked as they formed or extended. For the positive direction (pushing towards the west), a black colour was used, and for the negative direction (pushing towards the east) a red colour was employed. Each crack was assigned the step number at which they occurred or extended. A record of crack sizes was also kept at the end of each peak at the zero-load point.

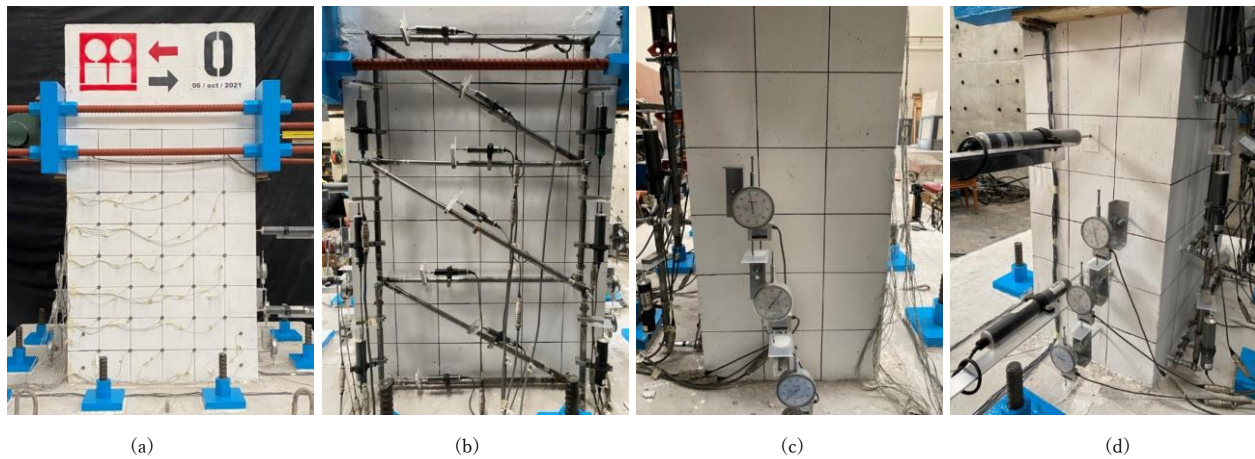


Fig. 3.18—Specimen CO at the beginning of the test: (a) north; (b) south; (c) east and (d) west face (courtesy: S. M. Alcocer)

3.3.2 Specimen CO*

This specimen is the same as specimen CO with the difference of being tested using a computer controlled hydraulic actuator (see section 3.2.6, Fig. 3.11c). Also, the concrete of the column and foundation are slightly different in their mechanic properties, as observed after the concrete cylinder tests (see Table 3.3).

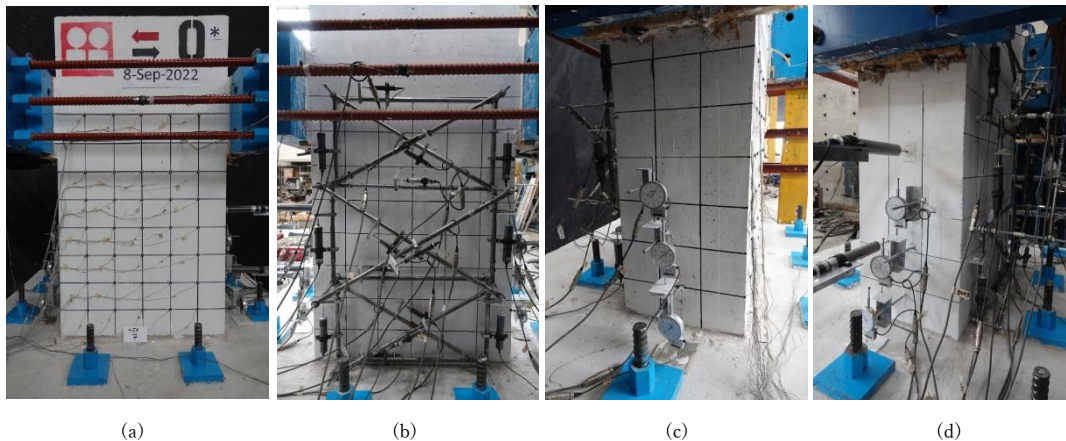


Fig. 3.19—Specimen CO at the beginning of the test: (a) north; (b) south; (c) east and (d) west face (courtesy: S. M. Alcocer)*

3.3.3 Specimen S8

Specimen S8 (specimen S-3-1/4-h/2-A-2 in Table 3.1) had a steel jacket, consisting of steel angles designated as LI with a flange width of 50.8 mm (2 inches) and a thickness of 6.35 mm (1/4 inch), placed at the corners of the column and with a length of 97 cm. Additionally, the SJ reinforcing was completed with a batten with a thickness of 6.35 mm and a width of 76.2 mm (3 inches), spaced at 42.5 cm.

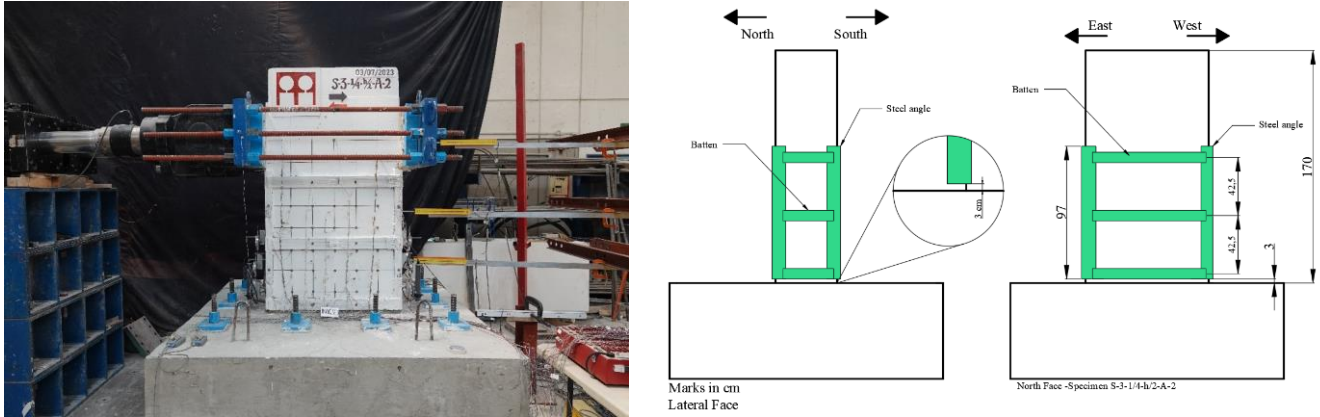


Fig. 3.20—Detail of specimen S8

3.3.4 Specimen S9

Specimen S9 (specimen S-3-1/4-h/2-A-6 in Table 3.1) had a SJ, made up of steel angles designated as LI with a flange width of 152.4 mm (6 inches) and a thickness of 6.35 mm (1/4 inch), placed at the corners of the column with a length of 97 cm (see Fig. 3.21). Additionally, the steel reinforcing was completed with a batten with a thickness of 6.35 mm and a width of 76.2 mm (3 inches). The battens were spaced at 42.5 cm.

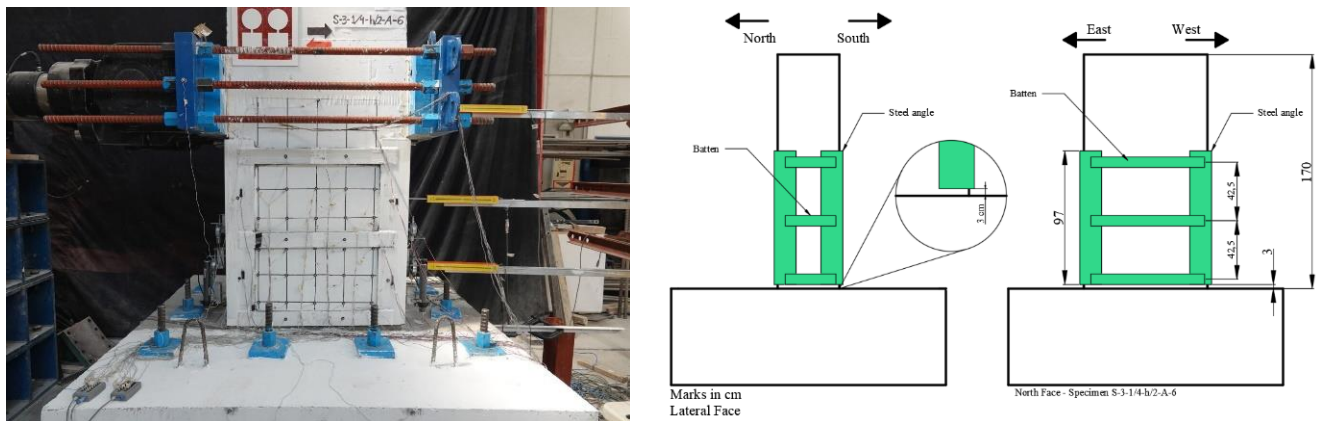


Fig. 3.21—Detail of specimen S9

3.4 Parameter Definition

The analysis of the behaviour of the tested models is generally carried out through the values and trends of different parameters that relate their geometric, mechanical and structural properties for each model. This part describes the definitions of some parameters, in order to interpret the global and local performance of each model.

3.4.1 Drift Ratio and Hysteresis Curve

The drift ratio R is the ratio between the total horizontal displacement Δ_T measured at the level of application of the lateral load, using an SDP, and the height h at which this load is applied, this is $R = \Delta_T/h$. It is commonly indicated as a percentage because it is a dimensionless parameter. The horizontal displacement is composed of the lateral flexural deformation Δ_F and the lateral shear deformation Δ_S , that is $\Delta_T = \Delta_F + \Delta_S$ (which can lead to a yield penetration or not). The angle generated between the deformed configuration and the original configuration approximates the tangent of the same angle. Deformation is usually expressed in terms of drift.

The phenomena that present a system which state depends not only of the actual conditions, but also the precedent, is denominates hysteresis. The hysteresis curve of a model is the graphic representation of the relation between the lateral load and the deformation that it causes, in terms of drift (Aguilar-Ramos, 1997). In this case, it is the evolution of the lateral stiffness of an element, like the studied column.

3.4.1.1 Drift Components

The lateral deformation that occurs in the column (due to shear and bending) allows us to analyse the behaviour and failure mode of the column, this deformation include elastic an inelastic. According to Aguilar-Ramos (1997), if the expansion of the element in its plane due to the deformation of the concrete is neglected, the deformation of the columns under lateral loads can be attributed to two mechanical elements: shear and bending, so the total lateral displacement Δ_T can be divided into two components, the lateral displacement due to pure shear and pure flexure deformation, Δ_S and Δ_F , respectively, the sum of these shear and flexural lateral deformation are the total lateral deformation $\Delta_T = \Delta_F + \Delta_S$. The approximation of the tangent of the angle θ_S is small in order, so it can be approximate, as $\theta_S = \tan(\theta_S) = \Delta_S/h$. Also, we can write drift $R = R_F + \gamma_S$, where R_F and γ_S are the drift consequence of the flexure and the contribution of angular deformation, respectively.

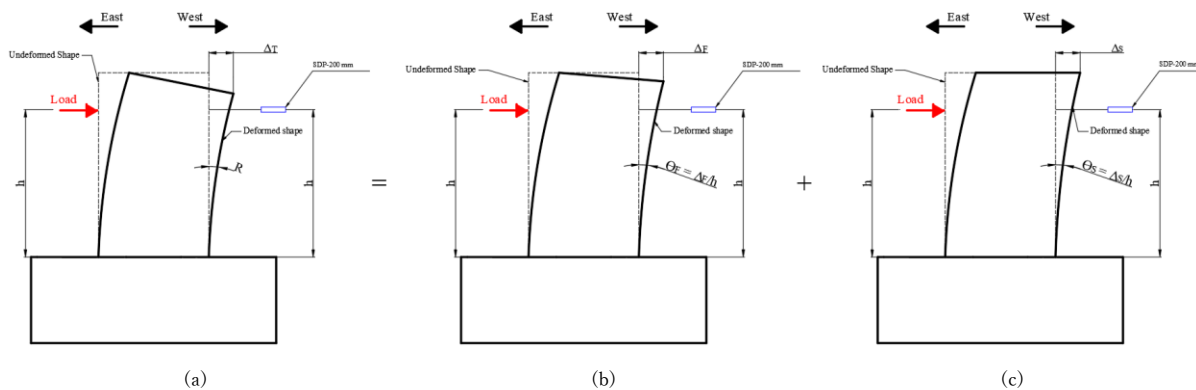


Fig. 3.22—Drift main components: (a) total lateral deformation; (b) lateral flexural deformation; (c) lateral shear deformation. Adapted from Aguilar-Ramos (1997).

3.4.2 Rotation

The rotations are determined from measurements taken by dial potentiometers located on the sides of the columns at three different heights. Curvature is calculated from rotation, what is the ratio of the rotation between the height between each dial potentiometer. The rotation is calculated with the expression in Eq. 3.4.

$$\theta_i = \frac{\ell_{Ei} - \ell_{Wi}}{a_i} \tag{Eq. 3.4}$$

where θ_i is the column rotation in the i region, ℓ_{Ei} and ℓ_{Wi} are the east and north lecture of the micrometre, and a_i is the horizontal distance between the micrometres in a height b_i (see Fig. 3.23).

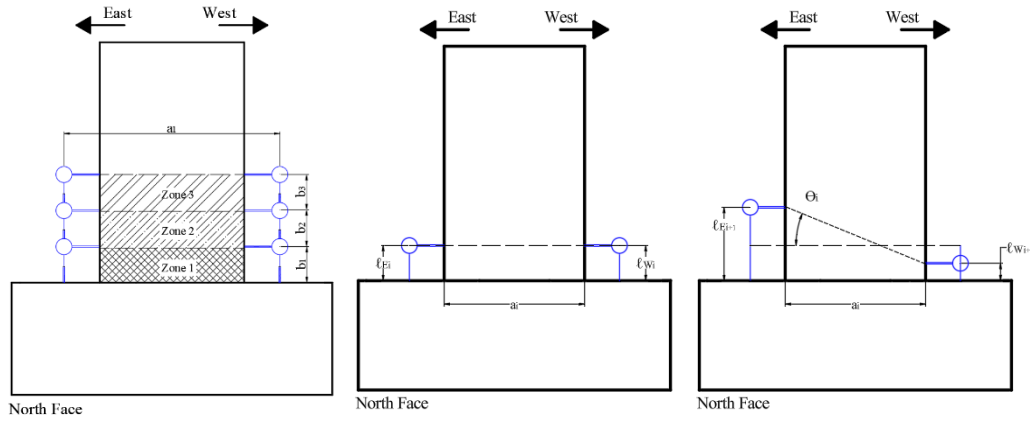


Fig. 3.23—Zones established for the calculation of rotations and curvatures

3.4.3 Shear Distortion

To calculate the shear distortion, the configuration of inclined crossed displacement transducers was used (see Fig. 3.15b). The initial length is measured. During the test, the transducers record the displacements, using this data, the strain was obtained by dividing each displacement by the initial length. This operation can be expressed as $\varepsilon_i = \delta_i / L_0$, where ε_i is the strain at time i ; δ_i is the measured displacement at time i ; and L_0 is the initial length. Subsequently, the absolute values of the strain of both diagonals were added to obtain the angular deformation of the studied section. Finally, the shear distortion at time i is calculated using Eq. 3.5.

$$\gamma_i = \frac{|\varepsilon_{1i}| + |\varepsilon_{2i}|}{a_i} \tag{Eq. 3.5}$$

where $|\varepsilon_{1i}| + |\varepsilon_{2i}|$ are the sum of the absolute values of strain recorded in each diagonal, and a_i is the horizontal distance between the displacement transducers in a height b_i .

3.5 Experimental Results

In the case of specimens C8 and C9, the pictures of the specimens tested erroneously display negative values for both load and displacement control when the column is pushed westward. It is essential to note that, for consistency across all test results, black-marked cracks in the pictures observed during westward pushing should be associated with positive values of displacement and load, while red-marked cracks formed during eastward pulling should be linked to negative values. It is crucial to clarify that the curves presented in this chapter have been appropriately adjusted with the correct signs in accordance with the details outlined in section 3.2.7.

3.5.1 Specimen CO

Specimen CO was tested on October 06, 2021. The crack pattern was consistent on both faces of the column, regardless of the load level or drift. Cracks exhibited characteristics typical of a non-ductile column, as a sudden shear failure occurred, leading to a displacement far exceeding the anticipated amount for that cycle. The column's damage analysis was performed by examining the north face.

3.5.1.1 *Damage Evolution*

Here are four stages of the damage sequence observed during the test. The first crack recorded occurred during load control, during -98.06 kN load (-10 t), in the bottom of the column (see Fig. 3.24b), in the column-foundation joint, the second crack occurred during +98.06 kN load (+10 t), at the opposite place of the first crack (see Fig. 3.24c). The first inclined crack, with an approximate inclination of 45° degrees, appeared simultaneously on the north and south faces at a drift of +0.0024. The same inclined crack appeared in the opposite direction at a drift of -0.0026. At a drift of +0.005, four inclined cracks were identified, with a maximum crack thickness of 2.6 mm. When the load was returned to zero, the cracks closed to a value between 0.1 mm and 0.15 mm (see Fig. 3.26). During drift +0.01, the inclined cracks extended across the entire diagonal, causing a sudden lateral displacement of the column, leading the model at a drift of +0.023 (as observed in Fig. 3.30, after the maximum positive peak) and a maximum load +844.35 kN (+86.1 t). During this cycle, the thickness of existing cracks increased, measuring up to 12 mm on the north and south faces. At the same time, new inclined cracks with small thicknesses emerged. For higher drift, the inclined cracks on the north and south faces increased in thickness, although some cracks closed when returning to zero displacement. Additionally, the concrete core began to crush, and the cracks reached the middle section of the column. In the lower portions of the east and west faces, as well as in the centre of the column, the concrete started to crush.

The end of the test was determined by a brittle failure (shear failure) that occurred at a drift of +0.02. When the cover at the centre of the column began to spall from the core, the reinforcing steel became visible, and the lateral load dropped to 18.3% of its peak strength. Flexural cracks in the upper and lower parts of the east and west faces opened due to the inclined cracks that crossed the column (see Fig. 3.28e). This type of failure is attributed to the significant separation of transverse reinforcing, which does not contribute significantly to shear strength and does not help generate substantial ductility capacity.

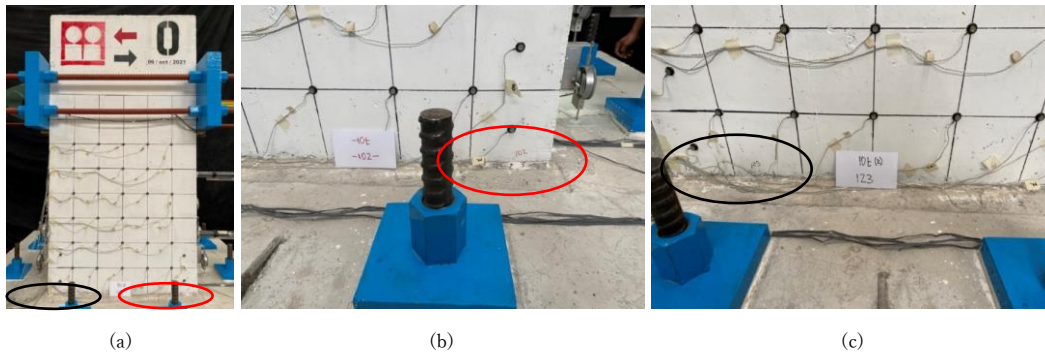


Fig. 3.24—First cracks: (a) front face; (b) first crack; (c) second crack

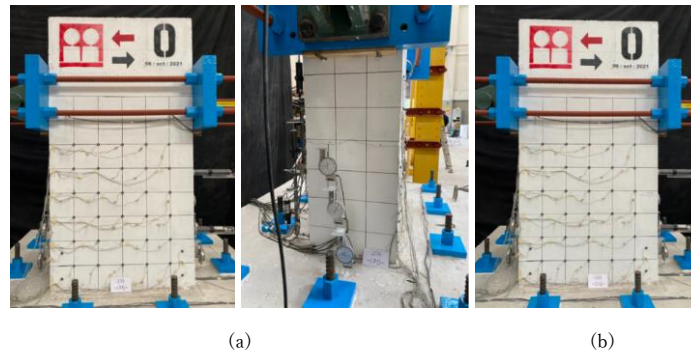


Fig. 3.25—First horizontal cracks at middle height: (a) load = +196.1 kN, east face; (b) load = -196.1 kN, west face

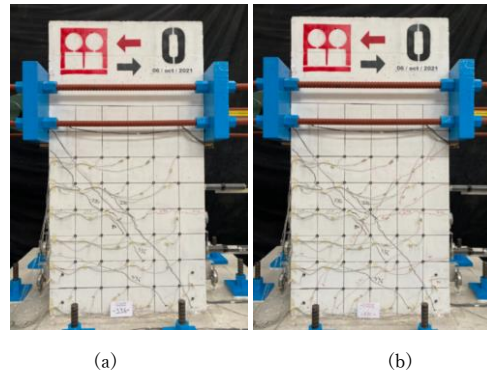


Fig. 3.26—Damage at drift +0.005 and -0.005 respectively: (a) load = -636.5 kN; (b) load = +649.7 kN (courtesy: S. M. Alcocer)

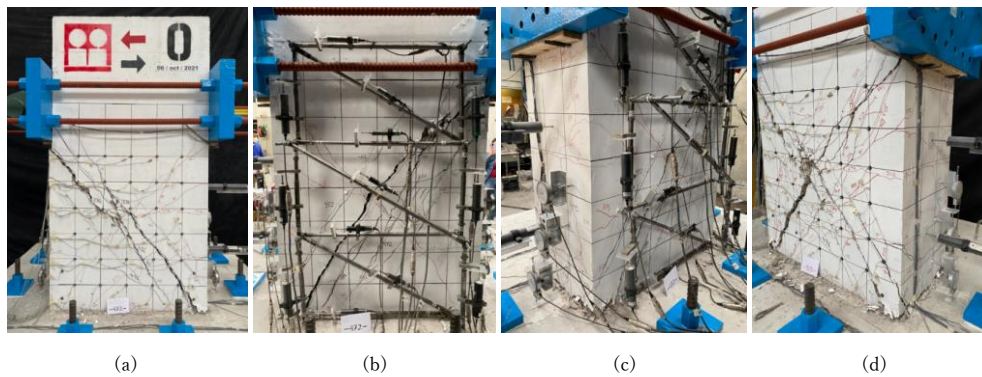


Fig. 3.27—Damage at drift ±0.01: (a) Drift +0.01; (b) south face; (c) west face; (d) damage at -0.01 (courtesy: S. M. Alcocer)

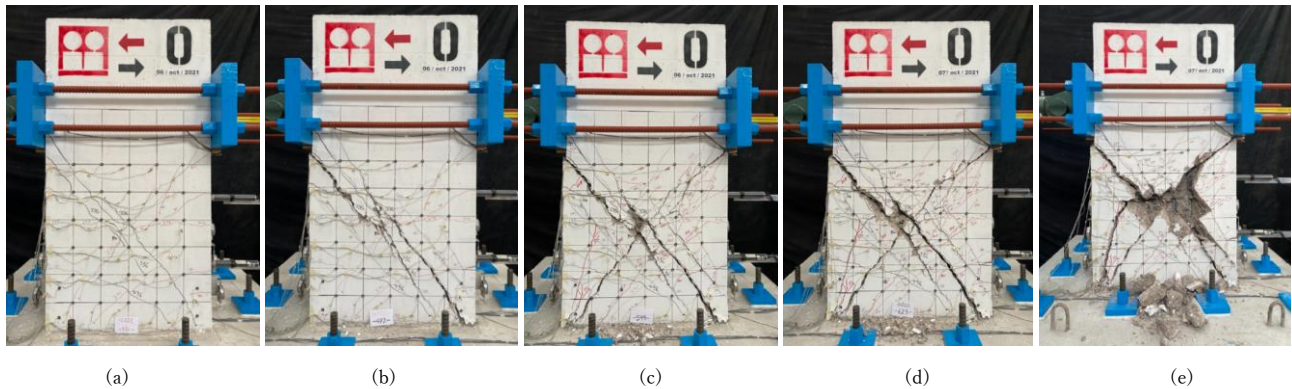


Fig. 3.28—Crack evolution: (a) drift +0.005; (b) drift +0.01; (c) drift +0.015; (d) drift +0.02; (e) final state (courtesy: S. M. Alcocer)

3.5.1.2 Final Damage State

In Fig. 3.29, a photograph of the final state of the column damage is presented, once the instrumentation had been removed. In this figure, a more or less uniform distribution of column crack can be observed, with a concentration of damage at the centre of the column (concrete crushing). The column cover spalled at the centre, revealing some of the longitudinal and transverse reinforcing bars. After removing the cover with the most damaged zones, it was observed that some longitudinal reinforcing bars on the north face showed slight buckling. This occurred when the load was applied in the positive direction, the reinforcing bars on the north face buckled. Additionally, these bars were under tension when the test went out of control, reaching a drift of +0.023.



Fig. 3.29—Column O final state, end of test (courtesy: S. M. Alcocer)

3.5.1.3 Hysteresis Behaviour

The lateral load-to-drift ratio hysteresis curves are shown in Fig. 3.30. The hysteresis curve of specimen CO is noticeably symmetrical with stable loops during the first cycles. The cycles performed before the first significant inclined crack exhibited approximately linear elastic behaviour. In the positive peak point (0.008, 843.8), where the first inclined cracks with maximum openings of up to 2.6 mm had already appeared in previous cycles, a drift of +0.023 was reached, consequence of a sudden drop in strength and stiffness, the displacement went from 10.7 mm to 28.48 mm, as the hydraulic jack continued to move at the moment of column failure. From this cycle onwards, up to 51% of the strength have lost in the negative direction (“A” mark in Fig. 3.30). By the point (0.02, 193.2), 78% of the column's maximum strength has been lost. The model exhibited linear stiffness up to a drift of +0.0007. Subsequently, there were slight losses of stiffness until reaching a drift of +0.008, at which point the

maximum strength was reached. The stiffness and strength then dropped suddenly. The lack of transverse reinforcing contributed to severe damage in the core of the column, as well as the significant displacement generated by the column failure.

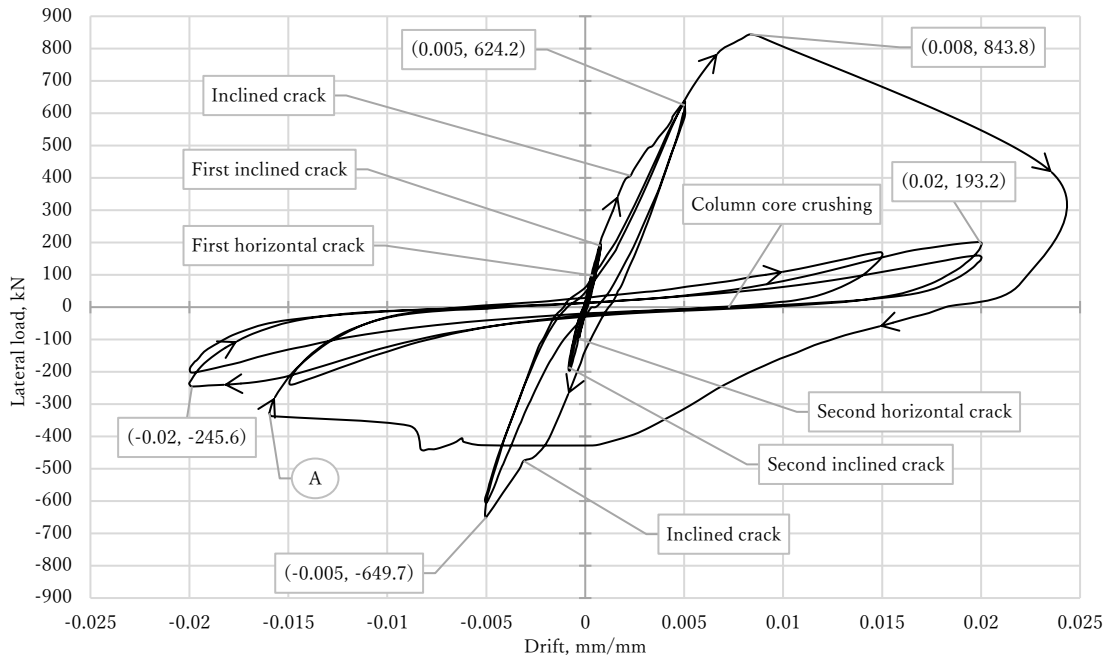


Fig. 3.30—Hysteresis plot of specimen CO

3.5.1.4 Column Rotation

Fig. 3.31 shows the rotation of Zones 1, 2, and 3, calculated using recordings from micrometres (see Fig. 3.15c). The rotation in Zone 1 of the column was the more stable, exhibiting well-defined hysteresis loops, very similar to the hysteresis curve of the column. In Zone 2 (see Fig. 3.31) after the positive peak of lateral load, the next positive peak stayed with the same rotation, after that, the next positive peak (0.002, 193) reached 1.53 times the rotation of the maximum peak of lateral load. Finally, the Zone 2 reached the maximum rotation of 0.003 mm/mm. For the Zone 3, a disruptive behaviour appears after the peak of lateral load.

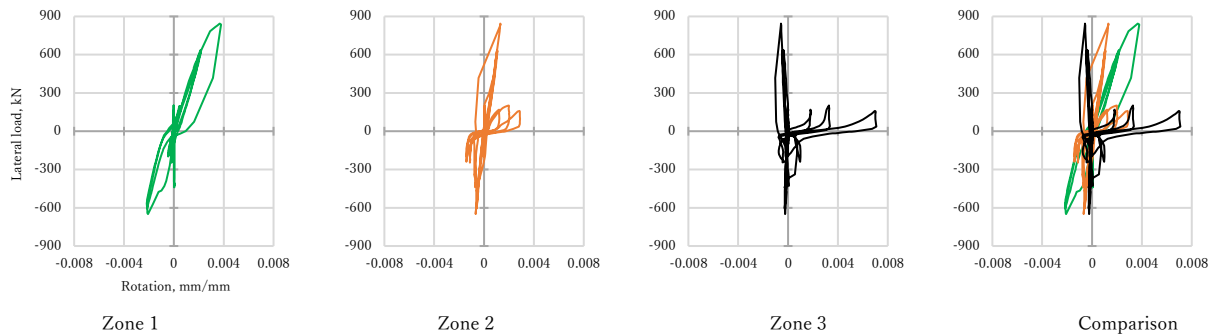


Fig. 3.31—Rotation of zones in concrete column core using micrometres

Fig. 3.32 shows the rotation of Zones 1, 2, and 3, respectively, calculated using the recording from the displacement transducer (see Fig. 3.15b). Comparing the Zone 1 of the curvature measured with micrometres and displacement transducers,

it is clear the more stable and symmetric response of the north face of the column core, and in the Fig. 3.32, the rotation increases after the positive peak of lateral load. For the Zone 2, both the micrometre and the displacement transducer rotation are alike. The difference in response of the Zone 3, comparing both curvatures, the calculated using displacement transducers reaches 1.57 times the rotation calculated with micrometres.

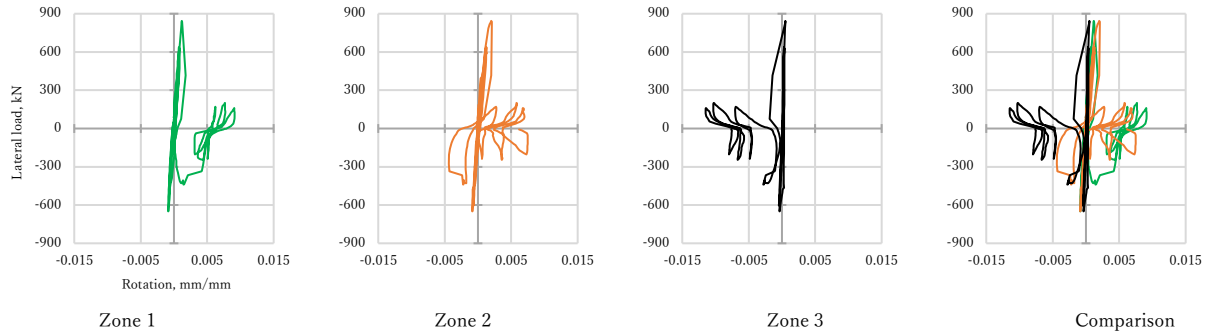


Fig. 3.32—Rotation of zones in concrete column core using displacement transducer

The column rotations registered in this test as well as further specimen’s test can be helpful to develop a simplified nonlinear model to predict the lateral response of RC columns rehabilitated with latticed SJ.

3.5.1.5 Foundation Rotation and Sliding

The rotation of the foundation was calculated as described in 3.4.2, using the micrometres installed in the foundation (see Fig. 3.15c), labelled as CHE and CHO and the distance between them (2,150.1 mm). The plot of the lateral load vs the rotation is shown in the Fig. 3.33a. The sliding of the foundation was traced using an SDP of 50 mm length, layered as DHL-0 (see Fig. 3.15a).

The plot of the lateral load vs the measured sliding is shown in Fig. 3.33b; the positive values of the displacement are in the west direction, the negative values are in the east direction, the maximum sliding recorded was +0.18 mm. The values of rotation and displacement did not affect the overall lateral behaviour of the specimen, so these values were considered negligible.

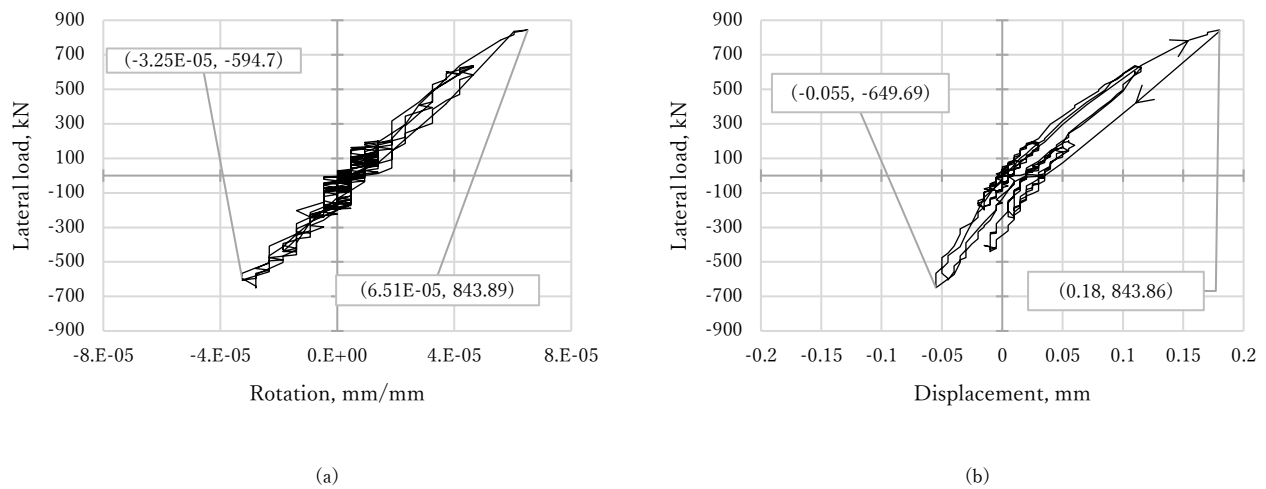


Fig. 3.33—Foundation history of rotation (a) and sliding (b) of the specimen CO

3.5.1.6 Strain Gauges Readings

In this section, the plots of the internal instrumentation, the strain gauges installed in the reinforcing steel, are shown. The main objective to measure the strain of reinforcing steel was to identify the yield with a respective lateral load. The yield of the reinforcing steel is assumed that is reached when the strain surpasses the yield limit ($\pm 2,300 \mu m$) and exists a residual strain.

As expected for the specimen CO, the strain gauges located in the top of the core of the column remained elastic. This is the case of the strain gauges marked with green dots in Fig. 3.34. The only reinforcing steel that yielded was that marked with the red dots in Fig. 3.34. The reason why additional reinforcing steel did not reach yielding may be due of the brittle failure mode of the column. The yielding history of strain gauges can be seen in Table 3.5. Yielding related to the hysteresis curve is shown in Fig. 3.35 were strain gauges that recorded yield are labelled.

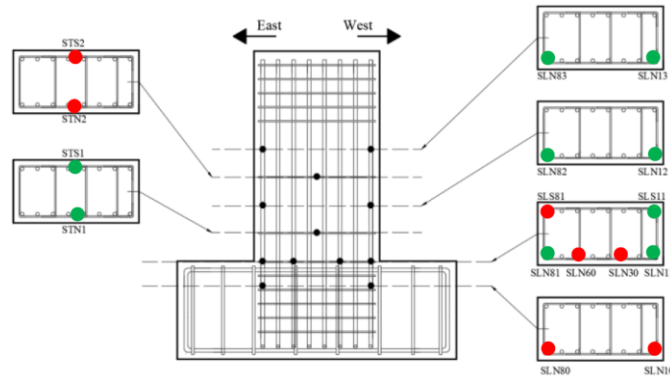


Fig. 3.34—Internal strain gauges that recorded yielding: red (yield); green (elastic)

Table 3.5—Internal strain gauge yielding history of specimen CO

Strain Gauge	Load step @ yield	Strain μm	Lateral load kN	Displacement mm	Drift ratio mm/mm
SLN30	331	6,511	542.3	6.04	0.005
SLN10	473	7,221	843	9.6	0.008
SLN60	473	8,114	843	10.06	0.0083
SLN80	473	16,642	836	10.7	0.0088
SLS81	371	-2,144 ^[1]	-649	-6.04	-0.0050
STN2	474	11,000	821	10.65	0.0087
STS2	471	6,000	819	10.51	0.0087

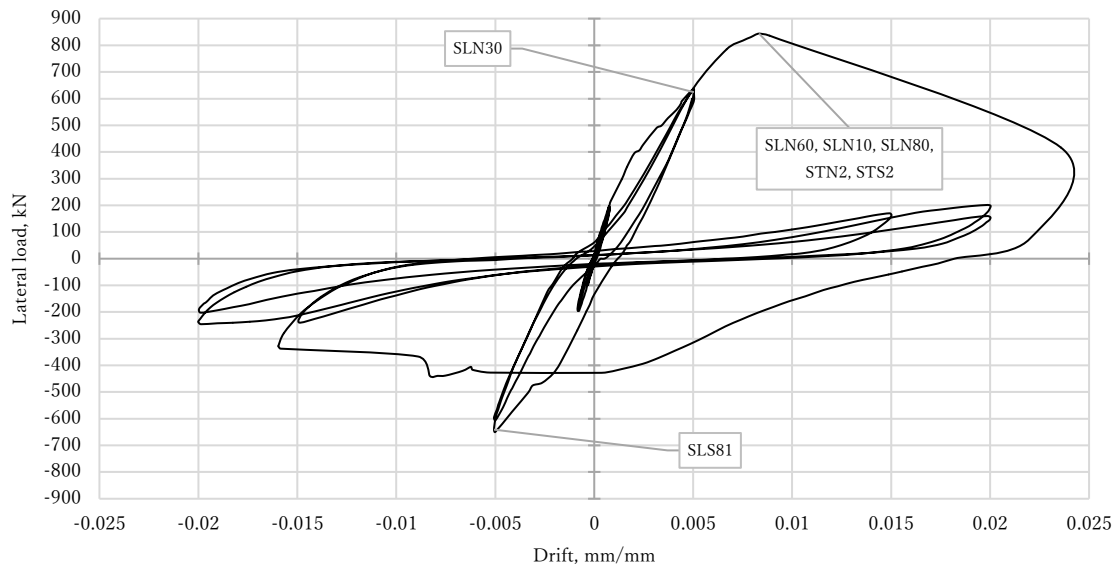


Fig. 3.35—Yielding recorded by strain gauges in specimen CO

3.5.2 Specimen CO*

The specimen CO* was tested on September 08, 2022. The crack pattern was consistent on both faces of the column, regardless of the load level or drift ratio. The cracks exhibited characteristics typical of a non-ductile column. As in the previous specimen, the column's damage analysis was performed by examining the north face.

3.5.2.1 Damage Evolution

Four stages of the damage sequence were observed during the test. Unlike specimen CO, the first crack occurred during the first load control +196.13 kN (+20 t), the crack appeared in the bottom of the east face (see Fig. 3.36a). During the second load control +196.13 kN the second horizontal crack appeared at middle height of the column, and on the first load control at a -196.13 kN the same crack appeared symmetrically in the west face (see Fig. 3.36c).

The first lateral crack appeared at a drift of +0.005, this can be seen in Fig. 3.37a, also, the opposite lateral crack appeared at a drift of -0.005 (see Fig. 3.37b), both lateral cracks appeared in the main diagonals of the column, accompanied by lateral cracks nearby. At a first drift of +0.01, the horizontal cracks in the east face started to grow (see Fig. 3.38b), at this time, the principal inclined cracks increased in width, and in the load history the lateral load was the maximum recorded for the positive values (+701 kN). At a first negative drift of -0.01, the lateral load was the maximum recorded for the negative values, which is -650 kN. At a second drifts to ± 0.01 , the lateral load recorded decreased to ± 620 kN. At a first drift of +0.015, vertical cracks appeared in the east face (see Fig. 3.39a) near the top of the column. At a second drift of +0.015, the vertical cracks in the east face increased notoriously in length and width (see Fig. 3.40a), these cracks did not appear in the west face, so the damage was not symmetric. Also, in the north face the principal inclined crack of the drift increased in width more than the principal inclined crack at a second drift of -0.015 (see Fig. 3.40).

At a first drift of +0.02, related to a lateral load +199 kN, the principal inclined crack in the north face increased dramatically (see Fig. 3.41), reaching 10 mm in width. The damage recorded on the north face was noticeable. At a first drift of -0.02, related

to a lateral load of -326 kN, the principal inclined crack of the negative drift also increased in width and length (see Fig. 3.42), but this in a minor quantity compared to the principal inclined crack at a positive drift of +0.02. Now, at a second drifts to ± 0.02 , the damage in all the faces of the column increased, even pieces of concrete spalled (see Fig. 3.43), most damaged faces were the east and south sides. The end of the test was determined by a brittle failure (shear failure) that occurred at a drift of +0.025. When the cover at the centre of the column began to spall from the core, the reinforcing steel became visible, and the lateral load dropped to 22% of its peak strength. Flexural cracks in the upper and lower parts of the east and west faces opened due to the inclined cracks that crossed the column. This type of failure is attributed to the significant separation of transverse reinforcing, which does not contribute significantly to shear strength and does not help generate substantial ductility capacity, like in the case of specimen CO.

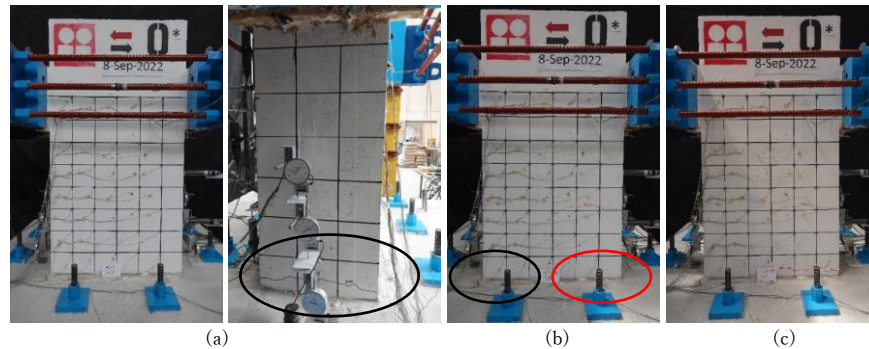


Fig. 3.36—First horizontal cracks at load control protocol: (a) +196.13 kN; (b) second +196.13 kN; (c) -196.13 kN

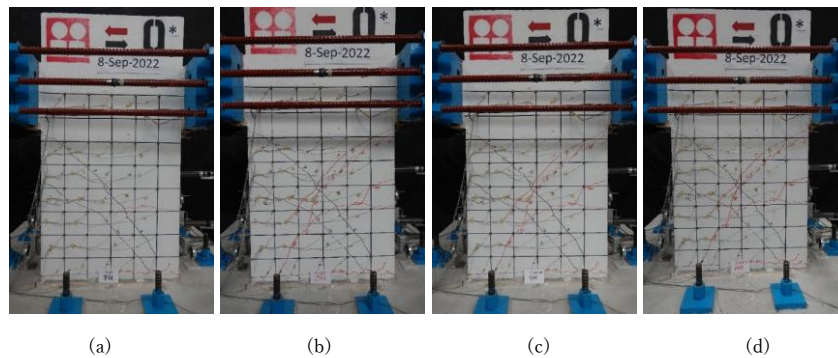


Fig. 3.37—First inclined cracks at drifts: (a) +0.005; (b) -0.005; (c) second +0.005; (d) second -0.005

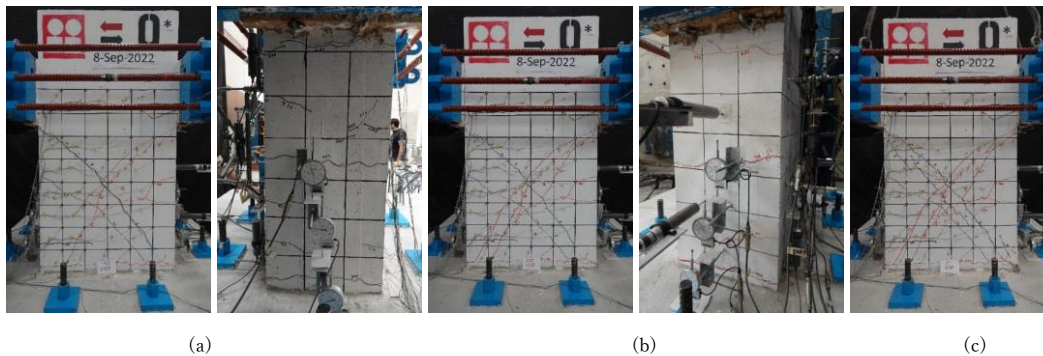


Fig. 3.38—Damage at drift of: (a) +0.01; (b) -0.01; (c) zero drift

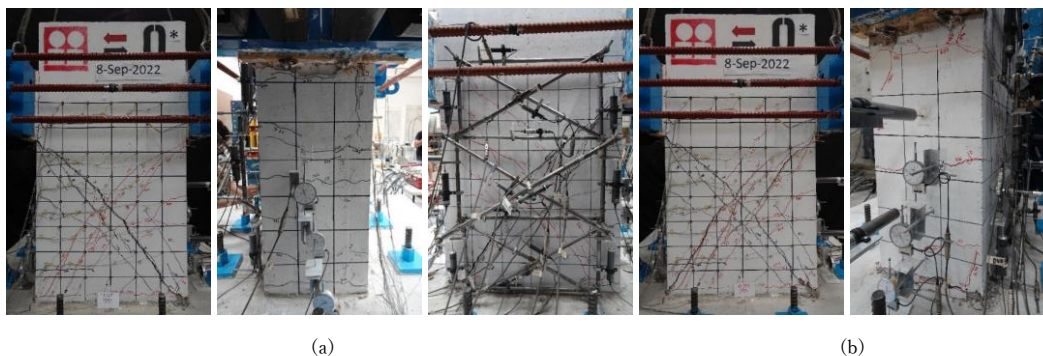


Fig. 3.39—Damage at a drift of: (a) +0.015; (b) -0.015

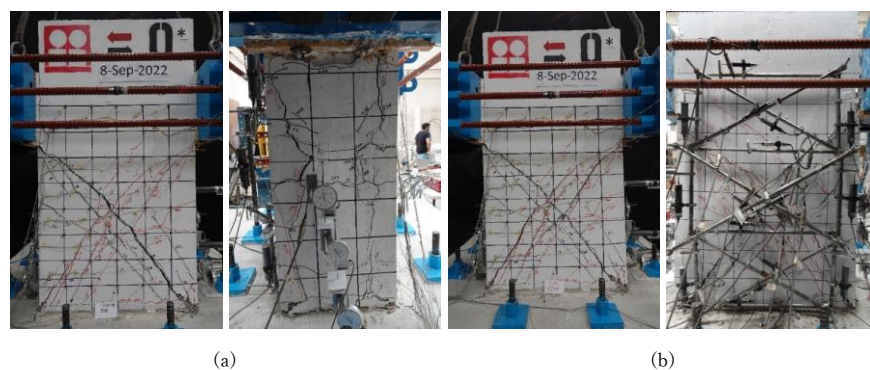


Fig. 3.40—Damage at a second drift of: (a) +0.015; (b) -0.015



Fig. 3.41—Damage at a drift of +0.02



Fig. 3.42—Damage at a drift of -0.02

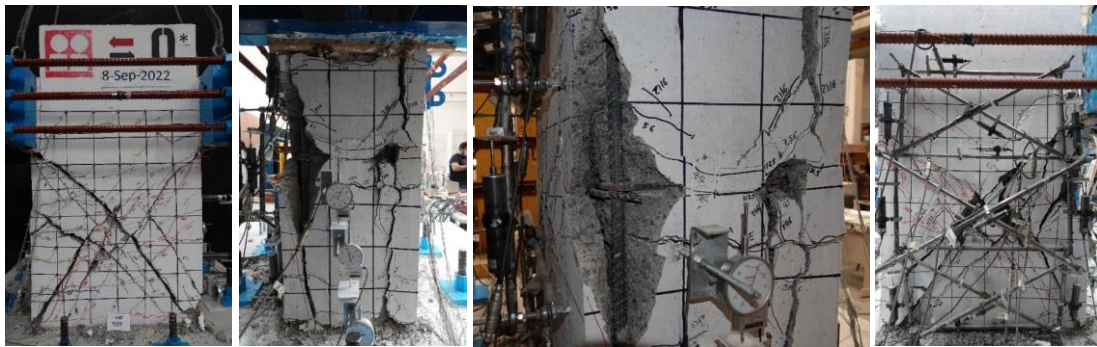


Fig. 3.43—Damage at a second drift of +0.02



Fig. 3.44—Damage at a second drift of -0.02

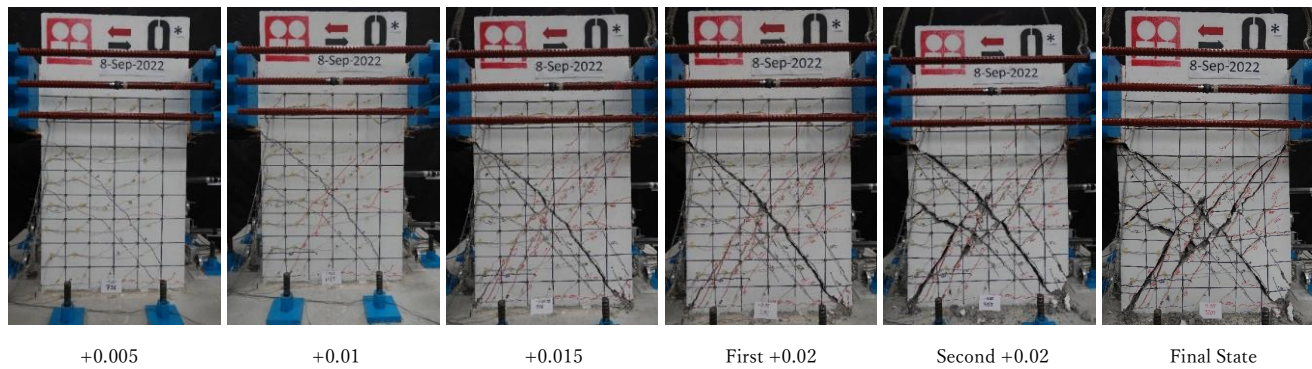


Fig. 3.45—Crack evolution of specimen CO for positive drift peaks*

3.5.2.2 Final Damage State

In the Fig. 3.46, a photograph of the final state of the column damage is presented. In this figure, a more or less uniform distribution of column crack can be observed, with a concentration of damage at the centre of the column (concrete crushing). The column cover spalled at the centre, revealing some of the longitudinal and transverse reinforcing bars. After removing the cover with the most damaged zones, it was observed that some longitudinal reinforcing bars on the north face showed slight buckling. The damage pattern was slightly different than the observed in specimen CO.



Fig. 3.46—Final damage state

3.5.2.3 Hysteresis Behaviour

The hysteresis behaviour is shown in Fig. 3.47. The hysteresis curve of column CO* is noticeably symmetrical with stable loops during the first cycles. The cycles performed before the first significant inclined crack exhibited approximately linear elastic behaviour. In the positive peak point (0.008, 701), trying to reach the drift of 0.01, the maximum lateral load was recorded. In contrast to specimen CO, when reaching the peak load, the lateral displacement stayed at 9.6 mm without any sudden shifts. This was achieved by utilizing a computer-controlled hydraulic jack, which ensured precise displacement control and maintained a constant value upon reaching the peak load. The difference in the positive and the negative maximum peak of lateral load is about 7.8%, which is acceptable as a symmetric response. By the point (0.01, 363), 48% of the column's maximum strength has been lost. The model exhibited linear stiffness up to a drift of +0.00062. Subsequently, there were slight losses of stiffness until a drift of +0.008 was reached, at which point the maximum strength was achieved.

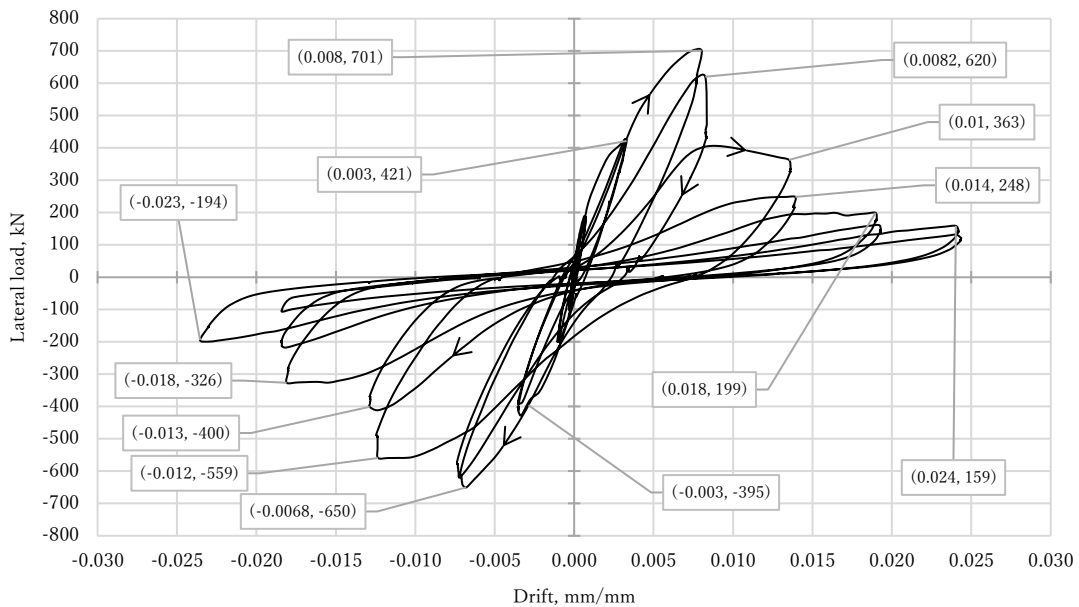


Fig. 3.47—Hysteresis plot of specimen CO*

3.5.2.4 Column Rotation

Fig. 3.31 shows the rotation of Zones 1, 2, and 3, respectively, calculated using micrometre records (see Fig. 3.15c). The rotation in Zone 1 of the column was the most stable, exhibiting well-defined hysteresis loops, very similar to the typical hysteresis curve. The observed asymmetry is attributable to the damage that occurred in this region. In Zone 2 (Fig. 3.31b), after the positive peak of the lateral load, the next positive peak maintains the same rotation. After that, the next positive peak (0.002, 193) reaches 1.53 times the rotation of the maximum peak of lateral load. Finally, Zone 2 reaches a maximum rotation of 0.003 mm/mm. In Zone 3, a disruptive behaviour appears after the peak of lateral load (Fig. 3.31c).

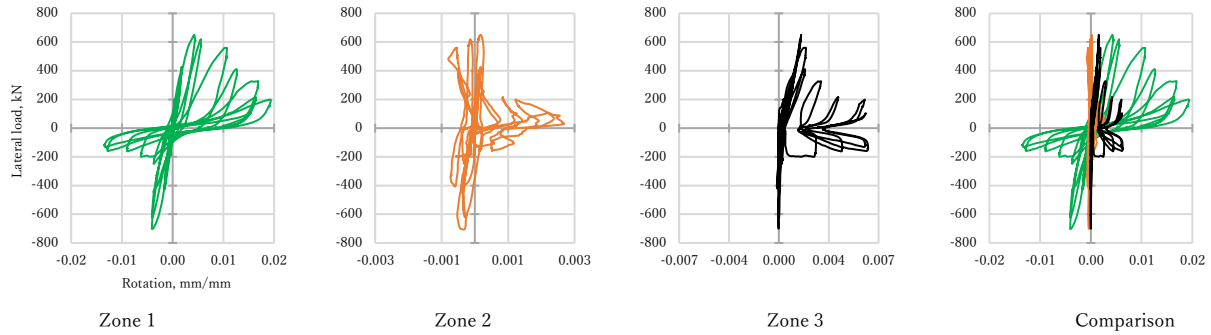


Fig. 3.48—Rotation of zones in concrete column core using micrometres

Fig. 3.49 shows the rotation of Zone 1, 2, and 3, respectively, calculated using the record of the displacement transducer. Comparing the Zone 1 of the curvature measured with micrometres and displacement transducers, it is clear the more stable and symmetric response of the south face of the column core, being a linear response. For the Zone 2, the displacement transducer rotation was more stable, with a response quite linear in the majority of the cycles. The difference in response of the Zone 3, comparing both curvatures, the calculated using displacement transducers had symmetry in the positive and negative range, until the last cycles have been reached.

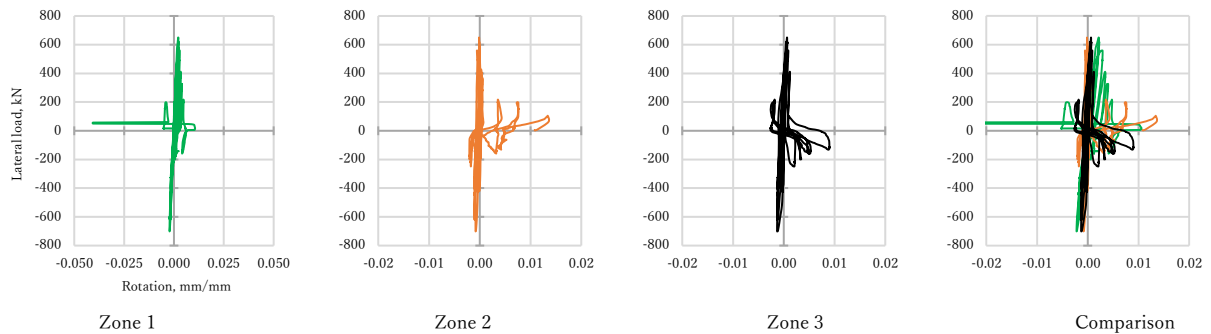


Fig. 3.49—Rotation of zones in concrete column core displacement transducers

3.5.2.5 Foundation Rotation and Sliding

The rotation of the foundation is calculated as described in 3.4.2, using the micrometres installed in the foundation. The plot of the lateral load vs the rotation is shown in Fig. 3.50a. The plot of the lateral load vs the measured sliding is shown in Fig. 3.50b; the positive values of the displacement are in the west direction, the negative values are in the east direction, the maximum sliding recorded was +0.185 mm. This value es quite similar to those of the specimen CO. In the case of rotation, the graph moved from the origin in some point of the test, the phenomena that caused this haven't been discovered. Also, in the lateral

load vs sliding, the graph also moved from the origin, but this occurred in the last cycles of load. The values of rotation and displacement are negligible.

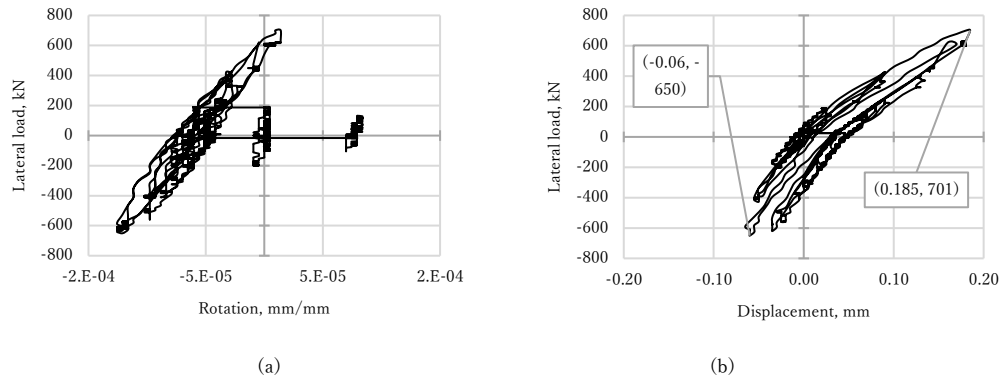


Fig. 3.50—Foundation history of rotation (a) and sliding (b) of the specimen CO*

3.5.2.6 Strain Gauges Readings

As defined before in specimen CO, the yield of the reinforcing steel is assumed that is reached when the strain surpasses the yield limit ($\pm 2,300 \mu m$) and exists a remain strain.

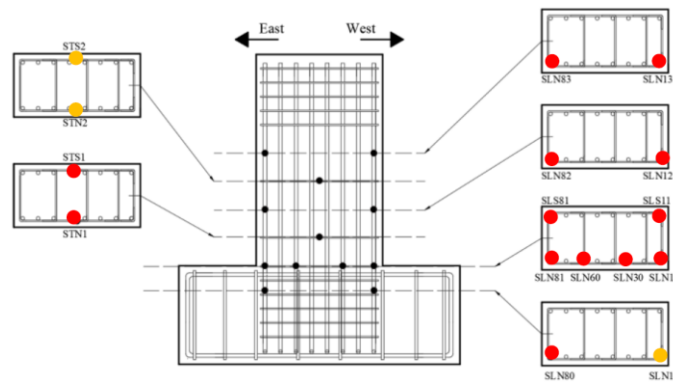
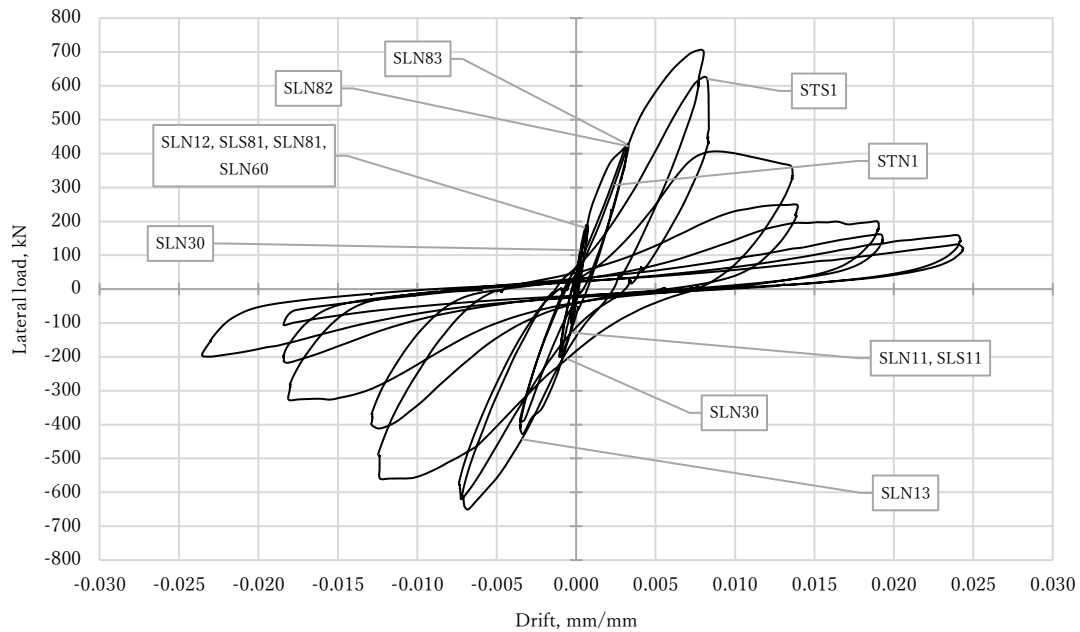


Fig. 3.51—Internal strain gauges that recorded yielding: red (yield); green (elastic); yellow (damaged or not recorded)

Table 3.6—Internal strain gauge yielding history of specimen CO*

Strain Gauge	Load step @ yield	Strain μm	Lateral load kN	Displacement mm	Drift ratio mm/mm
SLN83	751	7,700	421.7	3.96	0.0033
SLN13	887	11,524	-412	-4.23	-0.0035
SLN12	412	5,668	-198	-1.23	-0.0010
SLN82	751	8,210	405	3.36	0.0028
SLN81, SLS81	325	3,552	186.9	0.78	0.0007
SLN11	174	3,143	-98	-0.33	-0.0003
SLN30	884	9,476	-415	-4.2	-0.0035
SLN60	1,122	16,076	700	8.82	0.0070
SLS11	163	3,267	-92.5	-0.24	-0.0002
SLN80	1,137	17,152	619	9.27	0.0077
STN1	758	3,333	315.3	3.3	0.0023
STS1	1,128	4,876	626	9.27	0.0078



*Fig. 3.52—Yielding recorded by strain gauges in specimen CO**

3.5.3 Specimen S8

Specimen S8 was tested on July 03, 2023. The principal behaviour of the column was controlled by bending, because the lateral deformation seems like the behaviour of a cantilever beam. The crack patterns were more distributed along the column core compared to specimen CO.

3.5.3.1 Damage Evolution

The following sections describe in detail the distinct stages of damage progression observed during the test. Each phase reflects critical points in the overall sequence, capturing key transitions from initial to final specimen's behaviour. This breakdown provides a comprehensive view of the damage evolution, offering insights into the mechanisms at play during each stage of the testing process.

Specimen S8 exhibited flexure-controlled behaviour. The first horizontal crack (see Fig. 3.53a), with a thickness of 0.1 mm, appeared on the east face during the first cycle of load control at +196 kN (+20 t) in the middle height of the column; for further reference, this crack is labelled as "LE". In the next cycle at -196 kN, a horizontal crack appeared on the west face with a thickness of 0.15 mm; for further reference, this crack is labelled as "LW". Continuing with the load control, crack widths remained in the range of 0.1 to 0.2 mm until the end of the load control. The LE and LW cracks also appeared symmetrically on the south face.

Starting with the displacement control stage, the first inclined crack occurred at a drift of +0.005, with a related force of +353 kN (+36 t), with a thickness of 0.3 mm in both north and south faces (see Fig. 3.54a, b); for further references, this crack is labelled as "A". Back to zero drift, the A crack remained with a thickness of 0.15 mm. In the next cycle of drift -0.005 the opposite inclined crack appeared (see Fig. 3.54c), labelled from now on as "Z" crack.

In the next cycle at a drift of +0.005, a transverse crack appeared parallel to steel batten of the east face, this is shown in the Fig. 3.55a. Also, the principal inclined cracks increased its length and new small inclined cracks formed in middle height of the column. In the zero drift the A and Z cracks remains open with a thickness of 0.15 mm.

At a drift of +0.01, associated with a lateral load of +606 kN (+61.8 t), the Z crack reached a width of 0.5 mm. A new inclined crack appeared, reaching a width of 0.6 mm (see Fig. 3.56d); this crack is labelled as 'B'. Additionally, at the next drift of -0.01, an inclined crack symmetrically opposite to crack B appeared; this new crack is labelled as 'Y'. At a drift of -0.03, the white wash of the steel angle fell off, indicating the strain in the steel (see Fig. 3.58). During the peak at a drift of +0.035, the white wax of the batten fell off, and at the next negative drift of -0.035, the batten exhibited bending. At this stage, the A crack reached a thickness of 1.25 mm. At a drift of +0.045 (Fig. 3.60), the fall-off of the white wash on the steel jacket became more pronounced, and the crack pattern near the steel angles and batten increased.

At a drift of +0.06 it was evident the bending of the steel angle and the deformation out-of-plane of the batten (Fig. 3.62). The A and Y cracks reached its maximum width at a drift of +0.055, with a thickness of 5 mm and 6 mm, respectively. Reaching the drift of +0.07, related to a lateral load of -225.5 kN (-23 t) the longitudinal bar of the east face fractured (Fig. 3.64). Another bar fractured in the west face reaching the drift of +0.08, related to a lateral load of +217 kN (+22.15 t).

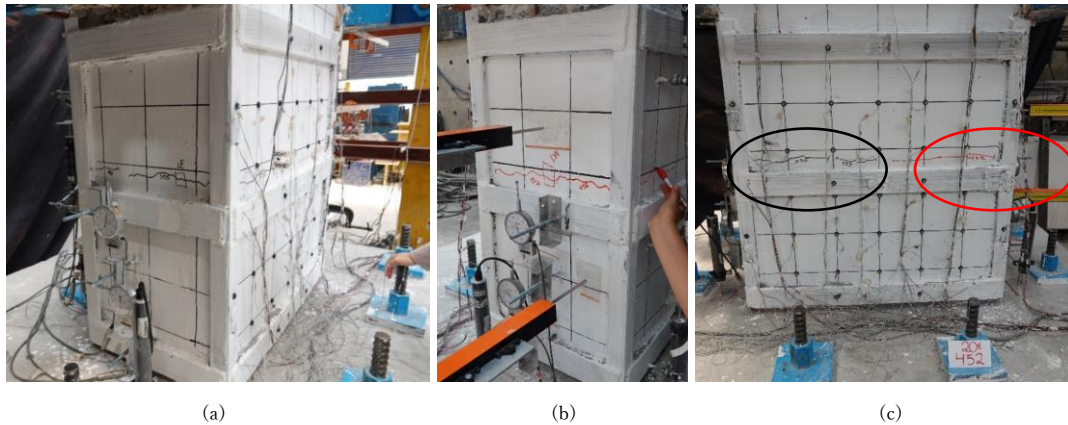


Fig. 3.53—Specimen S8: (a) first horizontal crack LE in east face; (b) in west face LW; (c) north face

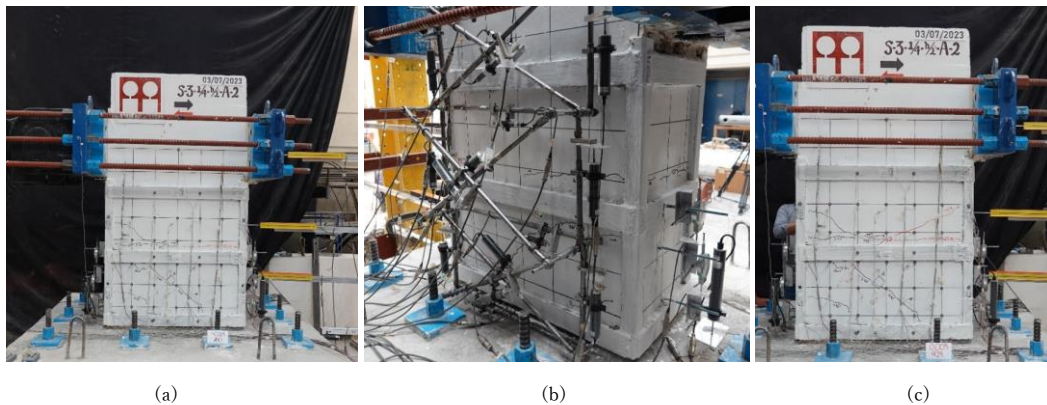


Fig. 3.54—First inclined crack: (a) north face; (b) south face; (c) second inclined crack



Fig. 3.55—(a) Transverse crack parallel to steel batten at a drift of +0.0005

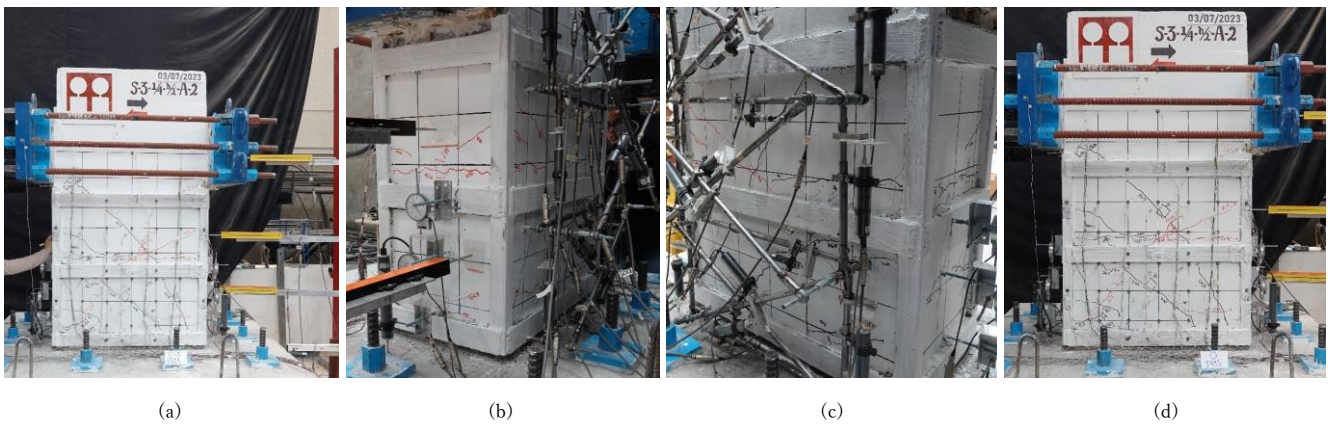


Fig. 3.56—Damage at a drift of +0.01: (a) north face; (b) south face; (c) west face; (d) zero load

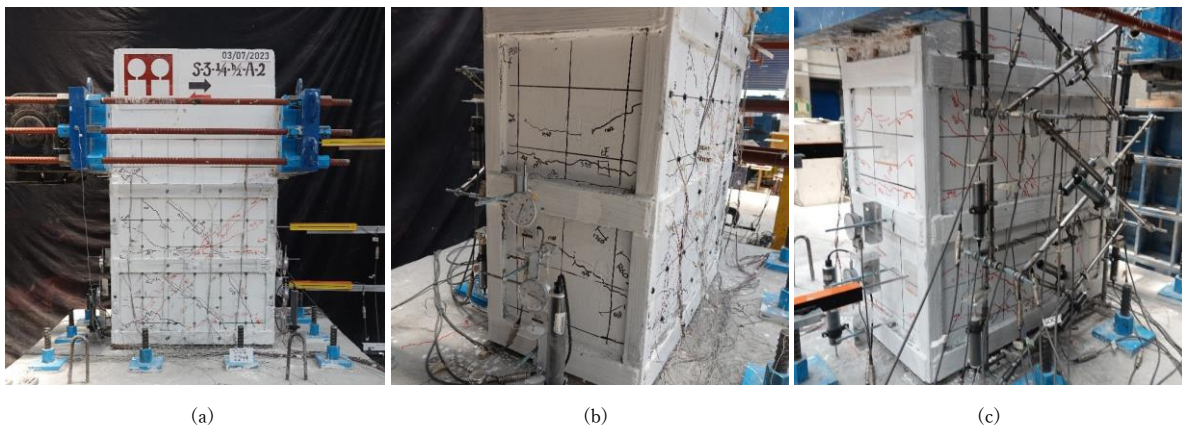


Fig. 3.57—Damage at a drift of +0.02: (a) north face; (b) east face; (c) south and west face



(a) (b) (c)
Fig. 3.58—Damage at a drift of +0.03: (a) north face; (b) damage in foundation-column joint; (c) south and west face



(a) (b) (c)
Fig. 3.59—Damage at a drift of +0.04: (a) north face; (b) white wash peeling on batten; (c) south and west face



(a) (b) (c) (d)
Fig. 3.60—Damage in the steel jacket at a drift of +0.045



(a) (b) (c)

Fig. 3.61—Damage at a drift of +0.05: (a) north face; (b) concrete crack in foundation-column east face joint; (c) fell off the white wash of middle batten



(a) (b) (c)

Fig. 3.62—Damage state at a drift of +0.06: (a) north face; (b) bottom batten buckling; (c) south face



Fig. 3.63—Damage state at a drift of -0.06



Fig. 3.64—Damage state at a drift of +0.07



Fig. 3.65—Damage state at a drift of +0.08

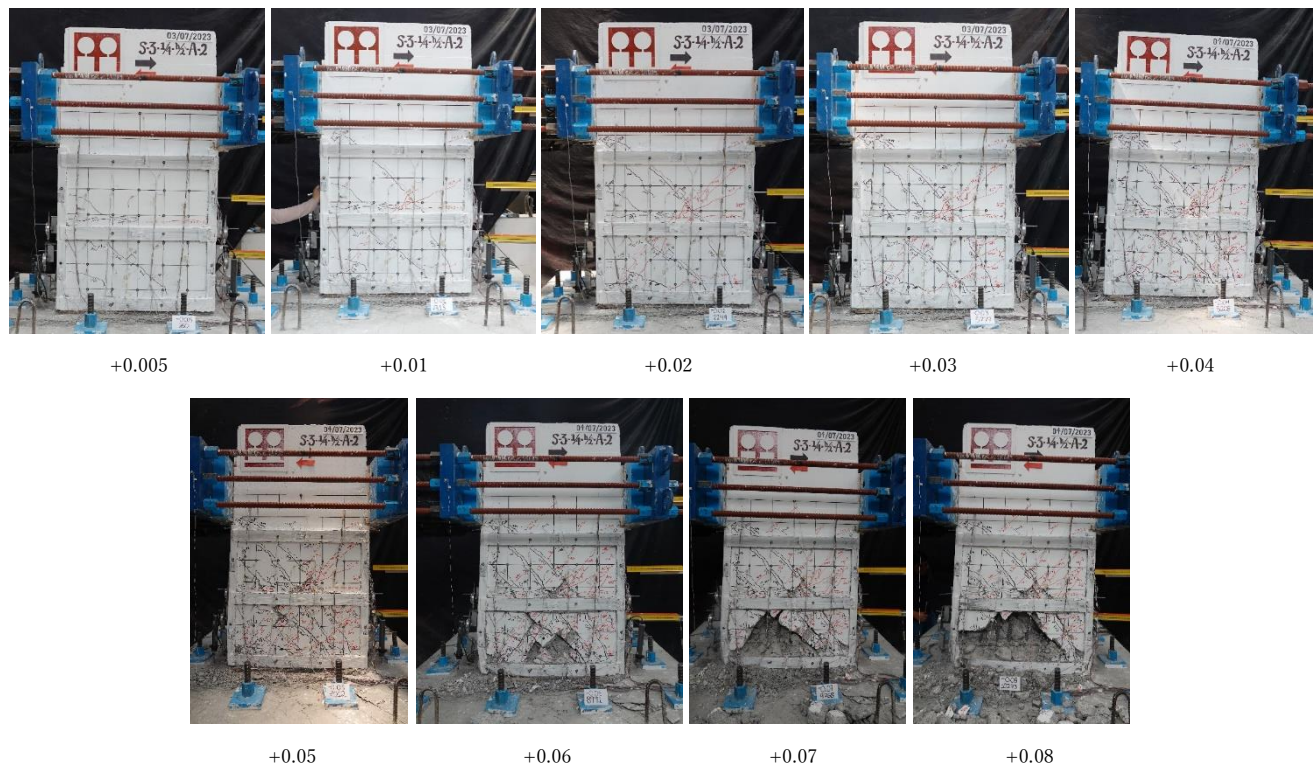


Fig. 3.66—Damage evolution of the positive drift peaks

3.5.3.2 Final Damage State

The final damage state, presented in Fig. 3.67, compared to the damage at the end of the test of specimen CO, shows a similar column core damage path. However, when comparing the stage of damage at each drift peak, the inclined cracks in specimen S8 are thinner and shorter. Additionally, the crack pattern was more widely distributed along the column core. The examination of specimen S8 to determine the exact location of the fracture in the longitudinal steel is shown in Fig. 3.68. The fracture was localised in the foundation-column joint; this is logical because this joint experienced the greatest strains and moments.



Fig. 3.67—Final damage state



Fig. 3.68—Fracture of longitudinal bars in specimen S8 in east and west face

3.5.3.3 Hysteresis Behaviour

The hysteresis behaviour of the specimen S8 is shown in Fig. 3.69. The graph also indicates points on the curve where the first inclined crack, maximum shear force, and fracture of longitudinal bars were observed. The hysteresis curve is notably symmetrical with stable loops during the initial cycles and along the majority of the cycles before the drift of +0.035. Cycles performed before the first inclined crack exhibited linear elastic behaviour. At a drift of +0.022, the column reached a maximum load of +869 kN (+88.69 t) for positive cycles, and subsequently, the strength degraded. The peak maximum load resisted for negative cycles was -867 kN (-88.62 t). At a drift of +0.057, the fracture of the first longitudinal bar on the east face occurred (fracture due to low-cycle fatigue, probably), and a sudden drop in strength was observed. The second bar fractured at drift of +0.059 on the west face, and after the bar's rupture and the subsequent decrease in strength, the stiffness remains until the end

of the half-cycle. A final half-cycle was performed with the target drift of +0.08, reaching a maximum drift of +0.077 and a lateral load of +242 kN (+24 t). Finally, the strength decreased by 72.9% compared to the peak maximum.

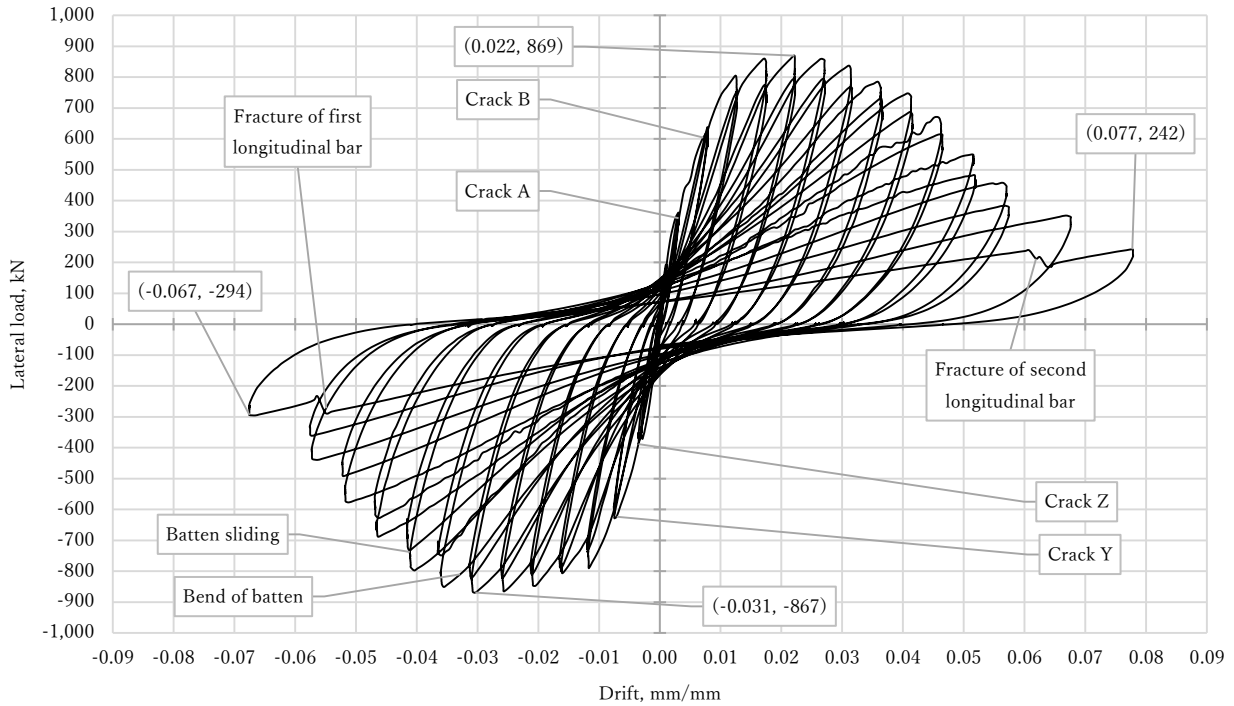


Fig. 3.69—Hysteresis plot of specimen S8

3.5.3.4 Column Rotation

The rotation of Zone 1, calculated using the readings from the micrometres shown in Fig. 3.70, shows well-defined hysteresis cycles. It appears that the response is linear within the same range of loads as the global hysteresis response of the column. A different pattern emerges in the rotation of the same zone when calculated using the displacement transducers (see Fig. 3.71). When comparing the rotation response of the other zones, it remained linear, regardless of the instrumentation used to calculate the rotation, except for the last cycles, as shown in Fig. 3.70 and Fig. 3.71.

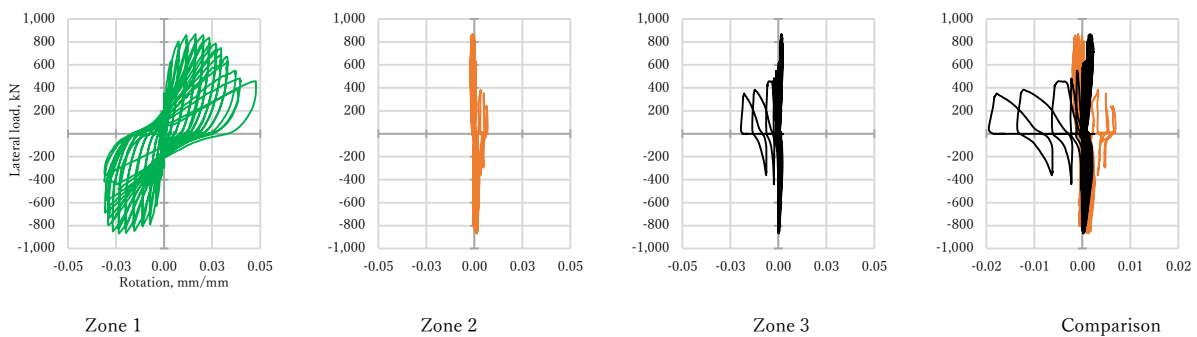


Fig. 3.70—Rotation of zones in concrete column core using micrometres

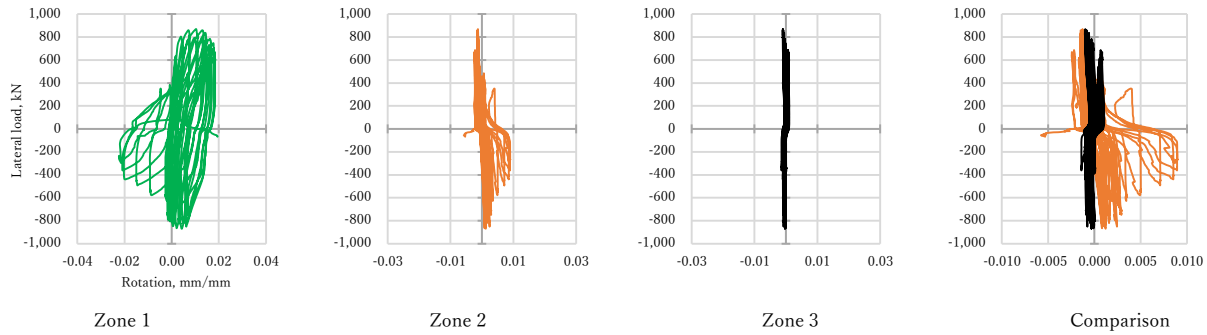


Fig. 3.71—Rotation of zones in concrete column core using displacement transducer

3.5.3.5 Foundation Rotation and Sliding

As well as in the previous specimens, the rotation and sliding of foundation were recorded. In the test of specimen S8, the maximum lateral displacement recorded for the foundation was 1.2 mm, this occurred at the peak of lateral load, as shown in Fig. 3.72b; the magnitude of lateral displacement was 6.67 times larger than the maximum displacement recorded in specimen CO. Also, the lateral load versus displacement curve shows that the foundation had a permanent displacement after the linear behaviour of the hysteresis curve (after the 0.2 mm displacement of the foundation). The rotations were more stable, exhibited a semi linear behaviour.

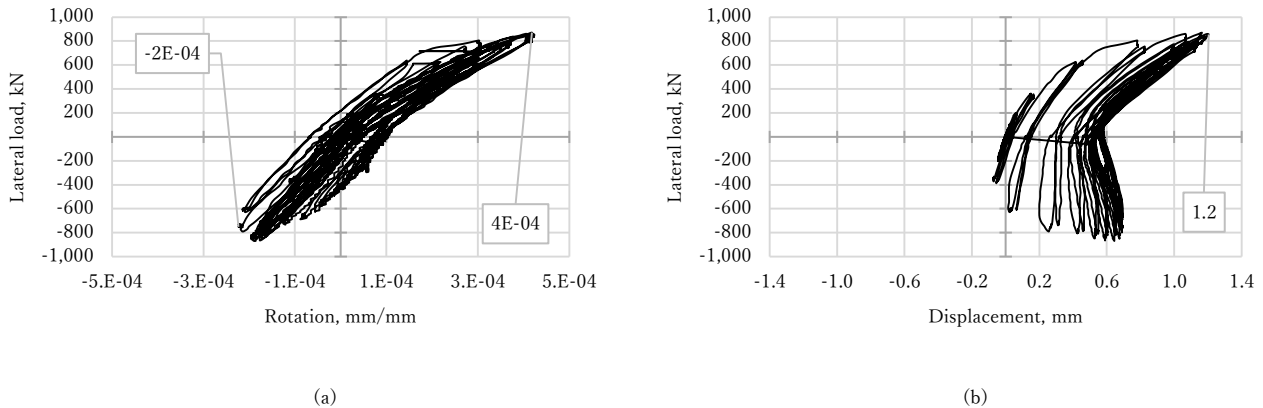


Fig. 3.72—Foundation history of rotation (a) and sliding (b) of specimen S8

3.5.3.6 Crack Width History

Fig. 3.73 illustrates the progression in width for each labelled crack, presenting a plot of width versus lateral load. The paired graphs facilitate a comparison between each crack and its corresponding counterpart. The curves reveal a semi-symmetrical pattern in crack width under cyclic loading conditions. Upon comparing cracks LE and LW, it becomes evident that the most substantial crack, as supported by photographic evidence, was the crack LE. Cracks A and Y exhibited the largest crack width similarity. However, their symmetry is barely discernible, with crack A predominantly larger during cycles of positive loading (pushing westward), whereas crack Y widened during cycles of negative loading (pulling eastward). This observation aligns with the inherent characteristics of the cracks. Cracks B and Z exhibited varying widths; when comparing their maximum recorded widths, crack B was three times wider than the maximum width recorded for crack Z. As expected, the crack with the maximum width was those in the principal diagonal, which is the A crack.

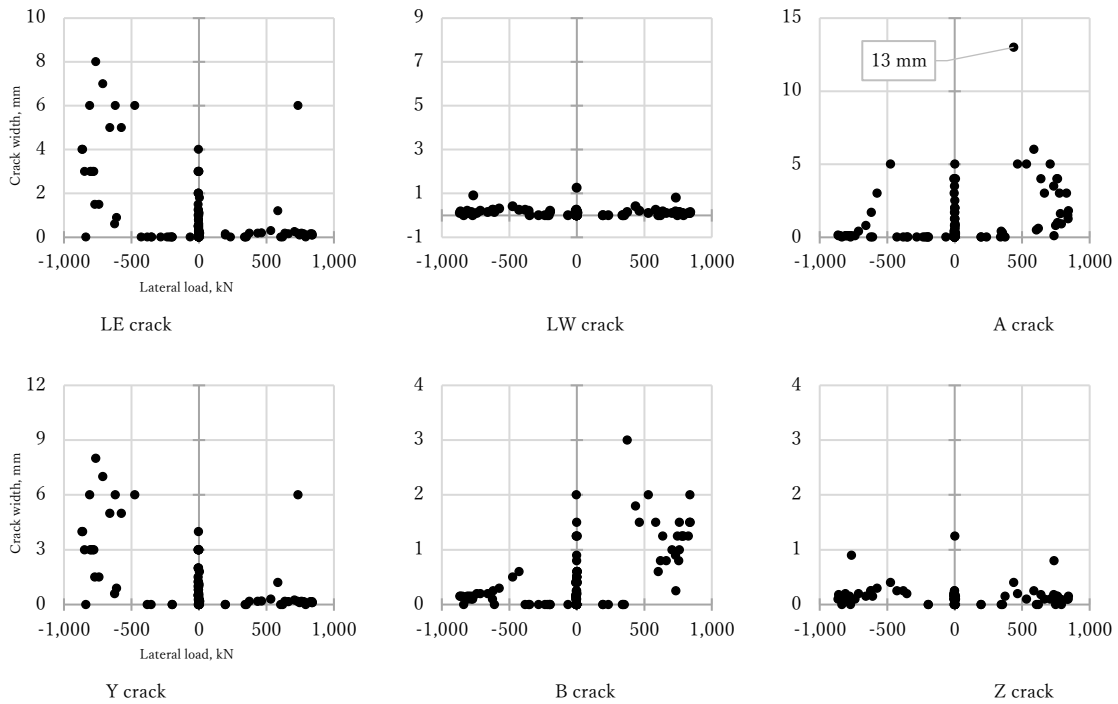


Fig. 3.73—Crack width history for labelled cracks for Specimen S8

3.5.3.7 Strain Gauges Readings

3.5.3.7.1 Internal Strain Gauges

For specimen S8, some strain gauges recorded yielding, as indicated by the red-marked dots. In some strain gauges, the signal recording failed (yellow-marked dots); this could be due to damage to the strain gauge cables during the pouring of the concrete

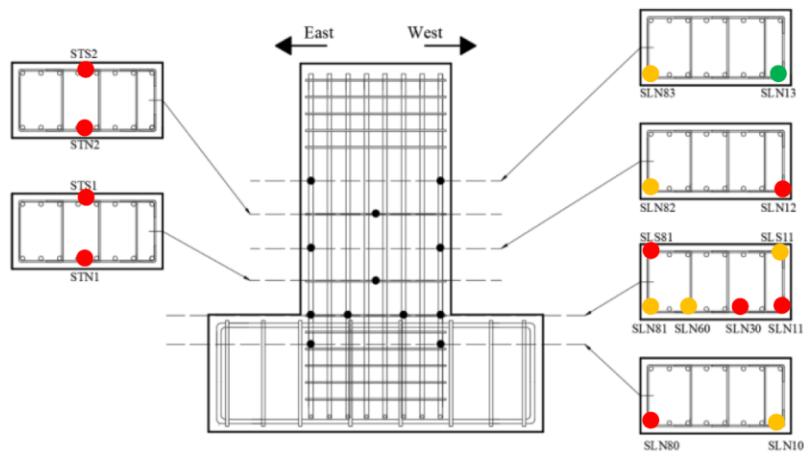


Fig. 3.74—Internal strain gauges that recorded yielding: red (yield); green (elastic); yellow (damaged or not recorded)

Table 3.7—Internal strain gauge yielding history of specimen S8

Strain Gauge	Load step @ yield	Strain μm	Lateral load kN	Displacement mm	Drift ratio mm/mm
SLN80	3,639	-2,715	-808	-25.38	-0.0211
SLS81	1,752	2,845	630	9.51	0.0079
SLN30	1,868	3,000	-771	-13.35	-0.0111
SLN11	1,866	2,425	-689	-10.89	-0.0090
SLN12	4,748	7,183	-782	-36.84	-0.0307
STN1	1,757	2,819	765	13.14	0.0109
STS1	4,164	3,000	619	24.51	0.0204
STS2	1,499	3,200	-609	-9.03	-0.0075
STN2	1,499	3,900	-609	-9.03	-0.0075

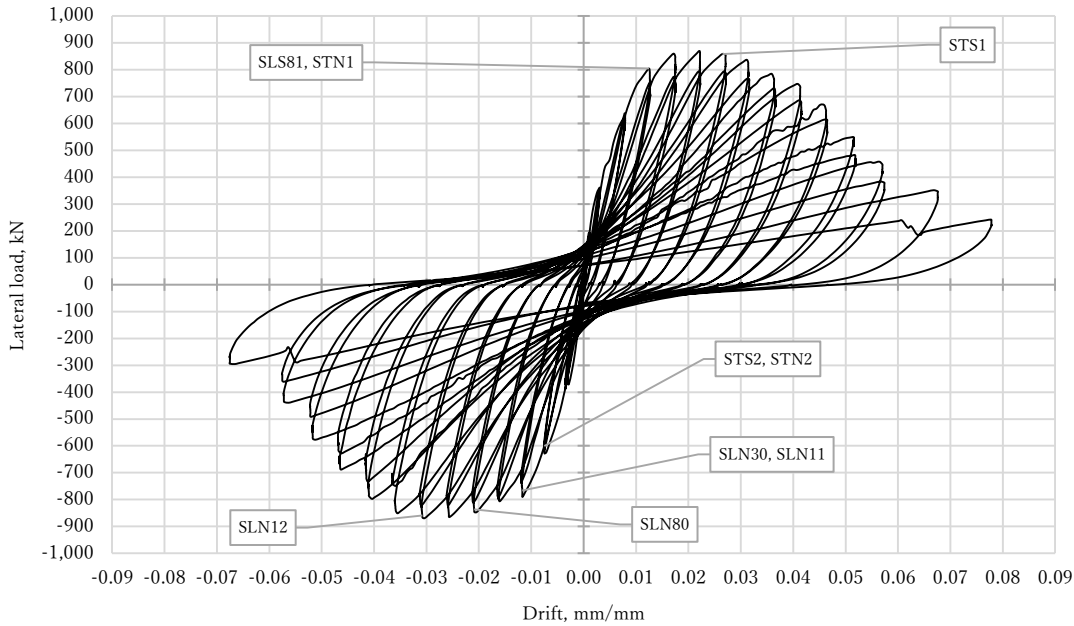


Fig. 3.75— Yield recorded by strain gauges in specimen S8

3.5.3.7.2 External Strain Gauges

To investigate all parameters involved in the nonlinear response of the specimens with SJ, the strain recorded by external strain gauges installed in the steel jacket is studied. The steel jacket has a theoretical strain yield limit of $\pm 2,100 \mu\text{m}$. Fig. 3.76 shows the strain gauges that recorded yielding in the steel angles and battens. Table 3.8 presents the data related to the first instance of yielding. Fig. 3.77 shows the hysteresis curve with the respective labels of yielding recorded by strain gauges. The experiment predominantly recorded strain in tension, with strain gauge AE1 being the sole recorder of initial yielding in compression. The steel jacket's yielding exhibited asymmetry, evident from unexpected yielding locations such as AL1.

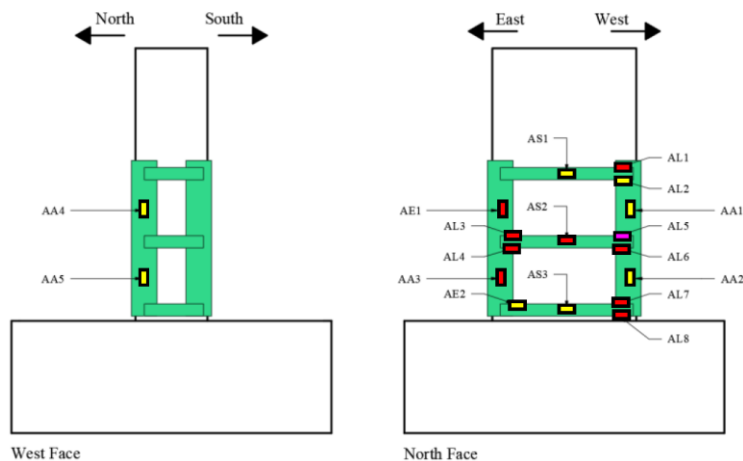


Fig. 3.76—External strain gauges that recorded yielding: red (yield); yellow (elastic); purple (damaged or not recorded)

Table 3.8—External strain gauge yielding history of specimen S8

Strain Gauge	Load Step	Strain μm	Lateral load kN	Displacement mm	Drift mm/mm
AS2	6,541	2,275	679	48.54	0.040
AL1	7,006	2,502	614.6	50.79	0.042
AL3	3,775	2,020	859.2	31.8	0.026
AL4	3,519	7,223	761.4	26.7	0.022
AL6	4,002	10,716	-865	-30.81	-0.026
AL7	4,481	2,469	807.6	34.68	0.029
AL8	5,020	2,865	-727	-33.09	-0.0275
AA3	8,001	1,822 ^[1]	535	61.86	0.051
AE1	6,525	-2,192	506	34.26	0.028

^[1] The strain recorded by AA3 did not surpass the yielding limit, however, there are evidence of a residual deformation due to a plastic strain.

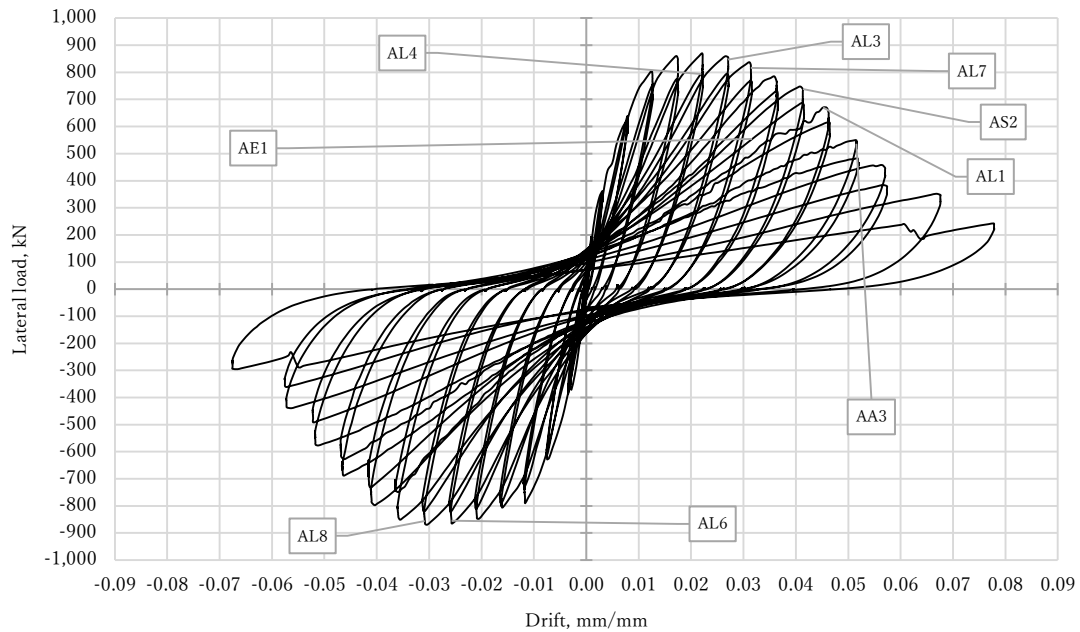


Fig. 3.77—Yield recorded by external strain gauges of specimen S8

3.5.4 Specimen S9

Specimen S9 was tested on June 13, 2023. Like the specimen S8, the crack pattern was distributed along the column core, and although there was presence of inclined cracks, these did not concentrate on the main diagonal. The lateral behaviour was controlled by bending, like the specimen S8, but in the final drift, the final damage was less severe in the core column core.



Fig. 3.78—Specimen S9 at the beginning of the test

3.5.4.1 Damage Evolution

The damage stages are presented next, as usual, the first horizontal crack appeared at middle span of the column (now the crack is labelled as “LE”), in the east face, at load control of +196 kN (+20 t) (see Fig. 3.79), the width of the crack was 0.3 mm. In the next load cycle, with a peak force of -196 kN (-20 t) another horizontal crack symmetric to LE crack appeared, with a width of 0.3 mm (now this crack is labelled as “LW”). At the displacement control, at a drift of +0.0005 the first inclined crack appeared (labelled as “A”), with a width of 0.3 mm, in the next drift of +0.0005 with a thickness of 0.35 mm, the opposite inclined crack appeared (labelled as “Z”) with a related lateral force of +356 kN (see Fig. 3.80).

The LE crack reached 0.8 mm width at a drift of +0.01 (see Fig. 3.81), related to a force of +694 kN (+70.8 t) and a lateral displacement of +9 mm; the LW crack reached the same thickness at the opposite drift cycle ($R = -0.01$), and in the foundation-column joint a horizontal crack appeared.

At a drift of -0.015 a crack appeared along the superior steel batten, as is shown in the Fig. 3.82, near the load plates, in the south face. At this drift, the Z crack reached 1.25 mm width. At a drift of ± 0.02 the principal inclined cracks reached 1.55 mm of average width, and the maximum lateral force reading was +912 kN (+93 t). At a drift of ± 0.03 the crushing of the concrete in the foundation-column joint was evident (see Fig. 3.84), at this cycle of lateral load, the peak lateral force was about +931 kN (+95 t) with a related lateral displacement of 32.37 mm.

At a drift of +0.035 it was observed the fell off of the white wash of the middle steel batten (see Fig. 3.85), this in the peak of lateral load +827.6 kN (+84.4 t), related to a displacement of +37.7 mm. At a drift of ± 0.04 , the fell off of the white wash of superior steel battens start to shows more evidently, and the concrete near the foundation-column joint started to spall. At a drift of ± 0.05 the principal inclined cracks reached a width of 5 mm, also, the mid steel batten starts to bent out of its longitudinal axis, as seen in Fig. 3.87. Reaching the first drift cycle to -0.055, a longitudinal bar fractured, related to a lateral displacement of -49 mm (see Fig. 3.88), also the fell off of the white wash in the lower steel batten was more notable; going through the second cycle drift of -0.055 another longitudinal bar cracked, related to the east face of the column.



Fig. 3.79—First horizontal crack at load control of ± 196 kN

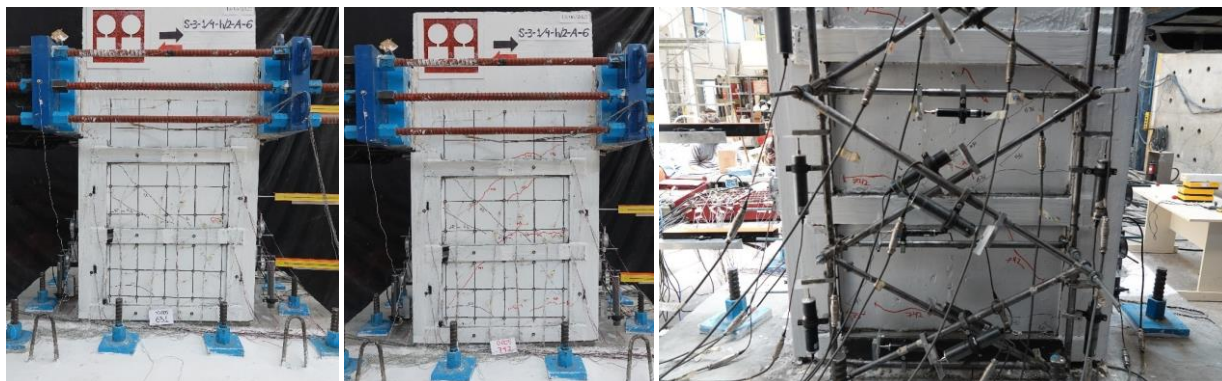


Fig. 3.80—First inclined cracks at drift of ± 0.0005

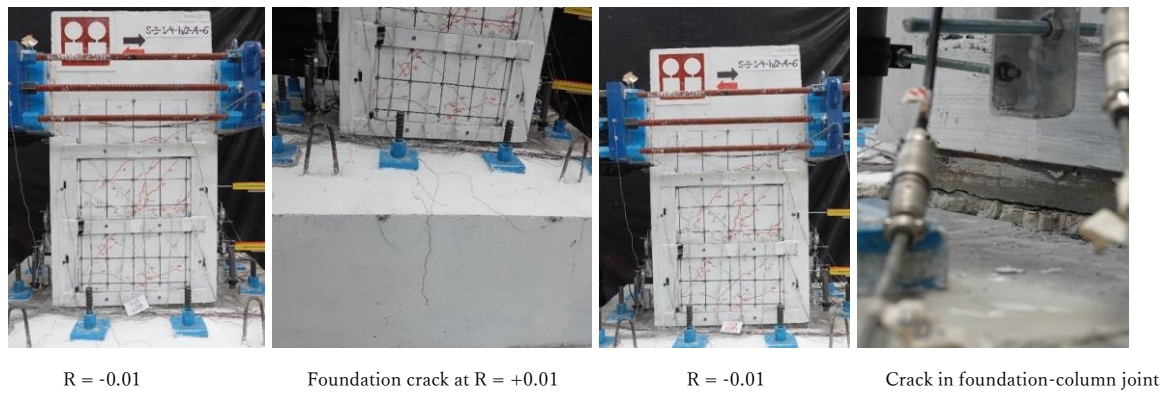


Fig. 3.81—Damage at drift of ±0.01

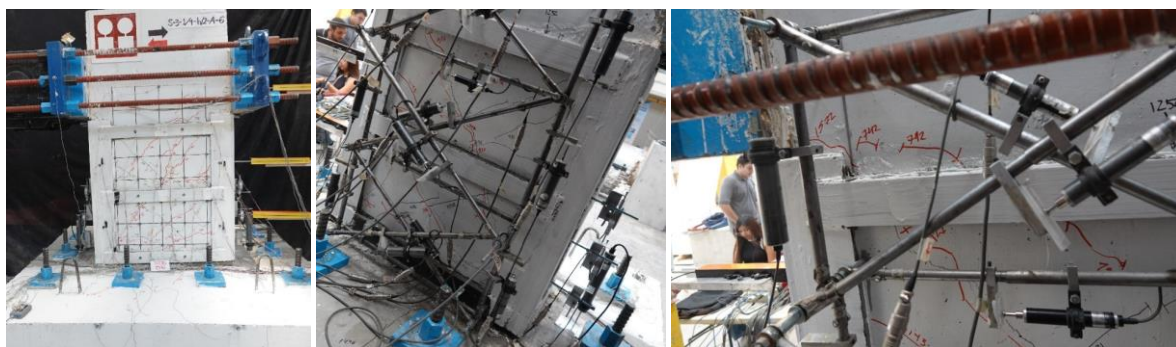


Fig. 3.82—Damage state at drift of -0.015



Fig. 3.83—Damage state at drift of ±0.02

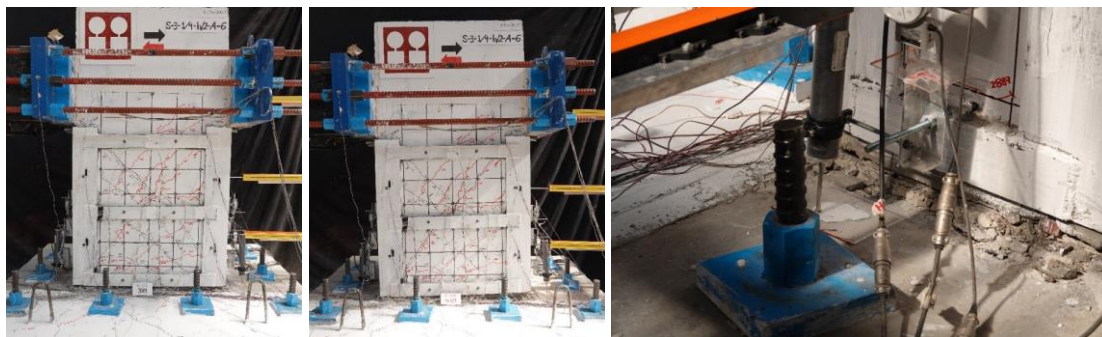


Fig. 3.84—Damage at drift of ±0.03

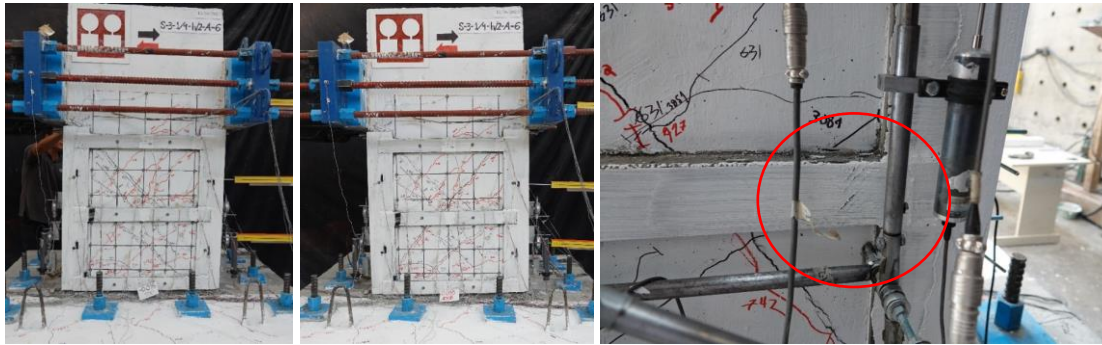


Fig. 3.85—First appearance spalling of white wash in middle steel batten at drift of +0.035



Fig. 3.86—Damage state at drift of ± 0.04



Fig. 3.87—Damage state at drift of ± 0.05



Fig. 3.88—Damage state at drift of ± 0.055 when occurred the fracture of a longitudinal bar related to east face

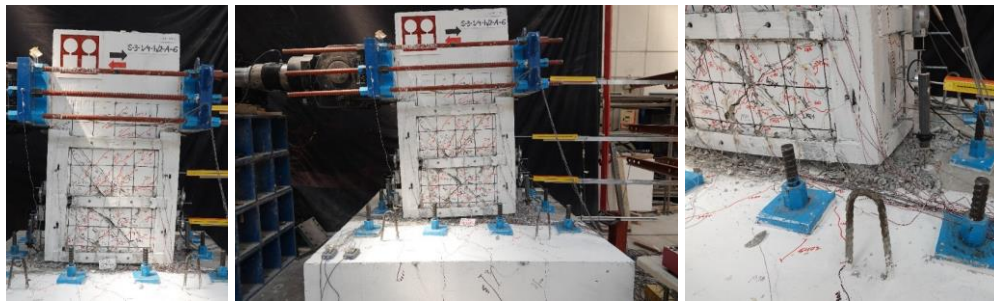


Fig. 3.89—Damage at drift of ± 0.06

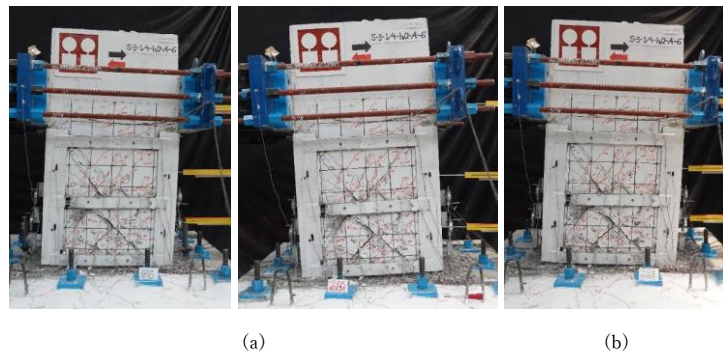


Fig. 3.90—Damage state at: (a) drift ± 0.07 ; (b) drift $+0.08$

The compilation of the damage stages is presented in Fig. 3.91. The cracks formed during the peak drifts are predominant in the main diagonal but are not concentrated in it. Additionally, the most damaged zone is in the foundation-column joint, where the concrete spalled and was crushed during the maximum load peaks of each displacement control cycle.

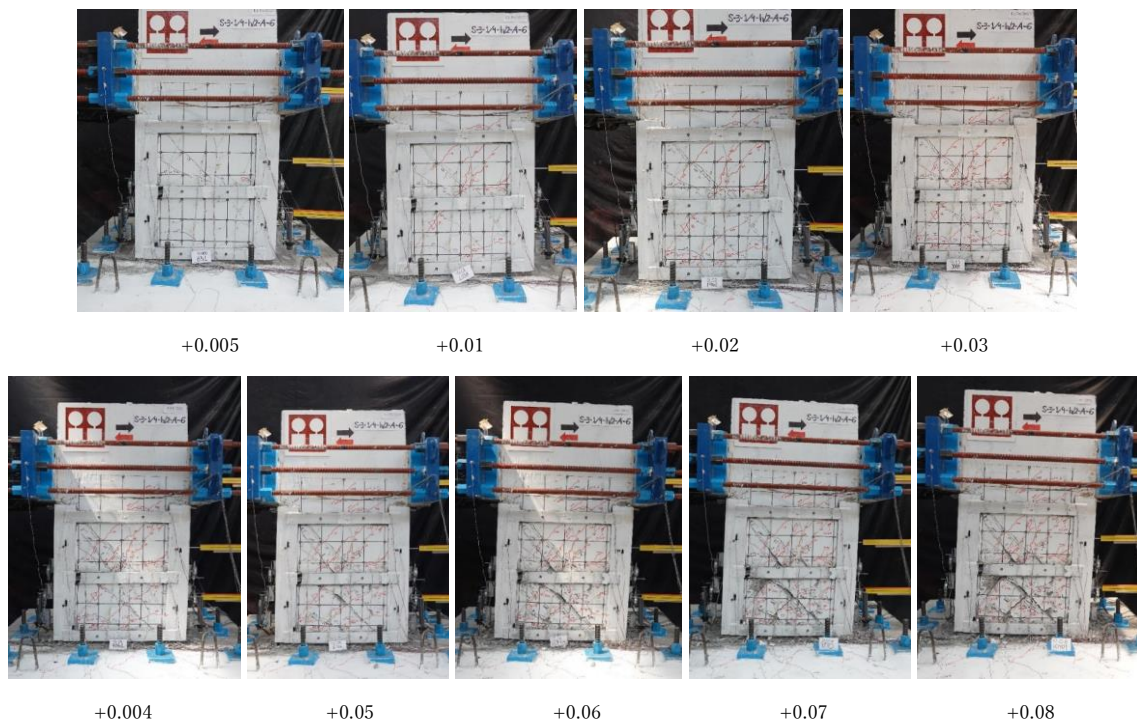


Fig. 3.91—Damage evolution of the negative drift peaks

3.5.4.2 Final Damage State

The final state of damage is presented in Fig. 3.92. It is evident the difference between the S8 and S9 specimen, this last specimen had less damage at the column core, and the concrete remains tie.



Fig. 3.92—Final damage state of specimen S9

The exploration of the specimen S9 to inspect the fracture of the longitudinal bars are shown in Fig. 3.93. The first two fractures presented during the displacement control were in the west face of the column, and the third fracture was in the east face. As in specimen S8, the fracture presented are located in the foundation-column joint.



Fig. 3.93—Fracture of longitudinal bars in specimen S9 in west and east face

3.5.4.3 Hysteresis Behaviour

The hysteresis plot is depicted in Fig. 3.94. Here, the linear behaviour of the specimen remains until the appearance of the first inclined crack. The maximum lateral load recorded is +961 kN in the positive quadrant and -820 kN in the negative quadrant, with both peak loads recorded at a similar drift. However, the general behaviour is quite symmetric, similar to the hysteresis curve of specimen S8; the difference is that in specimen S9, three longitudinal bars fractured (see Fig. 3.93). The residual lateral strength, compared with both maximum load peaks, is 0.59 for the positive quadrant and 0.52 for the negative quadrant, respectively.

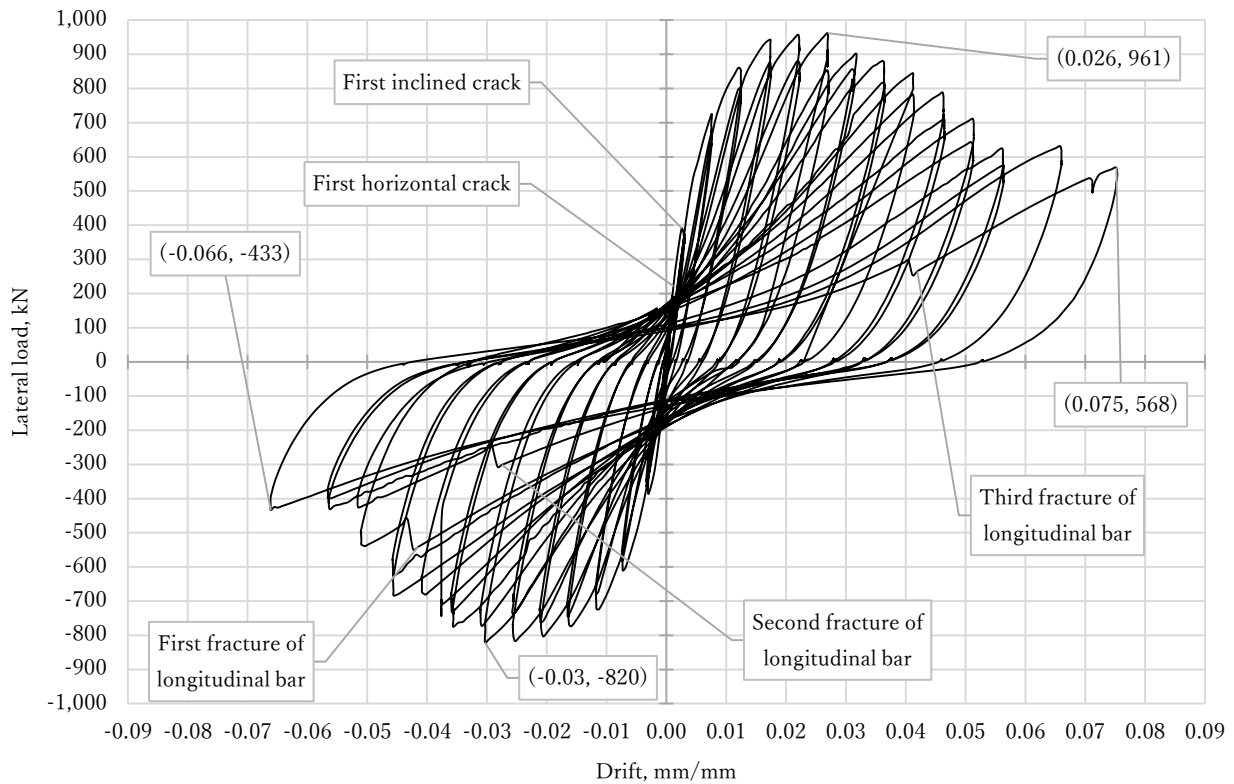


Fig. 3.94—Hysteresis plot of specimen S9

3.5.4.4 Column Rotation

The rotation of the Zone 1 calculated with the record of the micrometres, shown in the Fig. 3.95, are well defined hysteresis cycles, it appears that the response is linear in the same range of loads that in the global hysteresis response of the column. Something different appears in the rotation of the same zone when it is calculated using the displacement transducers (see Fig. 3.96). Comparing the further rotation response of the other zones, it remains elastic, independent of the instrumentation used to calculate the rotation. The sudden movement of the graph in Fig. 3.96 to the right of the origin was due to the pause and restart of the test, where there was a likely movement of the displacement transducer.

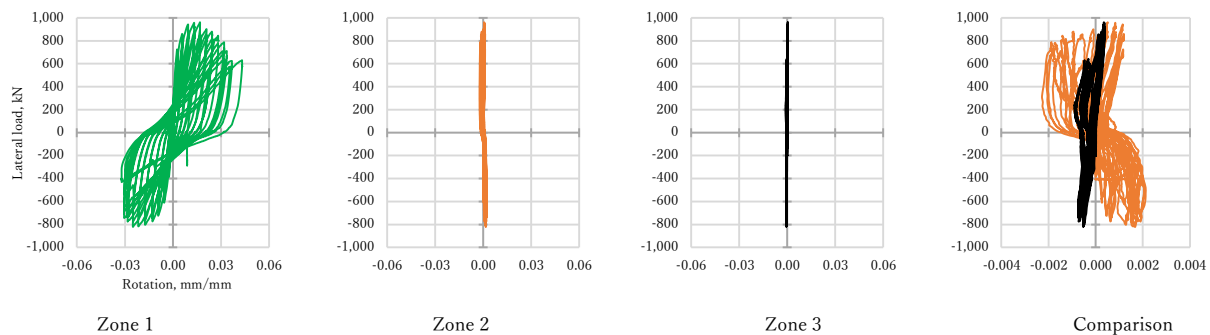


Fig. 3.95—Rotation of zones in concrete column core using micrometres

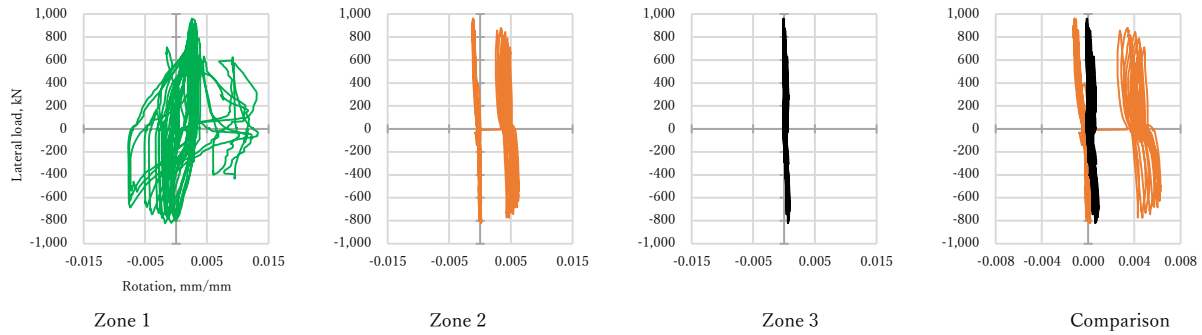


Fig. 3.96—Rotation of zones in concrete column core using displacement transducers

3.5.4.5 Foundation Rotation and Sliding

The maximum lateral displacement in the foundation recorded by the transducers was 2.725 mm, related to a force of 880 kN, at this time, the rotation also was the maximum calculated of 0.0018 mm/mm. The magnitude of lateral displacement was up to 15 times larger than the maximum displacement recorded in specimen CO, and 2.27 times than the specimen S8. Also, the lateral load versus displacement curve shows that the foundation had a permanent displacement after the linear behaviour of the hysteresis curve (after the 0.15 mm displacement of the foundation).

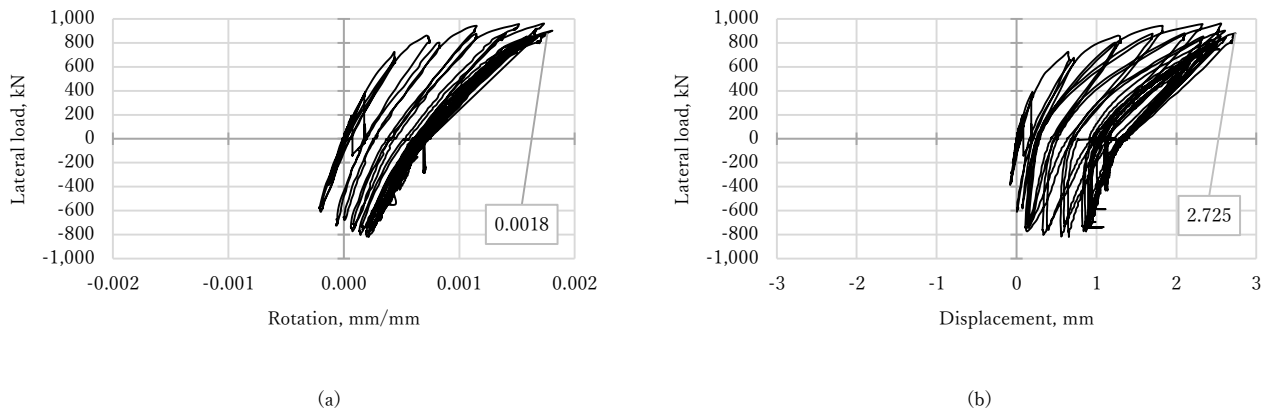


Fig. 3.97—Foundation history of rotation (a) and sliding (b) of specimen S9

3.5.4.6 Crack Width History

Fig. 3.98 illustrates the progression in width for each labelled crack, presenting a plot of width versus lateral load. For this test, the B crack labelled in the previous specimens did not appear during the test of specimen S9. However, analysing the curves reveals a semi-symmetrical pattern in crack width under cyclic loading conditions, although less pronounced compared to the crack history of specimen S8.

Cracks A and Y exhibited the greatest magnitude of crack width similarity. However, their symmetry is barely discernible, with crack A predominantly widening during cycles of positive loading (pushing westward), whereas crack Y widened during cycles of negative loading (pulling eastward). This observation aligns with the inherent characteristics of the cracks. Cracks B and Z exhibited varying widths; when comparing their maximum recorded widths, crack B was three times wider than crack Z. As expected, the crack with the maximum width was that in the principal diagonal, which is crack A.

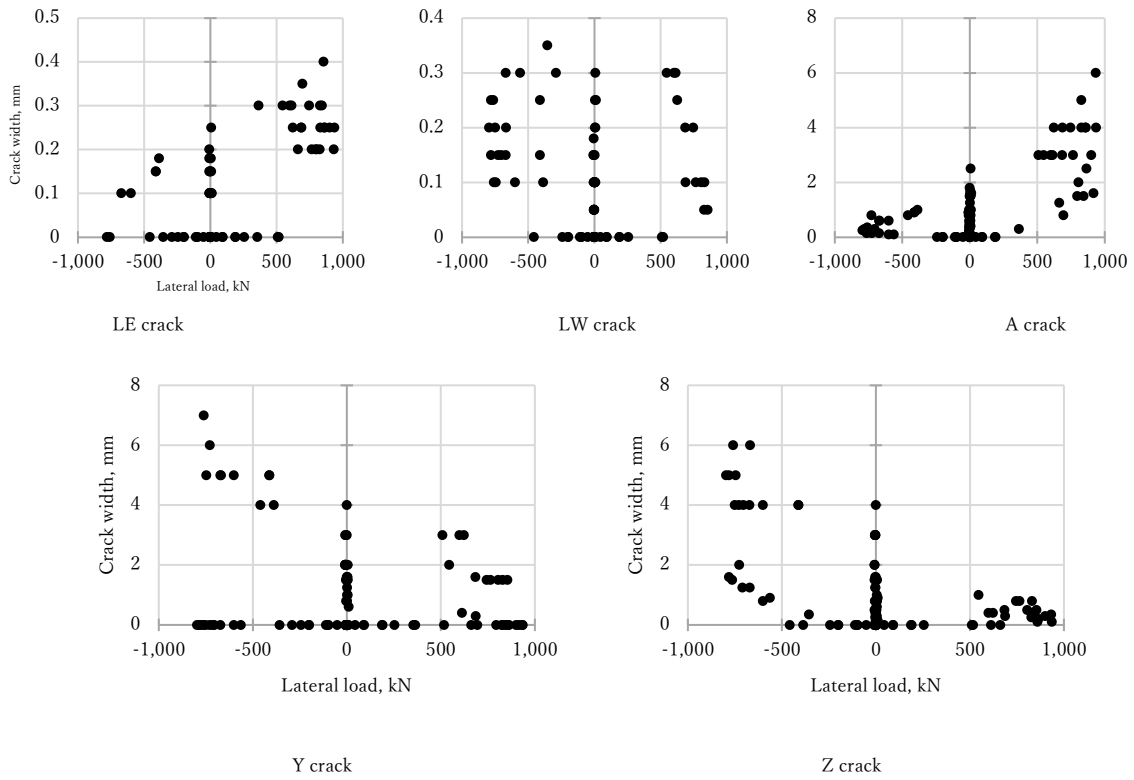


Fig. 3.98—Crack width history for labelled cracks for Specimen S9

3.5.4.7 Strain Gauges Readings

3.5.4.7.1 Internal Strain Gauges

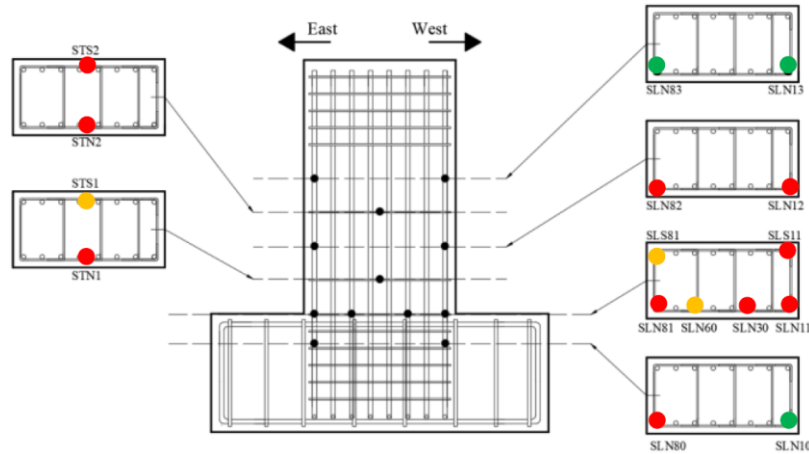


Fig. 3.99—Internal strain gauges that reached yielding: red (yield); green (elastic)

Table 3.9—Internal strain gauge yielding history of specimen S9

Strain Gauge	Load step @ yield	Strain μm	Lateral load kN	Displacement mm	Drift ratio mm/mm
SLN80	4,146	5,000	878	36.27	0.0302
SLN81	1,048	8,000	672	9.03	0.0075
SLN11	1,153	9,000	-588	-8.79	-0.0073
SLS11	1,566	6,000	-672	-11.7	-0.0097
SLN30	1,567	6,200	-670	-11.68	-0.0097
SLN12	5,474	8,055	-719	-43.08	-0.0359
SLN82	4,880	7,628	808	43.65	0.0363
STN2	1,144	5,650	-600	-8.76	-0.0073
STS2	1,592	6,837	-693	-14.1	-0.0117

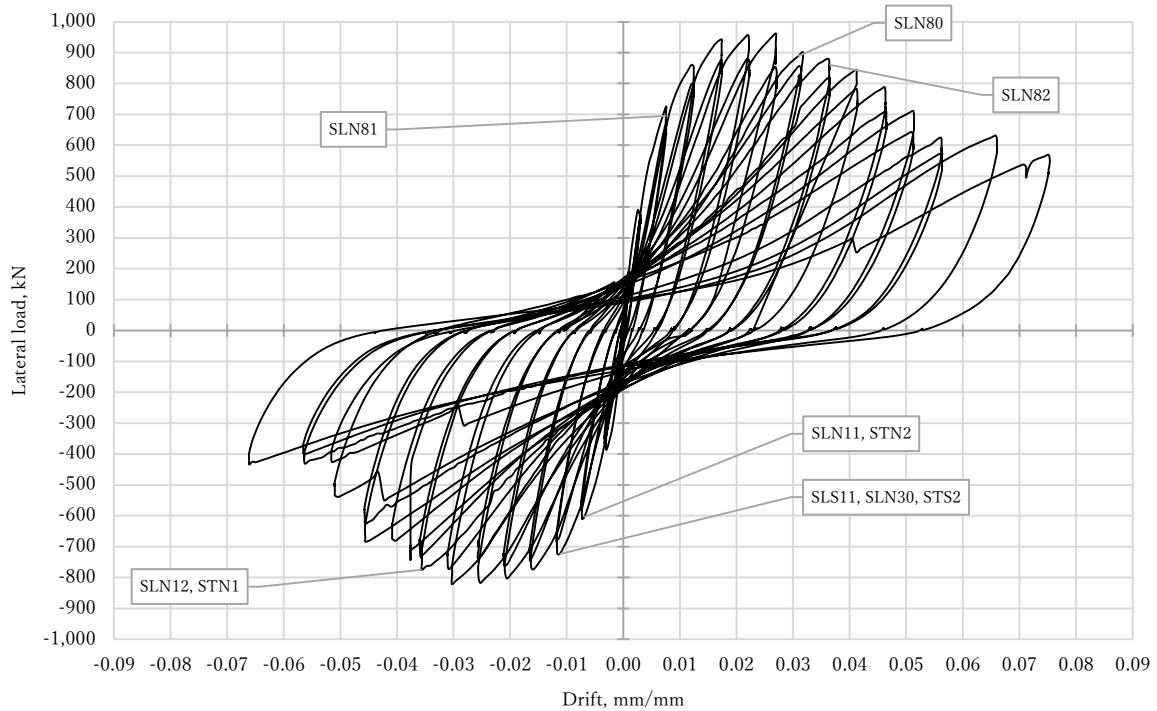


Fig. 3.100—Yielding recorded by strain gauges in specimen S9

3.5.4.7.1 External Strain Gauges

Fig. 3.101 shows the strain gauges that recorded yielding of steel angles and battens. In the Table 3.10 the data related to the first instant of yielding are shown. In Fig. 3.102 the hysteresis curve with the respective labels of the yielded recorded by strain gauges are shown. All the first yield strain recorded was in tension. The middle batten in the north face exhibited symmetric yielding.

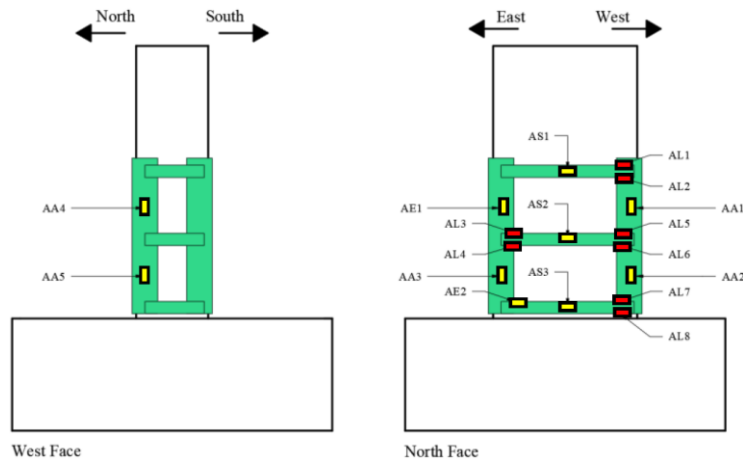


Fig. 3.101—External strain gauges that recorded yielding: red (yield); yellow (elastic); purple (damaged or not recorded)

Table 3.10—External strain gauge yielding history of specimen S9

Strain Gauge	Load Step	Strain μm	Lateral load kN	Displacement mm	Drift mm/mm
AL1	2,887	4,339	-761.4	-24.6	-0.020
AL2	3,062	2,567	397.3	12.84	0.011
AL3	2,303	2,432	-744.7	-19.77	-0.016
AL4	2,185	2,310	876	20.76	0.017
AL5	2,452	5,788	916	26.64	0.022
AL6	2,887	2,711	-761	-25.23	-0.021
AL7	3,103	3,902	909	32.34	0.027
AL8	3,684	3,460	-760	-26.61	-0.022

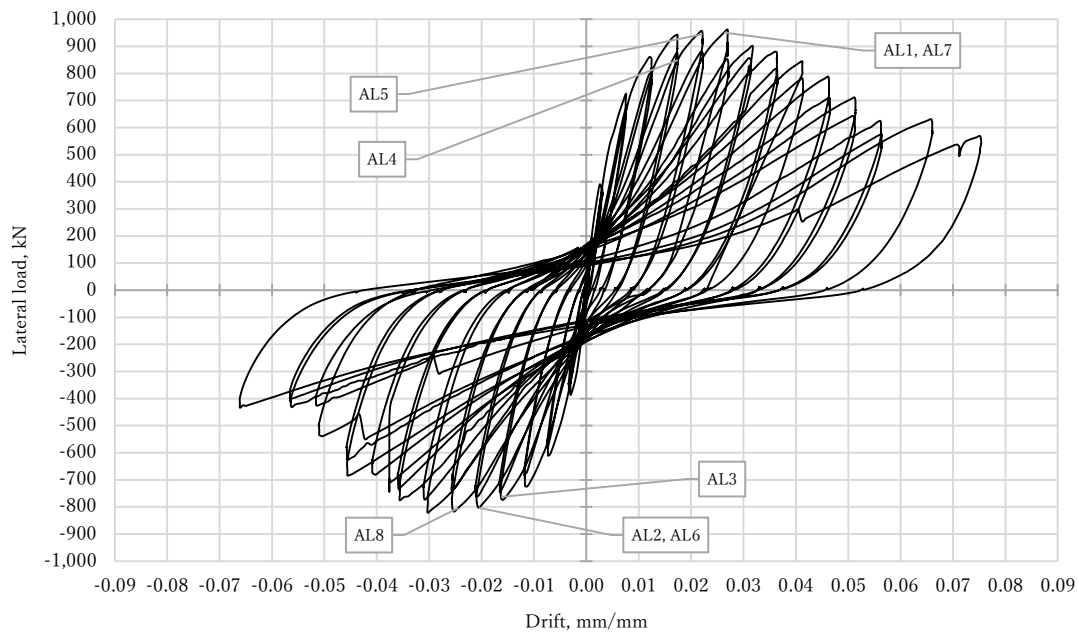


Fig. 3.102—Yielding recorded by external strain gauges of specimen S9

3.5.5 Comparison

In this section, a comparison of several results from the experimental study is presented. The primary focus is to highlight the differences observed, particularly in specimens that utilised steel jacketing. These comparisons aim to underscore the variations in performance and characteristics attributable to the use of steel jacketing in the experimental specimens.

3.5.5.1 Crack Pattern

One of the key aspects to analyse is the crack pattern, as it provides insight into the extent of damage and enables the identification of potential failure modes of the element, based on the data collected from experimental tests. Table 3.11 presents a photographic comparative of the crack patterns presented in the positive drift peaks up to 0.02.

As evident, crack patterns in specimen CO and CO* are alike, being more damaged the CO* in each drift peak. The difference in peak lateral load and crack pattern can be explained with the variance in the mechanical properties of concrete of each column, but not by the use of different load hydraulic jacket. As usual, concrete mixture changes its properties from batch to batch, because a perfect quality control does not exist; the mixture of specimen CO (poured in October, 2021) may vary with the mixture of the column of specimen CO* (poured in September, 2022).

There may be some deviation in the quality of materials or the fabrication procedure that can explain the difference in peak lateral strength and crack pattern, even when the mixture specifications are the same for all specimens, perfect and constant properties of concrete cannot be guaranteed. Anyway, the variation in the mechanical properties of concrete is an issue in every day's construction, so the experimental procedure it is close to what happens on a day-to-day basis in the construction industry.

The primary observation regarding crack patterns between specimens with and without steel jacketing is the visible damage. Specimens S8 and S9 exhibit less crack width compared to CO and CO* specimens at the same drift peaks. Additionally, the damage in specimens S8 and S9 is more evenly distributed throughout the core of the column, whereas the cracks in CO and CO* specimens are concentrated along the main diagonals.

When comparing specimens S8 and S9, damage appears quite similar during the initial drift cycles. However, the difference becomes more pronounced once the peak lateral load is reached, with crack pattern becoming more pronounced in S8 compared to S9. This is evident in Table 3.12, where the spalled of concrete is notable in specimen S8 in drift 0.06 and forward. The specimen S9 also had spalled of concrete but, it was minimum compared con specimen S8. Although the hysteresis curves of both specimens are similar, here it can be appreciated the confining effect generated by having larger steel angles. It seems that having larger steel angles helps to keep the cracked concrete confined, preventing detachment, and also assists in limiting crack opening.

Table 3.11—Crack pattern comparison of positive drifts up to +0.02

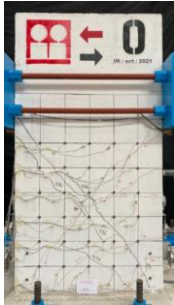
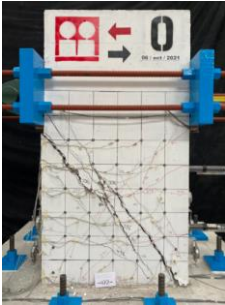
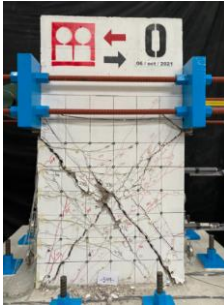
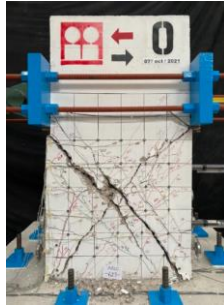
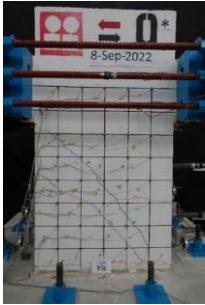
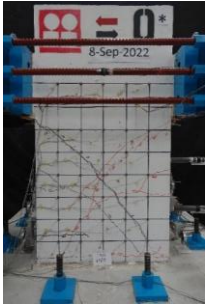
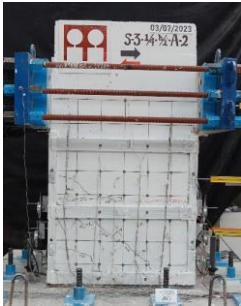
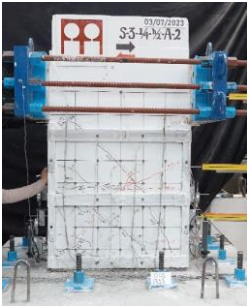
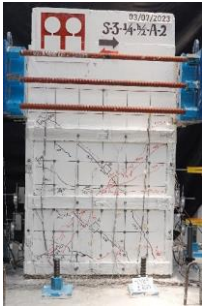
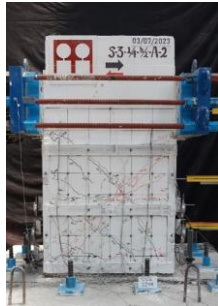
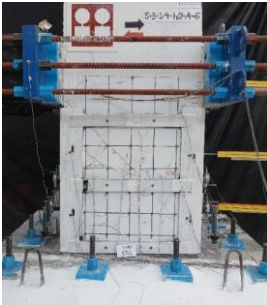
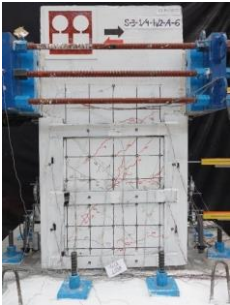
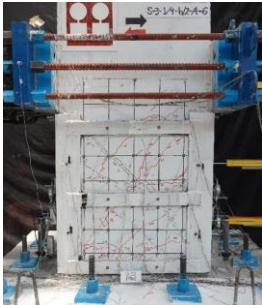
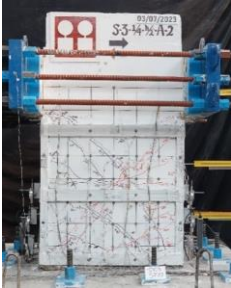
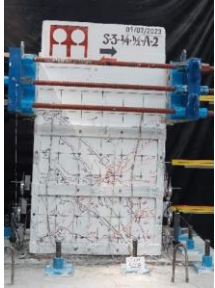
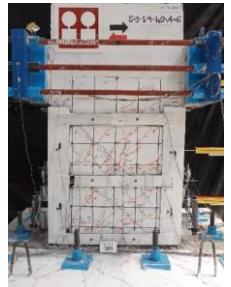
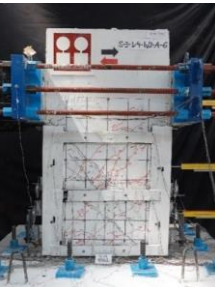
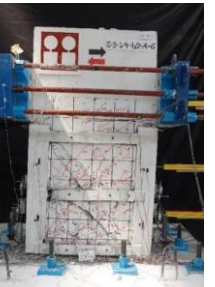
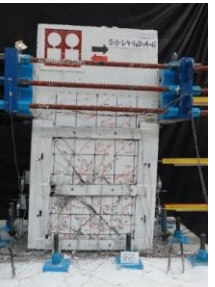
Specimen	Drift Ratio			
	+0.005	+0.01	+0.015	+0.02
CO				
CO*				
S8				
S9				

Table 3.12—Crack pattern of specimens S8 and S9 in higher drift peaks

Specimen	Drift Ratio				
	+0.03	+0.04	+0.05	+0.06	+0.07
S8					
S9					

3.5.5.2 Lateral Load Bearing Capacity

The strength of a structure denotes its capacity to withstand the maximum load. In the column test, measurements were taken of the maximum load that the column could bear, along with any lateral loads or strengths related to specific phenomena like initial inclined crack or first yielding of longitudinal and transverse reinforcing. The analysis of the column's strength primarily involved comparing the experimentally recorded values with those derived from the design expressions specified in the Mexico City's Design Code (CDMX, 2023a). In a member lacking shear reinforcing, the concrete is presumed to resist shear. Conversely, in a member with shear reinforcing, part of the shear strength is assumed to be supplied by the concrete, while the remainder is provided by the shear reinforcing (ACI, 2019). Based on the shear strength of RC members, published in NTC-Concreto-2023 (CDMX, 2023a) and ACI 318-19 (ACI, 2019), without using strength-reduction factors, the nominal shear strength is calculated as follows:

$$V_R = V_C + V_S \tag{Eq. 3.6}$$

$$V_C = \left(0.17\lambda_s\sqrt{f'_c} + \frac{N_u}{6A_g} \right) b_w d \tag{Eq. 3.7}$$

$$V_S = \frac{A_v f_{sy} d}{s} \tag{Eq. 3.8}$$

where the V_c and V_s are the shear strength taken by the concrete and transverse reinforcing steel, respectively; N_u is the axial load, positive in compression (in this case equals to zero); λ_s is the reduction factor that takes in consideration the specific weight of concrete, taken equal to 1.0 for normal weight concrete (CDMX, 2023a), and for ACI (2019) λ_s is the size effect factor calculated using Eq. 3.9; b_w and d are the width and the distance from extreme compression fibre to centroid of longitudinal compression reinforcing, respectively; s is the centre-to-centre spacing of transverse reinforcing; f_{sy} is the yielding stress of transverse steel; and A_v is the area of shear reinforcing within spacing s .

$$\lambda_s = \sqrt{\frac{2}{1 + 0.004d}} \leq 1 \quad \text{Eq. 3.9}$$

Evaluating the Eq. 3.6 to Eq. 3.9, using the average value of f'_c for the specimens, and the value of $\lambda_s = 1.0$ (to be conservative), the shear strength is 450.25 kN. The calculated shear force from Eq. 3.6 evidently indicates an underestimation of the nominal strength, with a magnitude difference 1.87 times comparing to the peak positive strength of specimen CO. In line with the preceding statements, the column's strength to lateral loads relies on both the diagonal tensile strength of the concrete's effective area to withstand shear forces and the quantity and type of transverse reinforcing. Subsequent behaviour following crack is contingent upon the transverse reinforcing. There are several ways to assess in a more accurate manner the shear strength of the specimens without jacketing, like adding the contribution of the reinforcing bars by the dowel effect, or incurring more precisely the size effect (Bažant, 1999; Carloni et al., 2017), but in this case the design code calculus is only for comparison.

Evaluating Eq. 3.10 from CDMX (2023b) for the shear strength bearing capacity of existing RC columns, and using the values described next, the shear strength is 335 kN. This value is lower than the calculated using Eq. 3.6 as expected for evaluations of already built RC structures in rehabilitation codes.

$$V_{col} = k_{nl} \left[\alpha_{col} \left(\frac{A_v f_{ytE} d}{s} \right) + \lambda \left(\frac{0.5 \sqrt{f'_{cE}}}{d \frac{M_u}{V_u}} \sqrt{1 + \frac{P_{UG}}{0.5 A_g \sqrt{f'_{cE}}}} \right) 0.8 A_g \right] \quad \text{Eq. 3.10}$$

where $k_{nl} = 1.0$ for ductility less or equal to 2; $\lambda = 1.0$ for normal weight concrete; P_{UG} is the axial force, equal to zero due to the lack of axial force applied; A_g is gross cross-sectional area of the element in mm^2 ; A_v is the area of shear reinforcing within spacing s ; f_{ytE} is the expected yield strength of the transverse reinforcement in MPa; f'_{cE} is the expected compressive strength of concrete in MPa; the ratio $d M_u / V_u$ is the largest ratio between the moment M_u and the shear force V_u at the neutral axis of the column under design loads considering the combination of permanent loads and accidental seismic loads, but it shall not be greater than 4 nor less than 2; and $\alpha_{col} = 1.0$ for $s/d \leq 0.75$, and $\alpha_{col} = 0$ for $s/d \geq 1.0$.

3.5.5.3 Response Envelopes

The response envelopes are curves generated from the lateral load versus drift response of tested models. In Fig. 3.103, the envelope curves for the four tested models are depicted. These envelopes were derived from the maximum shear force values during semi-cycles at identical drift levels (the peak values). Within this figure, three primary stages can be discerned in the overall behaviour of the tested column. The initial stage displayed a linear correlation between load and drift, which concluded shortly after the emergence of the first inclined crack at 0.5% drift.

Following the first inclined crack and reaching the maximum strength of the model, an intermediate stage became evident. The third stage was characterized by the maximum shear strength achieved, the ultimate drift experienced by the specimens, and their subsequent strength degradation.

By comparing the hysteresis curve envelopes of each specimen, as illustrated in Fig. 3.103, a noticeable increase in lateral deformation capacity is observed in specimens S8 and S9. Furthermore, the maximum lateral load capacity of the column increased by as much as 1.13 times. The disparity in lateral stiffness among the specimens is noteworthy, with specimen CO being the stiffer, this phenomenon can be explained by the variation in the modulus of elasticity of the concretes (see Table 3.3 in section 3.2.5), as evidenced by the curves of concrete cylinders (see section 7.1.2 and 7.1.3).

The response envelopes of both S8 and S9 specimens are alike, being the S9 attaining the highest strength in the positive load (push), and the specimen S8 had the highest peak lateral load strength in the negative direction (pull). This symmetry observed in the overall behaviour of all specimens can be attributed to the difficulty in creating perfectly symmetrical conditions during displacement impositions. Additionally, variations in material properties may contribute to this imperfect symmetry, in combination of the appearance of the important cracks in the column's specimens.

The primary distinction between specimens S8 and S9 lies in the small damage observed during the tests in the central zone of the column, with S9 exhibiting fewer cracks. and also, the loss of white wash in the battens, attributed to the strain of this elements, being the specimen S8 the one who had more strain demand in the steel jacket.

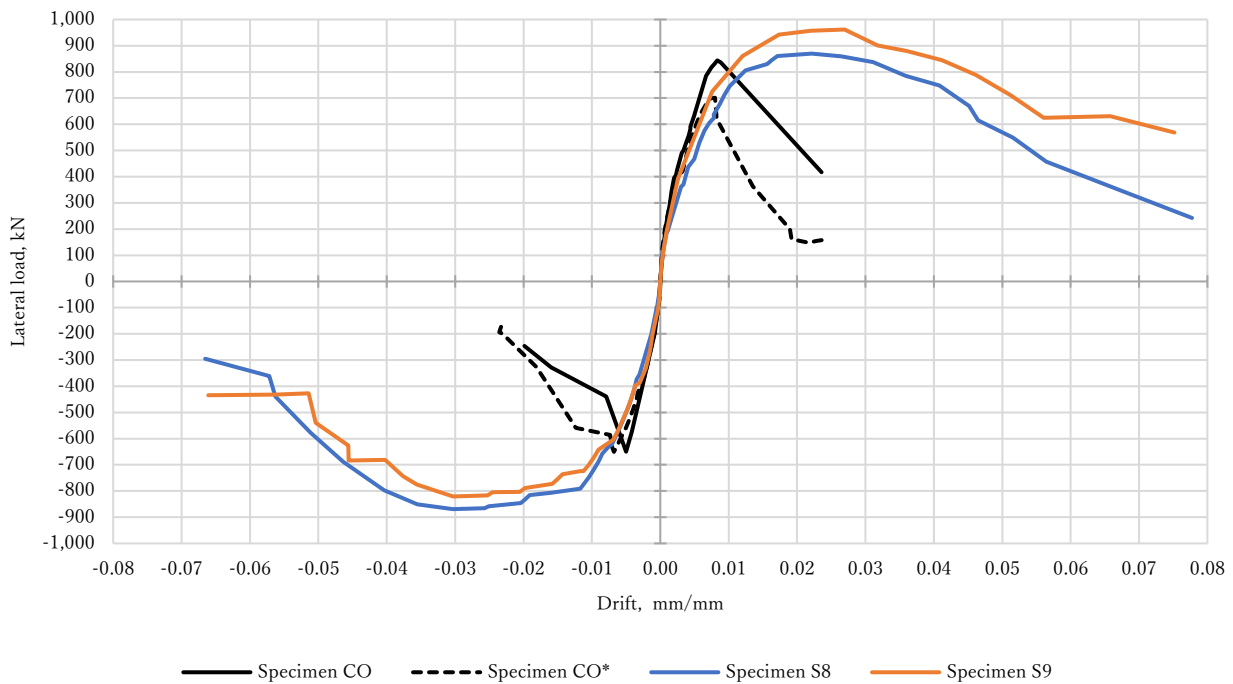


Fig. 3.103—Backbone curves of hysteresis curves

3.5.5.4 Stiffness

Just like strength, the stiffness of structures is a highly important parameter for studying their behaviour under seismic actions. The reduction in stiffness of columns is commonly attributed to several factors, including the decrease in the modulus of elasticity of cracked concrete, deterioration of bond between steel and surrounding concrete, and the cyclical opening and closing of residual cracks. This section provides a comparison of elastic stiffness and cyclic stiffness of the column with experimentally recorded values. Analysing these values leads to the derivation of several significant conclusions, which are outlined in this section. Generally, the stiffness of a structure relies on the geometric properties of its components and the mechanical characteristics of the materials employed in its construction. Typically, the initial stiffness of a reinforced concrete column is determined through an elastic analysis, incorporating nominal geometric properties and mechanical material properties.

The elastic stiffness of the models was determined through the application of elasticity theory expressions. Given that the column test was performed under a cantilever loading system, the elastic stiffness can be computed using the following expression, which encompasses both the flexural and shear components (M. Gere & J. Goodno, 2009):

$$K_e = \left(\frac{L^3}{3E_c I} + \frac{L}{A_{sv} G} \right)^{-1} \tag{Eq. 3.11}$$

where L is the length of the beam, in this case is 1,200 mm; I is the moment of inertia with respect to the centroidal axis of the cross-sectional area in the direction of deformation; A_{sv} is the transverse shear section area of the column, equal to the gross section area divided by 1.8; and G is the shear modulus, calculated using Eq. 3.1.

Evaluating the Eq. 3.11 the elastic stiffness using the average elastic and shear modulus of the concrete is 498.96 kN/mm (50.88 t/mm), that is 1.61 times larger than the elastic stiffness calculated from the test data of specimen CO, which was 309.5 kN/mm (31.56 t/mm). The elastic stiffness and the real stiffens can be compared in Fig. 3.104, were only the positive values are plotted for comparison.

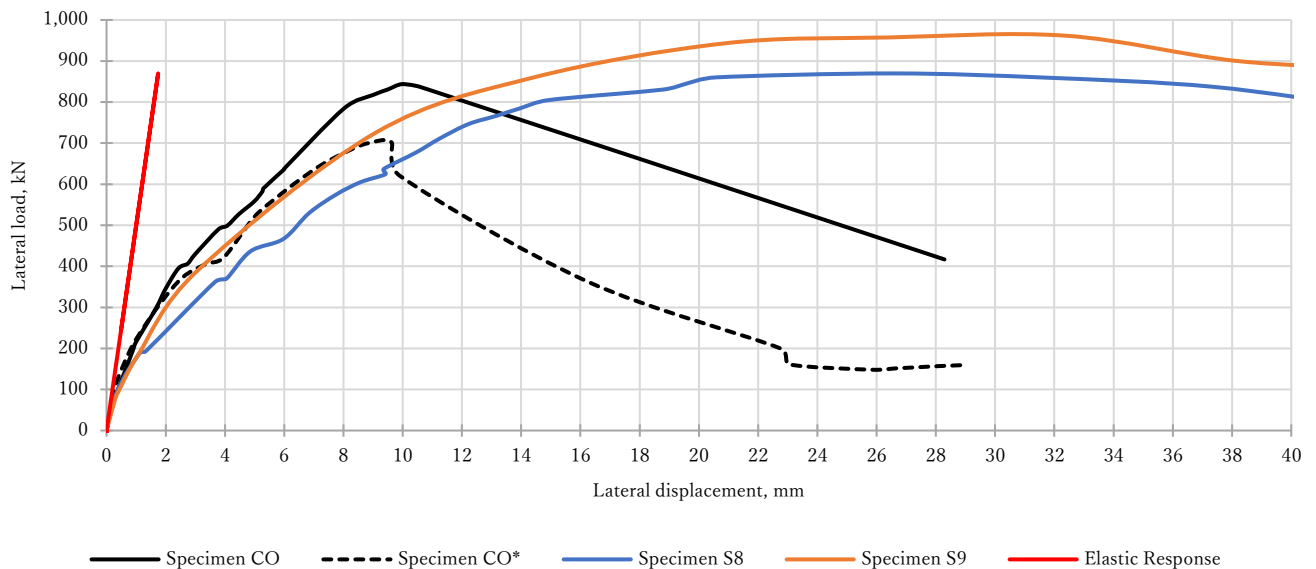


Fig. 3.104—Elastic stiffness comparison

The difference in the elastic stiffness to the real stiffness can be explained by the hypotheses adopted in the theoretical framework of elastic stiffness, as it involves a scenario where a perfect fixed support condition exists, unlike in the experiment. Alternatively, the differences in the elasticity modulus at various points within the specimen body may account for the discrepancy, given the inability to ensure material homogeneity. The effects of the support condition are explored in Chapter 4.

The deterioration of stiffness within a structure is linked to the increase of drift and damage levels. Examining this stiffness degradation is particularly valuable as it provides insight into the structure's residual capacity at any point during testing or under specific damage conditions. There are two parameters that can be used to describe the stiffness degradation of a structure. The first one, known as cycle stiffness, involves evaluating the loss of stiffness during complete load cycles. The second parameter, equivalent stiffness, allows understanding the evolution of stiffness in each half-cycle of loading; that is, for each change in the loading direction.

The stiffness of each cycle is calculated as follows:

$$K_c = \frac{P^+ + |P^-|}{R^+ + |R^-|} \quad \text{Eq. 3.12}$$

where P^\pm , is the lateral load of the positive and negative semi-cycle, respectively; R^\pm is the drift of the positive and the negative semi-cycle, associated to the lateral load P^\pm , respectively. In the Fig. 3.105 the normalized stiffness degradation (K_{c_i}/K_{c_0}) versus the drift is plotted, where K_{c_i} is the stiffness evaluated with Eq. 3.12 for the i cycle, and K_{c_0} is the elastic stiffness evaluated using Eq. 3.11. It is evident that specimen CO and CO* exhibit a faster stiffness degradation, reaching a reduction of 97% of the initial stiffness at a drift of 0.02. The curves of the jacketed columns follow a parabolic trend such that for a drift of 2%, the stiffness had degraded by 80%. The contrast in stiffness degradation between specimen CO and CO* can be observed, even though they are identical columns. As previously mentioned, the difference in these specimens might stem from variations in the properties of the concrete.

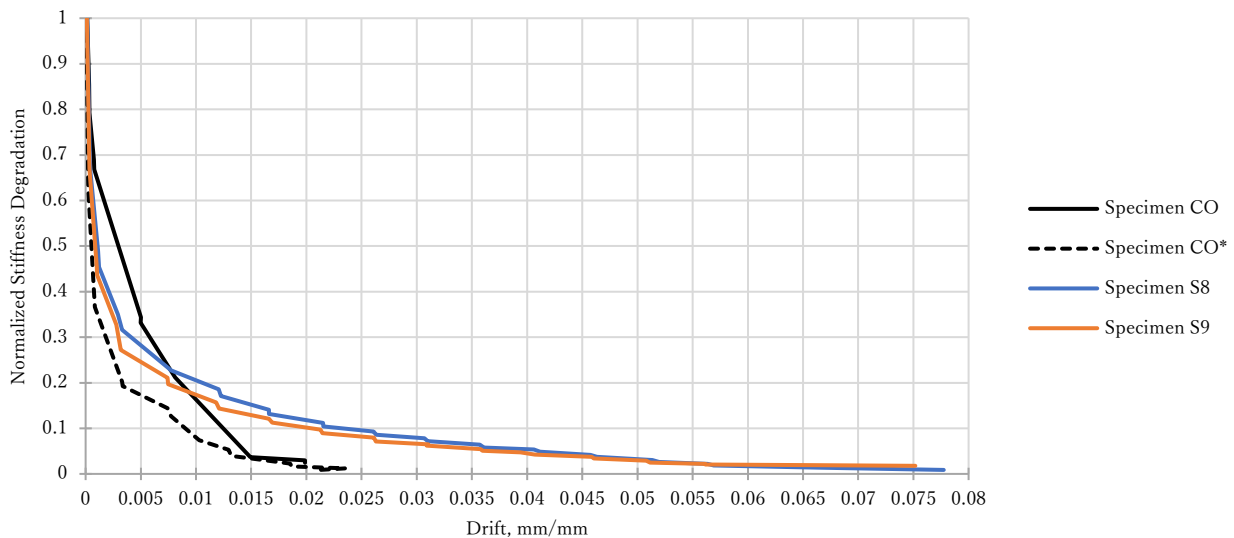


Fig. 3.105—Stiffness degradation of studied specimens

3.5.5.5 Ductility

In addition to considerations of strength and serviceability, ductility is a significant factor that must be addressed in structural design. It is crucial to ensure that if a structure is subjected to extreme loading leading to failure, it will exhibit ductile behaviour. This means the structure should not fail abruptly and brittlely without warning, but rather should be capable of significant strains near its maximum load-carrying capacity. The ability of a structure to undergo large strains before failure provides clear warning signs and can prevent total collapse, potentially saving lives. The ductility ratio is commonly employed to evaluate the ductility of a flexural member and, consequently, the efficacy of a retrofit method. However, the ductility ratio is ambiguously defined and can be misleading in the literature. One of the simplest definitions of ductility, μ , is that of the next equation:

$$\mu = \frac{\Delta_u}{\Delta_y} \quad \text{Eq. 3.13}$$

where Δ_u is the ultimate lateral deformation; and Δ_y is the yield lateral deformation. With this simple definition, it can be calculated the ductility of each specimen tested, using the backbone curves. However, various definitions of yield and ultimate displacements have been utilized in the literature. The ultimate displacement is commonly defined at the point on the descending branch where the lateral strength decreases to a specified percentage of the peak strength, typically ranging from 10 to 30 percent (Yu-Fei et al., 2005). Here, the yield lateral displacement used for calculate the ductility of each specimen is the lateral displacement related to the first appearance of an inclined crack, and the ultimate lateral deformation is defined to those related to a loss of 20% of the maximum lateral load bearing capacity. The Table 3.13 shows the ductility of each specimen, it is notable the higher ductility of specimens S8 and S9, reaching up to 7.3 times the ductility of specimen CO and CO*.

Table 3.13—Ductility of each specimen

Specimen	Δ_y mm	Lateral load related to Δ_y kN	Δ_u mm	Lateral load related to Δ_u kN	μ
CO	6.04	636.45	16.00	675.04	2.64
CO*	3.96	421.68	8.31	560.94	2.10
S8	3.66	361.66	61.44	695.20	16.79
S9	3.09	390.86	55.38	768.80	17.92

3.5.5.6 Strain Gauges Comparison

Comparing when the yielding of reinforcing steel is reached and in which bars is this yielding is presented is interesting. The Fig. 3.106 shows the lateral displacement related to the recorded beginning of yielding of the monitored reinforcing bars. Some of the strain gauges recorded yielding for almost the same lateral displacement, but in different cycle, e.g., for the STN2 the lateral load related to the first yield strain are ± 10 mm for CO, CO* and S9 specimens. The Fig. 3.107 shows the lateral displacement related to the first yield strain recorded in the steel jacket. Here, none of the strain gauges installed in the middle span of the steel battens for the specimen S9 reached yielding; for this specimen, the more demanded zones were the ends of the steel battens as exposed in Fig. 3.107.

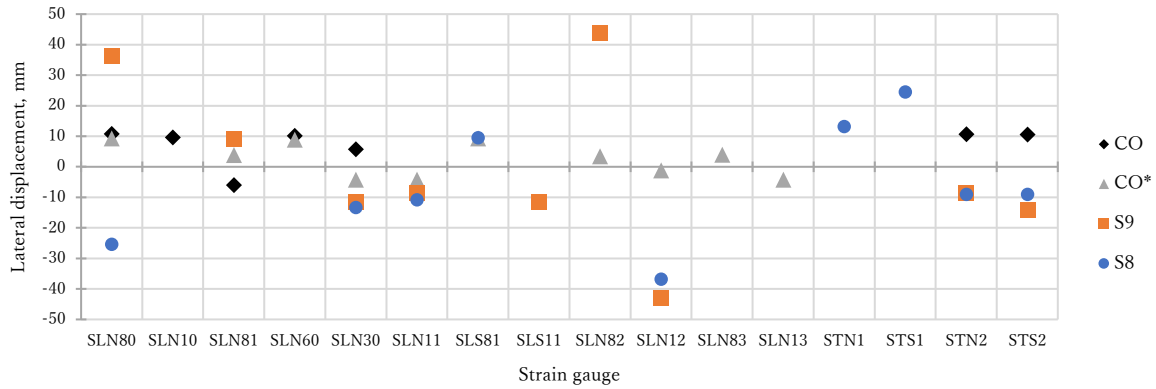


Fig. 3.106—Lateral displacement related to the beginning of yield of the monitored reinforcing bars

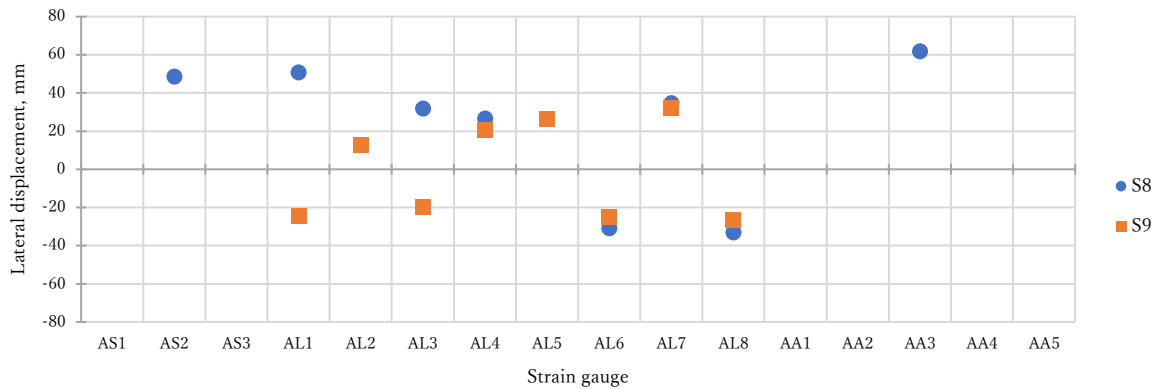


Fig. 3.107—Lateral displacement related to the beginning of yield of the monitored steel jacket

3.5.5.7 Column Local Deformation

The recorded diagonal displacement of the concrete column by the DD1, DD2 and DD3 diagonal face transducers (see Fig. 3.15b) is depicted in the Fig. 3.108. Here, the comparison of the displacement of the diagonals in the tested specimens shows the work done by the steel jacketing as controlling the strain of the concrete column. It can be seen in the Fig. 3.108 that despite the major drift capability of the jacketed columns, the middle diagonal local strain is less compared to CO and CO* specimens. Nevertheless, the C8 and C9 specimens had major strain in the DD1 diagonal, this also is true for the horizontal local strain recorded by DH1 transducer in Fig. 3.109.

The local horizontal strain, recorded by the horizontal transducers DH1, DH2, DH3 and DH4 are depicted in Fig. 3.109, were the maximum local strains in specimens S8 and S9 are recorded by the DH1 and DH2 transducers. As in the Fig. 3.108, the steel jacketing reduces the local strain in the upper zones, compared to specimen CO and CO*, despite the major lateral drift demand for the S8 and S9 specimens.

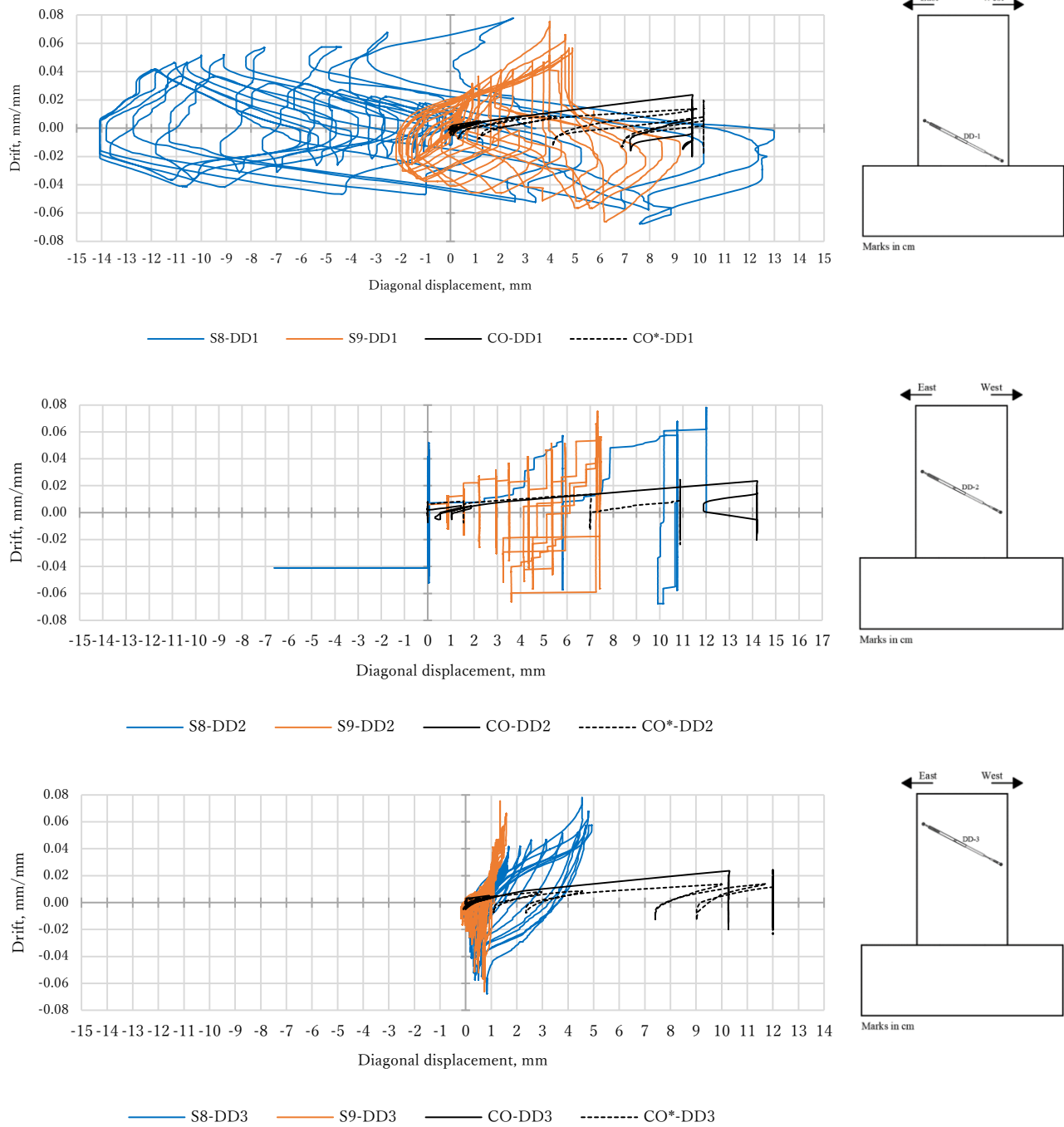


Fig. 3.108—Diagonal displacement recorded by face transducers

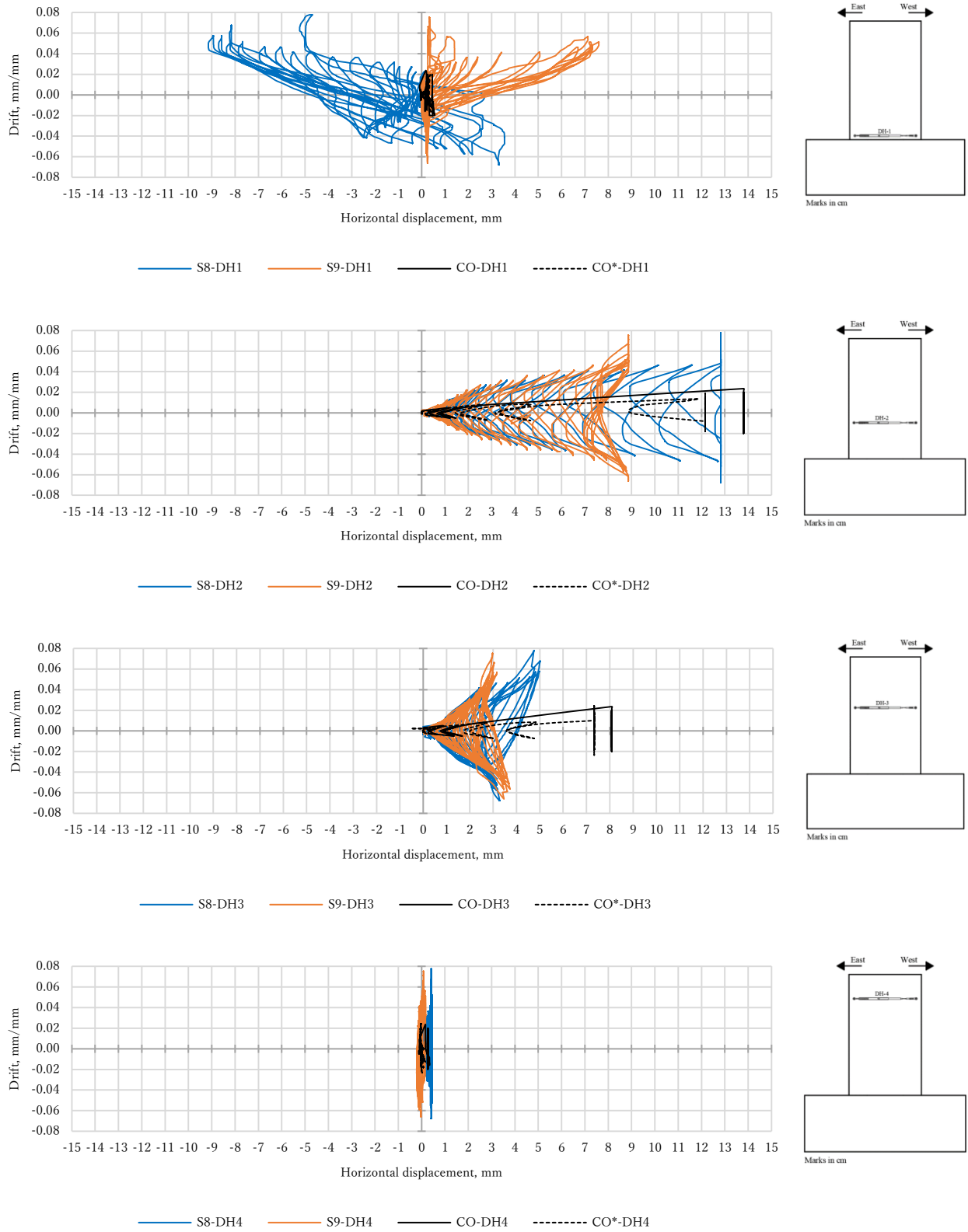


Fig. 3.109—Horizontal displacement recorded by face transducers

4 FINITE ELEMENT ANALYSIS

Summary

In this chapter, the analysis procedure is comprehensively explored, with a detailed breakdown provided for clarity and understanding. Additionally, the formulation of the Finite Element Method (FEM) is delved into, with its theoretical foundations and practical application elucidated within the study. The approach for the FE analysis is monotonic, using a lateral incremental displacement imposition. Finally, the mathematical results derived from the analysis are presented and discussed, offering insights and interpretations that further enrich the understanding of the subject matter.

4.1 Theoretical Basis

Recognizing that a comprehensive nonlinear formulation is not obligatory for analysing the entire structure is crucial. In numerous instances, a simplified, or even linear, formulation can be employed to rearrange the model. Evaluating whether the inaccuracies arising from a simplified formulation are acceptable is a matter of engineering expertise and practical judgment. The simplest formulation, e.g., linear formulation, is characterized by the following assumptions (Červenka et al., 2013):

- The constitutive equation is linear, e.g., the generalized form of Hooke's law is used;
- The geometric equation is linear that is, the quadratic terms are neglected. It means that during analysis, we neglect change of shape and position of the structure;
- Both loading and boundary conditions are conservative, e.g., they are constant throughout the whole analysis irrespective of the structural strain, time, etc;
- In general, linear constitutive equations are applicable to a material that is significantly distant from its failure point, typically up to 50% of its maximum strength. This, of course, varies with the material type; for instance, rubber should be treated as a nonlinear material at an earlier stage. However, for typical civil engineering materials, the aforementioned assumption is deemed satisfactory.

Nonlinear analysis can be classified according to a type of nonlinear behaviour (Červenka et al., 2002):

- Consideration is required only for nonlinear material behaviour, which is frequently encountered in standard reinforced concrete structures. Due to serviceability constraints, strains remain relatively small. Nevertheless, it is essential to factor due to the notably low tensile strength of concrete;
- The deformations, involving either displacements or a combination of displacements and rotations, attain magnitudes that require incorporating the deformed structure's shape into equilibrium equations. Nevertheless, the relative deformations (strains) remain modest. Utilizing geometric equations with quadratic terms becomes

essential, while the constitutive equations remain linear. This category of nonlinear analysis spans a broad spectrum of stability issues;

- The last group uses nonlinear both material and geometric equations. In addition, it is usually not possible to suddenly apply the total value of load but it is necessary to integrate in time increments (or loading increments). This is the most accurate and general approach but unfortunately is also the most complicated.

There are two basic possibilities for formulating the general structural behaviour based on its deformed shape. The Lagrange Formulation, in which we are interested in the behaviour of infinitesimal particles of volume dV . Their volume will vary depending on a loading level applied and, consequently, on the number of current deformations (this method is usually used to calculate civil engineering structures); The Euler Formulation, which the essential idea of Euler's formulation is to study the "flow" of the structural material through infinitesimal and fixed volumes of the structure (this is the favourite formulation for fluid analysis, analysis of gas flow, turbulence etc. where large material flows exist).

For structural analysis, however, Lagrangian formulation is better, and therefore attention will be restricted to this. Two forms of the Lagrangian formulation are possible. The governing equations can either be written with respect to the undeformed original configuration at time $t = 0$ or with respect to the most recent deformed configuration at time t . The former case is called Total Lagrangian Formulation (TLF) while the latter one is called the Updated Lagrangian Formulation (ULF). Determining the optimal formulation is challenging as each has its merits and limitations. The choice typically relies on the specific structure under analysis, and the decision is a matter of engineering judgment. In general, when the constitutive equations are sufficient, results from both methods are usually identical. ATENA currently uses Updated Lagrangian Formulation, and supports the highest, e.g., level of nonlinear behaviour (Červenka et al., 2013).

4.1.1 Finite Element Formulation

In this section, information about the finite elements currently integrated into ATENA is founded. With a few exceptions, the elements incorporated into ATENA are predominantly built using an isoparametric formulation (Červenka et al., 2013) containing linear and/or quadratic interpolation functions. The isoparametric formulation employed for one, two, and three-dimensional elements falls within the category of "classic" element formulations. The preference for this approach is not based on its superior properties, but rather on its versatility and general applicability without hidden complexities. Importantly, these elements are easy to comprehend, a crucial factor, especially in nonlinear analysis. For instance, it is highly undesirable to introduce element-related challenges into issues associated with material modelling.

4.1.1.1 3D Solid Elements

ATENA finite element library includes Tetra (Tetrahedral) element (see Fig. 4.1), with 4 to 10 nodes, and Brick (Hexahedral) element, with 8 to 20 nodes. These isoparametric elements are numerically integrated by Gauss quadrature (Červenka et al., 2013). For the macroelements to model concrete and steel plates, Brick and Tetra elements are used, respectively.

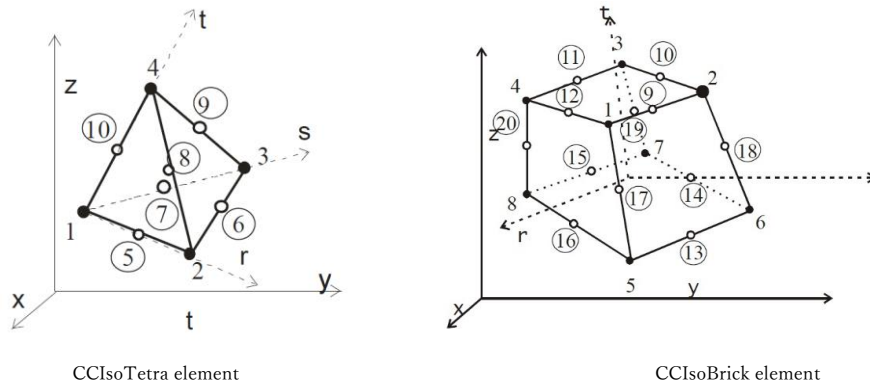


Fig. 4.1—3D Solid Elements in ATENA (Červenka et al., 2013)

4.1.1.2 Truss 3D Elements

In cases where extensive model detailing is unnecessary, steel reinforcing is commonly represented using Truss elements, as illustrated in Fig. 4.2. Truss elements symbolize members subjected to tension or compression, aligning well with the axial behavior of steel reinforcing. These elements, integrated by Gauss integration with 1 or 2 points for linear or quadratic interpolation (corresponding to elements with 2 or 3 nodes), are applicable for both 2D and 3D analysis problems. Alternatively, for a more precise representation, beam elements can be employed. These one-dimensional elements assume that the structure's behavior is predominantly influenced by axial and bending strains. However, for the purposes of this work, a simpler modelling approach will be adopted, so Truss element with two nodes was used.

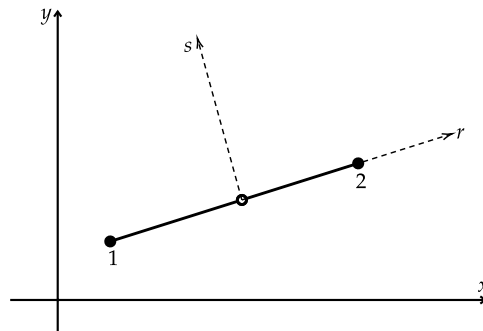


Fig. 4.2—Truss 3D element CCIsoTruss in ATENA (2013)

4.1.1.3 External Cable

External pre-stressing cables are reinforcing bars, which are not connected with most of the concrete body, except of limited number of points, so called deviators, as shown in Fig. 4.3. This element type is denoted in ATENA as CCEXternalCable. Each cable has two ends provided with anchors. The anchor, where the pre-stressing force is applied is denoted as the *active anchor*, the anchor on the other side is the *passive anchor*. The points between the anchors are called *deviators* (or links). After applying post-tensioning, the cable is fixed at anchors. In the deviators, cable can slide while its movements and the forces are governed by the law of dry friction. For the anchor bars presents in the experiment (see section 3.2.8) the ATENA CCEXternalCable are used to model the post-tensioned bars. The element stiffness is $k = E_s A / L$ where A , L are the cable cross section and the length, respectively, and E_s is the actual secant or tangent modulus derived in the same way as in case of other reinforcing using bilinear or multi-linear law.

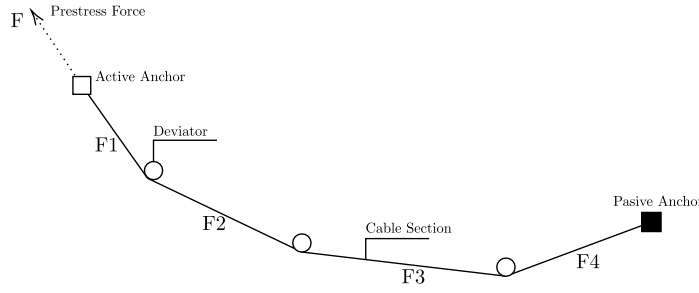


Fig. 4.3—ATENA CCEXternalCable element (adapted from ATENA)

4.1.1.4 Interface Element

The contact between two or more macroelements can be of two principal types: perfect connection, in which the interface elements are used to model a contact between two surfaces with a perfect connection with a perfect stress-force-strain transmission between macroelements; and contact element, which are used to model non-perfect connection in where a friction surface or gap are important to model. This interface element is derived from the same isoparametric elements of 3D solid elements. The interface is delineated by two lines (or surfaces in 3D), located on opposing sides of the interface. In its initial (undistorted) form, these lines/surfaces may coincide or have a slight separation between them (Červenka et al., 2013). In such instances, it is referred to the interface as having a nonzero thickness. The interface element has two states:

- Open state: There is no interaction of the contact sides;
- Closed state: There is full interaction of the contact sides. In addition, friction sliding of the interface is possible in case of interface element with a friction model.

Penalty method is employed to model the above behaviour of the interface. For this purpose, Červenka et al. (2013) define a constitutive matrix of the interface in the form:

$$\underline{F} = \begin{Bmatrix} F_\tau \\ F_\sigma \end{Bmatrix} = \begin{bmatrix} K_{tt} & 0 \\ 0 & K_{nn} \end{bmatrix} \begin{Bmatrix} \Delta_u \\ \Delta_v \end{Bmatrix} = \mathbf{D}\underline{u} \tag{Eq. 4.1}$$

in which Δ_u, Δ_v are the relative displacements of the interface sides (sliding and opening displacements of the interface) in the local coordinate system r, s and K_{tt}, K_{nn} are the shear and normal stiffness, respectively, and \mathbf{D} is the material stiffness matrix. This coefficient can be regarded as stiffness of one material layer (real or fictitious) having a finite thickness. It should be understood that the layer is only a numerical tool to handle the gap opening and closing. F_τ and F_σ are forces at the interface, (again at the local coordinate system). For the purpose of the numerical analysis, the 3D interface element with CCIsoGap<XXXXXXXX> (8 node element for a linear geometry) is used for simplicity (see Fig. 4.4). The stiffness coefficients depend on the gap state.

The interface is considered open, if the normal force $F_\sigma > R_{ti}$ (R_{ti} is the interface tensile strength force) and the corresponding constitutive law is (stress free interface):

$$\begin{Bmatrix} F_\tau \\ F_\sigma \end{Bmatrix} = \begin{Bmatrix} 0 \\ 0 \end{Bmatrix} \tag{Eq. 4.2}$$

The stiffness coefficients are set to small values but nonzero values of K_{tt}^{op}, K_{nn}^{op} .

The interface element is considered closed if $F_\sigma \leq R_{ti}$. The stiffness coefficients are set to large values of K_{tt}^{cl} , K_{nn}^{cl} . It should be noted that the stiffness coefficients are defined only for the purpose of the numerical iterative solution.

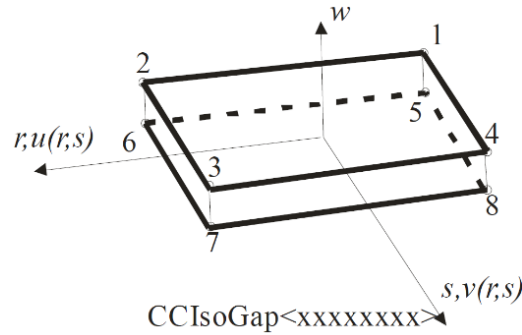


Fig. 4.4—ATENA CCIsoGap interface element (Červenka et al., 2013)

4.1.1.5 Global and Local Coordinate Systems for Element Load

Element loads can typically be specified in either a global or local coordinate system. The global coordinate system is universally accessible, making it the preferred method for inputting element loads due to its reliability and simplicity. However, certain elements are internally defined using a local coordinate system, which can also be utilized for defining element loads. For instance, local coordinate systems are established for various elements like plane 3D isoparametric elements, shell elements, and beam elements. Conversely, elements such as tetrahedrons and bricks are directly defined in the global coordinate system. Therefore, when specifying a local element load for these elements, it is treated as if it were entered in the global coordinate system. An exception to the above are truss elements. Although they are defined in the global coordinate system, they do support local element loads. Attention to detail is crucial when specifying a boundary load. Firstly, it is important to note that boundary loads are applied exclusively to an element's edge or surface, as opposed to a body load which affects the entire element. The local coordinate system is determined by the location of the loaded edge or surface (Červenka et al., 2013). Secondly, a boundary load definition must reference a selection containing the nodes to be loaded. The order of nodes in this selection is insignificant; what matters is the order in which they appear in the element incidences. When processing a boundary load, ATENA iterates through all of the element's surfaces and edges, following the specified order, and checks for relevant incidental nodes. If a tested node is found in the list of loaded boundary nodes, it is incorporated into the incidences of a new planar or line element. Later on, this element is employed to handle the boundary load. Its local coordinate system is potentially utilised for managing local/global load transformations.

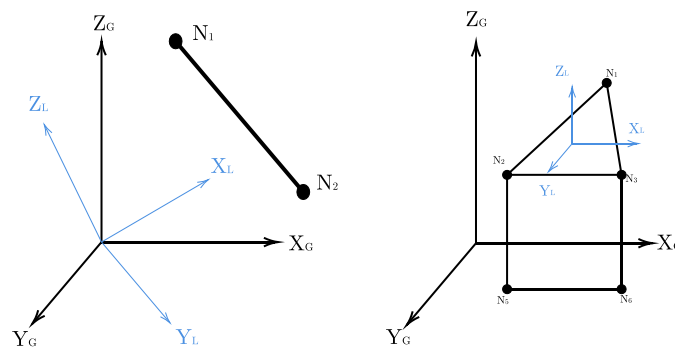


Fig. 4.5—Local and global coordinate systems for truss and 3D surface load solid element

4.1.2 Constitutive Models

Below is the key information needed to understand the nature of materials and the laws governing their behaviour. The goal of this thesis is not to cover the entire constitutive theory of material mechanics presented, so simplifications are offered to capture the basic approach.

4.1.2.1 *General Considerations*

Structural elements, along with entire structures, are malleable entities. This entails that they react to external forces by undergoing deformations (such as bending, axial, shear, and torsional) and displacements (including linear deflections and rotations). These deformations and displacements resulting from forces constitute the kinematic response of the structure or element to external actions. The diverse facets of structural response are encompassed within the realm of structural behaviour. Quantitatively, structural behaviour is delineated by the relationships between generalized forces and corresponding displacements. These relationships, known as constitutive laws, form the basis for understanding the mechanical properties of the materials employed in the structure and establishing constitutive laws for structural members (Crainic & Munteanu, 2013). Here, the constitutive models of materials used are presented, it is mechanical properties and the variables involved in each of it, the governing continuum equations for nonlinear analysis and nonlinear effects that are accounted for the study goals. The formulations shown are implemented in ATENA Software.

4.1.2.2 *Concrete*

The ATENA software define various concrete models, but the most commonly used to represent generalized concrete elements is the CC3DNonLinCementitious2, based on the SBETA¹ material. This material employs a purely incremental formulation instead of a total one for the fracturing aspect of the model. Consequently, CC3DNonLinCementitious2 proves beneficial for creep calculations or instances requiring alterations in material properties throughout the analysis (Červenka et al., 2013). For this reason, the CC3DNonLinCementitious2 is implemented in the RC elements for this analysis.

In the general concrete materials integrated in ATENA, the fracture-plastic model integrates constitutive models for both tensile (fracturing) and compressive (plastic) behaviour. Its fracture model draws upon the classical orthotropic smeared crack formulation and crack band model, incorporating the Rankine failure criterion and exponential softening. Additionally, it can function as either a rotated or fixed crack model. The hardening/softening plasticity model is founded on the Menétrey-Willam failure surface, utilizing a return mapping algorithm for integrating constitutive equations (Červenka et al., 2013).

ATENA software uses an integrated algorithm to combine a fracture-plastic model. The integrated algorithm relies on recursive substitution, facilitating the independent development and formulation of the two models. It accommodates scenarios where failure surfaces of both models are operational, as well as instances of physical transformations like crack closure. This model is adept at simulating concrete crack, crushing under intense confinement, and crack closure resulting from crushing in alternative material orientations (Červenka et al., 2002). The software basis the algorithm in the strain decomposition method, pioneered by De Borst (1986), which it is employed for the integration of fracture and plasticity models.

¹ The term SBETA originates from its initial usage in a previous program, where this material model was introduced. It stands for the abbreviation for reinforced concrete analysis in German, namely StahlBETonAnalyse.

Both models are developed within the framework of the return mapping algorithm pioneered by Wilkins (1963). This method ensures a solution for all magnitudes of strain increments².

The following effects on concrete behaviour are applied in ATENA (2013):

- Nonlinear behaviour in compression, including hardening and softening;
- Fracture of concrete in tension based on the nonlinear fracture mechanics;
- Biaxial strength failure criterion;
- Reduction of compressive strength after crack;
- Tension stiffening effect;
- Reduction of the shear stiffness after crack (variable shear retention);
- Two crack models: fixed crack direction and rotated crack direction.

It is important to note that distributed crack models emerged in response to discrete crack models. Their primary benefits lie in treating cracked solids as continuous entities, which eliminates the need for remeshing and allows for the description of material behaviour via stress-strain relationships. This approach maintains the integrity of the original mesh structure and does not constrain the orientation of crack planes (Juárez-Luna & González-Cuevas, 2022). While these models have been proposed to simulate microcrack bands, the focus has largely been on material response rather than a precise physical interpretation. Consequently, this concept is commonly viewed as a computational tool rather than a direct representation of physical phenomena.

One thing to have in consideration is that the smeared concept assumes a perfect bond between concrete and reinforcing. Direct modelling of bond slip, except for tension stiffening, is not feasible. However, on a macro-level, relative slip displacement between reinforcing and concrete can occur over a distance if the concrete is cracked or crushed, reflecting a genuine bond failure mechanism, especially for reinforcing bars (Červenka et al., 2002). Both smeared and discrete forms of reinforcing are subjected to uniaxial stress, with a constitutive law represented by a multi-linear stress-strain diagram. The detailed treatment of the theoretical background of this subject can be found, for example, in the book by Chen & Aref (1983).

4.1.2.2.1 Material Model Formulation

The material model formulation is based on the strain decomposition into elastic ε_{ij}^e , plastic ε_{ij}^p , and fracturing ε_{ij}^f components (De Borst, 1986; Červenka et al., 2013):

$$\varepsilon_{ij} = \varepsilon_{ij}^e + \varepsilon_{ij}^p + \varepsilon_{ij}^f \quad \text{Eq. 4.3}$$

The new stress state is then computed by the formula:

$$\sigma_{ij}^n = \sigma_{ij}^{n-1} + E_{ijkl}(\Delta\varepsilon_{kl} - \Delta\varepsilon_{kl}^p - \varepsilon_{kl}^f) \quad \text{Eq. 4.4}$$

where the increments of plastic strain $\Delta\varepsilon_{ij}^p$ and fracturing strain $\Delta\varepsilon_{ij}^f$ must be evaluated based on the used material models.

² The integrated algorithm needs to discern the division of strains into plastic and fracturing components while maintaining stress equivalence in both models. This algorithm is founded on a recursive iterative scheme. However, it is observed that such a recursive algorithm may fail to converge in certain scenarios, such as with softening and dilating materials. To address this, the recursive algorithm is augmented by a variation of the relaxation method to stabilize convergence.

It is important to note that the factor that controls the crack closure is regulated by the unloading factor f_U , which serves as a material parameter, and has the values $f_U \in (0; 1)$. When $f_U = 0$ it corresponds to unloading to origin (default value for backward compatibility), and when $f_U = 1$ means unloading direction parallel to the initial elastic stiffness. In the approach of the present study the f_U is not explored due to the type of comparison (monotonic displacement imposition) implemented in this research.

4.1.2.2 Parameters of Constitutive Model

The SBETA constitutive model for concrete includes 20 material parameters, which are designated by the user for the specific problem at hand. If these parameters are unknown, automatic generation can be facilitated using default formulas provided in the Table 4.1. In this scenario, only the cube strength of concrete f'_{cu} (nominal strength) needs to be specified, with the residual parameters calculated as functions of the cube strength. The formulas for these functions are derived from the CEB-FIP Model Code 90 and other reputable research sources (Červenka et al., 2013). The predefined parameters calculated in ATENA are shown in Table 4.1.

Table 4.1—Default formulas of material parameters

Parameter	Formula
Cylinder strength	$f'_c = -0.85f'_{cu}$ [MPa]
Tensile strength	$f'_t = 0.24(f'_{cu})^{2/3}$ [MPa]
Initial elastic modulus	$E'_c = (6000 - 15.5f'_{cu})\sqrt{f'_{cu}}$ [MPa]
Poisson's ratio	$\nu = 0.2$
Softening compression	$w_d = -0.5$ [mm]
Type of tension softening	Exponential (see Fig. 4.7)
Compressive strength in cracked concrete	$c = 0.8$ [MPa]
Tension stiffening stress	$\sigma_{st} = 0.0$ [MPa]
Shear retention factor	Variable
Tension-compression function type	Linear
Fracture energy	$G_F = 0.000025f'^{ef}_t$ [MN/m]
Orientation factor for strain localization	$\gamma_{max} = 1.5$

4.1.2.2.3 Equivalent Uniaxial Law

The nonlinear response of concrete under biaxial stress conditions is characterized using the concept of effective stress σ_c^{ef} and equivalent uniaxial strain ε^{eq} . Typically, the effective stress corresponds to one of the principal stresses. The equivalent uniaxial strain is introduced in order to eliminate the Poisson's effect in the plane stress state.

$$\varepsilon^{eq} = \frac{\sigma_{ci}}{E_{ci}} \quad \text{Eq. 4.5}$$

The equivalent uniaxial strain can be seen as the strain generated by stress σ_{ci} in a uniaxial test with modulus E_{ci} along the direction i . Under this premise, the nonlinearity, which means damage, arises solely from the predominant stress σ_{ci} . Further

elaboration can be found in Chen & Atef (1983). The comprehensive equivalent uniaxial stress-strain diagram for concrete is depicted in Fig. 4.6. The point U is an example of linear unloading behaviour, the transition from loading to unloading happens when the effective strain increment changes its sign. Upon subsequent reloading, the system follows a linear unloading trajectory until it returns to the last loading point U. At that point, the loading function restarts.

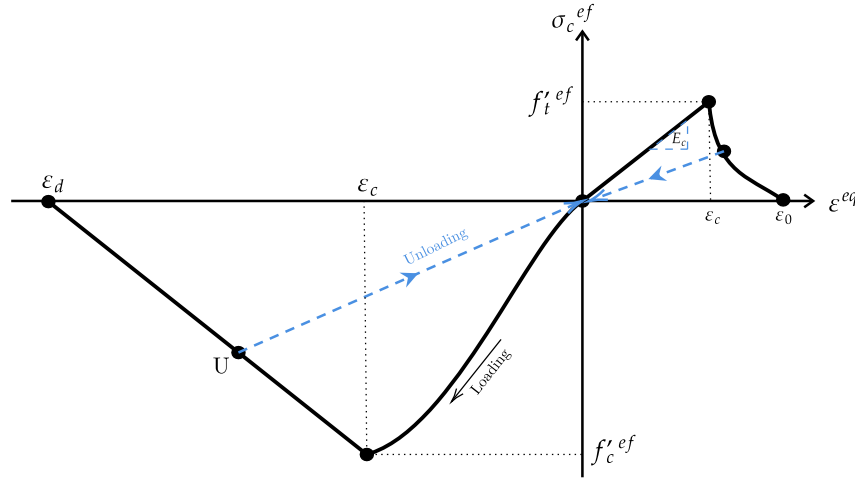


Fig. 4.6—Uniaxial stress-strain law for concrete. Adapted from ATENA (2013).

The above defined stress-strain relation is used to calculate the elastic and secant modulus for the material stiffness matrices. The secant modulus is calculated as:

$$E_c^s = \frac{\sigma_c}{\varepsilon^{eq}} \tag{Eq. 4.6}$$

The stiffness matrix of uncracked concrete conformed to the structure of an elastic matrix for isotropic materials is given in Eq. 4.7. It is expressed within the global coordinate system of x and y .

$$D_c = \frac{E}{1 + \nu^2} \begin{bmatrix} 1 & \nu & 0 \\ \nu & 1 & 0 \\ 0 & 0 & \frac{1 - \nu}{2} \end{bmatrix} \tag{Eq. 4.7}$$

In the aforementioned context, E represents the elastic modulus of concrete, determined through the equivalent uniaxial law. The Poisson's ratio ν remains constant.

4.1.2.2.4 Tension Before Crack

Concrete behaviour in tension, lacking of cracks, is presumed to follow linear elasticity. Here, E_c represents the initial elastic modulus of concrete, while f_t^{ref} means the effective tensile strength, as determined from the biaxial failure function outlined in 4.1.2.2.9.

$$\sigma_c^{ef} = E_c \varepsilon^{eq}, \quad 0 < \sigma_c \leq f_t^{ref} \tag{Eq. 4.8}$$

4.1.2.2.5 Tension After Crack

A hypothetical crack model is constructed around a crack-opening law and fracture energy, serving as a feasible method for simulating crack propagation in concrete. It is often employed alongside the crack band approach for enhanced accuracy in modelling. There are five models of softening included in ATENA, in the case of the actual study the Exponential Crack Opening Law model is used for simplicity and for its widely applicability. This function of crack opening was derived experimentally by Hordijk (1991).

$$\frac{\sigma}{f_t^{ef}} = \left(1 + \left(c_1 \frac{w}{w_c}\right)^3\right) \exp\left(-c_2 \frac{w}{w_c}\right) - \frac{w}{w_c} (1 + c_1^3) \exp(c_2), \quad w_c = 5.14 \frac{G_f}{f_t^{ef}}, \quad c_1 = 3, \quad c_2 = 6.93 \quad \text{Eq. 4.9}$$

where w is the crack opening; w_c is the crack opening at the complete release of stress; σ is the normal stress in the crack (crack cohesion); G_f is the fracture energy needed to create a unit area of stress-free crack; f_t^{ef} is the effective tensile strength derived from a failure function; and the crack opening displacement w is derived from strains according to the crack band theory (see 4.1.2.2.8).

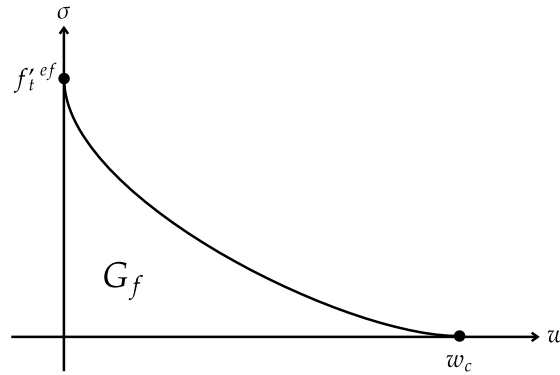


Fig. 4.7—Exponential crack opening law. Adapted from ATENA (2013).

4.1.2.2.6 Compression Before Peak Stress

The concrete stress-strain law in compression's ascending branch aligns with the formula advised in the CEB-FIP Model Code 90, as depicted in Fig. 4.8. This formula accommodates a broad spectrum of curve shapes, spanning from linear to curved, making it suitable for both standard and high-strength concrete (Červenka et al., 2013). The equations that describe the stress-strain law are the follow:

$$\sigma_c^{ef} = \frac{f_c^{ef}(kx - x^2)}{1 - (k - 2x)}, \quad x = \frac{\varepsilon}{\varepsilon_c}, \quad k = \frac{E_o}{E_c}, \quad E_c = \frac{f_c^{ef}}{\varepsilon_c} \quad \text{Eq. 4.10}$$

where σ_c^{ef} is the concrete compressive stress; f_c^{ef} is the concrete effective compressive strength; x is the normalized strain; ε is the strain; ε_c is the strain at the peak stress f_c^{ef} ; k is a shape parameter; E_o and E_c are the initial elastic modulus and the secant elastic modulus at the peak stress, respectively. The parameter k may have any positive value greater than or equal 1. Examples: $k = 1$ is for linear, $k = 2$ for parabola. As a consequence of the above assumption, distributed damage is considered before the peak stress is reached. Contrary to the localized damage, which is considered after the peak.

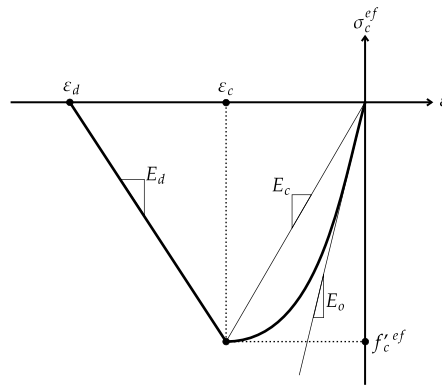


Fig. 4.8—Compressive stress-strain diagram

4.1.2.2.7 Compression After Peak Stress

In ATENA the softening law in compression is linearly descending. There are two models of strain softening in compression, one based on dissipated energy, and other based on local strain softening. In the modelled concrete used for the FEA, the fictitious compression plane model operates under the premise that compression failure occurs within a plane perpendicular to the direction of the compressive principal stress. All post-peak compressive displacements and energy dissipation are confined to this plane, with the displacement assumed to be size-independent (Červenka et al., 2013). This hypothesis finds support in experiments performed by Van Mier (1986). Analogous to the Fictitious Crack Theory for tension, this assumption defines the shape of the crack-opening law and fracture energy as material properties.

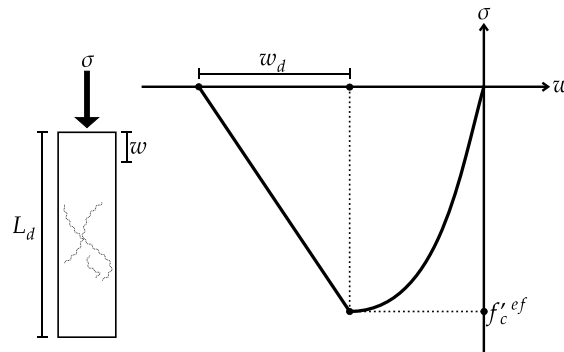


Fig. 4.9—Softening-displacement law in compression

In compression scenarios, the endpoint of the softening curve is determined by the plastic displacement, denoted as w_d . This indirectly defines the energy required to generate a unit area of the failure plane. Based on experiments performed by Van Mier (1986), the typical value for w_d is 0.5 mm for normal concrete, serving as the default for defining compression softening. The softening law transitions from a conceptual failure plane (as shown in Fig. 4.9) to the stress-strain relation applicable to the corresponding continuous material volume (as illustrated in Fig. 4.8). The slope of the softening segment of the stress-strain diagram is determined by two points: the peak stress point and a limit compressive strain ϵ_d at zero stress. This strain is derived from the plastic displacement w_d and a band size L'_d , according to the following expression:

$$\epsilon_d = \epsilon_c + \frac{w_d}{L'_d} \quad L'_d = \gamma L_d \quad \gamma = 1 + (\gamma^{max} - 1) \frac{\theta}{45} \quad \theta \in (0; 45) \quad \text{Eq. 4.11}$$

This formulation offers the benefit of decreased reliance on the finite element mesh. Band size L'_d is defined as the failure band in compression L_d (for tension is L_t) multiplied by the factor γ , which considers the element direction effect. Here, θ is the minimal angle $\min(\theta_1, \theta_2)$ (see Fig. 4.10).

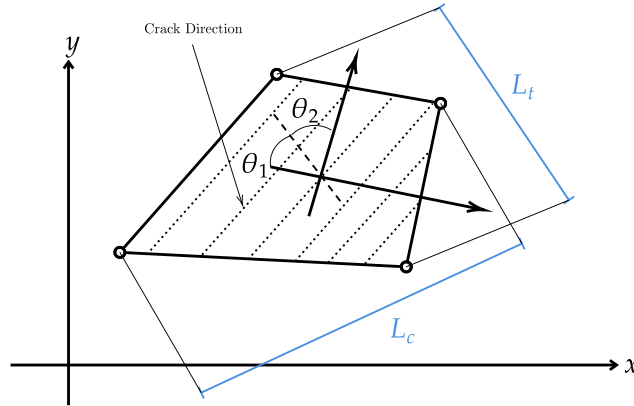


Fig. 4.10—Definition of localization bands. Adapted from ATENA (2013).

4.1.2.2.8 Fracture Process and Crack Width

Crack formation can be delineated into three distinct stages, as depicted in Fig. 4.11. Initially, there is an uncracked phase preceding the attainment of a tensile strength. Subsequently, crack formation occurs within the process zone of a potential crack, characterized by a reduction in tensile stress on the crack face due to a bridging effect. Finally, following the complete dissipation of stress, crack opening persists in the absence of stress. The crack width, denoted as w , is determined by computing the total displacement of crack opening within the crack band (Červenka et al., 2013).

The crack width w is calculated as a total crack opening displacement within the crack band, following:

$$w = \epsilon_{cr} L'_t \tag{Eq. 4.12}$$

where ϵ_{cr} is the crack opening strain, which is equal to the strain normal to the crack direction in the cracked state after the complete stress release.

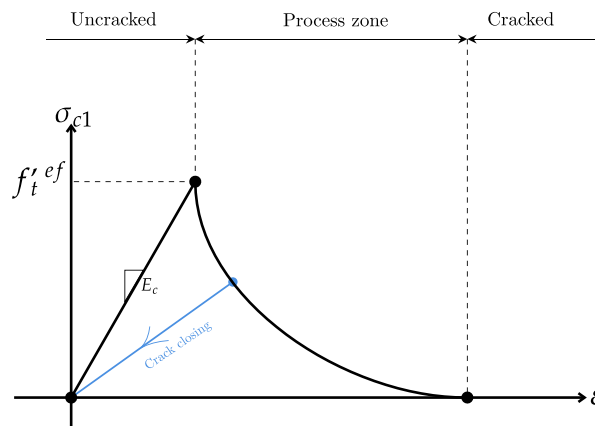


Fig. 4.11—Stages of crack opening. Adapted from ATENA (2013).

4.1.2.2.9 Biaxial Stress Failure Criterion of Concrete

The failure criterion for concrete in biaxial stress is given by the biaxial failure function according to Kupfer et al. (1969). Here, the failure function in the compression-compression stress state is given by Eq. 4.13.

$$f_c^{'ef} = f_c' \left(\frac{1 + 3.65a}{(1 + a)^2} \right), \quad a = \frac{\sigma_{c1}}{\sigma_{c2}} \quad \text{Eq. 4.13}$$

where σ_{c1}, σ_{c2} are the principal stresses in concrete and f_c' is the uniaxial cylinder strength. In the biaxial stress state, the strength of concrete is predicted under the assumption of a proportional stress path. In the tension-compression state, the failure function continues linearly from the point $\sigma_{c1} = 0, \sigma_{c2} = f_c'$ into the tension-compression region with the linearly decreasing strength:

$$f_c^{'ef} = f_c' r_{ec}, \quad r_{ec} = \left(1 + 5.3278 \frac{\sigma_{c1}}{f_c'} \right), \quad 0.9 \leq r_{ec} \leq 1.0 \quad \text{Eq. 4.14}$$

where r_{ec} is the reduction factor of the compressive strength in the principal direction 2 due to the tensile stress in the principal direction 1. In the tension-tension state, the tensile strength is constant and equal to the uniaxial tensile strength f_t' . In the tension-compression state, the tensile strength is reduced by the relation $f_t^{'ef} = f_t' r_{et}$, where r_{et} is the reduction factor of the tensile strength in the direction 1 due to the compressive stress in the direction 2 (Červenka et al., 2013).

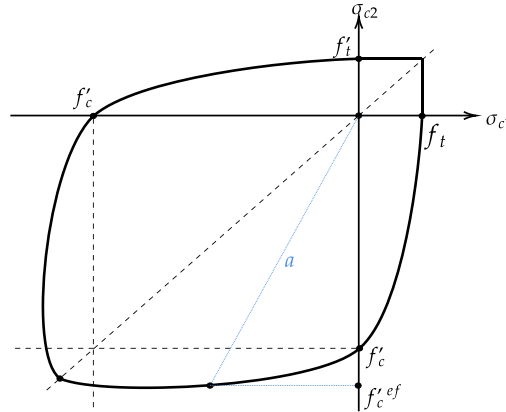


Fig. 4.12—Biaxial failure function for concrete. Adapted from ATENA (2013).

4.1.2.2.10 Tension Stiffening

In heavily reinforced concrete structures, cracks are unable to fully develop, and the concrete contributes to the stiffness of the steel. This phenomenon is known as tension stiffening, and it can be replicated in the CC3DNonLinCementitious2 material model by defining a tension stiffening factor denoted as c_{ts} . This factor represents the relative limiting value of tensile strength in the tension softening diagram, as depicted in Fig. 4.13. The tensile stress cannot drop below the value given by the product of $c_{ts} f_t'$. The recommended default value for c_{ts} is 0.4 as recommended by CEB-FIP Model Code 1990 (Červenka et al., 2013). However, in the FE model of this thesis, this value will be calibrated. There is also a tension stiffening effect in cracked concrete covered in ATENA. This phenomenon refers to how cracked concrete contributes to the tensile stiffness of reinforcing bars. This stiffness arises from either the uncracked concrete or partially opened cracks and it is a result of the strain localization process.

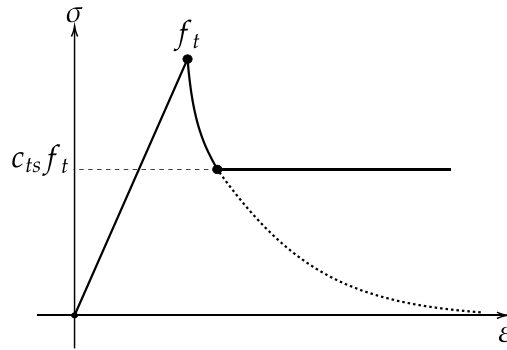


Fig. 4.13—Tension stiffening diagram (Taken from ATENA Theory)

4.1.2.2.11 Crack Spacing

In heavily reinforced concrete structures or those with large finite elements, where numerous reinforcing bars intersect each finite element, the crack band approach (see section 4.1.2.2.7) may produce overly conservative results, potentially leading to overestimated crack widths (Červenka et al., 2013). This stems from the assumption in the crack band approach that crack spacing exceeds the size of a finite element. However, in heavily reinforced structures or when employing large finite elements, crack spacing might actually be smaller than the finite element size, particularly with shell/plate elements. In such cases, where large finite elements often contain significant reinforcing, manually defining the crack spacing becomes beneficial to prevent overestimation of crack and subsequent larger deflections in calculations. ATENA software enables users to specify crack spacing manually, with this user-defined value utilized as the crack band size L_t in instances where the user-defined crack spacing is smaller than what would be calculated using Eq. 4.11.

4.1.2.2.12 Rotated and Fixed Crack Model

The Rotated Crack Model is implemented in CC3DNonLinCementitious2 material, as proposed by Vecchio (1986) and Crisfield (1989). In this model, the principal stress aligns with the principal strain direction. Consequently, there is no shear strain along the crack plane, necessitating definition of only two normal stress components, as depicted in Fig. 4.14.

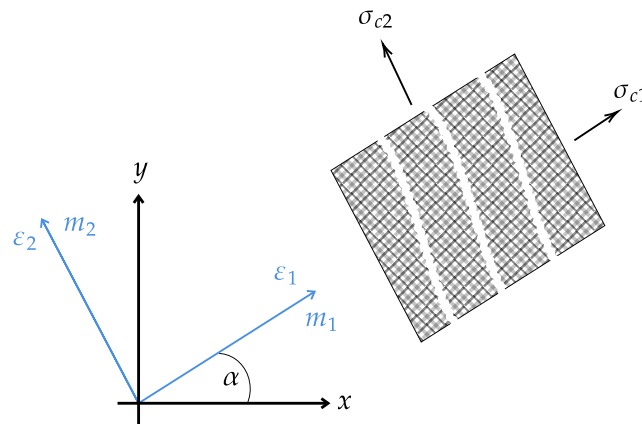


Fig. 4.14—Rotated crack model. Stress and strain state. Adapted of ATENA (2013).

If the principal strain axes rotate during the loading, the direction of the cracks rotate, too. In order to ensure the co-axiality of the principal strain axes with the material axes the tangent shear modulus G_t is calculated according to Crisfield (1989) as:

$$G_t = \frac{\sigma_{c1} - \sigma_{c2}}{2(\varepsilon_1 - \varepsilon_2)} \quad \text{Eq. 4.15}$$

For the Fixed Crack Model in CC3DNonLinCementitious2 material (Darwin & Pecknold, 1974; Červenka, 1985), in which the crack direction is given by the principal stress direction at the moment of the crack initiation. In uncracked concrete, the principal stress and strain directions align due to the assumption of isotropy in the concrete material. However, once cracking occurs, orthotropy is introduced. The weaker material axis, m_1 , is oriented perpendicular to the crack direction, while the stronger axis, m_2 , is aligned parallel to the cracks, as depicted in Fig. 4.15.

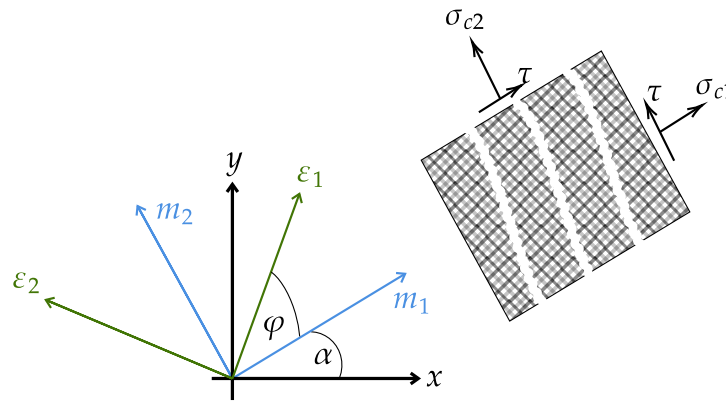


Fig. 4.15—Fixed crack model. Stress and strain state. Adapted of ATENA (2013).

The cementitious material family, like CC3DNonLinCementitious2, provides options for both fixed and rotated crack models. The fixed crack material parameter specifies the maximum residual tensile stress level at which the crack direction becomes fixed. Specifically, a value of 0.0 indicates a fully rotated crack model, while a value of 1.0 represents a fully fixed crack model. Intermediate values between 0.0 and 1.0 control the extent to which the crack direction is locked. For instance, a value of 0.7 means that the crack direction is fixed when it opens enough for the softening curve to reduce to 0.7 times the initial tensile strength (Červenka et al., 2013).

The choice between a fixed and rotated crack model depends on the specific problem at hand. For simpler cases with monotonic loading, such as the approach used in this thesis, the fixed crack model was chosen for its balance of sufficient accuracy and computational efficiency. However, for problems involving complex loading paths, load reversals (hysteresis), or where accurate crack propagation paths are required, the rotated crack model is generally preferred, despite its higher computational cost.

4.1.2.2.13 Yield Criteria

In the context of frictional materials, "yield" refers to the onset of inelastic behaviour, distinct from the metal creep behaviour known as "creep". Yield criteria are mathematical functions that describe closed surfaces in the space of principal stresses or strains. For a material's stress state to be permissible, its coordinates must lie on or within these surfaces; any state outside these

surfaces is considered inadmissible. In the current model, two yield criteria are used to account for the significant differences in the absolute magnitudes of the stress invariants when concrete transitions into the inelastic range under tension and compression. This dual criterion approach is necessary due to the distinct inelastic responses of concrete under different loading conditions. The principal stress space is often utilized in these models to simplify the representation of stress states and yield surfaces, providing a clear visualization of the permissible and inadmissible stress states. In ATENA Concrete model, the Rankine-Fracturing Model for Concrete Crack is used (Červenka et al., 2013). This Rankine criterion is:

$$F_i^f = \sigma'_{ii} - f'_{ti} \leq 0 \quad \text{Eq. 4.16}$$

In this criterion, it is assumed that strains and stresses are transformed into the material directions. For the rotated crack model used, these correspond to the principal directions. In the previous equation, σ'_{ii} identifies the trial stress and f'_{ti} is the tensile strength in the material direction i . The trial stress state is computed by the elastic predictor:

$$\sigma'_{ij} = \sigma'_{ij}{}^{n-1} + E_{ijkl} \Delta \varepsilon'_{kl} \quad \text{Eq. 4.17}$$

If the trial stress does not satisfy Eq. 4.16, the increment of fracturing strain in the direction can be computed using the assumption that the final stress state must satisfy:

$$F_i^f = \sigma'_{ii} - f'_{ti} = \sigma'_{ii} - E_{iikl} \Delta \varepsilon'_{kl} - f'_{ti} = 0 \quad \text{Eq. 4.18}$$

This equation can be further simplified under the assumption that the increment of fracturing strain is normal to the failure surface (Červenka et al., 2013), and that always only one failure surface is being checked. For failure surface k , the fracturing strain increment has the following form:

$$\Delta \varepsilon'_{ij} = \Delta \lambda \frac{\partial F_k^f}{\partial \sigma_{ij}} = \Delta \lambda \delta_{ik} \quad \text{Eq. 4.19}$$

After substitution Eq. 4.19 into Eq. 4.18 a formula for the increment of the fracturing multiplier λ is recovered.

$$\Delta \lambda = \frac{\sigma'_{kk} - f'_{tk}}{E_{kkkk}} = \frac{\sigma'_{kk} - f'_t(w_k^{max})}{E_{kkkk}}, \quad w_k^{max} = L_t (\varepsilon'_{kk} + \Delta \lambda) \quad \text{Eq. 4.20}$$

This equation must be solved by iterations since for softening materials the value of current tensile strength $f'_t(w_k^{max})$ is a function of the crack opening w , and is based on Hordijk's formula (defined in SBETA model). The crack opening w is computed from the total value of fracturing strain ε'_{kk} in direction k , plus the current increment of fracturing strain $\Delta \lambda$, and this sum is multiplied by the characteristic length L_t . The characteristic length as a crack band size was introduced by Bažant & Oh (1983). In this work, the crack band size L_t is calculated as a size of the element projected into the crack direction, as shown in the Fig. 4.16. Červenka et al. (1995) showed that this approach is satisfactory for low order linear elements, which are used throughout this study. They also proposed a modification to account for cracks that do not align with the edges of the elements.

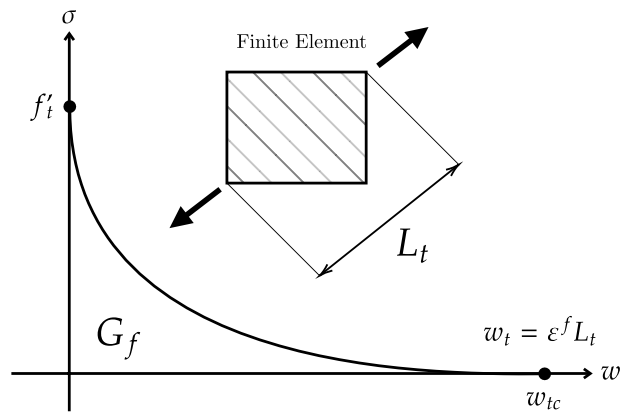


Fig. 4.16—Tensile softening and characteristic

4.1.2.3 Reinforcing Stress-Strain Laws

ATENA models steel reinforcement using the CCReinforcement material model. This reinforcement can be characterised in two primary forms: discrete and smeared (CCSmearedReinforcement). Discrete reinforcement typically takes the form of reinforcing bars represented using truss elements, which is the approach used in this research thesis. Discrete reinforcement assumes a state of uniaxial stress and employs a stress-strain law formulation (Červenka et al., 2013). In this research, the discrete reinforcement model (CCReinforcement) will be implemented using a multi-linear stress-strain law for simplicity and to support the monotonic approach used in the numerical analysis (see Fig. 4.17). This multi-linear law applies to both tension and compression³.

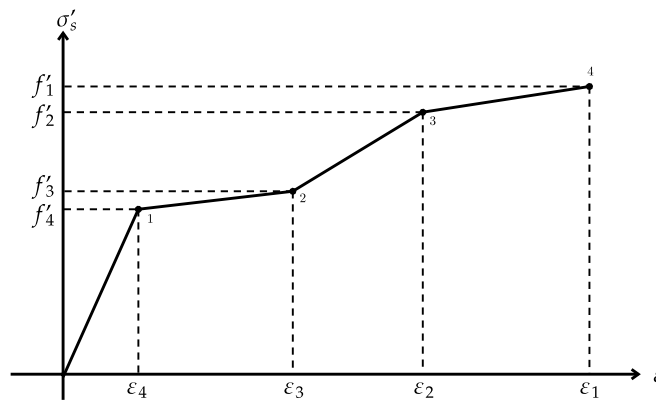


Fig. 4.17—The multi-linear stress-strain law for reinforcing

Within ATENA, there exists a material model designed to characterize the cyclic response of reinforcing steel, drawing from the work of Menegotto & Pinto. However, for the purposes of this study and given that we are focusing on simulating the overall response to progressively increasing monotonic lateral displacement imposition, the cyclic behaviour of the reinforcing steel will be disregarded.

³ Typically, all reinforcement material models in ATENA exhibit consistent behaviour under both tension and compression. However, the CCReinforcement model offers the option to disable the compressive response of the reinforcement material. This feature is beneficial for simulating reinforcement elements with very low bending stiffness, where compressive loading may cause buckling, making the compressive strength insignificant.

4.1.2.4 Interface Material Model

The interface material model (see section 4.1.1.4) is applicable for simulating contact between two materials, such as a construction joint between two concrete segments or the interface between a foundation and a concrete structure. This model adopts the Mohr-Coulomb criterion with tension cut off. The constitutive relation for a general three-dimensional scenario is described in terms of tractions on interface planes and relative sliding and opening displacements (Červenka et al., 2013).

$$\begin{Bmatrix} \tau_1 \\ \tau_2 \\ \sigma \end{Bmatrix} = \begin{bmatrix} K_{tt} & 0 & 0 \\ 0 & K_{tt} & 0 \\ 0 & 0 & K_{tt} \end{bmatrix} \begin{Bmatrix} \Delta v_1 \\ \Delta v_2 \\ \Delta u \end{Bmatrix} \quad \text{Eq. 4.21}$$

The initial failure surface aligns with the Mohr-Coulomb condition (Eq. 4.22), incorporating an ellipsoid in the tension regime. Once stresses break this condition, the surface transforms into a residual surface indicative of dry friction (see Fig. 4.18).

$$|\tau| \leq c - \sigma \cdot \phi, \quad \sigma \leq 0$$

$$\tau = \tau_0 \sqrt{1 - \frac{(\sigma - \sigma_c)^2}{(f - \sigma_c)^2}}, \quad \tau_0 = \frac{c}{\sqrt{1 - \frac{\sigma_c^2}{(f - \sigma_c)^2}}}, \quad \sigma = \frac{f_t^2 \phi}{c - 2f_t \phi}, \quad 0 < \sigma \leq f_t \quad \text{Eq. 4.22}$$

$$\tau = 0, \quad \sigma \geq f_t$$

In tension, the failure criterion is substituted with an ellipsoid. This ellipsoid intersects the normal stress axis at the value of f_t , forming a vertical tangent, while intersecting the shear axis at the value of c (e.g., cohesion) with a tangent equivalent to ϕ . The parameters for the interface model cannot be arbitrarily defined; there exists a certain dependence among some parameters.

When specifying the interface parameters, the following guidelines should be kept to:

$$0 < f_t \leq \frac{c}{\phi}, \quad f_t < c, \quad c, f_t, \phi > 0 \quad \text{Eq. 4.23}$$

It is recommended that the above parameters are always greater than zero. In cases when no cohesion or no tensile strength is required, some very small values should be prescribed (Červenka et al., 2013).

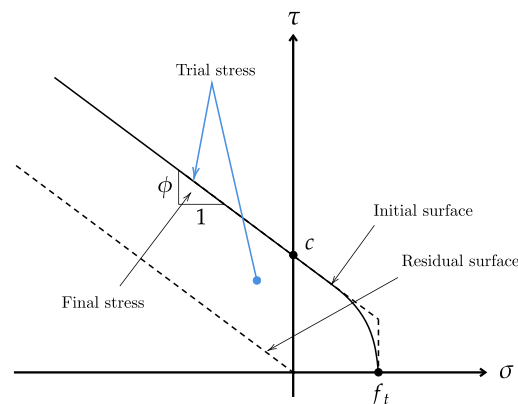


Fig. 4.18—Failure surface for interface elements. Taken from ATENA (2013).

The general material formulation parameters are K_{nn} and K_{tt} , which are the initial elastic normal and shear stiffness respectively of the interface element. To estimate the values of those parameters, ATENA recommends use $K_{nn} = E/t$ and $K_{tt} = G/t$, in which E and G are the minimal elastic modulus and shear modulus respectively of the surrounding material, and t is the width of the interface zone.

There are two additional stiffness values that need to be specified in the ATENA input, denoted as K_{nn}^{min} and K_{tt}^{min} . These values are used merely for numerical purposes after the element failure, in order to preserve the positive definiteness of the global system of equations. Theoretically, after the interface failure, the interface stiffness should be zero, which would mean that the global stiffness would become indefinite. These minimal K_{nn}^{min} and K_{tt}^{min} stiffnesses should be approximately 1/1000 times the initial ones.

4.1.3 Full Newton-Raphson Method for the Numerical Solution

ATENA solves the nonlinear structural behaviour through finite element method and its incremental loading criteria (Červenka et al., 2013). Different methods are available in ATENA for solving nonlinear equations, but the Full Newton-Raphson Method will be used for purposes of this research, this due to its reliability to solve a wide range of finite element problems.

One approach to nonlinear solutions involves dividing the load into a series of load increments. These increments can be applied either over multiple load steps or within each load step through several sub steps. After each incremental solution, ATENA adjusts the stiffness matrix to account for the nonlinear changes in structural stiffness before moving on to the next load increment. The ATENA program addresses this challenge by employing the Full Newton-Raphson Method, which ensures solution convergence to equilibrium (within a specified tolerance limit) at the conclusion of each load increment (Pizzocchero, 2014).

4.2 Modelling

The specimen's model was created by applying a symmetry plane parallel to the east-west direction (refer to Fig. 4.20). This is done to decrease the computational workload and taking advantage of the geometric symmetry of the column specimen and the loading system. The approach for the FE analysis is monotonic, using incremental displacement imposition.

The workflow for the creation and analysis of the model is the follow:

1. Material parameters;
2. Topology: definition of the geometrical model (macroelements);
3. Contacts definition;
4. Meshing;
5. Boundary conditions and supports;
6. Load steps;
7. Monitoring points;
8. Solution parameters;
9. Run;
10. Pre-processed (analysis of results).

4.2.1 Material Parameters

The materials in ATENA were modelled using the properties measured in material tests. The unknown mechanical properties were established in first instance using the theoretical approach given by ATENA and research papers. The material parameters presented below are the calibrated ones. The calibration of the material parameters involved a realistic variance of the materials used.

4.2.1.1 Concrete

For the concrete, the 3DNonlinearCementitious2 was used (see section 4.1.2.2). The Table 4.1 was considered for the properties of the concrete. The material properties calibrated for the model of the concrete are listed in Table 4.2. For all concrete elements, Poisson's ratio ν was constant and equals to 0.2.

Table 4.2—Properties defined for concrete macroelements

Specimen part	Basic				Tensile		Compressive			Shear		
	f'_{cc}	f'_{cu}	f_t	E_c	G_f	c_{ts}	w_d	ε_{cp}	$r_{c,lim}$	S_F	FSE	FCC
	MPa	MPa	MPa	MPa	MN/m	-	mm	-	-	-	-	-
Column CO	-20.45	24.06	1.49	20,153.1	0.00003720	0.10	-0.5	-0.000325	0.7	1	0.52	1
Column CO*	-18.79	22.11	1.16	17,775.3	0.00002908	0.10	-0.5	-0.000325	0.7	1	0.52	1
Column S8-S9	-20.18	23.75	1.00	13,662.8	0.0000250	0.10	-0.5	-0.000325	0.7	1	0.52	1
Foundation CO	-34.10	40.10	3.35	28,100	0.00007029	-	-0.5	-0.001001	0.8	20	0.52	1
Foundation CO*	-35.55	41.83	3.43	31,826	0.00007029	-	-0.5	-0.001001	0.8	20	0.52	1
Foundation S8-S9	-27.79	32.69	2.69	16,313.8	0.00006725	-	-0.5	-0.001001	0.8	20	0.52	1

In the Table 4.2, the material properties to perform the numerical analysis was defined as follow:

- f'_{cc} is the equivalent cubic concrete strength, equal to the cylinder concrete strength f'_c measured in laboratory test, multiplied by 0.85, this is $f'_{cc} = 0.85f'_c$. This is due to the conversion of the concrete cylinder strength f'_c (performed for this research) and the concrete cubic strength test f'_{cc} (which are used in ATENA);
- The f'_{cu} value is the average value of the f'_c recorded in the concrete cylinder tests of each specimen's concrete;
- For the f_t and E_c , the values were taken from the test data (see 3.2.5.2).
- For the fracture energy G_f , the value was calculated using the formula shown in the Table 4.1 and using f_t as f_t^{ref} . Despite the conservative of using f_t as f_t^{ref} , this approach does not lack of accuracy, as demonstrated in numerical results;
- The recommended value of the tension stiffening factor c_{ts} is 0.4 (Červenka et al., 2013). However, this parameter was calibrated and equal to 0.1. The reason for this value is the lack of confinement in the main transverse section of the column, resulting from the large spacing of stirrups;
- The softening compression parameter w_d was defined as -0.5 mm, as recommends Červenka et al. (2013). This parameter also was explored by Khedmatgozar Dolati (2023) in FEA calibrations comparing experimental data,

where he concluded that increasing this parameter rises the peak strength of each cycle after peak strength and postpones lateral and axial degradation;

- The ε_{cp} parameter is the plastic strain at compressive peak strength, which was taken from concrete cylinder tests.
- The $r_{c,lim}$ parameter is the reduction of compressive strength due to cracking. This parameter was established automatically by ATENA derived from the other parameters;
- The S_f parameter is the crack shear stiffness factor; it represents the stiffness of the concrete in the direction parallel to the crack plane after the crack has formed. It controls the shear stress that can be transferred through a cracked element. The value used for the FEM was defined according to the ATENA Theory (2023). However, for the column macroelement, this value was calibrated and defined as 1.0;
- The FSE parameter is the Failure Surface Eccentricity, defined automatically by ATENA;
- The FCC parameter, which is the Fixed Crack Model Coefficient, is recommended to be set to 1.0 by ATENA. A value of 1.0 indicates a fully fixed crack model, which is suitable for the monotonic approach implemented in the FEM (see 4.1.2.2.12).

Some material parameters are not listed in Table 4.2 because they remained constant in all specimens, these parameters were:

- The volumetric parameter β , this is a key cyclic parameter in the concrete model that significantly influences the behaviour, which represents the direction of plastic flow. This parameter determines the return direction. If $\beta < 0$ the material is being compacted during crushing, if $\beta = 0$ the material volume is preserved, and if $\beta > 0$ the material is dilating (Červenka et al., 2013). In general, the plastic model is non-associated, since the plastic flow is not perpendicular to the failure surface. Experimental tests used in the research of Khedmatgozar Dolati (2023) shows that concrete expands as it incurs more damage (this is also supported by the damage recorded in the CO and CO* experimental test). It has been observed that increasing β decreases the peak strength of cycles after the peak lateral strength is reached. Additionally, increasing the β factor results in a softer reloading slope beyond the capping point and causes axial degradation at a smaller drift ratio. However, although the β factor affects cyclic behaviour, this thesis does not focus on exploring the cyclic behaviour of the mathematical models;
- The crack spacing s_{max} is defined as 1.5 mm by default for ATENA, so this value is used and was not be explored for this research.

4.2.1.2 Steel Plates

For the steel plates in the model (USP, PSP and ALP) (see Table 4.4), the 3DElasticIsotropic material was used. For the analysis, the weight of the steel plates was not taken in consideration. For this material only two parameters were considered:

- Elastic modulus (using a linear stress-strain law) $E = 210,000$ MPa;
- Poisson's ratio $\nu = 0.30$.

4.2.1.3 Reinforcing Steel

The material used for the reinforcing steel is based in the multilinear law (see 4.1.2.3). The table below shows the points of the multilinear stress-strain law for the #8 and #3 reinforcing bars (refer to Fig. 4.17). The reinforcing used had the real transverse area of the bar diameter in the experiments.

Table 4.3—Definition points for the multilinear stress-strain law for reinforcing in the model

Bar diameter mm [in.]	f_1 MPa	f_2 MPa	f_3 MPa	f_4 MPa	ε_1 mm/mm	ε_2 mm/mm	ε_3 mm/mm	ε_4 mm/mm
9.525 [3/8]	-	510	440	440	-	0.0220	0.0139	0.0023
25.4 [1]	-	590	453	453	-	0.0220	0.0100	0.0023

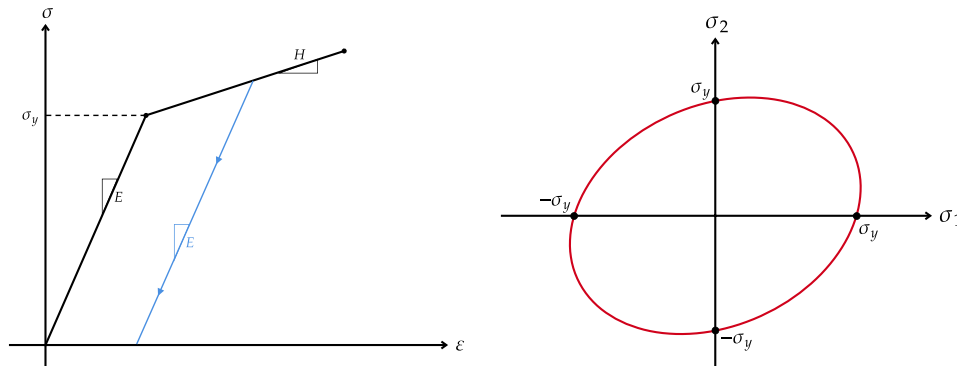
4.2.1.4 Post-tensioned Bars

The material parameter for the post-tensioned bars (anchors) is the simplest, being the elastic modulus the only variable to be defined. For this case, the elastic modulus used was defined as $E = 210,000$ MPa.

4.2.1.5 Steel Angles and Battens

The material for the steel jacketing was the 3D Bilinear Steel Von Mises. This material has the following material parameters:

- Elastic modulus, using a bilinear stress-strain law with hardening, $E = 210,000$ MPa;
- Poisson's ratio $\nu = 0.30$;
- Yielding stress, defined in material test, $\sigma_y = 310$ MPa;
- Hardening modulus $H = 0.0$ MPa (i.e., perfectly elasto-plastic).

**Fig. 4.19—Stress-strain and biaxial failure law**

4.2.1.6 3D Slab-Foundation Interface

The interface between the reaction slab and the foundation is defined as Interface Material Model. The parameters given for this material were calibrated according to the theoretical approach given in ATENA (2013) and were defined as follow:

- Normal stiffness $K_{nn} = 14,050$ MN/m³;
- Tangent stiffness $K_{tt} = 106.43$ MN/m³;
- Minimum normal stiffness $K_{nn}^{min} = 140.5$ MN/m³;
- Minimum tangent stiffness $K_{tt}^{min} = 0.106$ MN/m³;
- Tensile strength $f_t = 0.00001$ MPa;
- Cohesion $C = 0.0001$ MPa;
- Friction coefficient $\phi = 0.6$.

4.2.1.7 3D Steel-Concrete Interface for Steel Jacketing

The interface between the steel of the jacket and the concrete of the column is defined as Interface Material Model. The parameters given for this material were calibrated and defined as follow:

- Normal stiffness $K_{nn} = 1,373,000 \text{ MN/m}^3$;
- Tangent stiffness $K_{tt} = 792,100 \text{ MN/m}^3$;
- Minimum normal stiffness $K_{nn}^{min} = 13,730 \text{ MN/m}^3$;
- Minimum tangent stiffness $K_{tt}^{min} = 7,921 \text{ MN/m}^3$;
- Tensile strength $f_t = 0.1 \text{ MPa}$;
- Cohesion $C = 1 \text{ MPa}$;
- Friction coefficient $\phi = 0.1$.

For the normal and tangent stiffness in the 3D Steel-Concrete Interface and the 3D Slab-Foundation Interface, the proposed values were established based on the formulation defined in ATENA where the elastic modulus of the surfaces in contact played an important role along with the Poisson's coefficient.

4.2.2 Topology

The models of the specimens are formed of the macroelements shown in the Table 4.4. The specimens were modelled using a symmetry plane shown in Fig. 4.20. There are some results obtained in the numerical study that needs to be multiplied by 2; this is the case of the reactions at the base of the foundation.

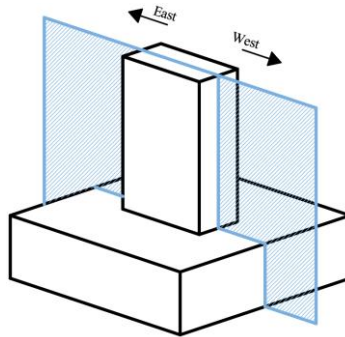


Fig. 4.20—Symmetry plane used in the FE model

Table 4.4—Macroelements for the specimens

Specimen part	ID	Number of elements	Material type	Type of FE
Column	CO	1	CC3DNonLinCementitious2	CCIsoBrick
Foundation	FO	2	CC3DNonLinCementitious2	CCIsoBrick and CCIsoTetra
Reaction Slab	RS	1	CC3DNonLinCementitious2	CCIsoBrick
Upper Steel Plates	USP	2	CC3DElastIsotropic	CCIsoTetra
Post-tensioned Steel Plates	PSP	6	CC3DElastIsotropic	CCIsoTetra
Application Load Plate	ALP	1	CC3DElastIsotropic	CCIsoTetra
#3 bars	R3	73	CCReinforcement	CCIsoTruss
#8 bars	R8	15	CCReinforcement	CCIsoTruss
Post-tensioned Bars	PTB	6	CCReinforcement	CCExternalCable
Steel Jacket	SJ	11	CC3DBiLinearStressVonMises	CCIsoTetra

The macroelements were defined using the global coordinate system. The global X, Y and Z axis are parallel to the north-south, east-west and Vertical directions of the experiment, respectively. The geometry of the macroelements were taken by the design drawings, this to avoid the update of each mathematical model for each specimen and due to the negligible variations in real specimen dimensions and design drawings. The purpose of the Upper Steel Plates (USP) is to apply the construction post-tensioned loads as a result of the attachment system for the lateral load application. The Application Load Plate (ALP) is a triangular-form steel 3D element which are used for the application of the lateral displacement imposition (further explanation will be covered in section 4.2.6).

For the reinforcing steel, the representations for the union of the longitudinal and transverse bars were defined using coincident nodes, so the ties share a coincident node to represent the contact with the longitudinal bars. For the post-tensioned bars, the definition of its geometry is by two points. The first point (the passive anchor) is connected to the bottom of the Reaction Slab (RS), and the second point (the active anchor which the post-tensioned force is applied) is connected to the upper part of the Post-tensioned Steel Plates (PSP), these plates will distribute the post-tensioned load to the foundation, as occurs in the experiment.

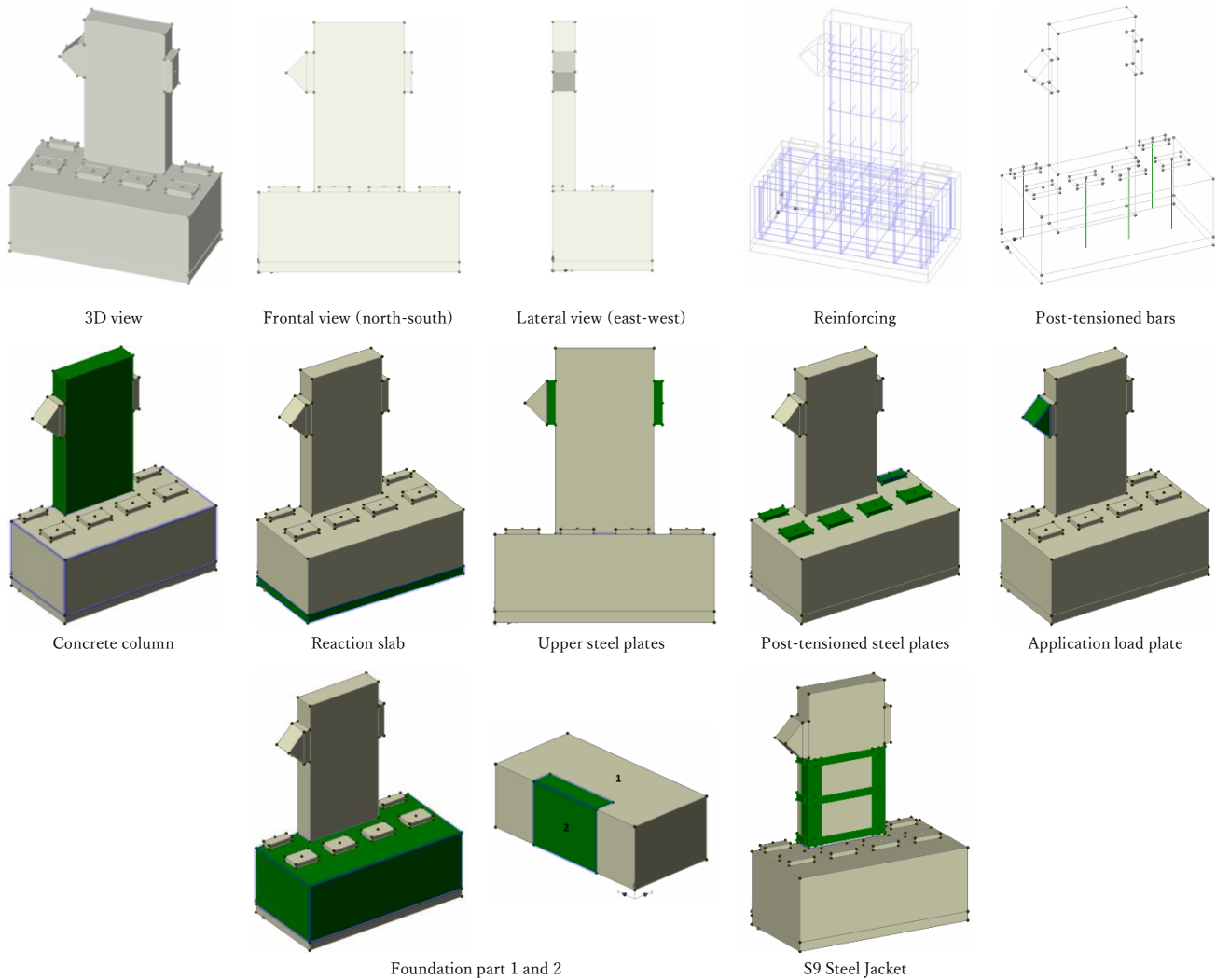


Fig. 4.21—General Macroelements for specimens

4.2.3 Meshing

ATENA generates automatic meshing for each macroelement individually. For the mesh size in reinforced concrete members ranging from 40 to 100 mm are recommended (Červenka et al., 2013). The FE elements used will be linear for time-efficiency purpose. The details of the mesh used in each macroelement is detailed in Table 4.5. For the column, the Brick element was used, this due to the simplicity and Khedmatgozar Dolati's recommendations (2023). However, for the steel plates, tetrahedral elements were necessary. Although linear tetrahedral elements are typically discouraged for stress analysis, they can be applied in this instance for modelling the steel plates. This decision is justified by the relatively lesser importance of accurately modelling stresses and strains in these regions compared to the concrete column itself. For the foundation, the Brick-Tetra element is needed due to the mesh compatibility for the foundation-column joint (see Fig. 4.22). The mesh compatibility of the other elements (USP, RS, and PSP) are not needed due to the lack of importance in these element contacts, this because the stress and strain in the contact areas does not affect the behaviour of concrete column. Furthermore, this mesh incompatibility can be managed using the definition of Perfect Contact between these macroelement surfaces (see section 4.2.4).

Table 4.5—Macroelements mesh information

Specimen part	ID	Maximum mesh size	Number of elements
		mm	
Column	CO	50	3,060
Foundation	FO	100	16,906
Reaction Slab	RS	100	200
Upper Steel Plates	USP	50	1,238
Post-tensioned Steel Plates	PSP	50	263
Application Load Plate	ALP	50	801
Steel Jacket S9	SJ9	30	2,766
			Total = 25,234

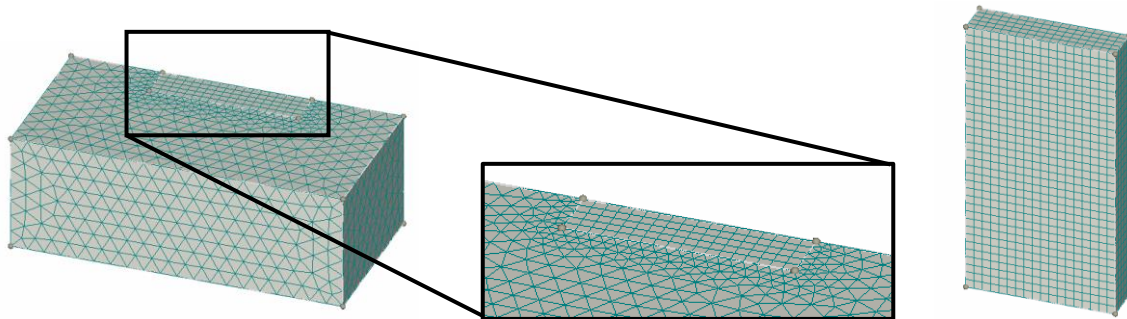


Fig. 4.22—Foundation-Column mesh compatibility

The size of the mesh of the column was defined due the necessity of mesh accuracy in the steel jacket-column interaction. A smeared mesh for the specimen CO and CO* with a maximum mesh size of 100 mm had good result agreement with the backbone experimental result. However, to have the same mesh size in all models, the fine mesh of max. 100 mm size was used. This helps with the compatibility of the entire model. For more information about the mesh role in the FE modelling, refer to Kitizig & Haussler-Combe (2011) and Červenka et al. (1995).

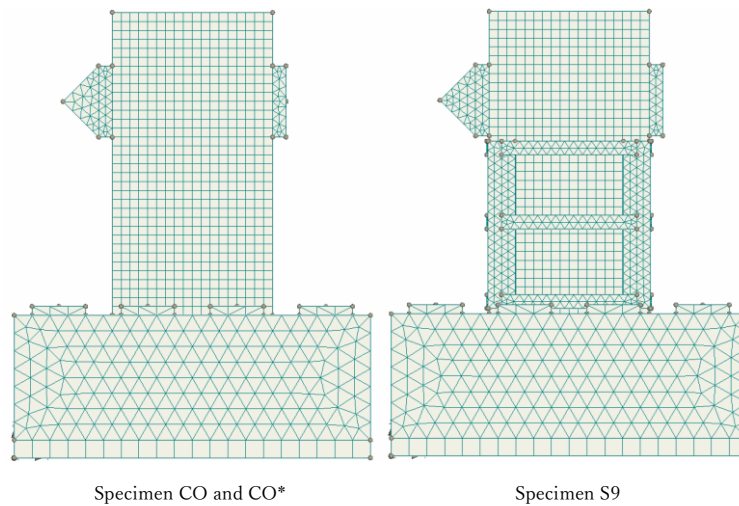


Fig. 4.23—Final mesh of specimens

4.2.4 Contacts Definition

A contact is created when two or more macroelements coincide geometrically. The automatic formulation of this contact is the type of a perfect contact. When dealing with contacts, it is feasible to ensure compatible meshes on both sides of the contact. Generally, ATENA supports contacts with incompatible meshes, but caution should be exercised when it is crucial to accurately model stresses and strain in the contact area.

In the present analysis, the contact regions between the concrete beam and steel plates are not expected to significantly affect the model's behaviour. Hence, enforcing full mesh compatibility on these contacts is unnecessary. This assumption allows for meshing the column with brick elements and the plates with tetrahedral elements, simplifying the model definition. However, it is important to acknowledge that this approach may result in some incompatibilities in the displacement field at these contacts. Nonetheless, given that in reality the connection between the steel plates and concrete would not be perfect either, these discrepancies are not considered a major issue in this case.

The perfect connection (PCo) definition between two or more surfaces is called a complex boundary condition known as master-slave boundary conditions, which falls under the category of Dirichlet conditions (Červenka et al., 2013). In this scenario, the conditions dictate that all degrees of freedom at a designated finite node, referred to as the slave node, mirror those of another node, termed the master node. When multiple master nodes are designated, they collectively constitute a finite element, with the degrees of freedom at the slave node approximated by the nodal degrees of freedom of the element, akin to how displacements are approximated within a finite element.

The contacts that have a 3D interface are shown in green (except for PSP, which is perfect connection) in the Fig. 4.24. For mesh compatibility and contact details refer to Table 4.6.

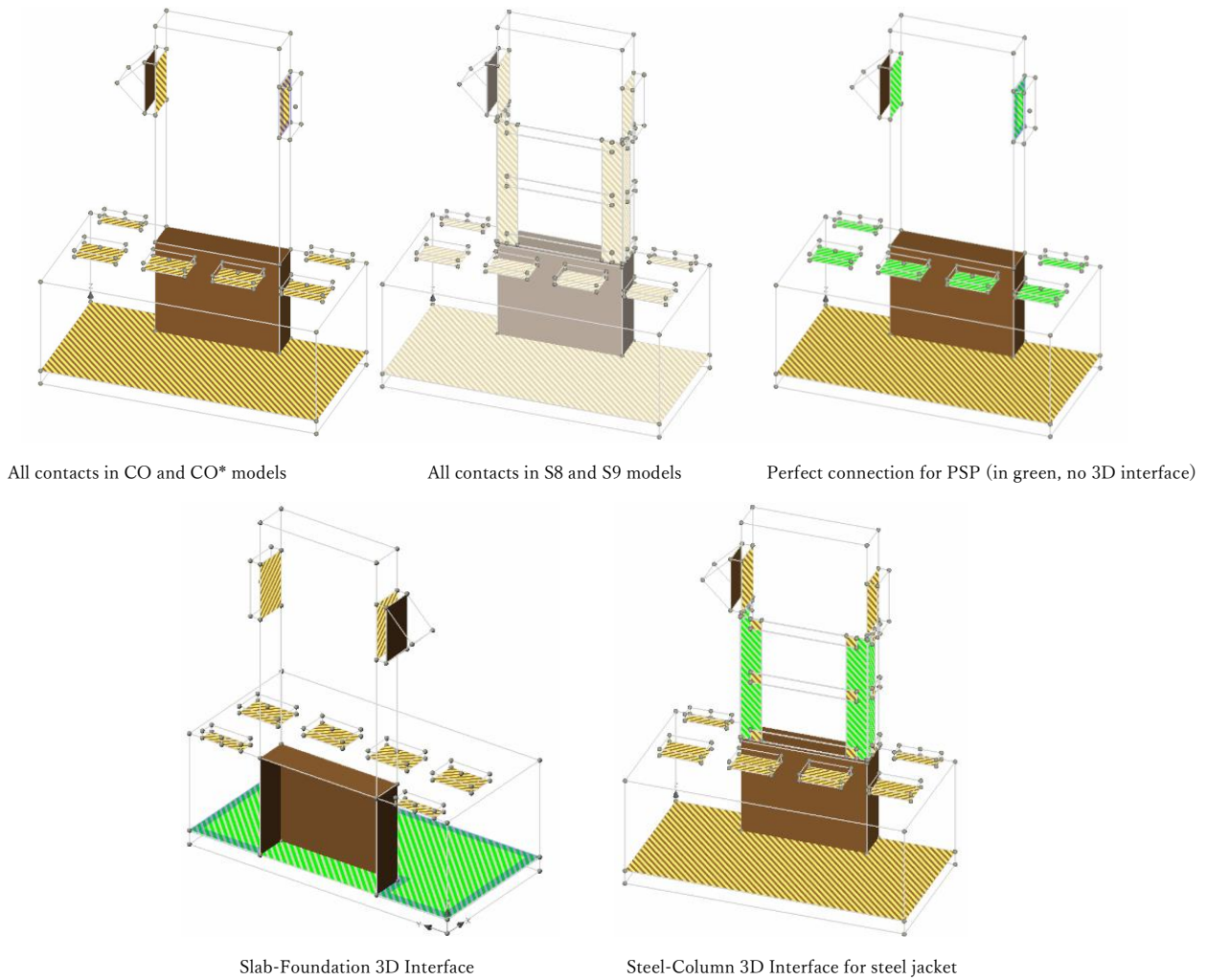


Fig. 4.24—Contacts in the model

Table 4.6—Model contact definition

Specimen part (Macroelement)	ID	Elements with Perfect Connection contact	Elements with 3D Interface contact	Mesh perfect compatibility
Column	CO	FO, USP	-	FO
Foundation	FO	CO, PSP	RS	RS
Reaction Slab	RS	-	FO	FO
Upper Steel Plates	USP	CO, ALP	-	ALP
Post-tensioned Steel Plates	PSP	FO	-	-
Application Load Plate	ALP	USP	-	USP
Steel Jacket S8	SJ8	-	CO	-
Steel Jacket S9	SJ9	-	CO	-

4.2.5 Boundary Conditions and Supports

The main boundary conditions of the model were derived from the symmetry plane. All the macroelement faces with direct contact with this plane have a displacement restraint normal to the symmetry plane. Since only a symmetric half of the specimen are analysed, it is necessary to enforce the axis of symmetry along the middle half of the specimen. This means that the global X displacements along this side should be equal to zero for all macroelement faces in contact with the symmetric plane, this include of course the FO, RS, CO, SJ8, SJ9, USP, ALP and PSP macroelement faces in contact with the plane.

In the Fig. 4.25, the red plane represents the restraint in the global X axis (normal to the plane and parallel to the north-south direction), the green represents the displacement restraints in the global X and Z (vertical) axis, and the blue plane represents the displacement restrain in the Z and Y (parallel to the east-west direction) global axis. All the four faces of the RS macroelement parallel to the Z global axis are restrained in the X and Z direction. The monitoring reactions to calculate the forces taken by the column due to the displacement imposition will be all parallel to the Y global axis (see section 4.2.7).

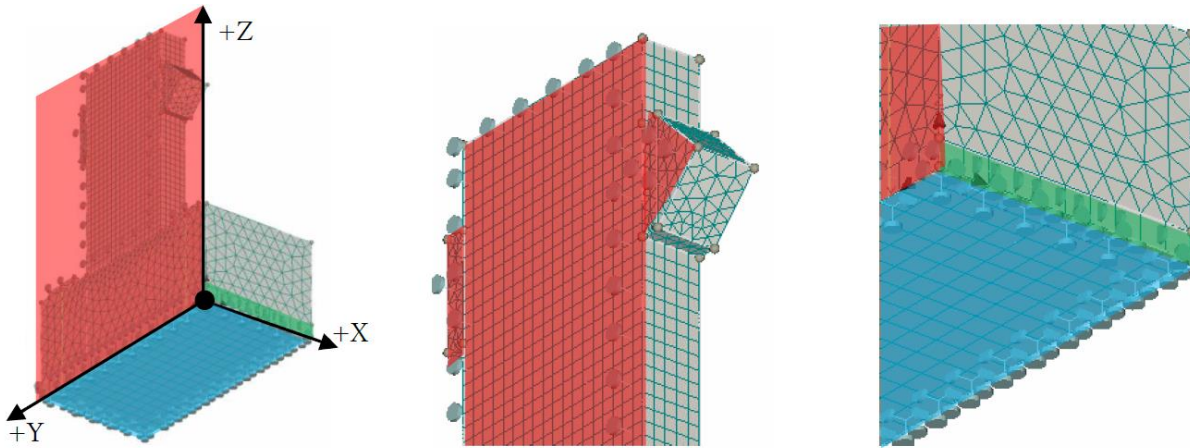


Fig. 4.25—Boundary conditions and supports of the model

4.2.6 Load Steps

The load steps are intricately tied to the experimental construction process; thus, the subsequent loads are applied in a hierarchical manner:

1. Supports (S): boundary conditions due to the symmetric plane and the reaction slab;
2. Body Forces (BF): this considers the load due to the weight of only the concrete foundation and column;
3. Anchor Post-tensioned Load (APL): a load equivalent of 210 kN in each anchor to simulate the post-tensioned derived from the attachment of the foundation in the reaction slab (see Fig. 4.26b);
4. Upper Steel Plates Load (USPL): this distributed load was due to the attachment of the lateral load system (see Fig. 4.26c);
5. Lateral Displacement Imposition (LDI): The displacement imposed by the hydraulic jack goes along the positive Y global axis at the edge of the ALP macroelement. This is implemented to facilitate lateral displacement with potential rotation of the ALP macroelement, effectively serving as the pivot point within the hydraulic jack mechanism. In the Fig. 4.26d, the lateral displacement is applied in the edge of the ALP macroelement.

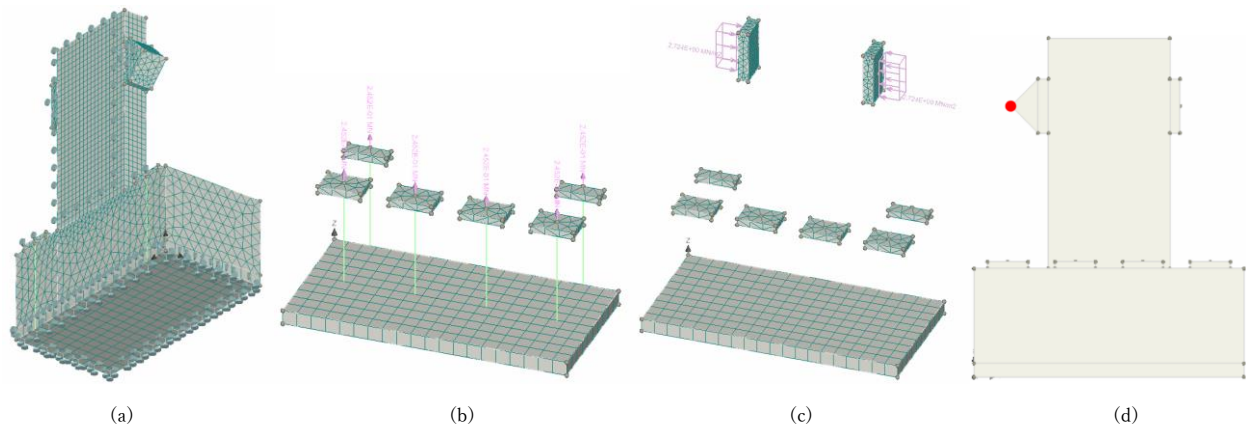


Fig. 4.26—Loads due to constructive process: (a) supports; (b) ALP load; (c) USPL load; (d) LDI load

The run steps are defined as shown in Table 4.7. For the steps in the table, the step 1 (supports) always needs to run at the same time of further steps, that is why always appears in the steps to run. For the step 5 (LDI), the number of steps to run depends on the ultimate displacement to be reached, e.g., if the step 5 is defined as 0.1 mm/step, to reach 90 mm of lateral displacement 900 steps of LDI are needed. The magnitude of step 5 affects the final results, the computational workload and the convergence. It is recommended to run multiple analyses in order to find the optimum magnitude of LDI step that gives good convergence and minimizes workload.

Table 4.7—Load steps to run

Load type	ID	Step	Number of steps	Steps to run
Supports	S	1	1	1
Body Forces	BF	2	1	1, 2
Anchor Post-tensioned Loads	APL	3	1	1, 3
Upper Steel Plates Load	USPL	4	1	1, 4
Lateral Displacement Imposition	LDI	5	300 to 500	1, 5

4.2.7 Monitoring Points

In nonlinear analysis, it is beneficial to track forces, displacements, or stresses within the model. This monitored data offers crucial insights into the structure's condition. For example, by monitoring applied forces or reactions, it becomes possible to ascertain whether the maximum load has been attained or not. In the model, several monitoring points were installed. To determine the force resisted by the specimen due to the lateral displacement imposition, the reactions in the Y global axis needs to be monitored. In Fig. 4.27 all reactions in each node of the RS macroelement for each step of the analysis are monitored (monitoring points named as MRS), thus all the reactions for each point needs to be integrated to determine the total resistant force of the specimen in the *i* step. Also, the integrated reactions for each step need to be multiplied by 2, this due to the symmetry of the model. The lateral displacement is monitored in the same place as in the experimental study. This monitored point (MLD) is recorded the global displacement in the Y axis direction. Another monitoring point record the same lateral displacement at the top of the FO macroelement to compare the lateral displacement in the model and in the experiments (monitoring point MLFD).

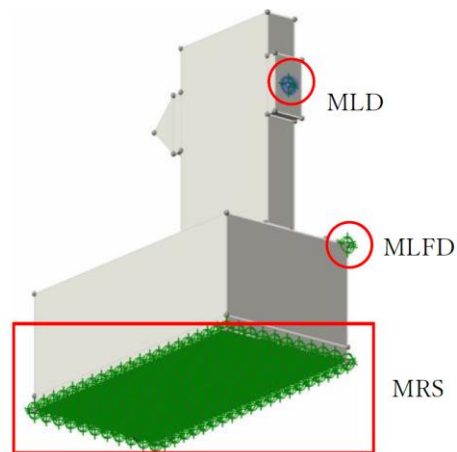


Fig. 4.27—General monitoring points

4.2.8 Solution Parameters

The solution method for all the models was the Newton-Raphson. The stiffness matrix was updated each iteration of the solution, with the stiffness type defined as tangent. The maximum number of iterations for each step was established as 80. The error tolerances were defined as shown in Table 4.8. The values of this table were taken based on ATENA recommendations (Červenka et al., 2013).

Table 4.8—Tolerances and limits defined for the Newton-Raphson solution method

Tolerance type	Value (unitless)
Displacement error	0.010
Residual error	0.010
Absolute residual error	0.010
Energy error	0.00010
Unbalance energy limit	0.80
Limit of line search iterations	2
Line search minimum and maximum limit	0.010, 1.0

4.3 Model Calibration

For model calibration, exhaustive analyses were performed to accurately represent the real response of the tested specimens. This involved exploring boundary conditions, mesh size, load steps, and material parameters.

4.3.1 Boundary Conditions

The boundary conditions were examined to accurately represent the stiffness observed in the experimental test. Initially, the base of the foundation was originally defined as fully restrained along all three global axes (X, Y, and Z) to simplify the model and represent the anticipated fixed restraint resulting from the post-tensioned applied to the foundation in the tests. Fig. 4.28 shows a comparison of the backbone curves from the experimental test and the Finite Element analysis. Comparing the FE lateral response with the backbone experimental curve of specimen CO, it is evident that the FEM with the fixed end is stiffer than the experimental curve. To solve that without modify the boundary conditions, the elastic modulus of the concrete needs to be reduced up to four times, which is an unrealistic solution. A more accurately solution was to change the boundary conditions implementing a 3D interface between the foundation and the reaction slab.

The parameters for the 3D interface material were adjusted alongside the overall concrete parameters. The final 3D interface parameters are detailed in section 4.2.1.6. For the analysis, the steps were the same as defined in Table 4.7. The lateral imposition was defined as 0.04286 mm per each step, with 500 steps for the lateral imposition, leading a total displacement of 21.43 mm. As pointed before, the difference in stiffness between the two types of support conditions is notable, highlighting the importance of accurately modelling them in accordance with experimental tests.

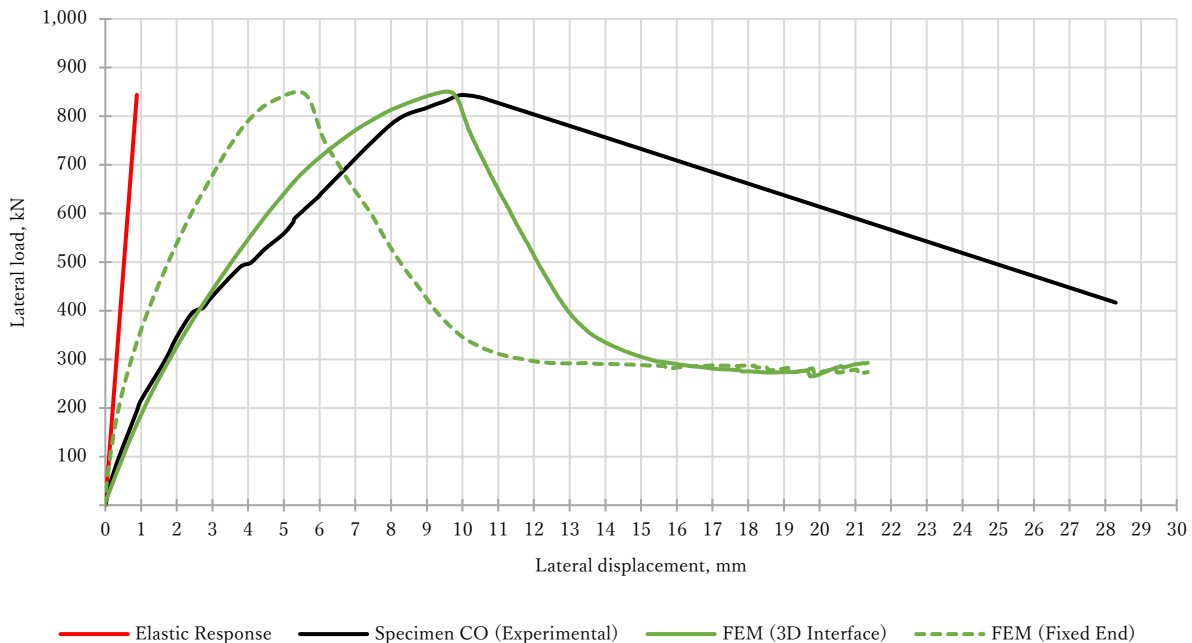


Fig. 4.28—Specimen CO FE results: comparison between fixed end response and 3D interface implementation

The crack failure derived from the FE analysis using the FEM with 3D interface is shown in the Fig. 4.29. It can be seen that the model can represent quite accurately the principal inclined crack that appeared in the experimental test, this shown by the plastic strain. Also, the Von Mises Stresses in the reinforcing steel bars are well represented and the reinforcing steel bars more demanded are in concordance, as recorded by the strain gauges.

It is important to remember that in Fig. 4.29, not all cracks have a physical meaning, this is due to the implementation of distributed crack model in ATENA. In Fig. 4.29 the plastic strain (scale unitless) exposes the strain concentrated in the main diagonal; this means that the FEM is describing the main inclined crack appeared in the experimental test of specimen CO.

For the reinforcing Von Misses stresses⁴ in Fig. 4.29 (scale shown in MPa), the more demanded reinforcement steel is the one near the tension zones (reinforcing bars in red, where yield stress was 440 MPa) in the column macroelement, and the stirrups in the core of the column. The two stirrups more demanded are the ones with large spaced length; this stress demand is related to the appearance of the main inclined crack and the plastic strain concentrated in the main diagonal of the column. Reinforcing steel bars of the foundation did not present high demands of stresses; pre-tensioned bars are highly demanded due to combining forces of pre-tensioned applied at the beginning and the lateral imposition in the model.

The tensors of principal strain⁵ in Fig. 4.29 are concentrated in the same zone as the plastic strain. These tensors describe the deformation of a material and it relates the displacement of points in a material to their original configuration. The tensors of principal stresses show the stress flow in the concrete column core, that is the stress flow derived from the displacement imposed. In the tensor of principal stresses, there are tensor stresses parallel to the main diagonal of the column, and in the upper part of the column due to the application of the post-tension force in the Upper Steel Plates.

The vectors of displacement in Y axes shown in Fig. 4.29 helps to visualize the overall displacement of the deformed body. These vectors shown that the principal lateral displacement in model CO is the upper portion of the columns that cracked diagonally and are being separated from the rest of the column, this leads to conclusion that the principal diagonal crack recorded in experimental test was well represented.

⁴ The Von Mises stresses are a combination of the principal stresses in all directions in an element.

⁵ In the field of continuum mechanics, the tensors of principal strain refer to a mathematical representation that characterizes the deformation of a material in terms of its principal strains.

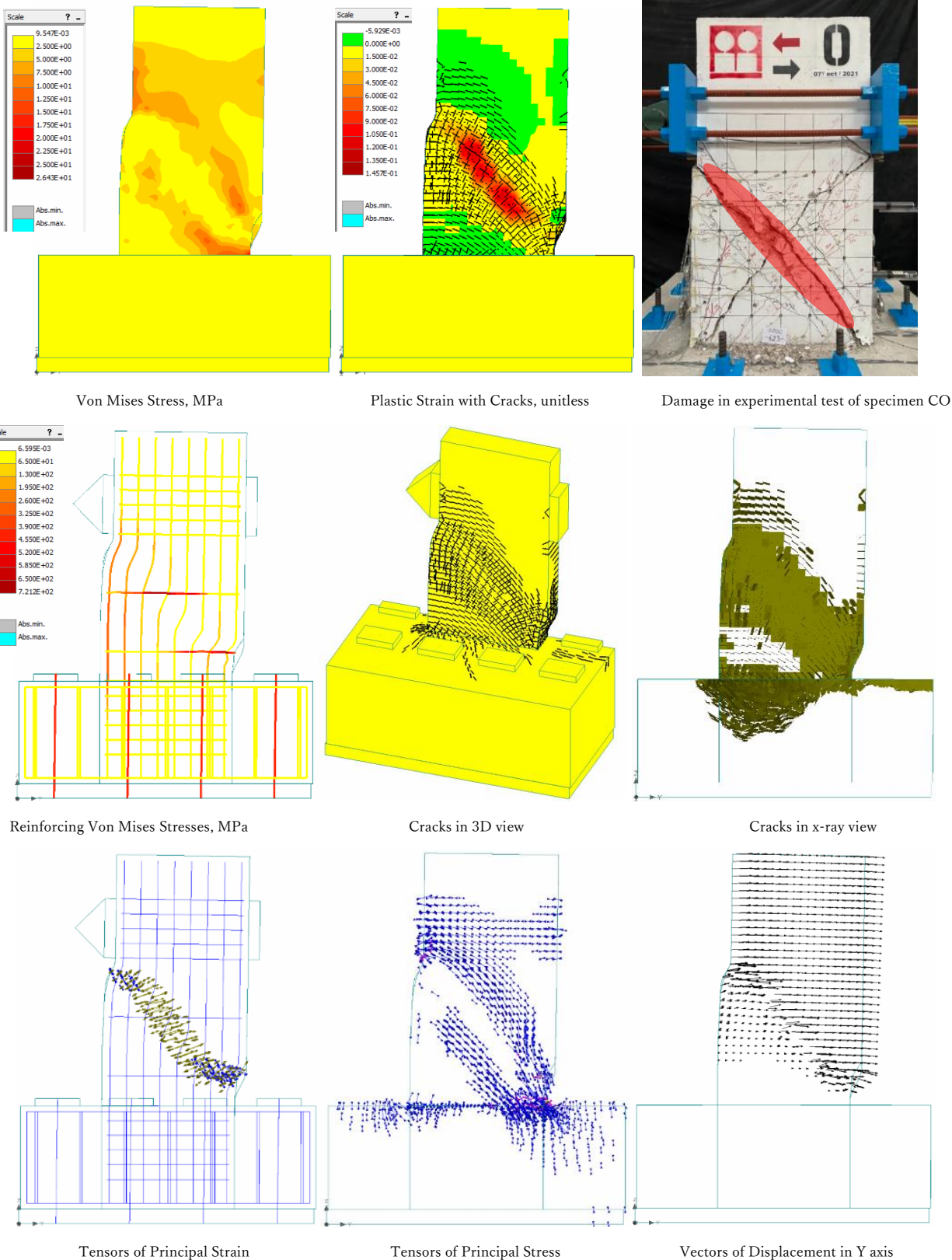


Fig. 4.29—Specimen CO FE response in step 500 with 3D Interface implemented

Fig. 4.30 presents the FE response results for specimen CO*. In this model, the 3D interface between the reaction slab and the foundation uses the same calibrated material parameters as those in specimen model CO. The results indicate a good agreement with lateral stiffness; however, the model failed to accurately depict the detailed real behaviour in the backbone curve from the experimental test. Additionally, there is a difference of 43 kN (6% error) at the maximum peak, and the model does not accurately represent the strength drop-off after the peak. The maximum peak of lateral strength is reached 1.8 mm before the experimental lateral displacement related to the maximum peak of the test (18% error); those differences may be due to the simplifications done to perform the FEA and the monotonic approach instead of cyclic.

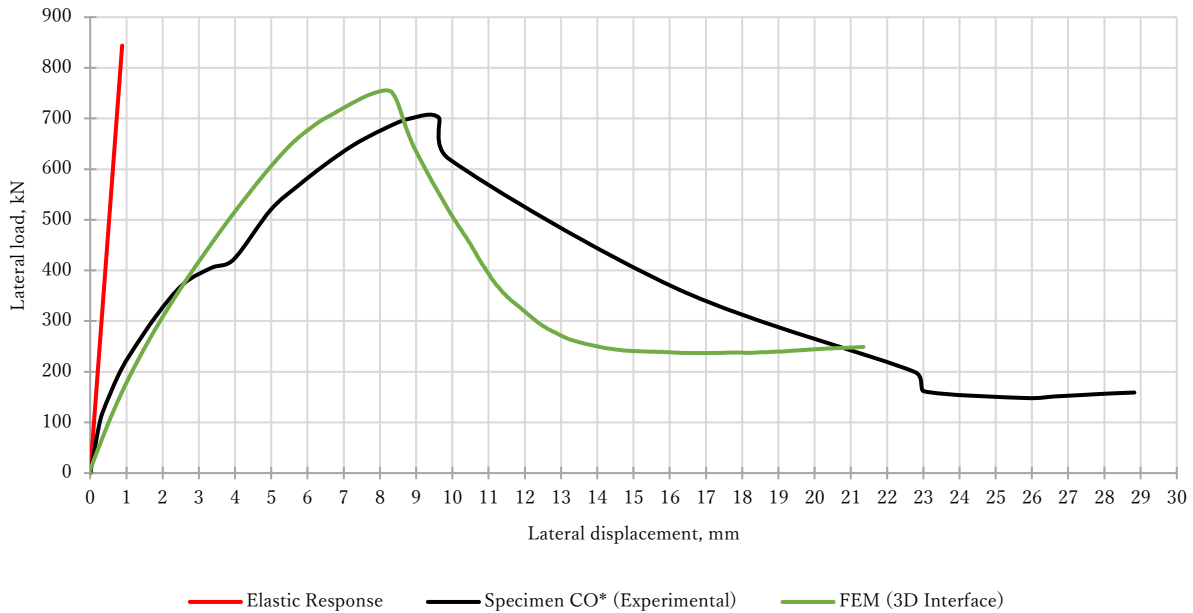


Fig. 4.30—Specimen CO* FE results

In the graphic results presented in Fig. 4.31 for specimen CO*, the Von Mises stress distribution in the main body of the model shows a strong similarity to that of the specimen CO model. However, a significant difference is observed in the primary failure mechanism, which is illustrated by the tensors of principal strain. Specifically, it is evident that the main shear failure, characterized by an inclined crack, is less inclined in the CO* model compared to the specimen CO model. This indicates a variation in the angle of shear failure between the two models. Furthermore, the Von Mises stress distribution in the reinforcing of the CO* model is quite similar to that in the specimen CO model. This suggests that while the overall stress patterns in the reinforcing are consistent between the two models, the primary structural failure behaviour differs, particularly in the inclination of the inclined shear crack, however, this difference did not scarify the accuracy.

The observed discrepancy in the numerical results representing the shear failure along the main inclined crack can be attributed to variations in the material properties between the CO and CO* model specimens. Specifically, the concrete used in the CO* model specimen exhibited increased brittleness compared to the concrete in the CO model specimen. This increased brittleness is characterized by lower values of the compressive strength f'_c and tensile strength f_t in the CO* model specimen. The lower f'_c and f_t values indicate that the concrete in the CO* specimen is less capable of withstanding compressive and tensile stresses, respectively, leading to a different failure behaviour under shear loading conditions, in a numerical manner. Consequently, these differences in material properties are crucial in explaining the variations in the numerical results for the shear failure along the main inclined crack between the two models.

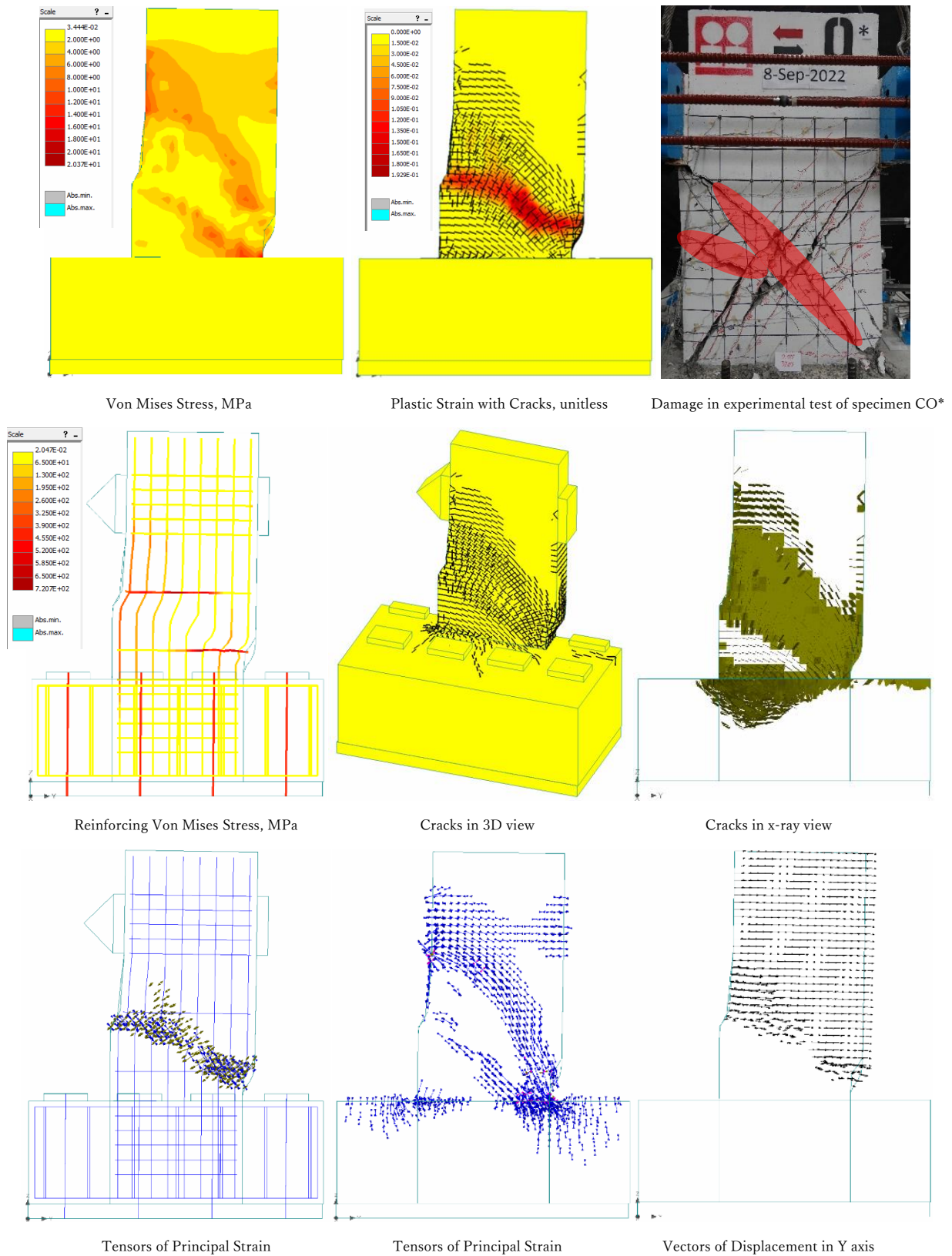


Fig. 4.31—Specimen CO* FE response in step 500 with 3D Interface implemented

Fig. 4.32 presents the results for model S9. Similar to the previous models, the S9 model incorporates a 3D interface surface between the foundation and the reaction slab, using the calibrated parameters of the CO and CO* models. The graph demonstrates good agreement in several key aspects, including lateral stiffness, peak lateral load, and the degradation of lateral strength. The agreement in lateral stiffness indicates that the model accurately captures the initial elastic response of the system to lateral loads. This is crucial for predicting how the specimen will behave under various loading conditions, particularly in the early stages before significant strain occurs. The peak lateral load agreement suggests that the model is effective in simulating the maximum load the structure can withstand before failure.

The accurate representation of lateral strength degradation is also important. This refers to the model's ability to represent how the structure's strength to lateral loads decreases after reaching its peak load. This degradation typically occurs due to material fatigue, crack, and other forms of damage. By capturing this behaviour, the model helps predict the long-term durability and performance of the structure under repeated loading conditions. Overall, the results shown in Fig. 4.32 validate the effectiveness of the S9 model in simulating the complex interactions between the foundation and the reaction slab, providing confidence in its use for structural analysis and design. Also, the simplification done by joining only the steel angles of the SJ to the column (and not the entire SJ including battens, as in the experimental test) shows that a simple model can represent the overall behaviour of the experiment of specimen S9.

The graphic results presented in Fig. 4.34 reveal several key insights into the structural performance of the S9 model. Notably, the reinforcing steel, particularly the longitudinal bars of the column, experiences higher strain demands in this model. This increased demand indicates that the longitudinal reinforcing is playing a critical role in resisting the applied loads. The crack pattern, as mathematically modelled, is observed to be more distributed along the main core of the column. This distribution is consistent with the experimental observations of the S9 specimen test, where cracks spread throughout the core of the column rather than being localized in a main diagonal as observed in CO and CO* specimens. This consistency suggests that the model accurately captures the complex crack behaviour under load, which is crucial for predicting the structure's performance and potential failure modes.

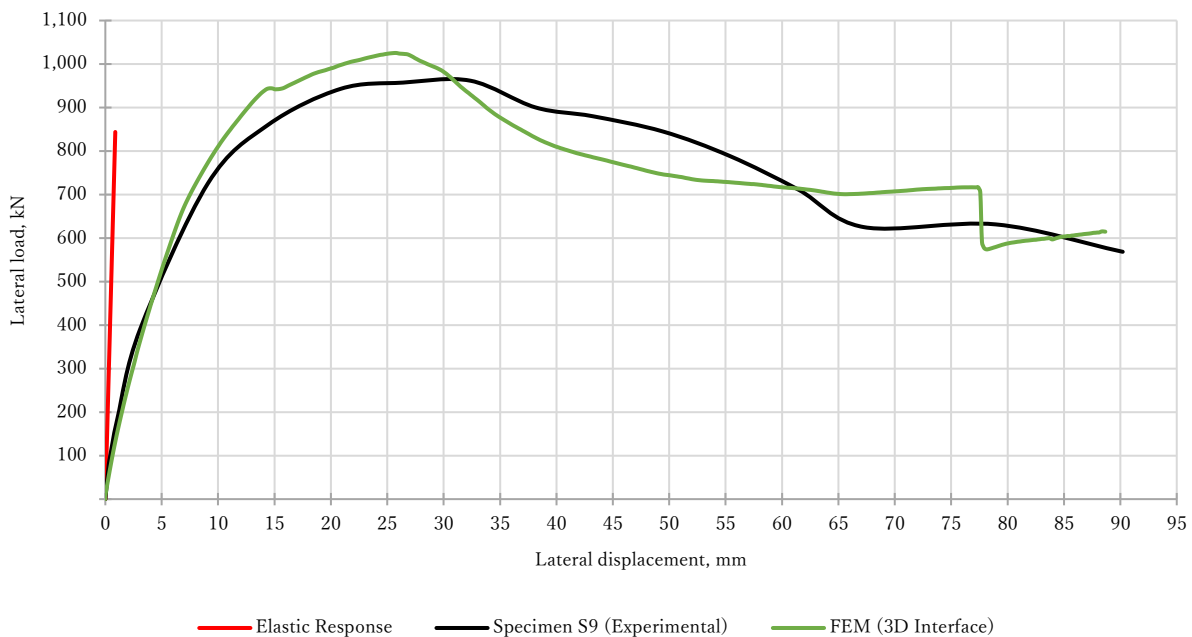


Fig. 4.32—Specimen S9 FE results

Furthermore, the principal plastic strain shows a notable concentration of strain in the centre of the column (see Fig. 4.34). This contrasts with the strain distribution observed in the previous CO and CO* specimen models, where the strain was concentrated in the main diagonal. The agreement between the modelled crack patterns and the experimental results, along with the accurate representation of strain concentrations, demonstrates a good level of accuracy in represent the real behaviour of the structure. This good accuracy validates the effectiveness of the S9 model in simulating the physical phenomena occurring within the column under load. It also underscores the model's reliability in being capable to represent future steel jacketing models and load conditions.

It is important to note the similarity in the overall behaviour of the modelled steel jacketing and the experimental test of specimen S9. Specifically, we can draw a comparison between the bending deformation of the steel battens observed in the FE model and the experimental test results. In the FE model, as shown in Fig. 4.34 (Tensor of Principal stress), the steel battens exhibit significant bending deformation. This computational simulation provides a detailed visualization of the stress distribution (Von Mises stress, where yield stress is 330 MPa) and deformation patterns within the steel jacketing under the lateral displacement imposition. Correspondingly, in the experimental test, similar bending deformation was observed (see Fig. 3.88 to Fig. 3.92 in section 3.5.4.1). This was evidenced by the flaking off of the white wash from the ends of the battens.

The loss of white wash occurred due to the high strain concentrations and subsequent bending at these locations, which mirrored the deformation patterns predicted by the FE model. This comparison highlights the reliability and accuracy of the FE model in predicting the real-world behaviour of the steel jacketing under similar conditions. The consistency between the computational results and experimental observations reinforces the validity of using such models for analysing and predicting structural behaviour in engineering applications.

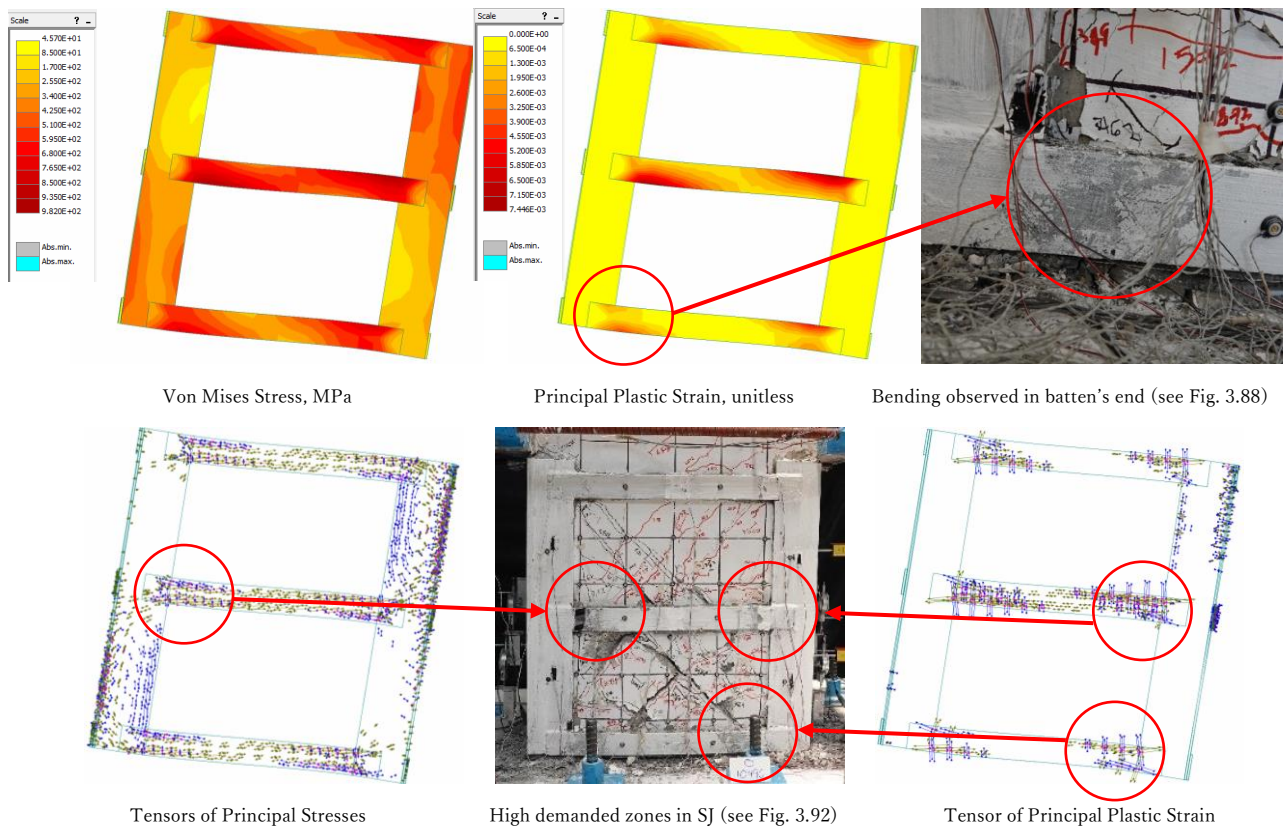


Fig. 4.33—Strain comparison for FEM and experimental test

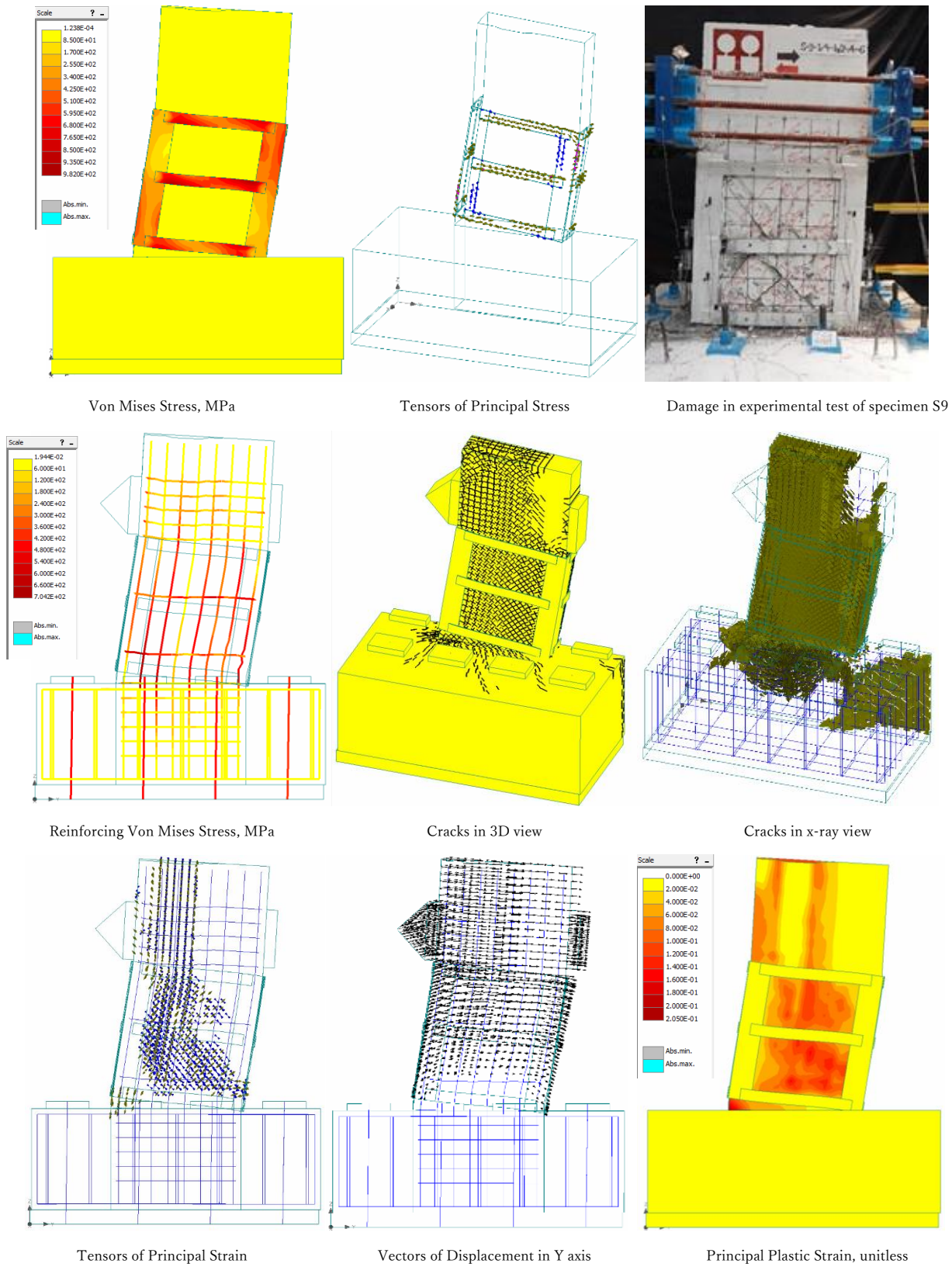


Fig. 4.34—Specimen S9 FE response in step 500 with 3D Interface implemented

The FEA successfully represented the failure of the longitudinal reinforcing steel bars related to the fractures observed in the experimental tests due to low-cycle fatigue, as shown in Fig. 4.35 and Fig. 4.36. Despite the simplifications in the FE model (monotonic approach, linear integration FE elements, etc.), the representation was accurate. However, the buckling of the west face reinforcing steel bar did not occur at a defined load step but progressed between load steps 300 to 500 (see stress state sequence in Fig. 4.37). Similarly, the fracture of the east face reinforcing steel bar, depicted in Fig. 4.36, involved a progressive stress process until failure. This failure was represented by an abrupt change in the Von Mises Stress state, occurring between load steps 450 and 460 (see Fig. 4.37). The sudden change in the Von Mises Stress colour from red to yellow in Fig. 4.37 between load steps 450 and 460 indicates a fracture in the east face reinforcing bar. This sudden loss of stress-bearing capacity caused a drop in the lateral load on the backbone curve of the FEA for specimen S9 (see Fig. 4.32).

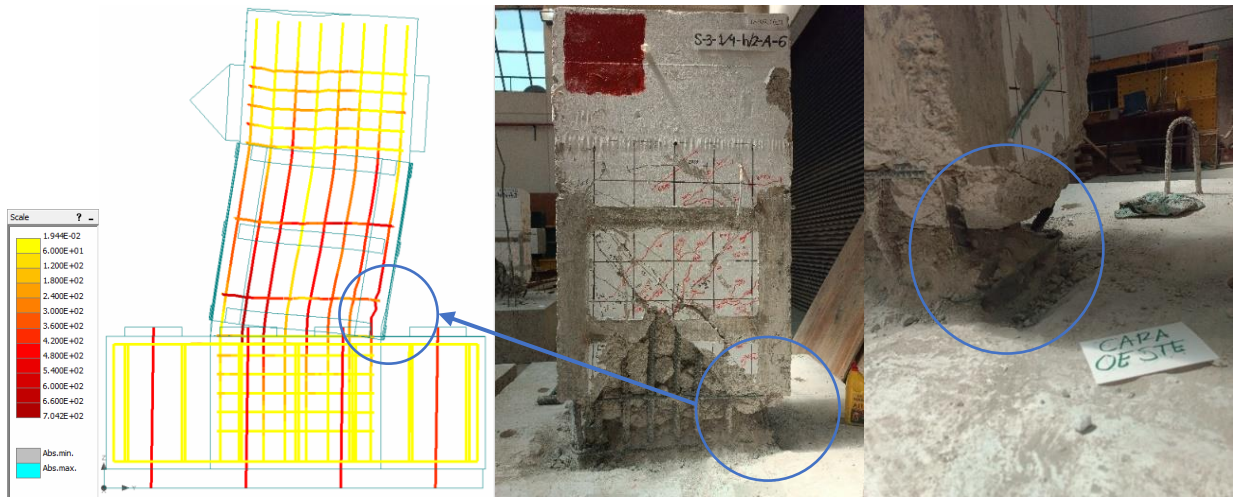


Fig. 4.35—Representation of buckling of west face reinforcing steel bar on load step 500 for specimen S9

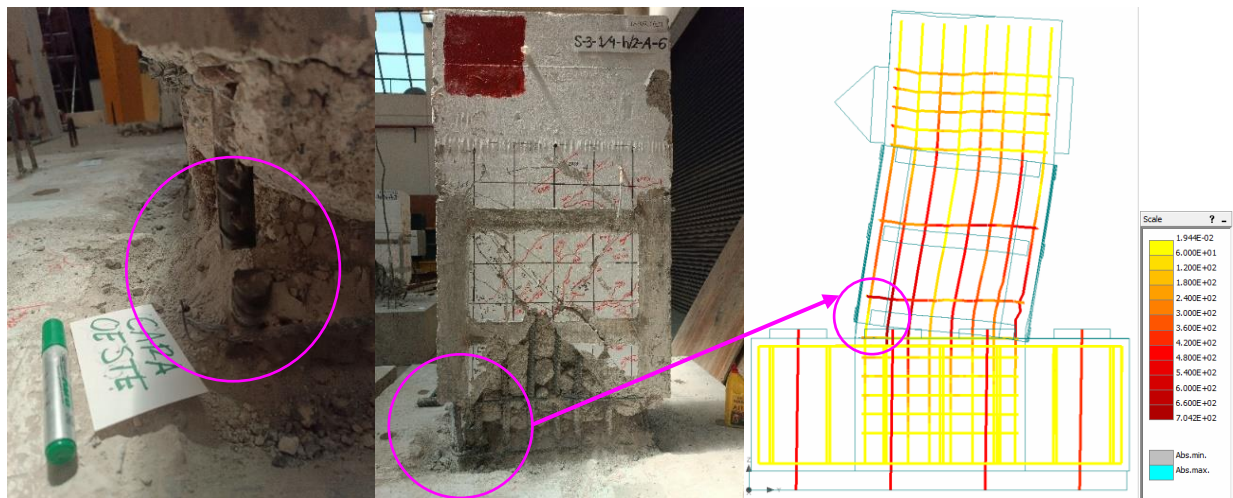


Fig. 4.36—Representation of fracture of west face reinforcing steel bar on load step 500 for specimen S9

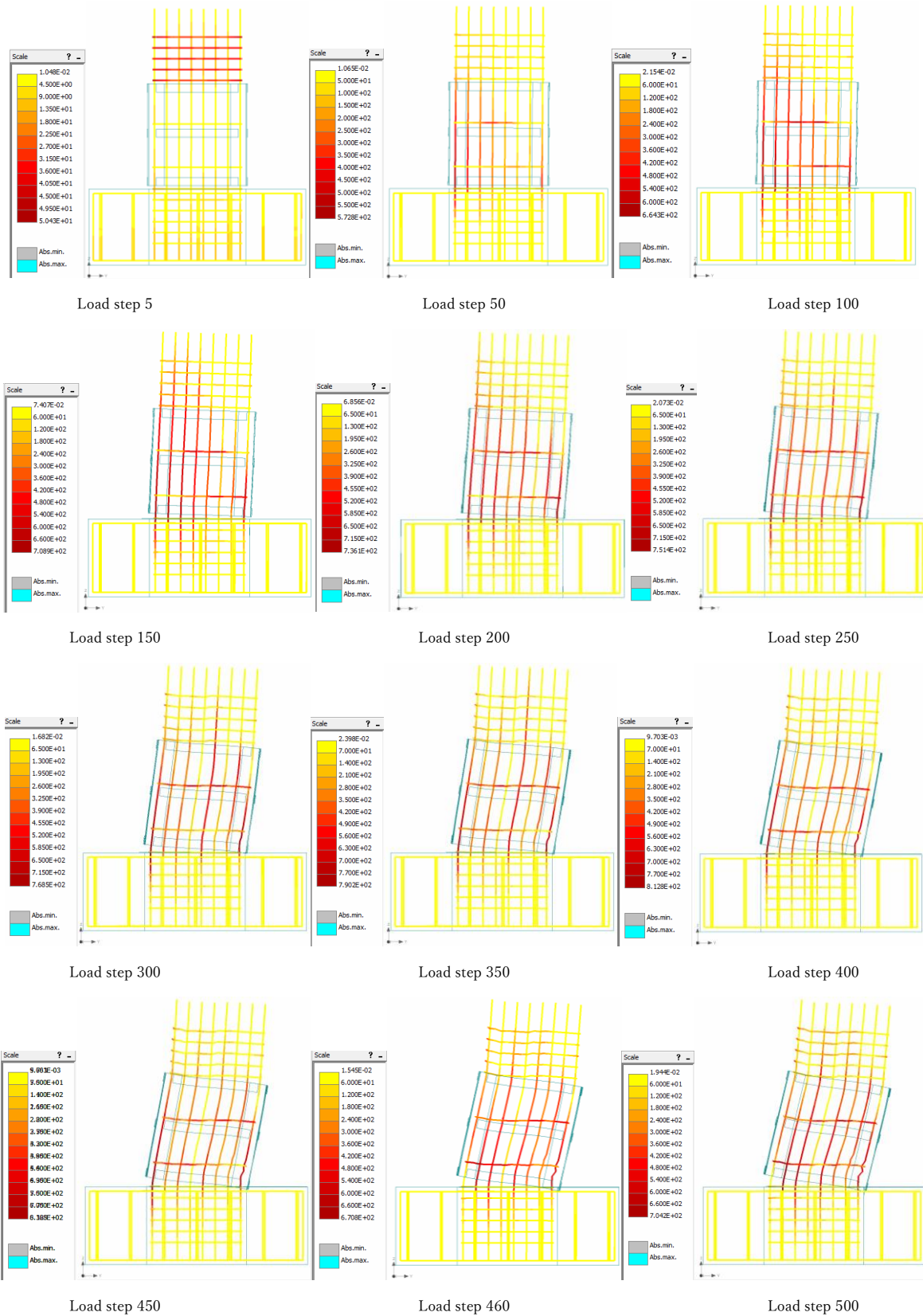


Fig. 4.37—Reinforcing steel Von Mises Stress state sequence for specimen S9

4.3.2 Mesh Analysis

The mesh calibration process was carried out using a big mesh for the benchmark specimen CO. Initially, a mesh size of 100 mm was employed for the column, foundation, and reaction slab macroelements. This choice of mesh size provided results that closely aligned with the expected outcomes, demonstrating that the selected size was adequate for capturing the essential structural behaviour of these components. However, to ensure accurate modelling and compatibility with the mesh of the steel jacket for the specimen model S9, which needed to be of a small mesh size (maximum mesh size of 30 mm), a more refined mesh was necessary in the concrete column, so the final mesh size for the modelled column for all column macroelements of all specimens was 50 mm maximum. The small size of the SJ mesh was due to accurately capture its detailed behaviour and interaction with the concrete column. As a result, it became imperative to adjust the mesh size of the concrete column to achieve consistency and precision in the simulation. The final mesh sizes of all macroelements were shown in Table 4.5. After considering these requirements for compatibility and tolerance error, the mesh size of the concrete column was reduced to 50 mm. This finer mesh size allowed for a more detailed and accurate representation of the column's response, particularly in areas of high stress concentration and complex interactions with the steel jacket and correct representation of the crack patterns shown in experimental test. The final mesh size of 50 mm ensured that the model could effectively simulate the structural behaviour of both the concrete column and the steel jacket, leading to more reliable and robust results.

All the finite elements used in the analyses were established to have only a linear integration. The recommendation for a better representation of the detailed nonlinear behaviour for concrete elements is to higher integration points in each finite element (Khedmatgozar Dolati, 2023), for example, 20 nodes in brick element instead of 8. However, as commented in previous chapters, the use of higher integration points for FEA lead to an increasing of computational workload. To work with the simplifications made in this approach, and to maintain simplicity and flexibility in the models, the FE elements only uses a linear integration points (see section 4.1.1).

4.3.3 Material Parameter Analysis

The material parameter analysis was an extensive exploration for the better fix of the most important parameters, especially those that controls the cracked behaviour of the concrete column. The most important parameters for the concrete were the fracture energy G_f that depends on the tensile strength of the concrete f_t , and the tension stiffening c_{ts} . The tensile strength, linked to the fracture energy, affects the peak strength of the FE model and the lateral displacement related to that peak strength. If the value of the f_t is taken as calculated with the Eq. 3.2 using the data recorded in the concrete cylinder test, the FE results diverge from the experimental values, having more lateral strength and making the model more ductile. It is necessary to reduce the value of the fracture energy to $0.75f_t$. This adjustment is considered appropriate because it accounts for the observed statistical divergence found in many experimental test⁶.

⁶ One of the main issues with modelling the nonlinear behaviour of concrete elements accurately is the determination of material parameters. Among these parameters, fracture energy stands out as particularly critical due to its significant impact on the final results of the model. Fracture energy represents the amount of energy required to propagate a crack through the concrete, and it influences the post-crack behaviour and failure mechanisms of the material. Accurately capturing this parameter is challenging because concrete is a heterogeneous material with complex microstructural characteristics that affect its fracture properties. Variations in the mix design, aggregate size, and distribution, as well as curing conditions, can all influence the fracture energy. Consequently, any inaccuracies in the measurement or estimation of fracture energy can lead to substantial discrepancies between the modelled and actual behaviour of concrete elements, affecting the reliability and predictive capability of the model. Therefore, ensuring precise determination of fracture energy is essential for achieving accurate simulations of concrete's nonlinear response under various loading conditions.

Experimental studies on concrete behaviour often show variability in measured tensile strength and fracture energy due to the heterogeneous nature of concrete. By reducing the fracture energy to 75% of the tensile strength, the model can more accurately reflect the actual behaviour of concrete under stress. This reduction helps in achieving better agreement between the finite element model results and experimental data, ensuring that the model does not overestimate the lateral strength and ductility of the concrete elements.

The recommended value for tension stiffening is 0.4 (Červenka et al., 2013). However, when applied in the FEA, this value resulted in an excessively high peak of lateral load and a noticeable divergence in the primary failure characteristics for specimen CO and CO*. Specifically, the anticipated modes of failure and the observed structural response did not align well with the empirical data for these specimens, indicating that the tension stiffening value of 0.4 was too high for accurate modelling. To resolve the inconsistencies observed with specimen CO and CO*, the tension stiffening value was meticulously explored and calibrated⁷. Through a series of adjustments and validations against experimental results, a tension stiffening value of 0.1 was determined to be more appropriate. This revised value led to numerical results that closely matched the observed behaviour of the specimens, providing a better overall agreement. The calibration process and the resulting improvements in numerical accuracy are detailed in the previous chapters. The impact of the tension stiffening in the FEM of specimen S9 is interesting. The tension stiffening value calibrated and used for all specimens was 0.1. This small value, initially set at 0.4, was calibrated and reduced in accordance with the small amount of reinforcement in the concrete column section of study. It is supposed that the tension stiffening value increases in high confined and high reinforced sections (Červenka et al., 2013), this was expected for the specimen model S9. However, the tension stiffening remains as 0.1 even in the model with the SJ, despite the fact that the steel jacket provides a passive confinement in the column.

4.4 Final Remarks

The models of specimens CO, CO*, and S9⁸ were developed with careful consideration of boundary conditions, calibration of material parameters, and the proposed mesh density and arrangement. These models produced numerical results that, while valuable, could be further refined to accurately capture hysteresis behaviour. Enhancing the models to represent hysteresis behaviour would allow for a more in-depth analysis of the detailed nonlinear lateral responses of the specimens studied in this thesis. By incorporating hysteresis behaviour, the models would provide a more comprehensive understanding of the cyclic loading responses and failure mechanisms, which are critical for assessing the structural performance under real-world conditions. This enhancement would also enable the extension of the research scope to accurately represent all other specimens from the Alcocer's experimental research (see Table 3.1). Such an extension would allow for a broader validation of the modelling approach and ensure that the findings are applicable to a wider range of scenarios. However, it is important to note that the monotonic approach used in this research has proven to be sufficiently robust for the purposes of this study. Despite its limitations in capturing cyclic behaviour, the monotonic analysis has provided important information (exposed in chapter 6) and allowed for the formulation of significant conclusions regarding the effectiveness of steel jacketing in enhancing the lateral load capacity of reinforced concrete structures.

⁷ Tension stiffening is an important factor to consider in the FEA of reinforced concrete structures. It accounts for the contribution of concrete between cracks to the overall stiffness of a reinforced concrete member. Realistic values for tension stiffening can vary based on factors such as the type of concrete, reinforcement details, and the loading conditions. However, general guidelines and typical values can be used as a starting point. Calibrating tension stiffening in FEA requires experimental data that captures the post-cracking behaviour of reinforced concrete.

⁸ Specimen S8 was not modelled because the experimental behaviour of the specimen S9 was of better interest due to its backbone response.

5 RECOMMENDATIONS

Summary

Recommendations derived from the comprehensive numerical and experimental study are described. These recommendations are based on detailed analysis and findings, providing insights and actionable guidance. They encompass observations, suggested improvements, and practical strategies aimed at enhancing the overall effectiveness and efficiency for experimental and numerical research, based on Afghani-Khoraskani (2015), Krawinkler et al. (1983) and Lonati et al. (2018) recommendations.

5.1 Experimental

The main issue when conducting an experimental study lies in the meticulous planning of activities. This is a crucial step to enhance efficiency, optimize time management, and minimize the waste of both labour and materials, thereby also reducing economic losses. Effective planning ensures that the experimental process is streamlined and productive, avoiding unnecessary delays and resource consumption.

An essential aspect of this planning phase is to first establish a comprehensive inventory of the materials, equipment, and instrumentation that will be utilized throughout the experimental research. This inventory serves as a foundational reference, enabling researchers to account for all necessary components and tools before the experimentation begins. By knowing exactly what is available and what needs to be procured, shortages or surpluses that could disrupt the research timeline or inflate costs can be prevented. Additionally, this thorough preparation allows for better coordination among team members, ensuring that everyone involved in the study is aware of the resources at their disposal and can plan their tasks accordingly. It also facilitates more accurate budgeting and financial planning, as all potential expenses are anticipated and accounted for. Overall, having a detailed and organized inventory contributes significantly to the smooth execution and success of the experimental study, ensuring that the research objectives are met efficiently and effectively (Afghani-Khoraskani, 2015).

Before conducting the test, it is crucial to ensure the proper functioning of all the instruments that will be used. This step is essential to prevent any failures in data recording, which could compromise the accuracy and reliability of the experimental results. To achieve this, a thorough pre-test calibration and verification of all equipment and instruments must be performed. Each device should be inspected for any signs of wear or malfunction, and calibrated according to the manufacturer's specifications or standard protocols. This includes checking sensors, data loggers, measuring devices, and any other relevant instruments to ensure they are operating correctly and providing accurate readings.

Additionally, performing a series of preliminary tests or dry runs can help identify potential issues with the instruments and allow for troubleshooting before the actual experiment begins. This proactive approach helps in detecting and addressing any malfunctions or discrepancies early on, thus minimizing the risk of data loss or errors during the main testing phase. By taking these precautions, ensuring that the instruments are in optimal condition can be ensured, thereby enhancing the reliability of the data collected. This meticulous preparation contributes to the overall success of the experimental study, as it ensures that the recorded data is accurate, consistent, and trustworthy (Krawinkler et al., 1983).

When working with concrete elements tested till failure, it is imperative to implement stringent safety measures to protect both personnel and the instrumentation installed on the specimen. The high loads and stresses involved in such tests can lead to sudden and unpredictable failures, posing significant risks (Lonati et al., 2018).

The minimum safety measures for personnel recommended are the follow:

- **Protective Gear:** All personnel should wear appropriate personal protective equipment (PPE), including hard hats, safety glasses, gloves, steel-toed boots, and hearing protection;
- **Training:** Ensure that all team members are trained in safety protocols and understand the potential hazards associated with the testing process;
- **Clear Zones:** Establish and enforce clear zones around the testing area. Only essential personnel should be allowed within these zones during critical phases of the test;
- **Emergency Procedures:** Develop and communicate an emergency response plan. This should include procedures for evacuating the area, first aid measures, and contact information for emergency services.

The minimum safety measures for instrumentation recommended are the follow:

- **Protective Enclosures:** Use protective enclosures or shields around sensitive instrumentation to protect against debris and sudden impacts during the failure of the concrete specimen;
- **Secure Mounting:** Ensure that all sensors, data loggers, and other equipment are securely mounted and unlikely to dislodge or become damaged during the test;
- **Regular Checks:** Conduct regular inspections of the instrumentation setup before and during the test to ensure that all equipment remains in good working condition and is correctly positioned.

The general precautions recommendations are the follow:

- **Monitoring and Communication:** Continuously monitor the structural integrity of the specimen and maintain open lines of communication among all team members to quickly address any signs of impending failure;
- **Controlled Environment:** Conduct tests in a controlled environment where external factors (such as weather conditions) do not introduce additional risks;
- **Documentation and Compliance:** Adhere to all relevant safety regulations and standards. Document all safety measures and ensure compliance with institutional and legal requirements.

By prioritizing these safety measures, the risks associated with testing concrete elements to failure can be significantly reduced. This not only protects the well-being of the personnel involved but also ensures the integrity and longevity of the instrumentation, leading to more reliable and accurate test results.

5.2 Numerical

For the creation of a mathematical model that can accurately represent the natural phenomena observed in the experimental test, several steps need to be accomplished in a hierarchical manner. Here are the key steps (Červenka et al., 2002):

1. Define the scope and objectives with problem identification: Clearly define the specific natural phenomena and experimental conditions you aim to model;
2. Objectives: Establish the goals of the mathematical model, including the level of accuracy and the parameters to be studied;
3. Data collection and analysis: Gather detailed and accurate data from the experimental tests. Ensure the data covers all necessary aspects of the phenomena;
4. Data analysis: Analyse the collected data to identify patterns, relationships, and key variables that will inform the model development;
5. Develop theoretical Framework with the Fundamental Principles: Identify and apply relevant scientific principles, laws, and equations that govern the natural phenomena;
6. Assumptions: Make justified assumptions to simplify the model while maintaining accuracy. Document these assumptions for transparency;
7. Formulate the mathematical model: Develop mathematical expressions and equations that represent the relationships and behaviours observed in the experimental data;
8. Modelling: Modell the structure, including differential equations, boundary conditions, and initial conditions;
9. Parameter estimation: Determine the key parameters that need to be estimated for the model;
10. Estimation techniques: Use statistical methods and optimization techniques to estimate the values of these parameters from the experimental data;
11. Model implementation with coding and software: Implement the mathematical model using appropriate computational tools and software. Ensure the code is well-documented and tested;
12. Simulation: Run simulations to test the model under various conditions and scenarios;
13. Model calibration with the adjust of parameters: Fine-tune the parameters and adjust the model to better fit the experimental data. This may involve iterative testing and modification;
14. Validation: Validate the model by comparing its predictions with independent sets of experimental data not used in the calibration process;
15. Robustness testing: Test the robustness of the model under different conditions to ensure its reliability;
16. Documentation and reporting: Document all steps taken, including the theoretical basis, assumptions, data analysis, and calibration process;
17. Reporting results: Prepare detailed reports and presentations to communicate the model's development, findings, and implications;
18. Review and refinement: Subject the model to peer review to gain feedback and identify any potential weaknesses or areas for improvement;
19. Continuous improvement: Refine and update the model as new data and insights become available, ensuring it remains accurate and relevant.

6 CONCLUSIONS

This research thesis has led to important conclusions, highlighting the use of finite element method to enhance the exploration of variables studied in the experimental programme. The principal conclusions derived from the experimental and numerical study are outlined below.

6.1 Experimental Tests

- The two specimens rehabilitated with latticed steel jacketing can successfully modify the brittle shear failure mode to a ductile flexural failure mode, being capable of inducing a plastic hinge in the foundation-column joint, which can help to dissipate energy due to ground motion. The change in the failure mode from shear to flexure significantly increases the strain capacity and ductility of the retrofitted columns, with an increase in ductility up to 7.3 times that of the benchmark specimens. The steel jacketing significantly enhances lateral displacement capacity compared to the benchmark specimens, enabling lateral displacement up to 3.23 times greater.
- A rectilinear jacket might not effectively confine the concrete before substantial dilation occurs, meaning before the concrete loses its confinement and exhibits its unconfined strength (Yu-Fei et al., 2005). However, it typically becomes less of an issue for a properly attached rectilinear jacket to provide adequate confinement once significant concrete dilation has occurred.
- The increased lateral displacements permitted by the metallic jacketing significantly raise the demands on strains in the longitudinal reinforcing steel, potentially causing low-cycle fatigue in the highly stressed steel under significant lateral drifts. In the experimental tests, fractures were observed in the longitudinal steel situated at fibres farthest from the neutral axis. When the steel fractured, there was a sudden decrease in lateral load strength, which promptly recovered due to stress redistribution towards the residual longitudinal steel.
- The steel jacketing can reduce the occurrence of cracks and control their width by providing passive confinement to the column. This confinement results from the constraint provided by the SJ, which controls the expansion of the RC column, principally managing the shear strain (Yu-Fei et al., 2005).
- The steel jacketing does not increase the lateral stiffness of the column but helps to reduce its deterioration under higher drift demands (after the peak lateral load).
- A larger steel angle can provide increased confinement of the column core by offering a greater contact area, which reduces crack spacing and thickness and helps prevent concrete detachment within the column core.

- Specimens with SJ increased the maximum shear capacity by up to 1.13 times. Nevertheless, it is important to highlight that while the gain in lateral strength may be minimal, the increase in ductility was substantial.
- The local diagonal and horizontal strains within the core of the concrete column are greater in the column-foundation zone for the S8 and S9 specimens at higher drifts. This is due to their enhanced lateral deformation capacity. However, compared to the CO and CO* specimens, these local deformations are relatively smaller.

6.2 Numerical Analysis

- The FEM can accurately represent the main shear failure presented in the experimental test of the CO and CO* specimens. Hence, the general lateral behaviour is in accordance with the experimental test if the boundary conditions implement a 3D interface friction surface to consider the lateral displacement of the foundation recorded in the experimental tests.
- The fracture of longitudinal reinforcing steel cannot be accurately modelled using the monotonic approach because low-cycle fatigue could not be modelled under a monotonic controlled displacement method. Consequently, the failure strain of the steel bars is higher than that observed under cyclic loading conditions.
- Despite the simplifications in the FEM for specimen S9, where only the steel angles of SJ are in contact with the concrete column (with a 3D interface), the overall lateral behaviour is accurately represented. This demonstrates that enhance the material model behaviour of the FEM is unnecessary to achieve good results for the monotonic approach implemented in this research.
- It is important to note that the monotonic approach employed in this research has proven to be sufficiently robust for the study's objectives. Despite its limitations in capturing cyclic behaviour, the monotonic analysis has provided comprehensive results and enabled a good comparison between FEM and experimental tests regarding the effectiveness of steel jacketing in enhancing the lateral load capacity of RC structures. The ability of the monotonic approach to highlight key performance improvements underscores its value in structural analysis and engineering applications.
- The most critical material parameters in the FEM analysis are fracture energy, tensile strength of the concrete column, and tension stiffening. These parameters significantly influence the overall response of the benchmark specimen CO and CO*. Changes in the tensile strength of the concrete alter the fracture energy, which in turn affects the main diagonal failure. This leads to discrepancies between the experimental and numerical peaks of lateral strength. To calibrate these parameters, the variation in the experimental concrete cylinder test was considered.
- The connection between the steel jacketing and the concrete column is crucial for accurately modelling the S9 specimen. A perfect bond between the steel jacket and the concrete column significantly impacts the structural response, particularly by increasing the lateral stiffness. This increase in stiffness can lead to discrepancies in the model if not properly accounted for. To address this, it was necessary to implement a detailed 3D interface between the steel jacket and the concrete column in the model. This interface allows for a more realistic simulation of the interaction between the two materials, capturing the distinctiveness of their behaviour under lateral loads. By incorporating this 3D interface, the model can more accurately represent the actual performance of the specimen,

ensuring that the lateral stiffness and overall structural response are correctly depicted. This improvement enhances the reliability and accuracy of the FEM analysis, providing better insights into the effectiveness of SJ in strengthening RC columns.

6.3 Future Works

This study has uncovered several critical insights into the overall lateral behaviour of rectangular section RC columns reinforced with SJ. One of the most significant findings is the enhancement of lateral capacity through the formation of a plastic hinge at the concrete-foundation joint, resulting from a change in the failure mode. These findings deepen our understanding of this reinforcing and rehabilitation technique, offering a new perspective on the nonlinear modelling of RC columns reinforced with SJ.

The results have significant theoretical implications, which can potentially improve existing frameworks for assessing the nonlinear behaviour of RC columns reinforced with steel jackets. Specifically, interest in incorporate the passive confining effect provided by SJ into the analysis. For this regard, a new theoretical framework may be required, suggesting that the design of RC columns should account for the restricted dilatancy of the main section due to the SJ. This new approach would better replicate this phenomenon for design codes, including the confining zone of the core section.

This work opens up several avenues for future research. Further studies could focus on develop a theoretical framework to include the hysteresis behaviour of the RC columns with SJ, which were beyond the scope of this research but are crucial for a more comprehensive understanding of the lateral specific behaviour of this rehabilitation/retrofitting technique and to expand the research on new variables for SJ, like the combined application of lateral cyclic imposition and axial load, a scenario more realistic.

The possible future works may involve:

- Propose a theoretical framework to address the cyclic behaviour for rehabilitation proposals in vulnerable RC columns;
- Modelling different SJ arrangements to validate the numerical model and expand the experimental study;
- The implementation of axial and lateral loads to further explore the nonlinear behaviour;
- Explore the influence of another material parameters like f_U and the related to 3D interface of SJ;
- The develop of an acceptance criterion to address the nonlinear lateral and axial behaviour.

While the findings of this work are interesting, it is important to consider the limitations of this study. These include the monotonic approach to explore the overall general behaviour of RC columns with SJ without axial force. A hysteresis approach should be addressed in future research to validate and extend the current findings.

7 APPENDIX

Summary

The stress vs strain test curves of the materials used in the experimental study are presented here, along with the records of internal and external strain gauges installed in specimens CO, CO*, S8, and S9.

7.1 Materials Stress vs Strain Test Curves

7.1.1 Reinforcing Steel used in Specimens CO, CO*, S1, S2 and S3

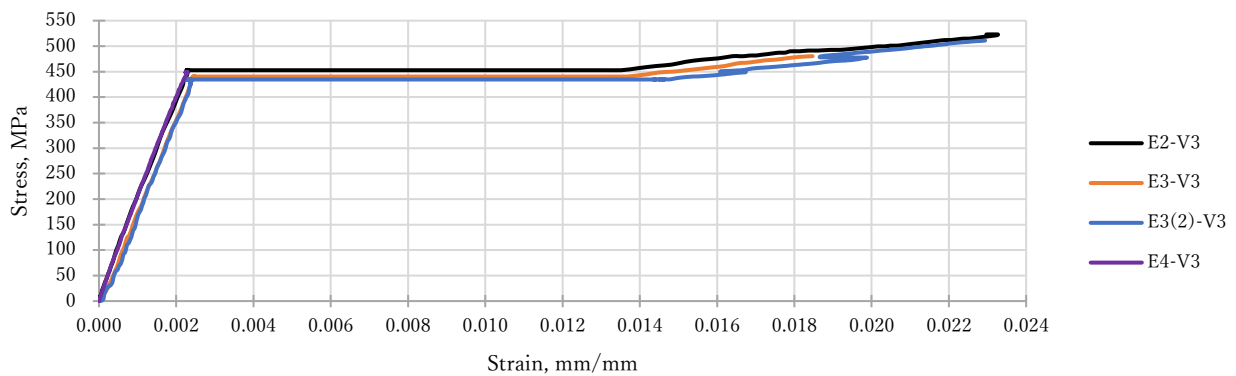


Fig. 7.1—Stress vs strain curves of reinforcing steel, Var. $\varnothing = 9.525 \text{ mm}$ [3/8 in]

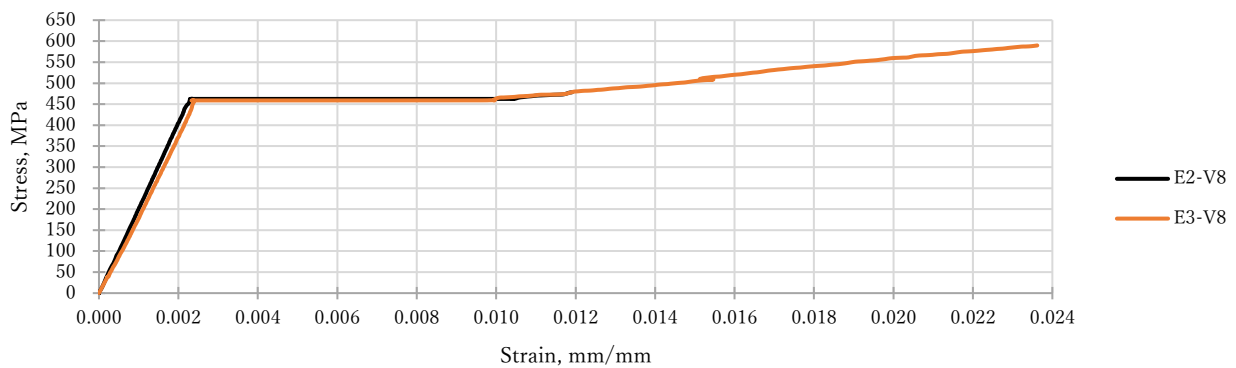


Fig. 7.2—Stress vs strain curves of reinforcing steel, Var. $\varnothing = 25.4 \text{ mm}$ [1 in]

7.1.2 Concrete Cylinder Test of Specimen CO

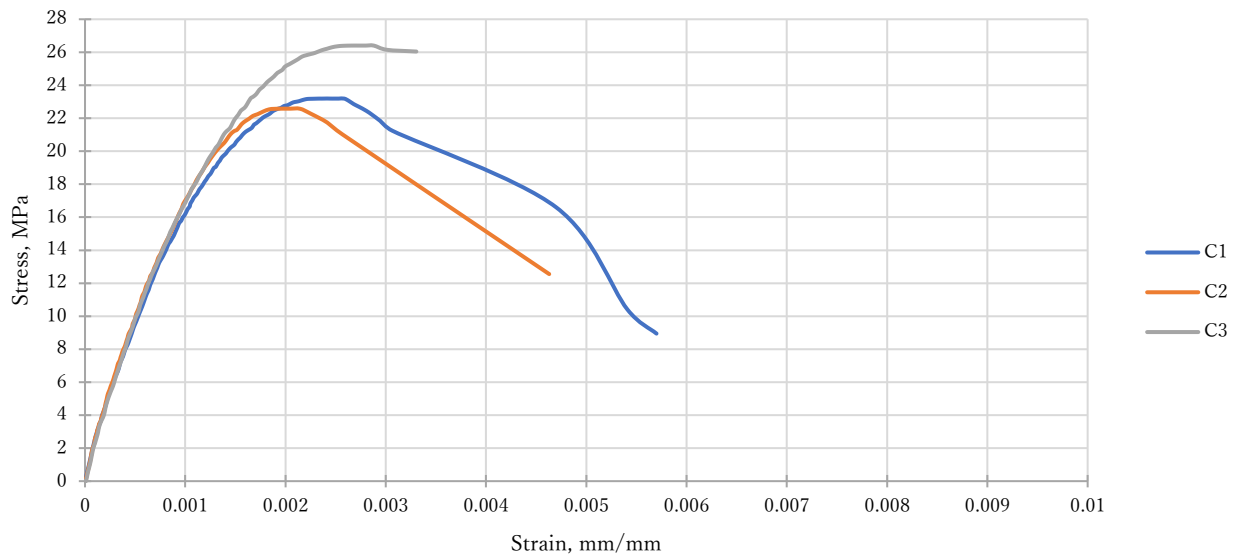


Fig. 7.3—Stress vs strain curves for concrete column cylinder test of specimen CO

7.1.3 Concrete Cylinder Test of Specimen S8 and S9

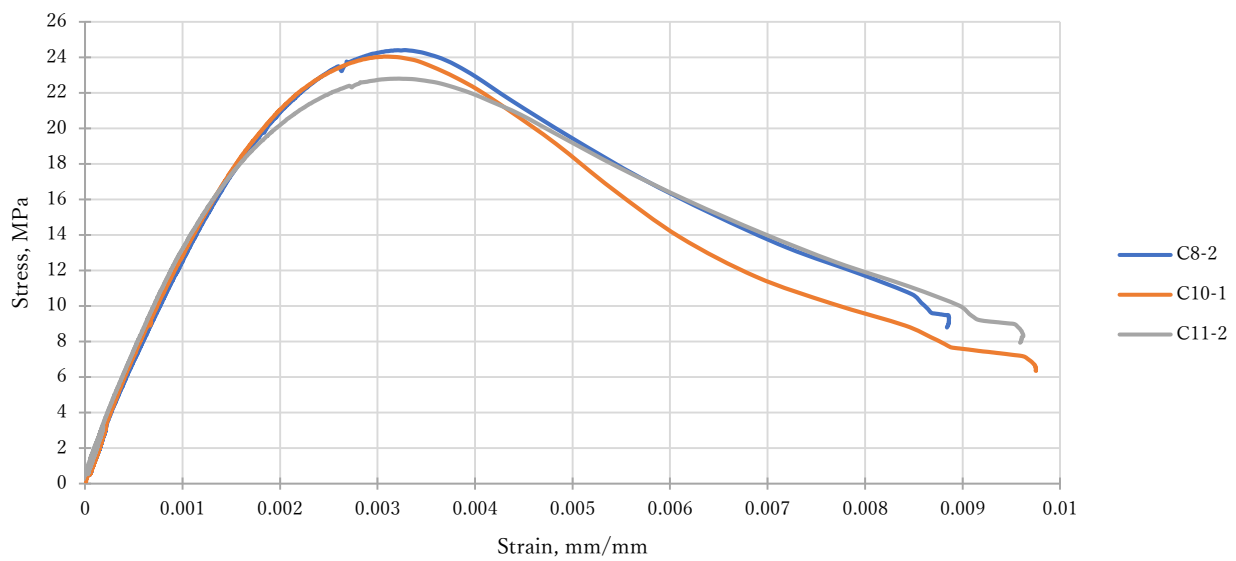


Fig. 7.4—Stress vs strain curves for concrete column cylinder test of specimen S8 and S9

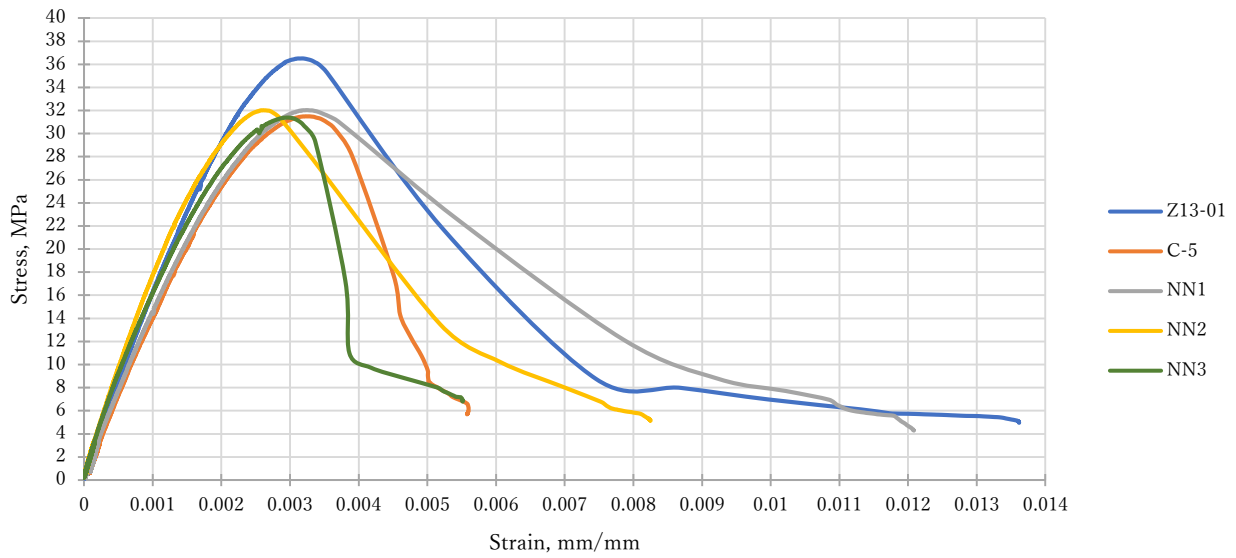


Fig. 7.5—Stress vs strain curves for concrete foundation cylinder test of specimen S8 and S9

7.1.4 Steel Test Curves of Angles and Battens

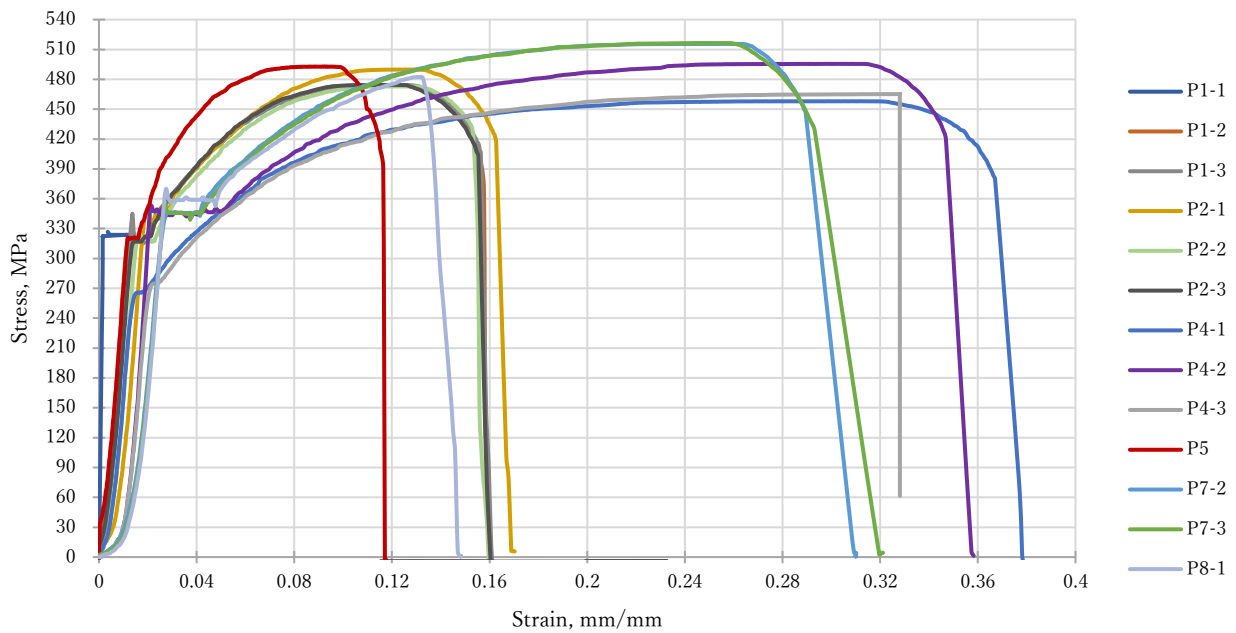


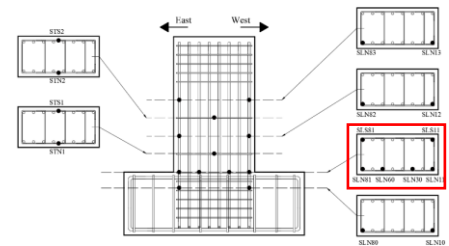
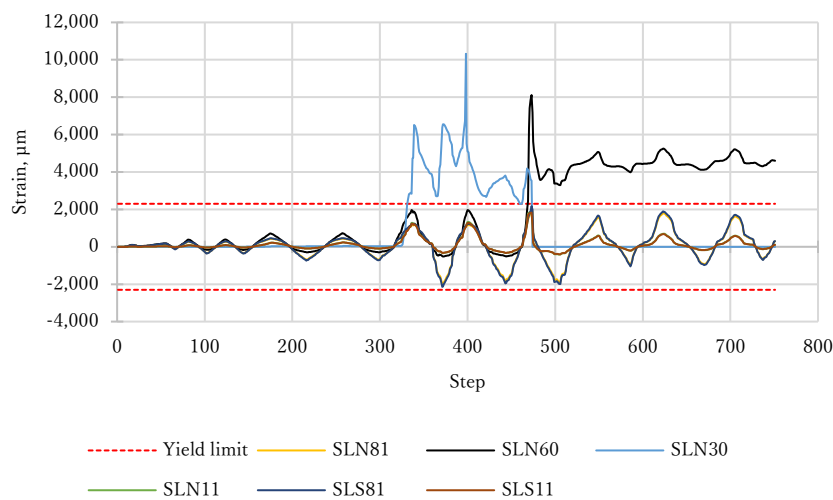
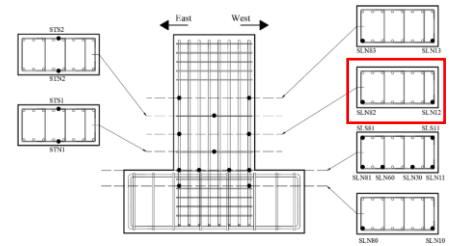
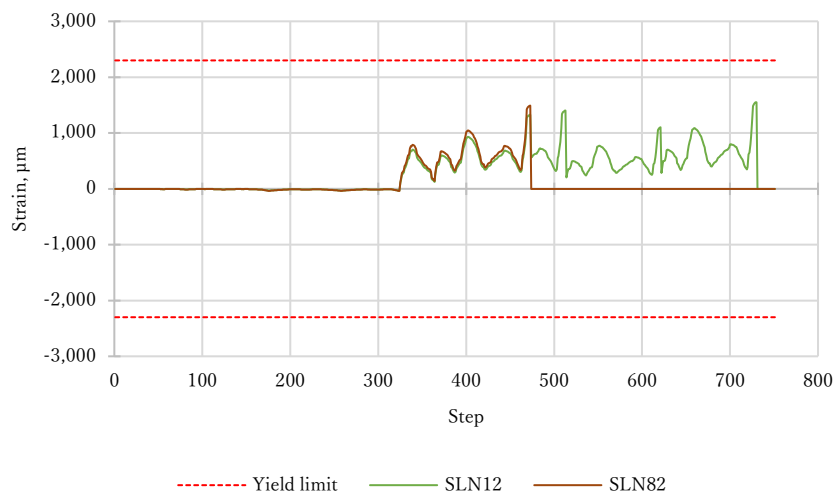
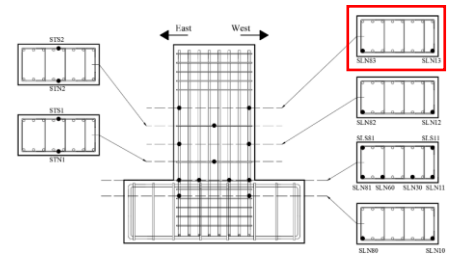
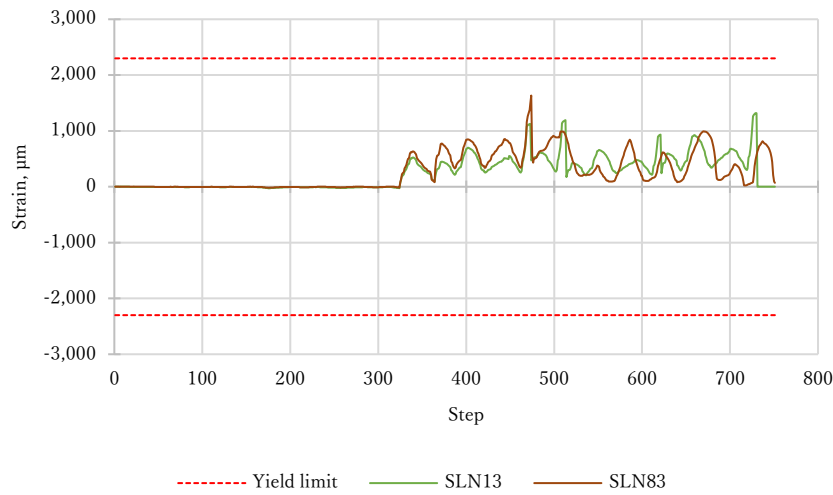
Fig. 7.6—Stress vs strain curves for steel of angles and battens of steel jacketing

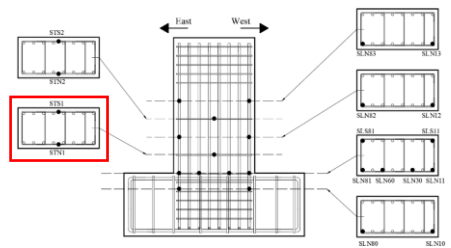
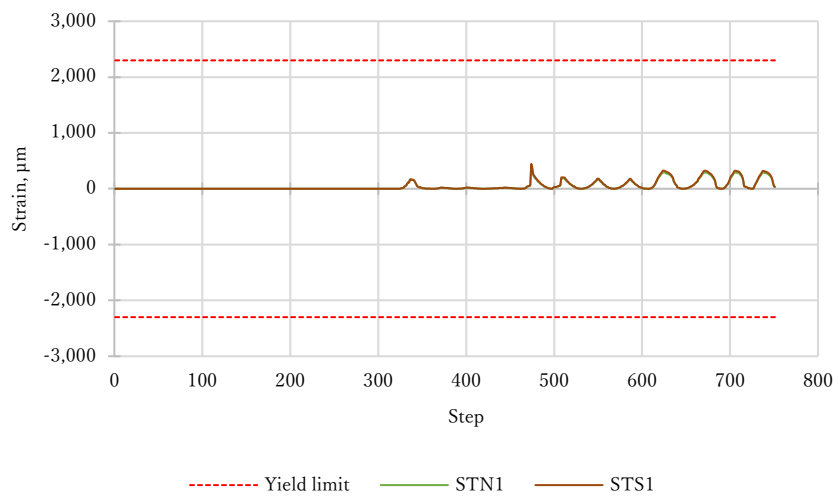
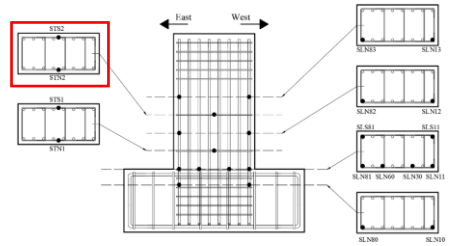
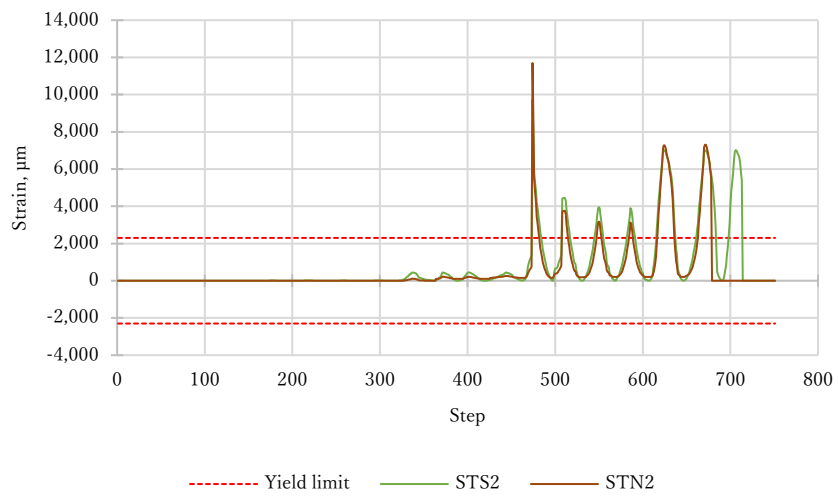
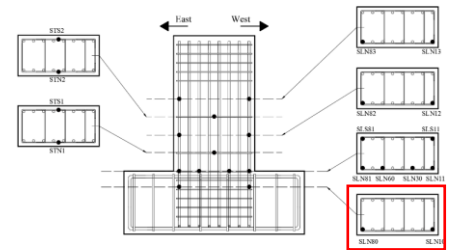
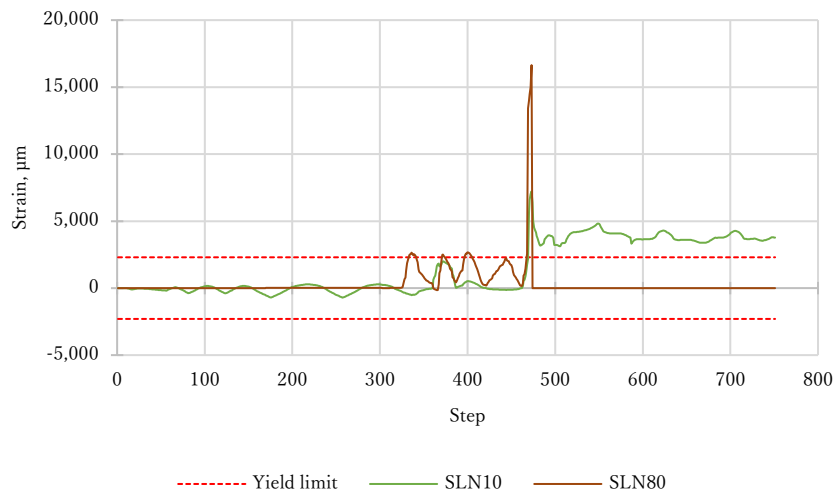
7.2 Strain Gauges Record of Internal and External Instrumentation

Table 7.1—Internal strain gauge nomenclature

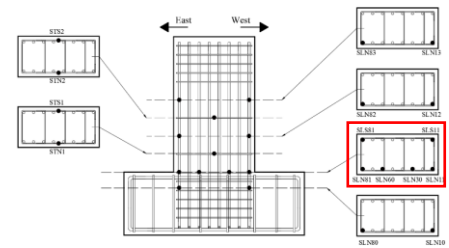
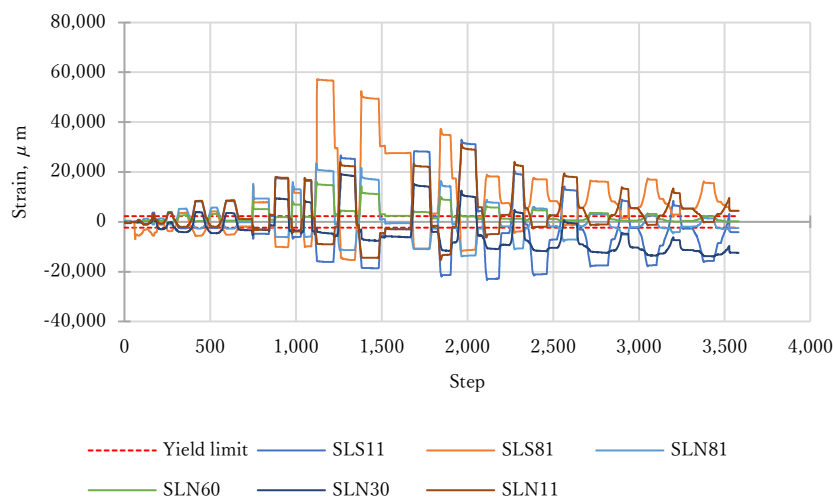
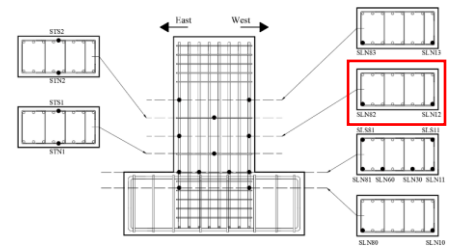
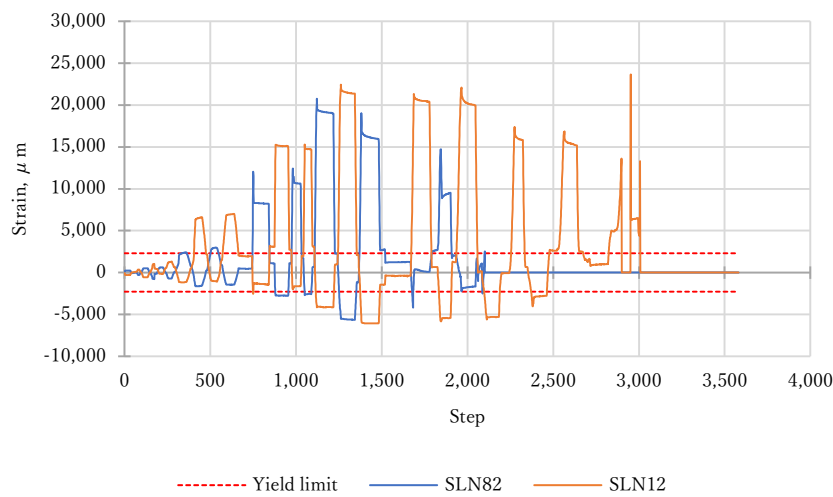
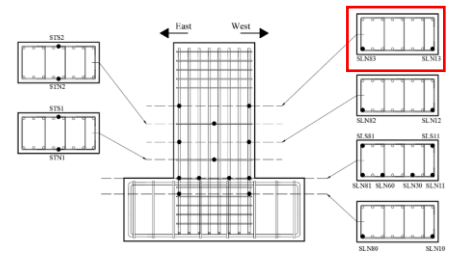
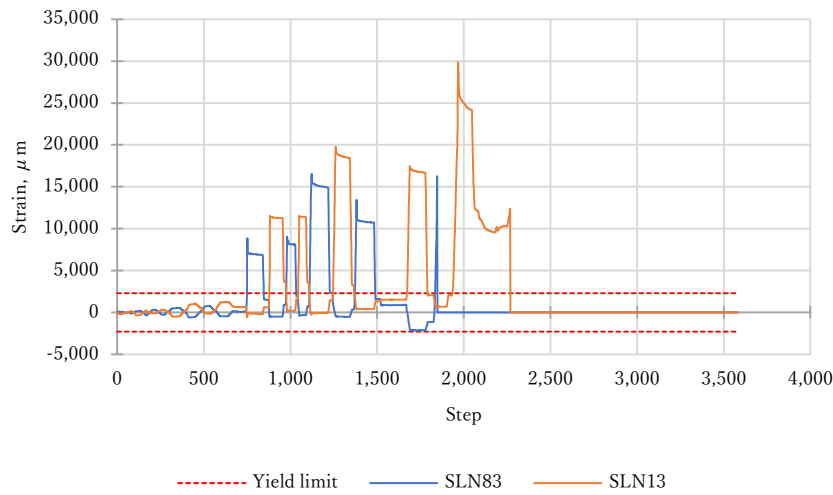
Name	Description
SLN80	Strain gauge (S) in longitudinal bar (L) of the north face (N), eight bar from right to left (8), first strain gauge on the bar bottom up (0).
SLN81	Strain gauge (S) in longitudinal bar (L) of the north face (N), eight bar from right to left (8), second strain gauge on the bar bottom up (1).
SLN82	Strain gauge (S) in longitudinal bar (L) of the north face (N), eight bar from right to left (8), third strain gauge on the bar bottom up (2).
SLN83	Strain gauge (S) in longitudinal bar (L) of the north face (N), eight bar from right to left (8), fourth strain gauge on the bar bottom up (3).
SLN10	Strain gauge (S) in longitudinal bar (L) of the north face (N), first bar from right to left (1), first strain gauge on the bar bottom up (0).
SLN11	Strain gauge (S) in longitudinal bar (L) of the north face (N), first bar from right to left (1), second strain gauge on the bar bottom up (1).
SLN12	Strain gauge (S) in longitudinal bar (L) of the north face (N), first bar from right to left (1), third strain gauge on the bar bottom up (2).
SLN13	Strain gauge (S) in longitudinal bar (L) of the north face (N), first bar from right to left (1), fourth strain gauge on the bar bottom up (3).
SLN60	Strain gauge (S) in longitudinal bar (L) of the north face (N), sixth bar from right to left (6), first strain gauge on the bar bottom up (0).
SLN30	Strain gauge (S) in longitudinal bar (L) of the north face (N), third bar from right to left (3), first strain gauge on the bar bottom up (0).
SLS81	Strain gauge (S) in longitudinal bar (L) of the south face (S), eight bar from right to left (8), second strain gauge on the bar bottom up (1).
SLS11	Strain gauge (S) in longitudinal bar (L) of the south face (S), first bar from right to left (1), second strain gauge on the bar bottom up (1).
STN1	Strain gauge (S) in transversal bar (T) of the north face (N), first bar from bottom up (1).
STN2	Strain gauge (S) in transversal bar (T) of the north face (N), second bar from bottom up (2).
STS1	Strain gauge (S) in transversal bar (T) of the south face (S), first bar from bottom up (1).
STS2	Strain gauge (S) in transversal bar (T) of the south face (S), second bar from bottom up (2).

7.2.1 Internal Strain Gauge of Specimen CO



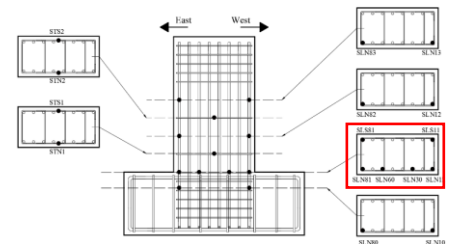
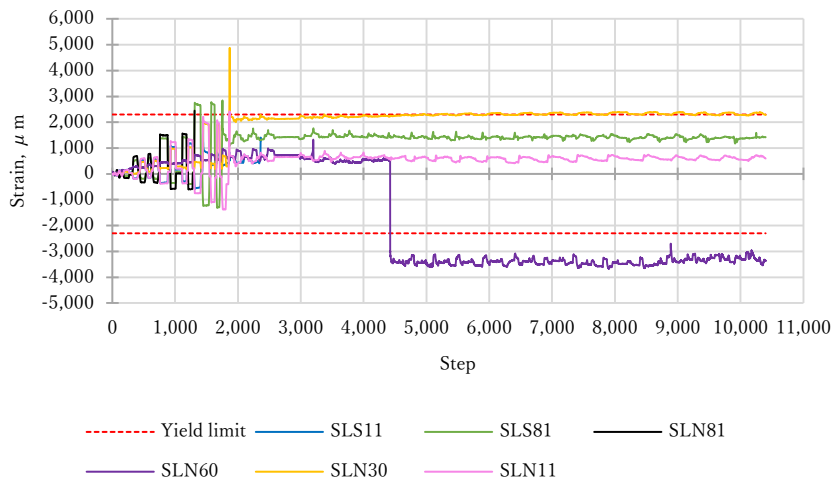
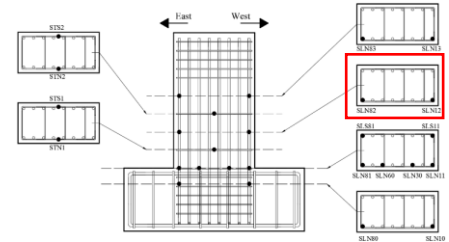
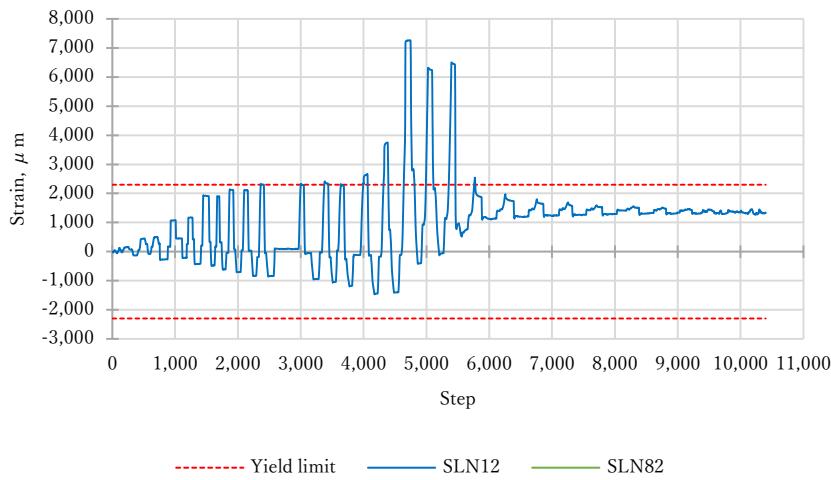
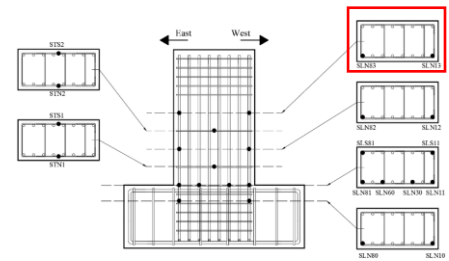
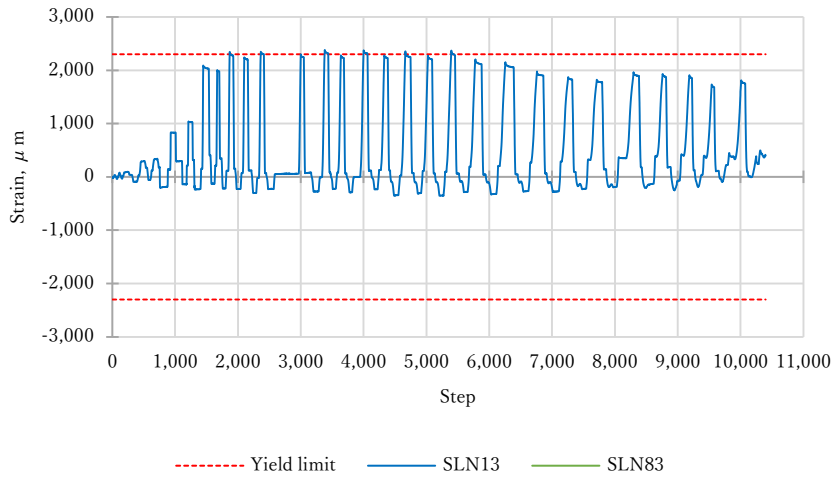


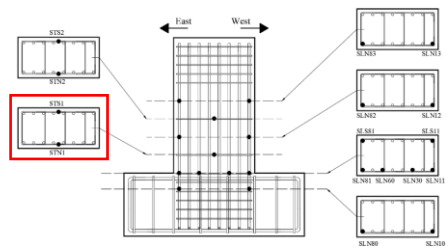
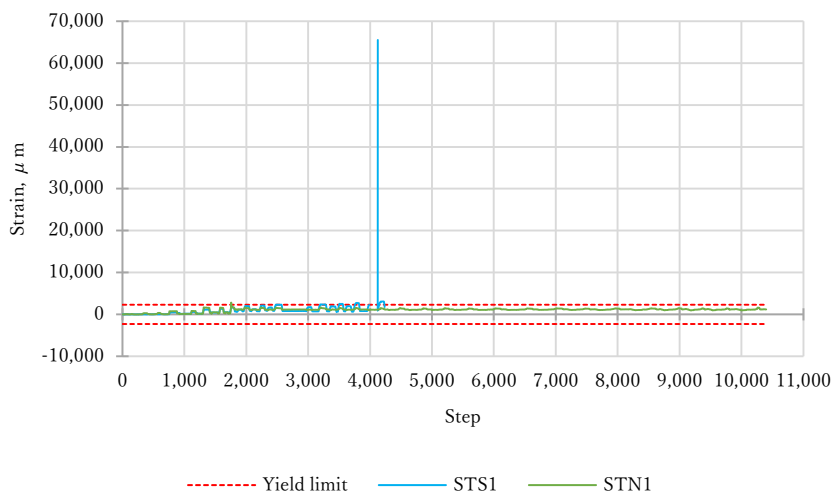
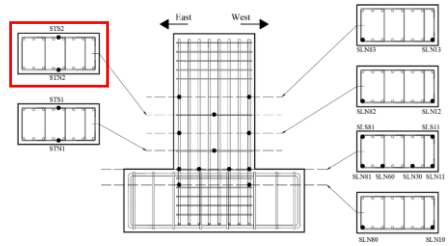
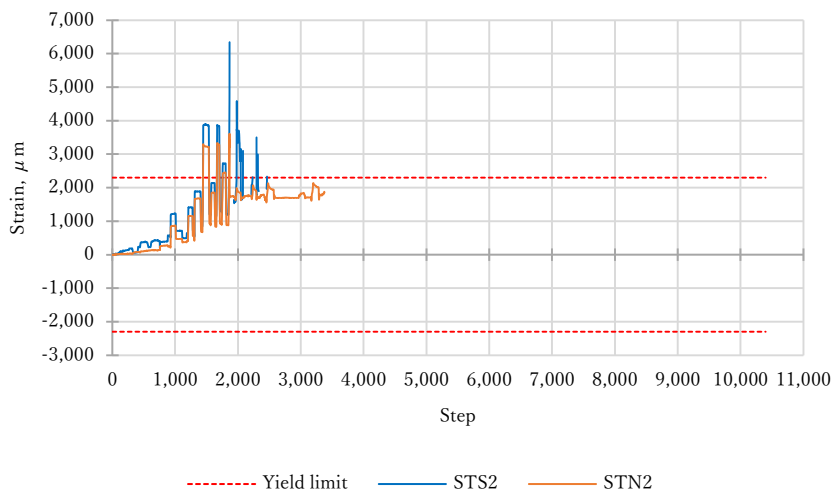
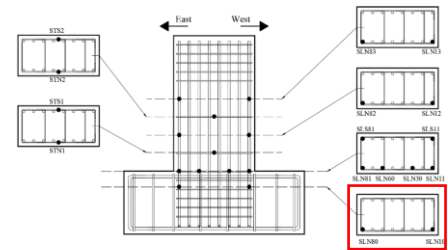
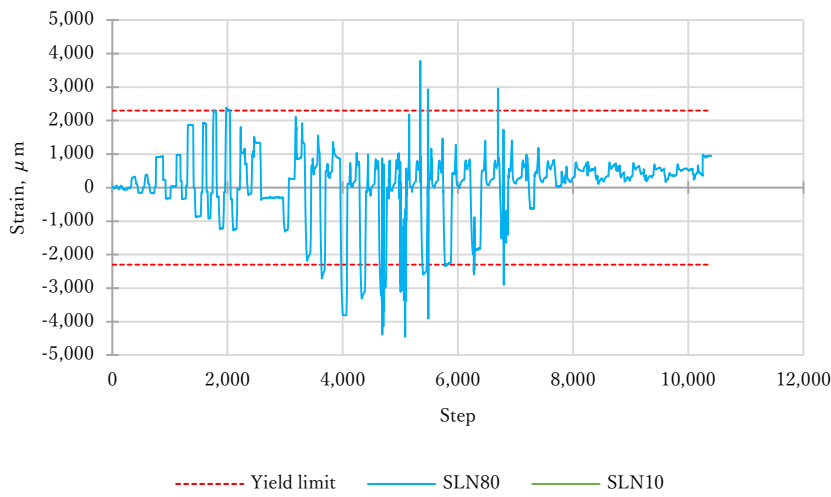
7.2.2 Internal Strain Gauge of Specimen CO*



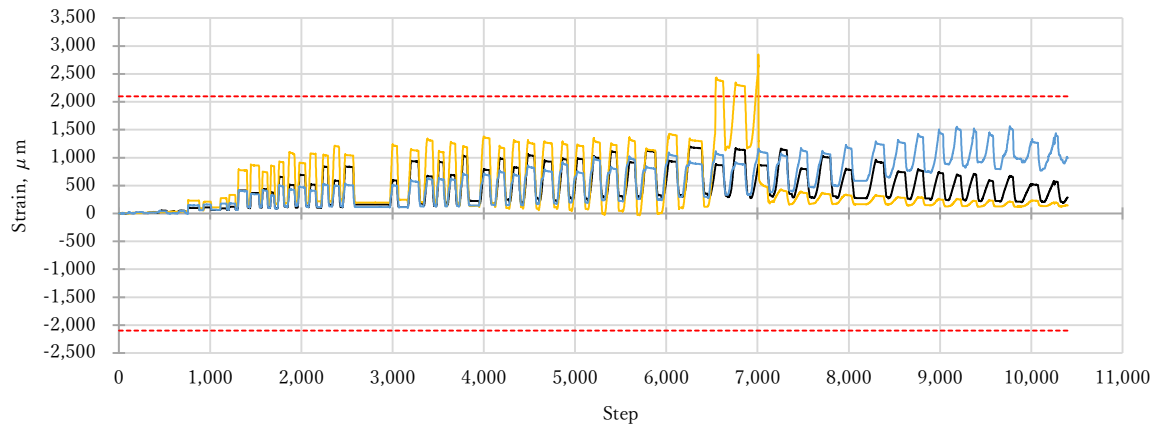
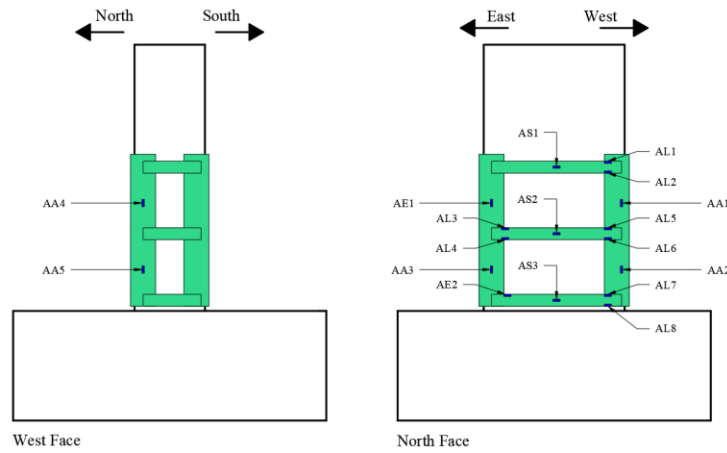
7.2.3 Strain Gauge of Specimen S8

7.2.3.1 Internal Strain Gauges

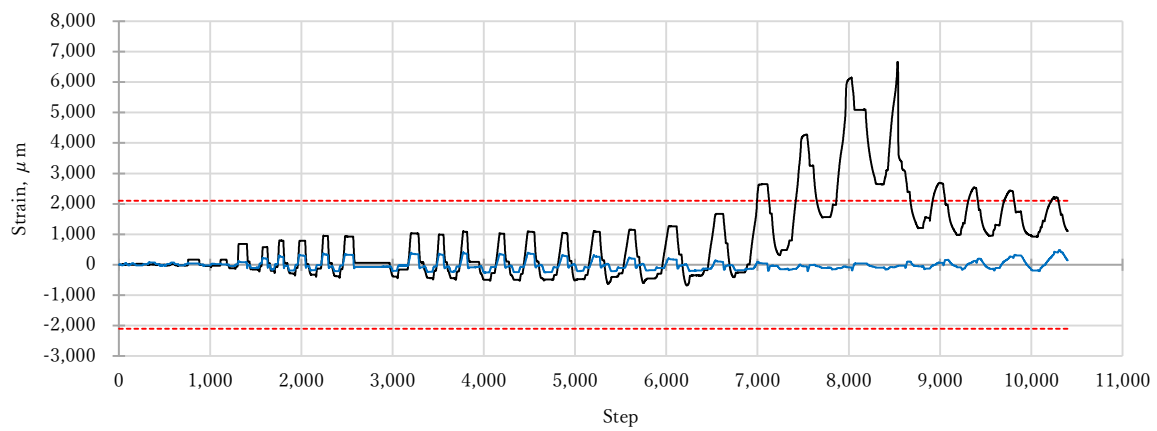




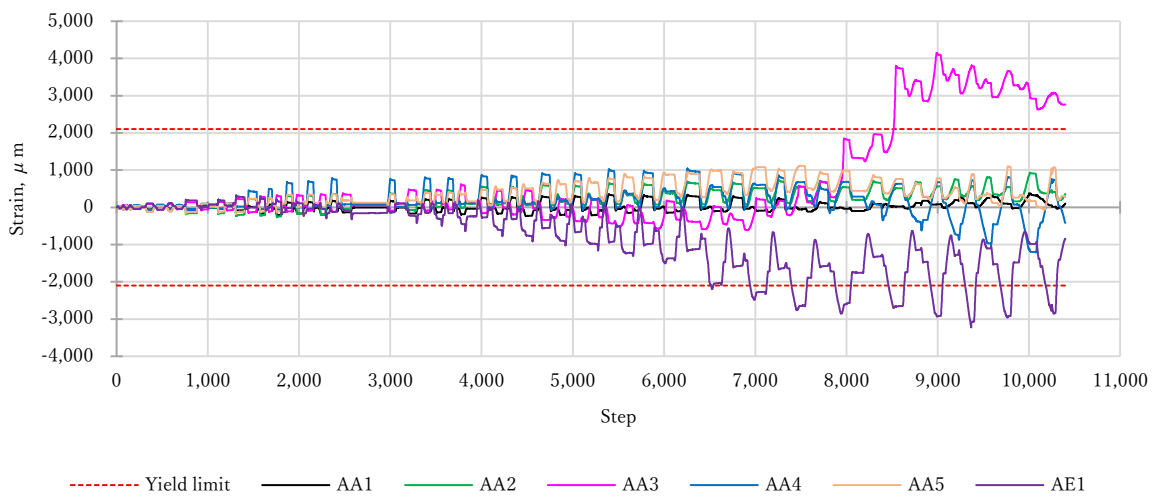
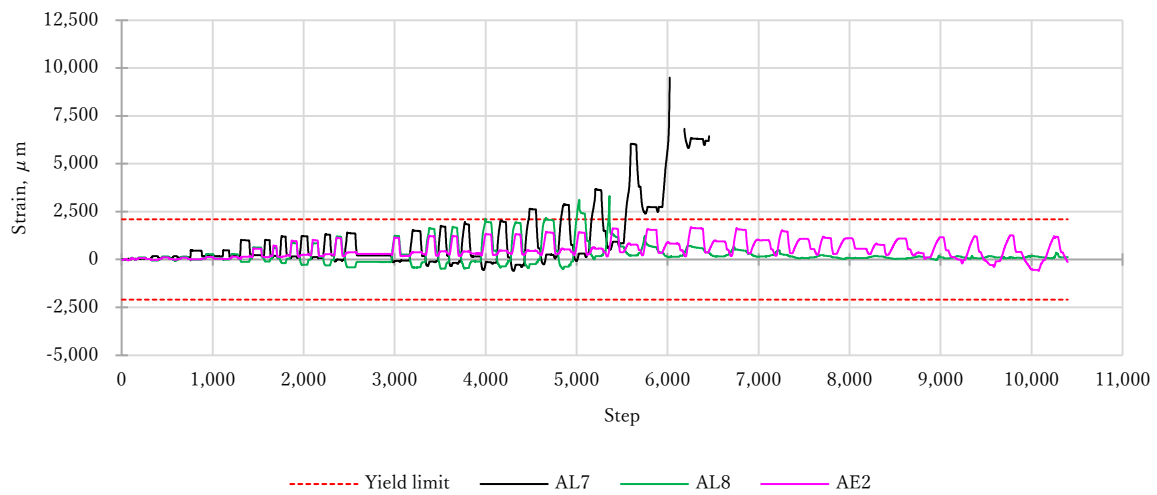
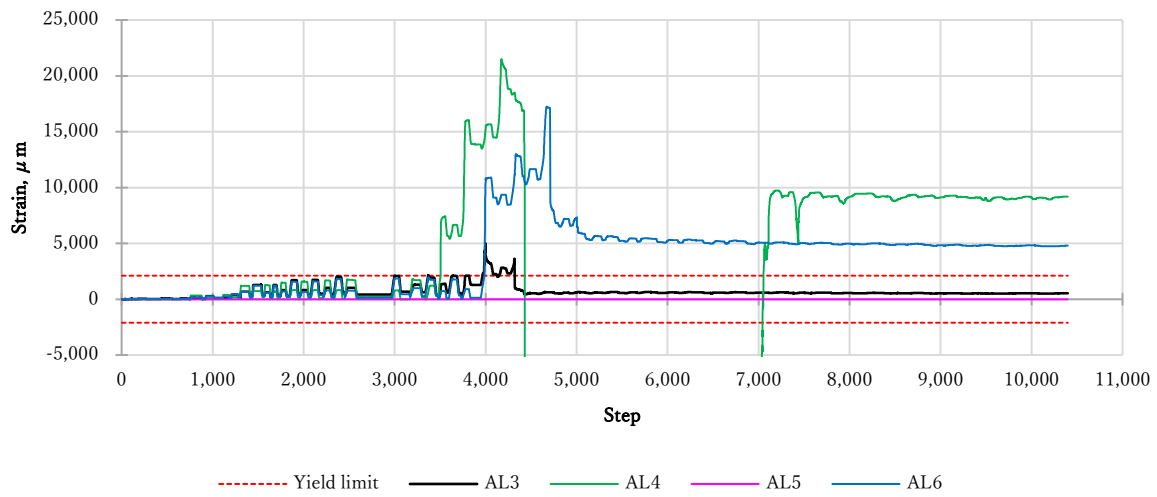
7.2.3.2 External Strain Gauges



----- Yield limit — AS1 — AS2 — AS3

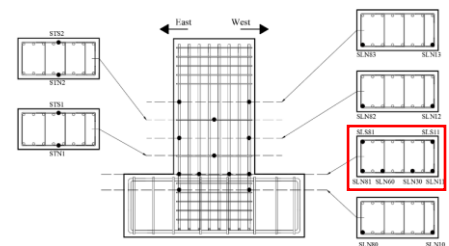
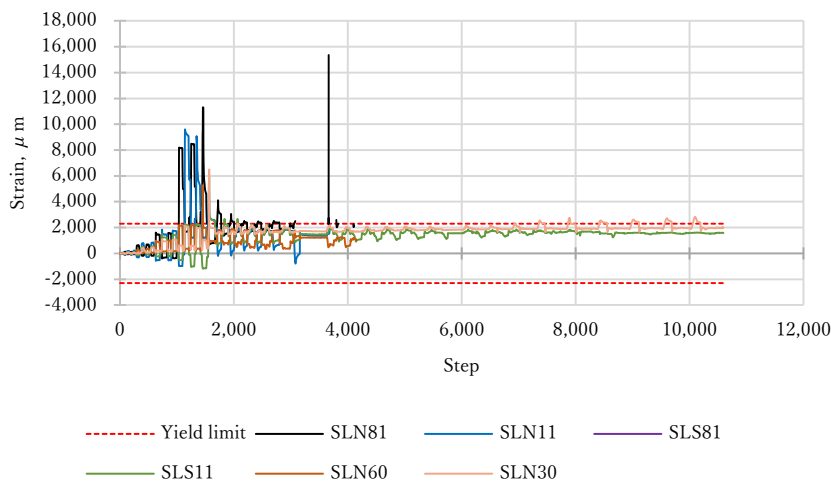
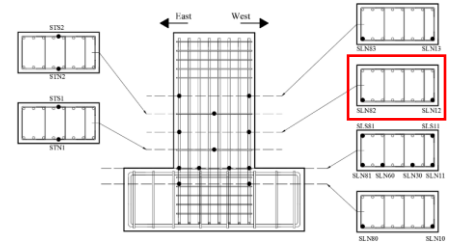
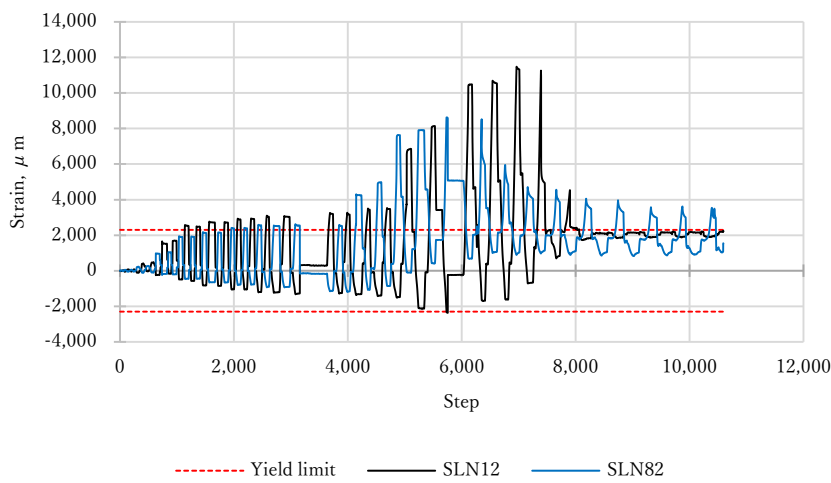
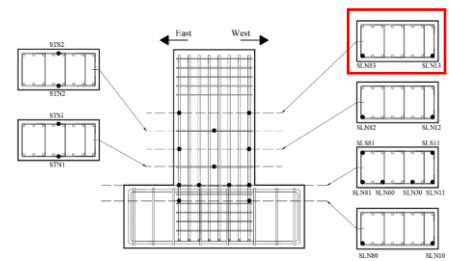
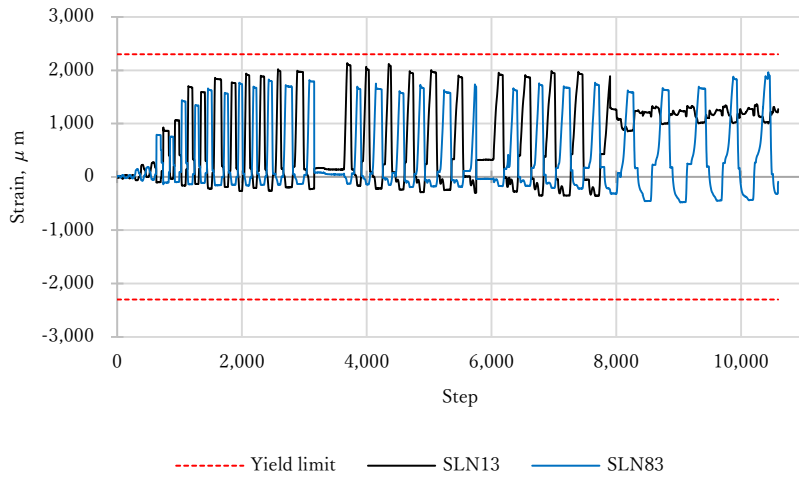


----- Yield limit — AL1 — AL2

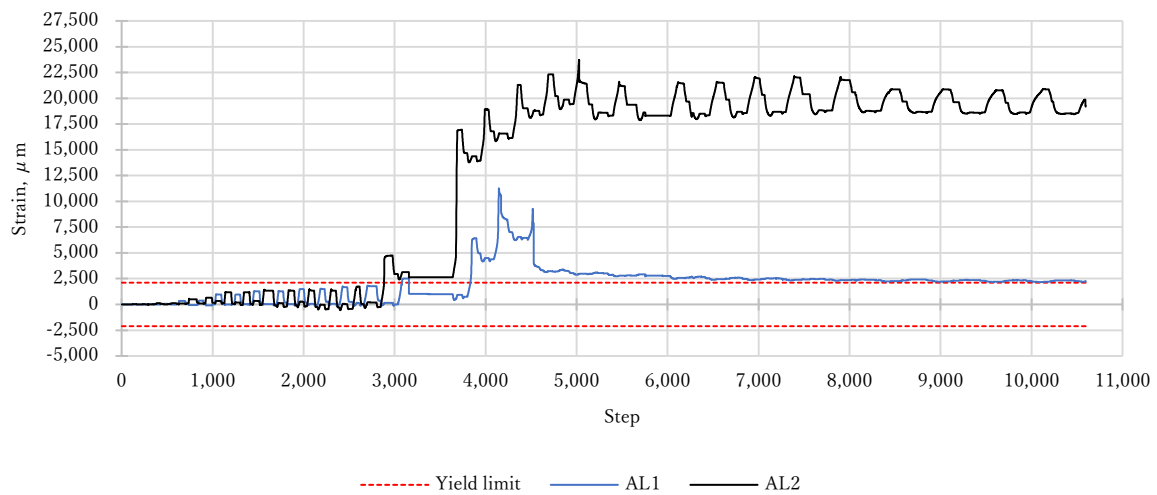
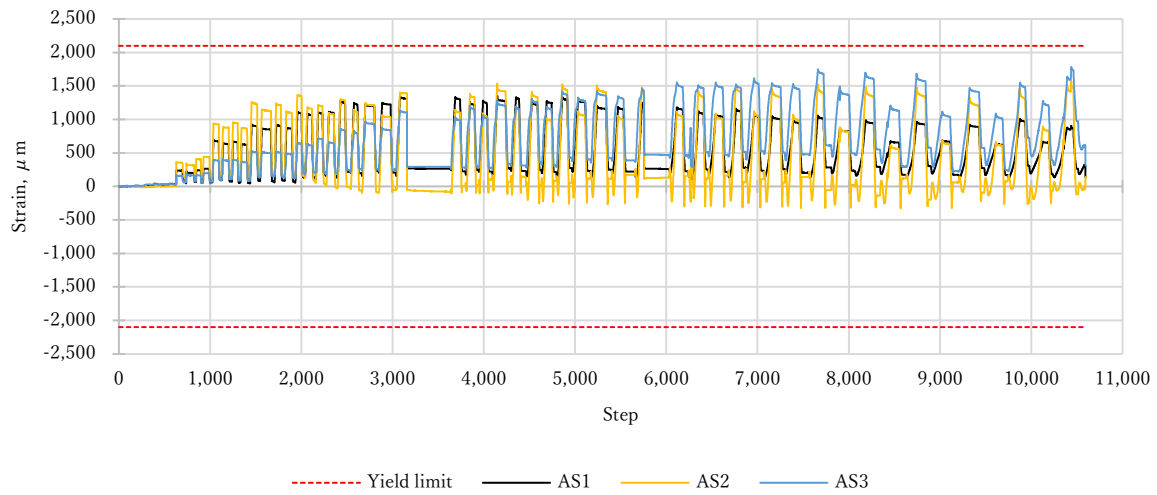
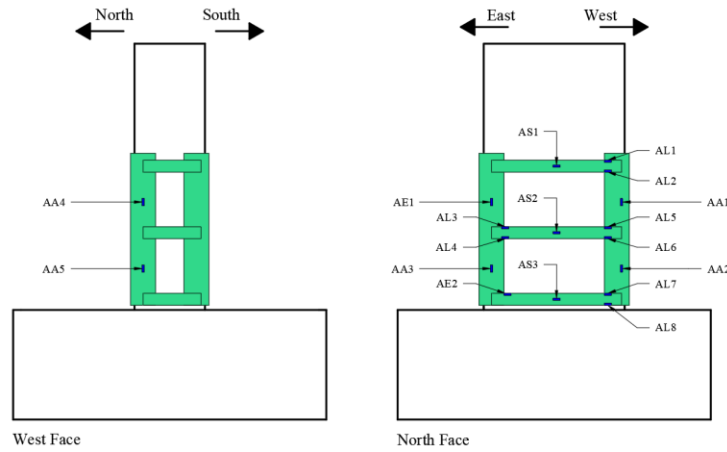


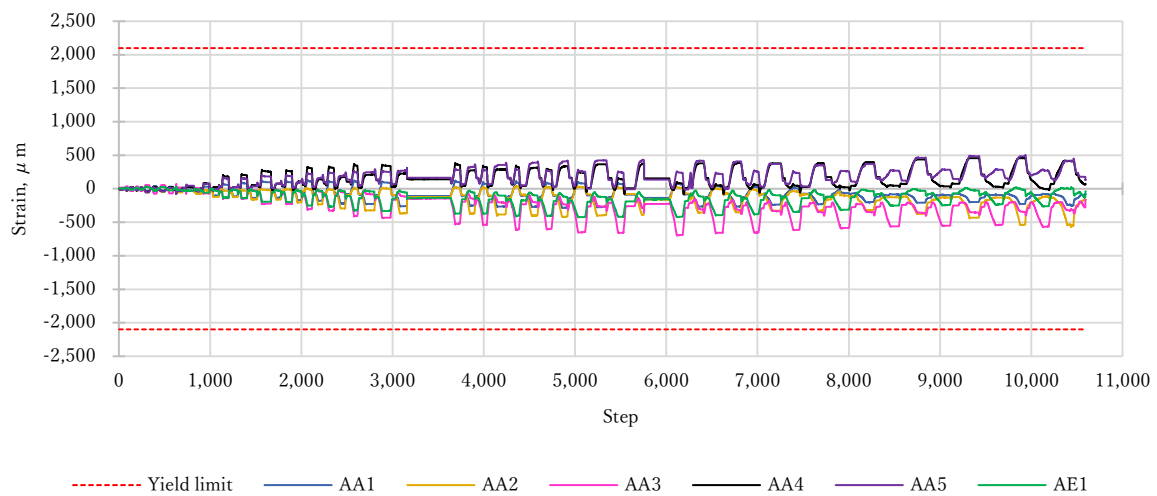
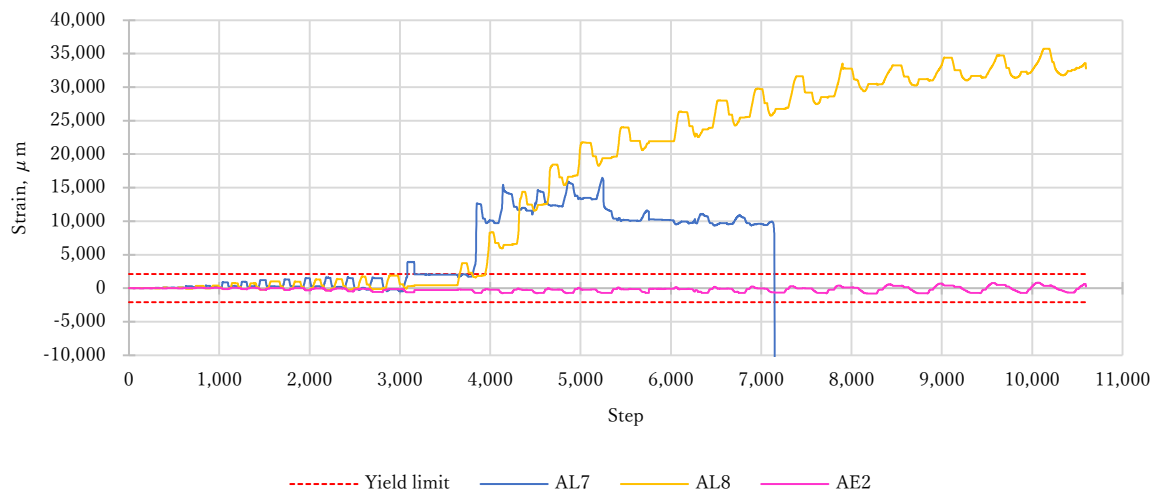
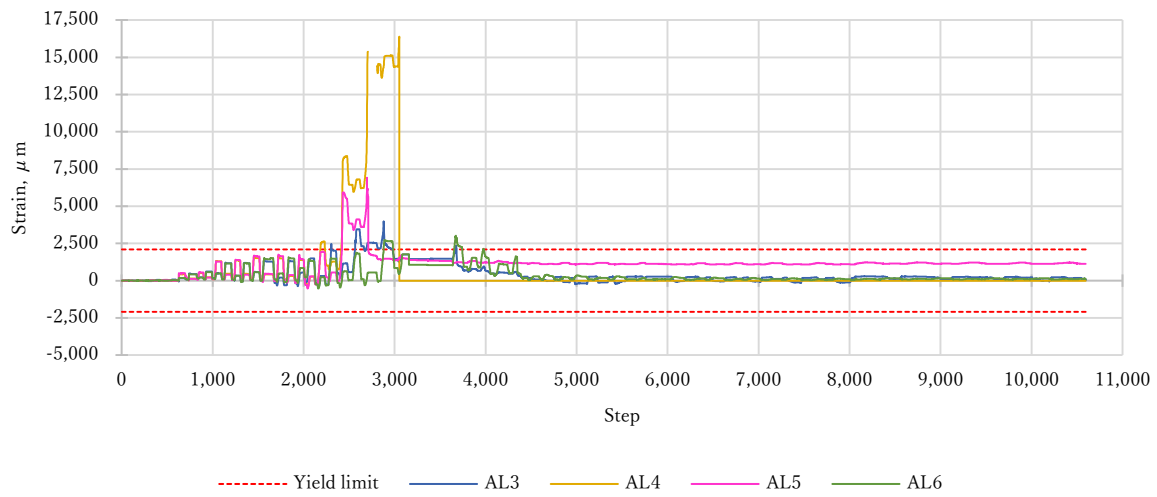
7.2.4 Strain Gauge of Specimen S9

7.2.4.1 Internal Strain Gauges



7.2.4.2 External Strain Gauges





8 REFERENCES

- Abdel-Hay Gabr, A., & Fawzy, Y. (2014). Behavior of Partially Defected RC Columns Strengthened Using Steel Jackets. *HBRC Journal*, 38. <https://doi.org/10.1016/j.hbrcj.2014.06.003>
- Aboutaha, R. S. (1994). Seismic retrofit of non-ductile reinforced concrete columns using rectangular steel jackets [Dissertation/Thesis].
- Aboutaha, R. S., Engelhardt, M. D., Jirsa, J. O., & Kreger, M. E. (1999). Rehabilitation of shear critical concrete columns by use of rectangular steel jackets [Article]. *Aci Structural Journal*, 96(1), 68-78.
- ACI. (2013). *ACI 374.2R-13 Guide for Testing Reinforced Concrete Structural Elements Under Slowly Applied Simulated Seismic Loads*. Farmington Hills, U.S.A.: American Concrete Institute
- ACI. (2019). *ACI 318-19 Building Code Requirements for Structural Concrete*. EE. UU.: American Concrete Institute
- Afghani-Khoraskani, R. (2015). Conclusions and Recommendations on Experimental Tests. In R. Afghani-Khoraskani (Ed.), *Advanced Connection Systems for Architectural Glazing* (pp. 115-123). Springer International Publishing.
- Aguilar-Ramos, G. (1997). *Efecto del Refuerzo Horizontal en el Comportamiento de Muros de Mampostería Confinada ante Cargas Laterales*. Universidad Nacional Autónoma de México. México, Distrito Federal.
- Alcocer, S. M. (2023). *Informe Técnico Parcial: Estudio Experimental de Columnas de Concreto Encamisadas con Elementos Metálicos*. <https://data.transparencia.cdmx.gob.mx/storage/app/uploads/public/653/96e/680/65396e6807bcc224821742.pdf>
- Alcocer, S. M., Rivera Vargas, D., Ayala Milián, A. G., Pérez Campos, X., Jean Perrillat, R., & Gallegos Suárez, A. (2022). *Los Sismos de Septiembre de 2017, Informe de la Sociedad Mexicana de Ingeniería Sísmica dentro de la serie Aprendiendo de los Sismos*. Sociedad Mexicana de Ingeniería Sísmica.
- Alper, I., & Fardis, M. N. (2014). Seismic Evaluation and Rehabilitation of Structures. In. Istanbul, Turkey: Springer.
- Badalamenti, V., Campione, G., & Mangiavillano, M. (2010). Simplified Model for Compressive Behavior of Concrete Columns Strengthened by Steel Angles and Strips. *Journal of Engineering Mechanics - ASCE*, 136. [https://doi.org/10.1061/\(ASCE\)EM.1943-7889.0000069](https://doi.org/10.1061/(ASCE)EM.1943-7889.0000069)
- Bazán, E., & Meli, R. (2000). *Diseño Sísmico de Edificios*. Limusa, Noriega Editors.
- Bazant, Z. P. (1999). Size effect on structural strength: a review. *Archive of Applied Mechanics*, 69 (9-10), 703-725. <https://doi.org/10.1007/s004190050252>
- Bazant, Z. P., & Oh, B. H. (1983). Crack Band Theory for Fracture of Concrete. *Volume 16*, 155-177. <https://doi.org/https://doi.org/10.1007/BF02486267> (Materials and Structures)
- Campione, G. (2013). RC Columns Strengthened with Steel Angles and Battens: Experimental Results and Design Procedure. *Practice Periodical on Structural Design and Construction*, 18, 1-11. [https://doi.org/10.1061/\(ASCE\)SC.1943-5576.0000125](https://doi.org/10.1061/(ASCE)SC.1943-5576.0000125)

- Carloni, C., Santandrea, M., & Wendner, R. (2017). An investigation on the "width and size effect" in the evaluation of the fracture energy of concrete [Proceedings Paper]. *Xxiv Italian Group of Fracture Conference, 2017, 3*, 450-458. <https://doi.org/10.1016/j.prostr.2017.04.065>
- Norma Técnica Complementaria para Diseño y Construcción de Estructuras de Concreto, NTC (2023a).
- Norma Técnica Complementaria para Evaluación y Rehabilitación Estructural de Edificios Existentes, (2023b).
- Chen, W.-F., & Atef, F. S. (1983). Constitutive Equations for Engineering Materials. *Computer Methods in Applied Mechanics and Engineering, 36* (3), 373-374. [https://doi.org/10.1016/0045-7825\(83\)90132-9](https://doi.org/10.1016/0045-7825(83)90132-9)
- Crainic, L., & Munteanu, M. (2013). *Seismic Performance of Concrete Buildings: Structures and Infrastructures Book Series, Vol. 9* (D. M. Frangopol, Ed. Vol. 9). CRC Press/Balkema.
- Crisfield, M. A., & Wills, J. (1989). Analysis Of RC Panels Using Different Concrete Models. *Journal of Engineering Mechanics, 115* (3), 578-597. [https://doi.org/10.1061/\(ASCE\)0733-9399\(1989\)115:3\(578\)](https://doi.org/10.1061/(ASCE)0733-9399(1989)115:3(578))
- Darwin, D., & Pecknold, D. A. W. (1974). *Inelastic Model for Cyclic Biaxial Loading of Reinforced Concrete* [Research Project](GI 29934). <https://kuscholarworks.ku.edu/entities/publication/cc29c401-bc11-4373-9fa5-e53d8145e866>
- De Borst, R. (1986). *Non-Linear Analysis of Frictional Materials* [PhD Thesis, Delft University of Technology]. The Netherlands. <https://repository.tudelft.nl/islandora/object/uuid%3Ad52ac7f8-d56f-4e0c-ab14-455ed02fcffe>
- Delgado, P., Rodrigues, V., Rocha, P. c., Santos, M., Arêde, A., Vila Pouca, N.,...Delgado, R. (2005, 2005/01/01/). *Seismic Retrofitting of Structural Elements. An Experimental Characterization*. 250th Anniversary of the 1755 Lisbon Earthquake,
- Dolce, M., Masi, A., Cappa, T., Nigro, D., & Ferrini, M. (2003, 2003). *Experimental Evaluation of Effectiveness of Local Strengthening on Columns of RC Existing Structures*.
- Elsamny, M. K., Hussein, A. A., Nafie, A. M., & Abd-Elhamed, M. K. (2013). *Experimental Study of Eccentrically Loaded Columns Strengthened Using a Steel Jacketing Technique*. World Academy of Science, Engineering and Technology, 7 (International Journal of Civil and Environmental Engineering), 900-907.
- Giménez, E., Adam, J., Ivorra, S., & Calderón, P. (2009). *Full-Scale Testing of Axially Loaded RC Columns Strengthened by Steel Angles and Strips*. Advances in Structural Engineering, 12, 169-181. <https://doi.org/10.1260/136943309788251704>
- Hassoun, M. N., & Akthem, A. A.-M. (2009). *Structural Concrete: Theory and Design* (5th ed.). John Wiley & Sons, Inc.
- Hordijk, D. A. (1991). *Local Approach to Fatigue of Concrete* [PhD Thesis, TU Delf]. Mekelweg 5, 2628 CD Delft, Netherlands. <https://repository.tudelft.nl/islandora/object/uuid%3Afa87147b-8201-47ed-83d7-b812b09c5fbb>
- Juárez-Luna, G., & González-Cuevas, O. M. (2022). *Estudio Numérico de la Continuidad del Refuerzo a Través del Sistema de Piso en la Rehabilitación de Columnas de CR con Ángulos y Soleras de Acero* (ISCDF/CEC-04/2022-04).
- Khalifa, E. S., & Al-Tersawy, S. H. (2014). *Experimental and Analytical Behavior of Strengthened Reinforced Concrete Columns with Steel Angles and Strips*. International Journal of Advanced Structural Engineering (IJASE), 6 (2), 6. <https://doi.org/10.1007/s40091-014-0061-6>
- Khedmatgozar Dolati, S. S. (2023). *Effects of Loading Protocol on the Strength and Deformation Capacity of Reinforced Concrete Column*. The University of Texas at San Antonio. San Antonio, Texas EE. UU.
- Kitzig, M., & Haussler-Combe, U. (2011). *Modeling of plain concrete structures based on an anisotropic damage formulation* [Article]. Materials and Structures, 44 (10), 1837-1853. <https://doi.org/10.1617/s11527-011-9741-x>
- Krawinkler, H., Zoheri, M., Lashkari-Irvani, B., Cofie, N., & Hadidi-Tamjed, H. (1983). *Recommendations for Experimental Studies on the Seismic Behaviour of Steel Components and Materials* [Research Project](61). https://stacks.stanford.edu/file/druid:qy317qj2969/TR61_Krawinkler_etal.pdf
- Kupfer, H., Hilsdorf, H. K., & Rüsche, H. (1969). *Behavior of Concrete Under Biaxial Stresses*. 66-52, 66.

- Lonati, S., Quiroga, B. F., Zehnder, C., & Antonakis, J. (2018). *On Doing Relevant and Rigorous Experiments: Review and Recommendations*. Journal of Operations Management, 64, 19-40. <https://doi.org/10.1016/j.jom.2018.10.003>
- M. Gere, J., & J. Goodno, B. (2009). *Mecánica de Materiales* (7 ed.). Cengage Learning Editores, S.A. de C.V.
- Makki, F. R., & Nimnim, S. T. (2015). *Rehabilitation of Structural Columns by Using Steel Angles*. International Journal of Scientific and Engineering Research, 6 (1), 981-987.
- Miranda, E. (2010). *Enhanced Building-Specific Seismic Performance Assessment*. Geotechnical, Geological, and Earthquake Engineering, 13 (Performance-Based Seismic Design and Retrofitting Methodologies), 183-191, Article 17. <https://doi.org/10.1007/978-90-481-8746-1>
- Murty, C. V. R., Goswami, R., Vijayanarayanan, A. R., Pradeep, K. R., & Mehta, V. V. (2022). *Introduction to Earthquake Protection of Non-Structural Elements in Buildings*. Gujarat State Disaster Management Authority.
- Nagaprasad, P., Sahoo, D. R., & Rai, D. (2009). *Seismic Strengthening of RC Columns Using External Steel Cage*. Earthquake Engineering & Structural Dynamics, 38, 1563-1586. <https://doi.org/10.1002/eqe.917>
- Park, R., & Paulay, T. (1933). *Reinforced Concrete Structures*. John Wiley & Sons, Inc.
- Pizzocchero, A. (2014). *Calibration and Validation of ATENA Concrete Material Model with Respect to Experimental Data* [Universita Degli Studi di Padova]. Padova PD, Italia.
- Salman, H. M., & Al-Sherrawi, M. H. (2018). *Finite Element Modeling of a Reinforced Concrete Column Strengthened with Steel Jacket*. Civil Engineering Journal, 4, 916-925, Article 5. <https://doi.org/http://dx.doi.org/10.28991/cej-0309144>
- Sen, D., & Begum, M. (2017). *A Comparative Study of Steel Angles and Strips Strengthened RC Columns*. Asian Journal of Civil Engineering, 18, 515-534.
- Sika. (2022). SikaGrout® Constructor Datasheet. In (01.02 ed.). México.
- Stelios, A. (2023). *Seismic Retrofit of Existing Reinforced Concrete Buildings*. John Wiley & Sons Ltd.
- Tarabia, A. M., & Albakry, H. F. (2014). *Strengthening of RC Columns by Steel Angles and Strips*. Alexandria Engineering Journal, 3(53), 615-626.
- USG. (2018). USG HYDRO-STONE® BRAND GYPSUM CEMENT SUBMITTAL SHEET. In U. I. S. Solutions (Ed.). EE. UU. Chicago: United States Gypsum Company.
- Van Mier, J. G. M. (1986). *Multiaxial Strain-Softening of Concrete*. Materials and Structures, 19 (3), 190-200. <https://doi.org/10.1007/BF02472035>
- Vecchio, F. J., & Collins, M. P. (1986). *The Modified Compression-Field Theory for Reinforced Concrete Elements Subjected to Shear*. Journal Proceedings, 83 (2), 219-231. <https://doi.org/10.14359/10416>
- Wilkins, M. L. (1963). *Calculation of Elastic-Plastic Flow*.
- Yu-Fei, W., Tao, L., & Deric J., O. (2005). *Fundamental Principles that Govern Retrofitting of Reinforced Concrete Columns by Steel and FRP Jacketing*.
- Červenka, V. (1985). *Constitutive Model for Cracked Reinforced Concrete*. Journal Proceedings, 82 (6), 877-882. <https://doi.org/10.14359/10409> (Journal ACI)
- Červenka, V., Pukl, R., Ožbolt, J., & Eligehausen, R. (1995). *Mesh Sensitive Effects in Smeared Finite Element Analysis of Concrete Fracture*. Proceedings of FRAMCOS2, 1387-1396. (Fracture Mechanics of Concrete Structures)
- Červenka, V., Červenka, J., & Jendele, L. (2013). *ATENA Program Documentation Part 1: Theory*. In. Prague: Červenka Consulting s.r.o.
- Červenka, V., Červenka, J., & Pukl, R. (2002). *ATENA - A tool for engineering analysis of fracture in concrete* [Article]. Sadhana-Academy Proceedings in Engineering Sciences, 27, 485-492. <https://doi.org/10.1007/bf02706996>